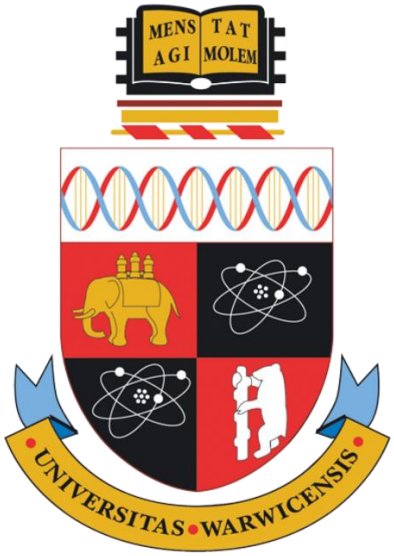

High Resolution Electrochemical Measurements for Corrosion

By

Lewis Yule

Thesis

Submitted to the University of Warwick for the degree of

Doctor of Philosophy

Supervisors: Prof Pat Unwin and Prof Barbara Shollock

Warwick Manufacturing Group

Department of Chemistry

September 2019

Contents

List of Figures i

List of Tables xii

Abbreviations xiii

Acknowledgements xiv

General Declaration xiv

Abstract xv

Chapter 1. Introduction 1

1.1 Context of corrosion science 1

1.2 Electrochemistry of corrosion 2

1.2.1 Corrosion cells: anodic and cathodic processes 2

1.2.2 Thermodynamics of corrosion reactions: The Nernst equation and Pourbaix diagrams 4

1.2.3 Kinetics of corrosion reactions: Butler-Volmer equation and mixed potential theory 7

1.3 Electrochemical measurement methods and experimental considerations 11

1.3.1 Electrochemical cells 11

1.3.2 Diffusion and mass transport at electrode surfaces 14

1.3.3 Chronoamperometry 17

1.3.4 Potential sweep voltammetry 18

1.4 Crystal structure and surface characteristics of metals and alloys 20

1.5 Microstructural influence on corrosion 23

1.5.1 Inclusions 24

1.5.2 Grain boundaries 26

1.5.3 Crystal orientation 28

1.6 Local electrochemical scanning methods used in corrosion 30

1.7 Scanning Electrochemical Cell Microscopy (SECCM) 35

1.8 Outline of thesis 39

1.9 References 41

Chapter 2. Experimental Methods 52

2.1 Chemicals and electrode materials 52

2.2 SECCM probe fabrication 54

2.3 SECCM operating system 56

2.4 Surface characterisation: electron microscopy techniques 58

2.4.1 Scanning Electron Microscopy (SEM) 58

2.4.2 Electron backscatter diffraction (EBSD) 59

2.4.3 Energy dispersive spectroscopy (EDS) 63

2.4.4 Focussed ion beam milling – Transmission electron microscopy (FIB-TEM) 63

2.5 SECCM for corrosion science: experimental challenges 64

2.5.1 Contamination between scanning points 65

2.5.2 Surface wetting 67

2.5.3 Unstable droplet size 69

2.5.4 Active/non-passivating electrolytes 71

2.6 References 72

Chapter 3. Scanning Electrochemical Cell Microscopy: A Versatile Method for Highly Localized Corrosion Related Measurements on Metal Surfaces 74

3.1 Abstract 74

3.2 Introduction 75

3.3 Experimental 77

3.3.1 Chemical reagents and electrode materials 77

3.3.2 Surface characterisation 78

3.3.3 Macroscale polarisation measurements 79

3.3.4 SECCM probe fabrication 79

3.3.5 SECCM set up 80

3.4 Results and Discussion 82

3.4.1 SECCM: operational principles and practical considerations 82

3.4.2 Crystallographic orientation and corrosion susceptibility in low carbon steel 89

3.4.3 Detecting and probing electrochemistry at MnS inclusions in low carbon steel 95

3.5 Conclusions 97

3.6 References 99

Chapter 4. Nanoscale Active Sites for the Hydrogen Evolution Reaction on Low Carbon Steel 104

4.1 Abstract 104

4.2 Introduction 105

4.3 Experimental 107

4.3.1 Electrode material and chemical reagents 107

4.3.2 Surface characterisation 108

4.3.3 SECCM probe fabrication 108

4.3.4 SECCM configuration 109

4.3.5 Density functional theory calculations 110

4.4 Results and Discussion 112

4.4.1 SECCM: operational principles 112

4.4.2 Hydrogen evolution reaction: crystallographic dependence 119

4.4.3 HER activity at grain boundaries 127

4.4.4 HER activity at manganese sulfide inclusions 131

4.5 Conclusions 133

4.6 References 135

Chapter 5. Nanoscale Electrochemical Visualization of Grain-Dependent Anodic Iron Dissolution from Low Carbon Steel 139

5.1 Abstract 139

5.2 Introduction **140**

5.3 Experimental **143**

5.3.1 Electrode material and chemical reagents **143**

5.3.2 Surface characterisation **143**

5.3.3 SECCM probe fabrication **144**

5.3.4 SECCM configuration **145**

5.3.5 Software and data processing **146**

5.3.6 Density functional theory calculations **147**

5.4 Results and Discussion **148**

5.4.1 SECCM: operational principles **148**

5.4.2 Spatially-resolved potentiodynamic polarisation experiments on low carbon steel **152**

5.4.3 Grain dependent anodic iron dissolution at low carbon steel **161**

5.4.4 STEM inspection of individual SECCM scanning sites **166**

5.4.5 Density functional theory calculations **167**

5.5 Conclusions **169**

5.6 References **170**

Chapter 6. Microstructural Control of the Absorption of Hydrogen into Polycrystalline Low Carbon Steel and Palladium **175**

6.1 Abstract **175**

6.2 Introduction **176**

6.3 Experimental **178**

6.3.1 Electrode materials and chemicals **178**

6.3.2 Surface characterisation **179**

6.3.3 Macroscale electrochemical measurements **180**

6.3.4 SECCM configuration **180**

6.4 Results and Discussion **182**

6.4.1 Hydrogen effects during chronoamperometry on low carbon steel..... 182

6.4.2 Cyclic voltammetry on palladium: macroscale vs. SECCM 187

6.4.3 Electrochemical mapping of palladium with SECCM 190

6.4.4 Influence of crystal orientation on hydrogen absorption on palladium 191

6.4.5 Probing hydrogen absorption at grain boundaries 197

6.5 Conclusions 200

6.6 References 201

Chapter 7. Summary 204

List of Figures

Figure 1. 1. Suspension failure due to extensive corrosion of the author's car……1

Figure 1. 2. Schematic of the formation of anodic and cathodic sites for Fe exposed to acidic electrolyte……3

Figure 1. 3. The construction of a simplified Pourbaix diagram (E vs pH) for iron in aqueous solution. **(a)** Catalytic electrochemical processes: (1) hydrogen evolution/oxidation reactions and (2) oxygen evolution/reduction reactions. **(b)** Iron dissolution processes including: (3) iron dissolution and (4) Fe^{2+}/Fe^{3+} reaction. **(c)** Processes associated with the formation of iron oxides: (5) Iron(III) oxide or ferric oxide. (6) and (7) magnetite oxide **(d)** (8) Iron(II) oxide formation (no charge transfer). **(e)** Final Pourbaix diagram for iron with reactions (1) to (8) included. Figure 1.3e was adapted from McCafferty (2010)……6

Figure 1. 4. Pourbaix diagram for iron with highlighted reaction domains: red = active, green = passive, blue = immune (cathodic processes)……7

Figure 1. 5. (a) and **(b)** Graphical representations of Butler-Volmer kinetics. Blue and red traces represent cathodic (reduction) and anodic (oxidation) processes respectively. Figure 1.5 was adapted from Stratmann and Frankel (2003)……9

Figure 1. 6. Simplified Evans diagram for a metal in acidic solution where the hydrogen evolution reaction (HER) acts as the cathodic counterpart reaction to metal dissolution. Blue and red traces represent cathodic (reduction) and anodic (oxidation) processes respectively. Figure 1.6 was adapted from Stratmann and Frankel (2003)……..10

Figure 1. 7. Schematic of a two electrode configuration. Figure 1.7 was adapted from Bard and Falkner (2001)……...12

Figure 1. 8. Schematic of a three electrode configuration. Figure 1.8 was adapted from Bard and Falkner (2001)……13

Figure 1. 9. Schematic diagrams of the diffusion patterns originating at inlaid electrodes for the cases of **(a)** a macroscale electrode exhibiting planar diffusion and **(b)** a microelectrode exhibiting spherical diffusion. Figure 1. 9 was adapted from Mallon (2013)……15

Figure 1. 10. *E-t* and *i-t* plots of chronoamperometry carried out using SECCM on low carbon steel in 5 mM H_2SO_4. Figure 1. 10 was adapted from Yule *et al* (2019)[16] and is also presented in Chapter 4……18

Figure 1. 11. *E-t* and *i-t* plots of cyclic voltammetry carried out using SECCM on low carbon steel in 5 mM H_2SO_4. Figure 1. 11 was adapted from Yule *et al* (2019) and is also presented in Chapter 5……19

Figure 1. 12. Simplified graphical representation of a Tafel plot for iron in acidic and neutral/basic media. Figure 1. 12 was adapted from McCafferty (2010)……20

Figure 1. 13. Electron backscatter diffraction (EBSD) maps of **(a)** polycrystalline low carbon steel and **(b)** annealed polycrystalline palladium……...21

Figure 1. 14. (a) Schematics of the unit cells for body centred cubic (BCC) and face centred cubic (FCC) crystal structures. **(b)** Low index orientations illustrated on a BCC cell……22

Figure 1. 15. (a) Stainless steel 304L surface, with MnS inclusions, imaged with (i) scanning electron microscopy (SEM) and energy dispersive spectroscopy (EDS) for (ii) Fe, (iii) Mn, and (iv) S. **(b)** Al 6061 surface, with MgSi inclusions and Fe impurities, imaged with (i) SEM and EDS for (ii) Al, (iii) Fe, (iv) Mg, and (v) Si……23

Figure 1. 16. Polarisation experiments, using the electrochemical droplet cell (EDC) method, of a MnS inclusion on 304 stainless steel in 1M NaCl. Polarisation curve 'a' shows the formation of a non-stable pit (curve shows repassivation after pitting event), whereas curve 'b' shows a stable pit as no repassivation is observed. Curve 'c' is taken on stainless steel with no inclusions present and thus no pitting event is observed. Figure 1. 16 was adapted from Webb *et al* (2001)……25

Figure 1. 17. Atomic force microscopy (AFM) maps showing variations in topography between grains after chemical etching on pure iron. Figure 1.17 was adapted from Schreiber *et al*…….29

Figure 1. 18. Schematic of local scanning probes used in corrosion science. **(a)** Scanning vibrating electrode technique (SVET) comprising of an oscillating detector, immersed in the electrolyte near the surface, measuring variations in potential gradient (indicated by dashed lines and the blue arrow). **(b)** Scanning electrochemical microscopy (SECM), comprising of an ultramicroelectrode (UME) positioned close to the surface, shown to be electrochemically reducing metal cations (produced by corrosion site) to metal solids. **(c)** Scanning kelvin probe (SKP), usually Au, oscillating above a thin layer of electrolyte covering a metal surface. A capacitance, *C*, is established when the probe and substrate are electronically connected. A contact potential difference, *CPD*, indicates the difference in fermi levels between the probe and substrate. Note that the schematic is not to scale……..33

Figure 1. 19. (a) Schematic of the electrochemical droplet cell method with and without the application of a silicon gasket. **(b)** Laser pulled glass capillary. **(c)** SEM image of the end of a

capillary of diameter 50 µm. **(d)** SEM image of the end of a capillary equipped with a silicon gasket. Figure 1. 19 was adapted from Lohrengel *et al* (2001)……...35

Figure 1. 20. Schematic of SECCM in dual barrel configuration, accompanied with a scanning transmission electron microscopy (STEM) image of the end of a duel barrel pipette of diameter 1 µm. Figure 1. 21 was adapted from Unwin *et al.* (2016)……..37

Figure 1. 21. Schematic of SECCM in single barrel configuration, accompanied with a STEM if a single barrel pipette of diameter 30 nm. Figure 1. 21 was adapted from Bentley *et al.* (2019)……38

Figure 2. 1. (a) EBSD map of an area of low carbon steel scanned using SECCM. **(b)** Topography, extracted using the approach distance of the SECCM probe during a scan, of the corresponding area of low carbon steel shown in **(a)**……..53

Figure 2. 2. Mounted samples **(a)** before polishing, **(b)** after polishing and **(c)** with wire attached……..54

Figure 2. 3. (a) Capillaries photographed before laser pulling. **(b)** Optical image collected using a microscope of the tip of a laser pulled capillary. **(c)** Optical images of a capillary during laser pulling. Figure 2. 1c was adapted from Sutter Instruments…….55

Figure 2. 4. (a) Generic SECCM positioning system with the key components labelled. **(b)** Mounting and encasement of the SECCM system…….57

Figure 2. 5. SEM image of the footprints left from SECCM measurements on low carbon steel……59

Figure 2. 6. (a) Schematic showing the origin of Kikuchi patterns originating from a crystal structure. **(b)** Kikuchi patterns originating from a copper substrate using EBSD. **(c)** EBSD software fitting predetermined Kikuchi patters to the experimental Kikuchi patterns shown in **(b)**. Figure 2.6a was adapted from O. Engler and V. Randle (2009).[7] Figures 2.6b and 2.6c were adapted from *"EBSD Explained: From data acquisition to advanced analysis"* Oxford instruments (2015)…….60

Figure 2. 7. EBSD maps of a low carbon steel surface. (a) Large area of low carbon steel with deformation apparent on the edge of the sample. (b) EBSD map of a freshly polishing low carbon steel surface. (c) EBSD map of a low carbon steel surface one month after polishing…61

Figure 2. 8. Image of the electron microscopy configuration for SEM, EBSD, and EDS analysis……..63

Figure 2. 9. SEM image of an SECCM scan performed on 304L stainless steel in 10 mM NaCl……...65

Figure 2. 10. SEM images of SECCM scans performed on low carbon steel in **(a)** 10 mM KNO_3 and **(b)** 10 mM H_2SO_4……66

Figure 2. 11. SEM images of SECCM scans performed on low carbon steel in **(a)** 10 mM KNO_3 and **(b)** 10 mM H_2SO_4……67

Figure 2. 12. SEM images of SECCM line scans performed on pure Ni in 50 mM KOH……..68

Figure 2. 13. SEM images of SECCM scan areas on 5052 Al in 50 mM H_2SO_4……68

Figure 2. 14. SEM images of SECCM line scans performed on pure Pd in 0.5 M H_2SO_4……..69

Figure 2. 15. SEM images of SECCM scans performed on low carbon steel in 10 mM H_2SO_4.....70

Figure 2. 16. SEM images of a SECCM scan performed on low carbon steel in 10 mM H_2SO_4……71

Figure 2. 17. SEM images of a SECCM scan performed on low carbon steel in 50 mM NaCl……...72

Figure 3. 1. (a) Schematic showing the voltammetric hopping-mode SECCM protocol employed to make spatially-resolved potentiodynamic polarisation measurements at a sample surface. The arrows indicate the path of probe across the surface. **(b)** Plots of the (i) *dc* and (ii) *ac* ionic current versus *z*-position as the micropipet probe is approached towards a low carbon steel surface. The surface was detected at an extension of 15.34 µm. **(c)** FE-SEM image of a 17×17 matrix of droplet 'footprints' on a low carbon steel surface, left after making spatially-resolved potentiodynamic polarization measurements using the SECCM setup outlined in (a). **(d)** Individual (red) and averaged (black) Tafel plots resulting from the row of droplet footprints highlighted by the yellow box in (c), obtained in a 10 mM KNO_3 solution at a sweep rate of 80 mV s^{-1}. The three 'regions' indicated in (d) correspond to: (1) cathodic, (2) passive and (3) the oxygen evolution reaction at the metal electrode surface. **(e)** Tafel plot taken from a macroscopic polarisation measurement of the low carbon steel in 10 mM KNO_3 at a sweep rate of 80 mV s^{-1}……..88

Figure 3. 2. Potentiodynamic polarisation experiments carried out at adjacent sites on a low carbon steel surface in 10 mM KNO_3 with a 2 µm diameter micropipet probe at sweep rates of (top to bottom) 0.5, 0.2, 0.1, 0.08, 0.05, 0.04, 0.02 and 0.01 V s^{-1}. The data are presented as **(a)**

i-E plots and **(b)** corresponding Tafel plots. The apparent shift in E_{corr} is caused by the increased contribution of nonfaradaic (charging) current to the total measured current with increasing sweep rate (see text)……...89

Figure 3. 3. (a) SEM image with the EBSD map superimposed and **(b)** the corresponding EBSD map of the area of the low carbon steel surface that was characterized with SECCM. The droplet 'footprints' remaining after each of the individual 256 potentiodynamic polarisation experiments are clearly visible in (a). **(c)** Grains deemed close enough to the low index planes are shown in **(i)**, **(ii)** and **(iii)** for (100), (101) and (111), respectively. **(d)** Representative Tafel plots obtained on the (100) (red trace), (101) (green trace) and (111) (blue trace) grains on the area of the low carbon steel surface shown in (a) and (b). The plots were obtained by averaging the *i-E* data collected during spatially-resolved potentiodynamic polarization measurements made with SECCM. 15, 12 and 26 individual measurements were averaged on the (100), (101) and (111) grains, respectively. The polarization experiments were carried out in 10 mM KNO_3 at a potentiodynamic sweep rate of 50 mV s^{-1} using a micropipet probe with a diameter of 2 µm. The highlighted section is of the potential region spanning –0.4 to +0.45 V vs. Ag/AgCl, which is shown magnified in the *i-E* plot. The dashed lines included above and below the traces represents the standard error of the data…….93

Figure 3. 4. (a) SEM image with the EBSD map superimposed and **(b)** corresponding EBSD map of the area of the low carbon steel surface that was characterized with SECCM. **(c)** Grains deemed close enough to the low index planes are shown in **(i)**, **(ii)** and **(iii)** for (100), (101) and (111), respectively. **(d)** Representative Tafel plots obtained on the (100) (red trace), (101) (green trace) and (111) (blue trace) grains on the area of the low carbon steel surface shown in **(a)** and **(b)**. The data were obtained by averaging the *i-E* data collected during spatially-resolved potentiodynamic polarization measurements made with SECCM. 41, 19 and 38 individual measurements were averaged on the (100), (101) and (111) grains, respectively. The polarization experiments were carried out in 10 mM KNO_3 at a sweep rate of 40 mV s^{-1} using a micropipet probe with a diameter of 2 µm. The highlighted section is of the potential region spanning –0.2 to +0.15 V vs. Ag/AgCl, which is shown magnified in the *i-E* plot. The dashed lines included above and below the traces represents the standard error of the data……...94

Figure 3. 5. (**a**) SEM image of MnS inclusions (indicated by coloured circles) on a low carbon steel surface. **(b)** Energy dispersive X-ray spectroscopy (EDS) responses of each of the inclusions, with the colours corresponding to the inclusions highlighted in **(a)**…….95

Figure 3. 6. (a) SEM images of adjacent droplet footprints with (2) and without (1 and 3) an MnS inclusion (indicated by a red circle). **(b)** Tafel plots obtained at the corresponding points labelled in (a). The potentiodynamic polarization experiments were performed in the SECCM

format (probe diameter = 2 μm) on low carbon steel in 10 mM KNO_3 at a sweep rate of 80 mV s^{-1}……...97

Figure 4. 1. (a) Schematic showing the SECCM hopping-mode protocol used to make spatially resolved electrochemical (i_{surf}−t) measurements on the substrate (working electrode) surface. The arrows indicate the path taken by the probe during the scanning. For this investigation, the diameter of the probe, x, was 150 nm and the 'hopping distance', d, was 800 nm. The nanopipet was filled with 5 mM H_2SO_4 solution (pH ≈ 2.3) and equipped with a Pd/H_2 QRCE. **(b) (i)** Landing potential, E_{app} = 0.463 V vs Ag/AgCl for 10 ms followed by E_{app} = −1.337 V vs Ag/AgCl for 10 ms and **(ii)** representative i_{surf}−t transient, taken from a single hop of a scanning experiment. **(c)** SEM image of a (40 × 40) pixel^2 (32 × 32) μm^2 grid, after SECCM-scanning, with the array of dots 'footprints' denoting the locations of the electrochemical measurements. **(d)** EBSD map obtained from the area delineated by the white box in (c)**. (e)** Corresponding topographical image of the area in highlighted in (c) and (d), constructed from the synchronously obtained z-height data (piezo-position at meniscus contact) in SECCM (no interpolation of data)……114

Figure 4. 2. (a) Plot of surface (substrate) current, i_{surf}, versus the extension of the z-direction piezo during the approach of the SECCM probe to a low carbon steel surface. In this case, the surface was detected at a z-piezo extension of 6.96 μm as indicated by the increase ('spike') in surface current, whereupon the approach was halted. The potential applied during the approach was +0.463 V vs Ag/AgCl. **(b)** Representative SECCM linear sweep voltammograms of low carbon steel in 5 mM H_2SO_4, where the substrate potential ($E_{applied}$) was swept cathodically (*i.e.*, from high to low potential) at 1 Vs^{-1} in air (blue trace) and under argon (red trace) using SECCM. The potentials chosen for chronoamperometry experiments are indicated: (1) Landing and preconditioning: +0.463 V and (2) HER: -1.337 V vs Ag/AgCl. **(c)** i_{surf} response from a single SECCM scanning site on low carbon steel in 5 mM H_2SO_4. Transient arising from an applied potential, E_{app}, of +0.463 V vs Ag/AgCl……..116

Figure 4. 3. (a) Average Qt (charge passed) response for all SECCM scanning sites arising from a -1.337 V vs Ag/AgCl pulse on low carbon steel in 5 mM H_2SO_4. **(b)** Graphic representation of the assumed volume of oxide film (Fe_2O_3) present at each SECCM scanning site on a low carbon steel surface. Charge required to remove 400 nm cylinder of 5 nm thickness of Fe_2O_3: $Q = \frac{V \cdot \rho_{Fe2O3} \cdot F \cdot z}{M_{Fe2O3}}$ where Q = charge transferred, F = Faraday's constant, z = number of electrons transferred, V = volume of Fe_2O_3 cylinder, ρ_{Fe2O3} = density of Fe_2O_3, M_{Fe2O3} = molar mass of Fe_2O_3……117

Figure 4. 4. SEM image of a collection of droplet 'footprints' on a low carbon steel surface. The size of the footprints is shown to be consistent. The enlarged regions show that the footprint

is not altered by the presence of a grain boundary and a measurement of the diameter of a footprint……...118

Figure 4. 5. (a) EBSD maps of the areas of the low carbon steel surface that were characterized with SECCM. **(b)** Spatially-resolved i_{surf} maps (2500 pixels) over a (40 × 40) μm^2 area, corresponding to the areas shown above in **(a)**. The i_{surf} values are the average of the last six data points (*i.e.*, 7.2 to 9.8 ms) and the data are presented as the recorded currents (no interpolation). With the SECCM footprint areas defined in the text, the maximum and minimum currents of 100 pA and 55 pA corresponds to current densities of *ca.* 80 and 44 mA cm^{-2}, respectively. The maps were taken at E_{app} = −1.337 V vs Ag/AgCl with a probe of 150 nm diameter containing 5 mM H_2SO_4……120

Figure 4. 6. (a) Grains within the area scanned with SECCM that have a crystal orientation within 10º of the (i) (100) (ii) (101) and (iii) (111) low index orientations of low carbon steel. **(b)** Histogram of the average surface currents, i_{surf}, measured from 7.2 to 9.8 ms from each of the measurement landing on the low index grains indicated in (a)……123

Figure 4. 7. Schematic of each of the low index crystal planes in the body centered cubic (BCC) crystal structure of iron (grey spheres) with the calculated hydrogen adsorption sites (white spheres)……125

Figure 4. 8. (a) EBSD map of a "cathodically active" grain boundary, with the misorientation between the two neighboring grains labelled inset. **(b)** Spatially-resolved i_{surf} map of the average response from 7.2 to 9.8 ms during a −1.337 V vs Ag/AgCl reduction pulse, in the area of the surface shown in (a). **(c)** and **(d)** EBSD-SECCM i_{surf} map comparisons for two more examples of grain boundaries with enhanced HER activity. There is no interpolation of data in the SECCM images……...129

Figure 4. 9. (a) EBSD image of the area scanned with SECCM (main text, Figure 4) with the grain boundary of interest highlighted. **(b)** The corresponding topography map, constructed from the *z*-height data collected synchronously during SECCM……..130

Figure 4. 10. (a) SEM image of the area of low carbon steel scanned with SECCM. The matrix of 50 × 50 scanning points (pixels) can be seen as dark spots on the surface. The darker spots, two of which are highlighted, are MnS inclusions. **(b)** Corresponding spatially resolved i_{surf} map (E_{app} = −1.337 V vs Ag/AgCl), with no interpolation of data. **(c)** Zoomed-in (i) SEM (ii) EDS sulfur map and (iii) i_{surf} images of the boxed area highlighted in (a) and (b). **(d)** EDS spectra of the left inclusion shown in (c). Note that the i_{surf} values are the average of the last six data points (*i.e.*, 7.2 to 9.8 ms)……132

Figure 4. 11. (a) and **(b)** Two further examples of areas of the low carbon steel surface scanned with SECCM containing MnS inclusions. In each case co-located maps are shown that are obtained with (i) SEM, (ii) EDS for sulphur and (iii) i_{surf} at −1.337 V (vs Ag/AgCl)……133

Figure 5. 1. (a) Schematic of the voltammetric hopping-mode protocol of SECCM, used herein. The direction of motion by the probe is indicated by the red arrows. In this study, the nanopipet was filled with 5 mM H_2SO_4 and equipped with a Pd/H_2 QRCE. **(b)** Plots of **(i)** z-extension, **(ii)** applied potential, *E*, **(iii)** surface current, i_{surf}, during a single "hop" of a voltammetric SECCM experiment (voltammetric scan rate, υ = 2 V s^{-1}). **(c)** SEM image taken of the low carbon steel surface, showing 15 individual droplet "footprints", after an SECCM scan. The nanopipet diameter was 150 nm, the hopping distance, *d*, between pixels was 1.2 µm and the droplet "footprint" diameter, *x*, for each measurement was measured as ≈450 nm……...151

Figure 5. 2. Scanning electron microscopy (SEM) image of an area of a low carbon steel surface that has been scanned using the voltammetric hopping mode SECCM protocol. The array consists of 3600 (60 × 60 $pixels^2$) individual measurements, each droplet "footprint" ≈450 nm in diameter, covering an area of 72 × 72 µm…….152

Figure 5. 3. (a) Potentiodynamic polarisation (*i*−*E*) curve (υ = 2 V s^{-1}), obtained by averaging the forward sweep of 3600 (60 × 60 $pixel^2$ covering 72 × 72 μm^2) individual measurements on a low carbon steel sample. The nanopipet was ≈150 nm in diameter and filled with 5 mM H_2SO_4. **(b)** Simplified Pourbaix diagram for Fe. Coloured arrows indicate the potential range covered by the potentiodynamic polarisation curve in (a) at pH 2.3, with the numbers on the plot correspond to the following: ① passive film formation, ② passive film reduction, ③ active iron dissolution and ④ cathodic processes (HER and ORR). **(c)** Spatially-resolved i_{surf} maps obtained at **(i)** 0.063 V **(ii)** -0.587V **(iii)** -0.547V and **(iv)** -1.437 V vs Ag/AgCl [indicated on the corresponding average *i*−*E* curve in (a)]. Note the different current scales. **(d)** Corresponding EBSD map, showing the crystallographic structure of the area scanned with SECCM in (c)……..156

Figure 5. 4. (a) Spatially-resolved i_{surf} map obtained at a potential of -0.447 V vs Ag/AgCl QRCE using the voltammetric SECCM configuration. The i_{surf} maps comprise 3600 pixels (60 × 60 $pixels^2$) over a 72 × 72 µm area, obtained with a nanopipet probe of diameter ≈ 150 nm containing 5 mM H_2SO_4. **(b)** *i*−*E* curves (υ = 2 V s^{-1}) obtained from the 5 highly active pixels (coloured traces) labelled in (a) versus the average response (black trace) obtained from the 3600 pixels across the surface. **(c)** Scanning electron microscopy (SEM) image of corresponding area scanned with SECCM shown in (a). **(d)** Zoomed-in SEM images of the "active pixels" (the centre spot of each 3 × 3 array of spots) indicated in (a) and (c)…….158

Figure 5. 5. (a) i–E curve (υ = 2 V s^{-1}), obtained by averaging the forward sweep of 3600 (60 × 60 $pixel^2$ covering 72 × 72 μm^2) individual measurements on a low carbon steel, performed in the voltammetric hopping mode SECCM configuration. The nanopipet was ≈150 nm in diameter and filled with 5 mM H_2SO_4. The reduction peak potential, V_p^{Red}, oxidation peak potential, V_p^{Ox}, and oxidation peak current, i_p, are labelled on the plot. Spatially-resolved maps of **(b)** V_p^{Red}, **(c)** i_p and **(d)** V_p^{Ox}……159

Figure 5. 6. (a) EBSD and **(b)** corresponding spatially-resolved full width at half maximum (FWHM, based on the anodic iron dissolution peak) maps, obtained from a low carbon steel surface. The maps in (b) were obtained in the voltammetric hopping mode SECCM configuration (υ = 2 V s^{-1}), with a nanopipet probe of ≈150 nm diameter containing 5 mM H_2SO_4……..160

Figure 5. 7. (a) Electron backscatter diffraction (EBSD) and **(b)** corresponding spatially-resolved oxidation peak current (i_p) maps, obtained from various areas of a low carbon steel surface. The maps in (b) were obtained in the voltammetric hopping mode SECCM configuration (υ = 2 V s^{-1}), with a nanopipet probe of ≈150 nm diameter containing 5 mM H_2SO_4……..161

Figure 5. 8. (a) EBSD maps identifying the grains that have crystal orientations within 10º of the low index orientations, **(i)** (100), **(ii)** (101) and **(iii)** (111). **(b)** i–E curve (υ = 2 V s^{-1}) obtained by averaging the individual measurements performed on each of the low-index orientations [red = (100), blue = (111) and green = (101)], using the voltammetric hopping mode SECCM configuration. The nanopipet was ≈150 nm in diameter and filled with 5 mM H_2SO_4. **(c)** Distribution of i_{surf} measured at -0.581 V vs Ag/AgCl [indicated by dashed line on (b)] on each of the low index orientations……165

Figure 5. 9. (a) Step-by-step outline of the focussed ion beam (FIB) milling procedure used to extract single SECCM droplet "footprint" sites for cross-sectional analysis. **(i)** Covering the scanning site of interest with a protective platinum layer. **(ii)** and **(iii)** Ga ion beam milling around selected section. **(iv)** Removal of the extract from the low carbon steel matrix. **(v)** Thinning of the extracted section. **(b)** Cross-sectional scanning transmission electron microscopy (STEM) image of the extract. **(c)** (i) STEM image of the cross section of a droplet "footprint" (nanopipet diameter = 2 μm in this experiment), accompanied by corresponding EDS analysis for **(ii)** iron, **(iii)** oxygen **(iv)** sulphur, and **(v)** platinum……..167

Figure 5. 10. Plot of i_{surf} measured at -0.581 V vs Ag/AgCl for each low index crystal orientations (100, 101 and 111) of low carbon steel in 5 mM H_2SO_4, against the energy required

to remove (and ionise) one monolayer of iron from each of the low index surface per atom removed……...169

Figure 6. 1. Diagram showing the adsorption and subsequent absorption of hydrogen into a metal……177

Figure 6. 2. (a) Schematic of the SECCM set up. **(b)** Photograph of the custom built environmental cell used to perform experiments under argon conditions……181

Figure 6. 3. (a) Cyclic voltammogram measured with SECCM on low carbon steel in 5 mM H_2SO_4, at a scan rate v = 2 Vs^{-1}. **(b)** Plots of the potential applied, *E*, and the measured surface current, *i*, response during a single SECCM measurement. **(c)** Transient response resulting from an anodic pulse of 1.1 V vs Pd/H_2, following a cathodic pulse at -0.8 V for 20 ms and 30 ms (red and green traces respectively) or -0.4 V for 20 ms (blue trace)……..184

Figure 6. 4. (a) SEM image of an area of low carbon steel scanned with SECCM. **(b)** Average transient response arising from a potential step to -0.8 V vs Pd/H_2. **(c)** Spatially resolved surface current map at 20 ms from the transient shown in **(b)**, collected using SECCM of the area shown in (a). **(d)** Average transient response arising from a potential step to +1.1 V vs Pd/H_2. **(e)** Surface currents maps taken at (i) 3.9, (ii) 4.94, (iii) 10.92, and (iv) 20.02 ms from the transient response shown in **(d)**……..186

Figure 6. 5. (a) Cyclic voltammogram (CV) recorded from annealed palladium wire in de-gassed 0.5 M H_2SO_4 at a scan rate of v = 0.5 Vs^{-1}. The presented CV is the response following 25 cycles. Note that a commercial Ag/AgCl (3.4 M KCl) reference electrode was used. **(b)** CV recorded from annealed platinum wire with the same conditions used as **(a)**. **(c)** CV recorded with SECCM on palladium foil in 0.5 M H_2SO_4 at scan rate of v = 2 Vs^{-1} after 5 cycles. The droplet diameter was ≈ 900 nm (100 pA of current corresponds to 15.7 $mA \cdot cm^{-2}$ of current density). **(d)** CV recorded with SECCM with the same conditions as **(c)** (under argon), showing the response from 10 cycles……189

Figure 6. 6. (a) Average cyclic voltammogram from all scanning points of an SECCM map carried out on annealed palladium in 0.5 M H_2SO_4. **(b)** EBSD map of the SECCM scanning area. Spatially resolved surface current maps recorded at **(c)** 0.7 V, **(d)** -0.2 V, and **(e)** -0.45 V vs Ag/AgCl, taken after 4 cycles……..191

Figure 6. 7. (a) SEM image of the SECCM scanning area on palladium. The scan covers a 200 × 175 µm area comprising of 41 × 35 (1435 total) individual scanning sites (pixels), with a hopping distance of 5 µm. The droplet diameter in this scan was ≈ 900 nm. (100 pA current ≈ 15.7 $mA \cdot cm^{-2}$ of current density). **(b)** EBSD map of the scanned area. **(c)** Plot of the deviations of each grain (labelled in **(b)**) relative to the low index orientations. **(d)** Spatially resolved

surface current map taken at -0.45 V vs Ag/AgCl after 4 cycles. **(e)** Plot of the average surface current in conjunction with the deviation relative to the low index orientations of each grain labelled in **(b)**……...194

Figure 6. 8. (a) SEM image of the SECCM scanning area on palladium. The scan covers a 138 × 63 µm area comprising of 45 × 20 (900 total) individual scanning sites (pixels), with a hopping distance of 3 µm. The droplet diameter in this scan was ≈ 2 µm. (100 pA current ≈ 3.18 mA·cm^{-2} of current density). **(b)** EBSD map of the scanned area. **(c)** Plot of the deviations of each grain (labelled in **(b)**) relative to the low index orientations. **(d)** Spatially resolved surface current map taken at -0.45 V vs Ag/AgCl after 4 cycles. **(e)** Plot of the average surface current in conjunction with the deviation relative to the low index orientations of each grain labelled in **(b)**……195

Figure 6. 9. (a) SEM image of the SECCM scanning area on palladium. The scan covers a 200 × 180 µm area comprising of 41 × 37 (1517 total) individual scanning sites (pixels), with a hopping distance of 5 µm. The droplet diameter in this scan was ≈ 2.8 µm. (100 pA current ≈ 1.62 mA·cm^{-2} of current density). **(b)** EBSD map of the scanned area. **(c)** Plot of the deviations of each grain (labelled in **(b)**) relative to the low index orientations. **(d)** Spatially resolved surface current map taken at -0.45 V vs Ag/AgCl after 4 cycles **(e)** Plot of the average surface current in conjunction with the deviation relative to the low index orientations of each grain labelled in **(b)**……...196

Figure 6. 10. Graphical representation of the misorientation of various high index orientations relative to the low index orientations of (100), (101), and (111)……...197

Figure 6. 11. (a) and **(b)**, SECCM scan areas of two regions on annealed palladium. The scans consist of **(a)** 30 × 29 sites (870 total) covering 116 × 112 µm, and **(b)** 36 × 36 sites (1296 total) covering 140 × 140 µm. Both scans employed a hopping distance of 4 µm. SEM images, EBSD maps, and surface current maps (for E = -0.4 V and -0.45 V vs Ag/AgCl) are shown in (i), (ii), (iii), and (iv) respectively……198

Figure 6. 12. (a) Surface current map, recorded with SECCM at -0.45 V vs Ag/AgCl, of a grain boundary on annealed palladium foil, accompanied with SEM images of the boxed areas. **(b)** Cyclic voltammograms of the scanning points indicated in **(a)**……200

Figure 7. 1. Summary of the findings relating the dependency of corrosion process on the microstructure of low carbon steel. The sections highlighted in red, green, and blue correspond to the results discussed in chapters……...209

List of Tables

Table 2. 1. Specification of capillary material, diameter and the pulling parameters used to fabricate pipettes for experiments in Chapters 3, 4, 5 and 6……55

Table 3. 1. Chemical composition of the low carbon steel determined using energy dispersive X-ray spectroscopy……78

Table 4. 1. Chemical composition of the low carbon steel determined using energy dispersive X-ray spectroscopy……..108

Table 4. 2. ΔG_H values calculated for each adsorption site on the (111) plane of Pt and each of the low index planes (100, 101 and 111) of Fe……..125

Table 4. 3. The calculated average ΔG_H deviations for each of the adsorption sites on the low index orientations of Fe from the average ΔG_H value calculated for Pt(111)……126

Table 5. 1. Chemical composition of the low carbon steel determined using energy dispersive X-ray spectroscopy……..143

Table 6. 1. Chemical composition of the low carbon steel determined using energy dispersive X-ray spectroscopy……..179

Abbreviations

AFM	Atomic force microscopy
BCC	Body centred cubic
CV	Cyclic voltammogram
DFT	Density functional theory
E_{app}	Applied potential
EBSD	Electron backscatter diffraction
EDC	Electrochemical droplet cell
EDS	Energy dispersive spectroscopy
E_{rev}	Reversible potential
FCC	Face centred cubic
FIB	Focussed ion beam
FPGA	Field-programmable gate array
HER	Hydrogen evolution reaction
i_{surf}	Surface current
LSV	Linear sweep voltammogram
OER	Oxygen evolution reaction
ORR	Oxygen reduction reaction
QRCE	Quasi-reference counter electrode
SECCM	Scanning electrochemical cell microscopy
SECM	Scanning electrochemical microscopy
SEM	Scanning electron microscopy
SEPM	Scanning electrochemical probe microscopy
SKP	Scanning kelvin probe
STEM	Scanning transmission electron microscopy
SVET	Scanning vibrating electrode technique
TEM	Transmission electron microscopy
UME	Ultramicroelectrode

Acknowledgements

Firstly, I would like thank both of my supervisors Prof Patrick R. Unwin and Prof Barbara A. Shollock for all of their support and encouragement throughout my PhD. I am extremely grateful and fortunate to have been given the opportunity to carry out research in the excellent facilities available in the Warwick Electrochemistry and Interfaces Group, and at Warwick Manufacturing Group.

I would especially like to thank Dr Cameron Bentley for acting as an excellent mentor throughout my PhD. A majority of the work in this thesis would not have been possible without Cameron's guidance.

Additionally, I would like to thank the members of the Warwick Electrochemistry and Interfaces group, particularly Dr Minkyung Kang, Dr Slava Shkirskiy, and Enrico Daviddi, for being excellent colleagues who were always willing to provide advice. Special thanks to Dr Geoff West for all of the advice and training he provided in the microscopy suite at WMG, and for acting as my supervisor for the final months of my PhD. I would also like to thank Tata Steel, Research and Development, for their funding support, and Dr Digvijay Thakur for his valuable input from an industrial perspective.

I appreciate the support from my parents, my brother, and the various housemates (Ted, Matt, and Alex) I've had during my PhD. Also a special thanks to Rosie for all of her encouragement and positivity throughout my time at Warwick.

Finally I would like to thank the Engineering and Physical Sciences Research Council (EPSRC) for their funding support.

General Declaration

The work presented in this thesis is entirely original and my own work, expect where acknowledged in the list below. I confirm that this thesis has not been submitted for a degree at another University. Material from this thesis has been published, as noted below.

The material in Chapter 3 was published as:

Scanning electrochemical cell microscopy: A versatile method for highly localised corrosion related measurements on metal surfaces. Lewis C. Yule, Cameron L. Bentley, Geoff West, Barbara A. Shollock, Patrick R. Unwin. *Electrochimica Acta*. **2019**, 298, 80-88

The material in Chapter 4 was published as:

Nanoscale Active Sites for the Hydrogen Evolution Reaction on Low Carbon Steel. Lewis C. Yule, Viacheslav Shkirskiy, Jolyon Aarons, Geoff West, Cameron L. Bentley, Barbara A. Shollock, Patrick R. Unwin. *The Journal of Physical Chemistry C*. **2019**, *Accepted*. Density functional theory calculations were performed by Viacheslav Shkirskiy and Jolyon Aarons.

The material in Chapter 5 was submitted for publication as:

Nanoscale Electrochemical Visualization of Grain-Dependent Anodic Iron Dissolution from Low Carbon Steel. Lewis C. Yule, Viacheslav Shkirskiy, Jolyon Aarons, Geoff West, Barbara A. Shollock, Cameron L. Bentley, Patrick R. Unwin. *Electrochimica Acta*. **2019**, *Submitted*. Density functional theory calculations were performed by Viacheslav Shkirskiy and Jolyon Aarons. Focussed ion beam milling and transmission electron microscopy were performed by Geoff West.

The material in Chapter 6 is to be submitted for publication as:

Microstructural Control of the Absorption of Hydrogen into Polycrystalline Low Carbon Steel and Palladium. Lewis C. Yule, Enrico Daviddi, Barbara A. Shollock, Cameron L. Bentley, Patrick R. Unwin. *Journal of Electroanalytical Chemistry* **2019**. The methodology behind the graphical representation plots of the orientations of individual grains relative to low index planes was developed by Enrico Daviddi.

Additionally, I have also contributed to the following publication whose results are not published in this thesis:

Correlative Electrochemical Microscopy of Li-Ion (De)intercalation at a Series of Individual $LiMn_2O_4$ Particles. Binglin Tao, Lewis C. Yule, Enrico Daviddi, Cameron L. Bentley, Patrick R. Unwin. *Angewandte Chemie* **2019**, 131, 4654-4659

Abstract

Scanning electrochemical cell microscopy (SECCM) is a recently developed technique that has the ability to perform multiple reproducible electrochemical measurements with very high spatial resolution at surfaces. Despite its success in the study of nanoparticle electrocatalysis and carbon nanomaterials, SECCM has yet to be applied to the field of corrosion science. This thesis presents the first efforts to utilise SECCM as a tool to study corrosion related phenomena. In this work, comparisons are made between SECCM and similar techniques that are currently used in corrosion science to identify where SECCM can be most effective and how it can improve on these existing methods. The corrosion related behaviour associated with the microstructural features of metals and alloys (*e.g. grain orientation*, *grain boundaries*, and *inclusions*) is a popular topic amongst researchers adopting high resolution electrochemical methods. Considering the recent success of applying SECCM to resolve the relationship between electrochemical behaviour and surface structure, this proved to be the ideal topic to introduce SECCM into corrosion science. The relationship between the crystal orientation of grains on polycrystalline metals and the rates of various corrosion related processes, including: *anodic dissolution*, *cathodic hydrogen evolution*, *passive behaviour*, and *hydrogen absorption*, in neutral and acidic media is revealed successfully in this work. The electrochemical behaviour of individual nanoscale inclusions and grain boundaries is also investigated. These results were collected using SECCM in combination with various complementary and correlative surface characterisation techniques (*e.g. electron backscatter diffraction*, and *energy dispersive spectroscopy)* applied to the same electrode region as the SECCM measurements, and computational methods (*e.g. density functional theory)*. In summary, this thesis has shown that SECCM has the ability to contribute significantly in the field of corrosion science.

CHAPTER 1
Introduction

1.1 Context of corrosion science

It was estimated in a study by the national association of corrosion engineers (NACE) that, in 2013, the global cost of corrosion was US$2.5 trillion, which was equivalent to 3-4% of the global Gross Domestic Product (GDP).[1] The origin of these costs stem from factors such as: maintenance, the replacement of components (Figure 1.1), and the development of new corrosion resistant alloys, complex surface treatments, and corrosion resistant coatings. In order to reduce these costs significant research into the understanding, prediction, and prevention of corrosion has and continues to take place.

Figure 1. 1. Suspension failure due to extensive corrosion of the author's car.

1.2 Electrochemistry of corrosion

Corrosion occurs as a result of multiple electrochemical processes. Electrochemistry is concerned with reactions taking place at the interface between an electrode and an electrolyte. When a metal surface comes into contact with an electrolyte, charge is transferred across the interface due to the transfer of ions from the electrode into the electrolyte (or vice versa), and from the transfer of electrons between ions in the electrolyte or those adsorbed onto the electrode surface.[2]

1.2.1 Corrosion cells: anodic and cathodic processes

During corrosion, the oxidation of metal atoms, *M*, from the surface can occur in suitable conditions:

$$M \rightarrow M^{z+} + ze^{-} \qquad (1)$$

an example of this is the oxidation of iron.

$$Fe \rightarrow Fe^{2+} + 2e^{-} \qquad (2)$$

This half-cell reaction results in the liberation of electrons which must be consumed by a corresponding reduction reaction to support the process. A common reduction process in acidic electrolyte is the hydrogen evolution reaction (HER):

$$2H^{+} + 2e^{-} \rightarrow H_2 \qquad (3)$$

Whereas in neutral media the oxygen reduction reaction (ORR) is more prevalent:

$$O_2 + 2H_2O + 4e^{-} \rightarrow 4OH^{-} \qquad (4)$$

Using the example of Fe in acidic solution, the complete corrosion reaction would be:

$$Fe + 2H^+ \rightarrow Fe^{2+} + H_2 \qquad (5)$$

On a metal surface, oxidation takes place at anodes and reduction takes place at cathodes and it is the formation of these electrochemical cells that often drives corrosion, as shown schematically in Figure 1.2. Anodes and cathodes can form randomly on the surface (uniform corrosion), or at fixed locations associated with surface heterogeneities which leads to localised forms of corrosion such as pitting, galvanic corrosion or intergranular corrosion. Surface heterogeneities, including grain boundaries, grains of different crystal orientation, inclusions and defects are often inevitable in metal alloys and are discussed further in section 1.4.

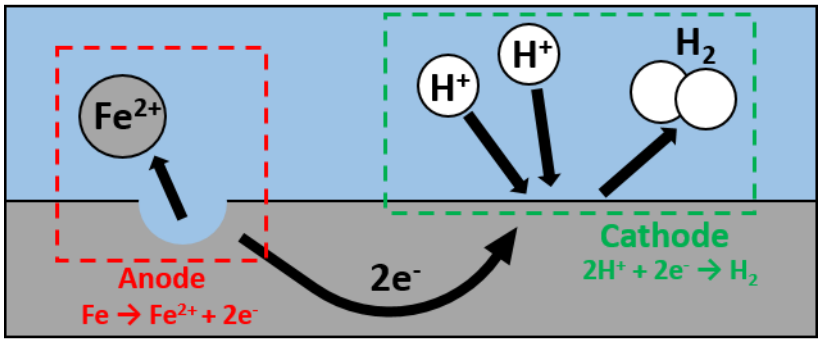

Figure 1. 2. Schematic of the formation of anodic and cathodic sites for Fe exposed to acidic electrolyte.

In some conditions, metals can become 'passive' due to the instantaneous formation of an oxide film which effectively inhibits active dissolution from the surface. This oxide film can form from an oxidation process such as:

$$M + \frac{z}{2}H_2O \rightarrow MO_{\frac{z}{2}} + zH^+ + ze^- \qquad (6)$$

for example, the passivation of iron can occur due to the following process:

$$2Fe + 3H_2O \rightarrow Fe_2O_3 + 6H^+ + 6e^- \qquad (7)$$

The characteristics of oxide films are strongly influenced by the conditions in which they form, such as the electrolyte, or the heterogeneity and chemistry of the substrate.[2] Understanding how each of these individual oxidation and reduction processes occur and what promotes/inhibits them on metal surfaces is crucial to the overall understanding of corrosion.

1.2.2 Thermodynamics of corrosion reactions: The Nernst equation and Pourbaix diagrams

Using basic thermodynamics, the tendencies for metals to corrode in given conditions can be predicted. The change of free energy, ΔG, can be used to quantify the driving force of an electrochemical process (Equation 9).[3] It is defined as the difference in free energy, G, of the products and reactants, where the free energy of a species is defined in Equation 8.

$$G = G^o + RTln(a) \qquad (8)$$

$$\Delta G = G_{products} + G_{reactants} \qquad (9)$$

G^o is the standard free energy (free energy in a standard state), R is the ideal gas constant, T is the temperature and a is the activity of the species. By substituting Eq. (8) into (9), ΔG can be written into a generalised form (Equation 10).

$$\Delta G = \Delta G^o + RTln\left\{\frac{\Pi(a_{products})i}{\Pi(a_{reactants})j}\right\} \qquad (10)$$

In an electrochemical cell, ΔG is also proportional to the reversible potential, E_{rev}, of a half-cell process:

$$\Delta G = -nFE_{rev} \qquad (11)$$

where n is the number of moles of electrons transferred and F is Faraday's constant which is equal the amount of charge per mole of electrons (96485 C mol^{-1}). The reversible potential, E_{rev}, of an electrochemical process (e.g. Equation 2) is defined as the electrode potential when the two different oxidation states of an element are in equilibrium. The standard electrode potential, E^o, can be defined for electrochemical half-cell reactions by measuring E_{rev} against a standard hydrogen electrode (SHE). For example, the half-cell process in Equation 2 has an E^o value of -0.44 V.[4] By substituting Equation 11 into 10, an equation that describes the reversible potential of an electrochemical half-cell where the oxidised and reduced species are not in their standard state can be produced. This equation is called the *Nernst* equation (Equation 12).

$$E_{rev} = E^0 - \frac{RT}{nF} ln \left\{ \frac{\Pi(a_{products})i}{\Pi(a_{reactants})j} \right\} \qquad (12)$$

This equation can be utilised to give an indication of the stability of metals in electrolytes with varying pH and electrode potentials through the use of Pourbaix diagrams.[5, 6] As these diagrams (also known as equilibrium diagrams) are constructed entirely based on the Nernst equation, they give information about the thermodynamic stability of the species, but they do not reveal anything about the kinetics of the processes. The construction of a simplified Pourbaix diagram for iron in aqueous solution is shown in Figure 1.3. These diagrams serve as a useful reference before performing electrochemical experiments on metals as they provide an indication as to what state the surface of the metal will be in at a given potential,[7] *e.g.* active, passive or immune, as shown in Figure 1.4.

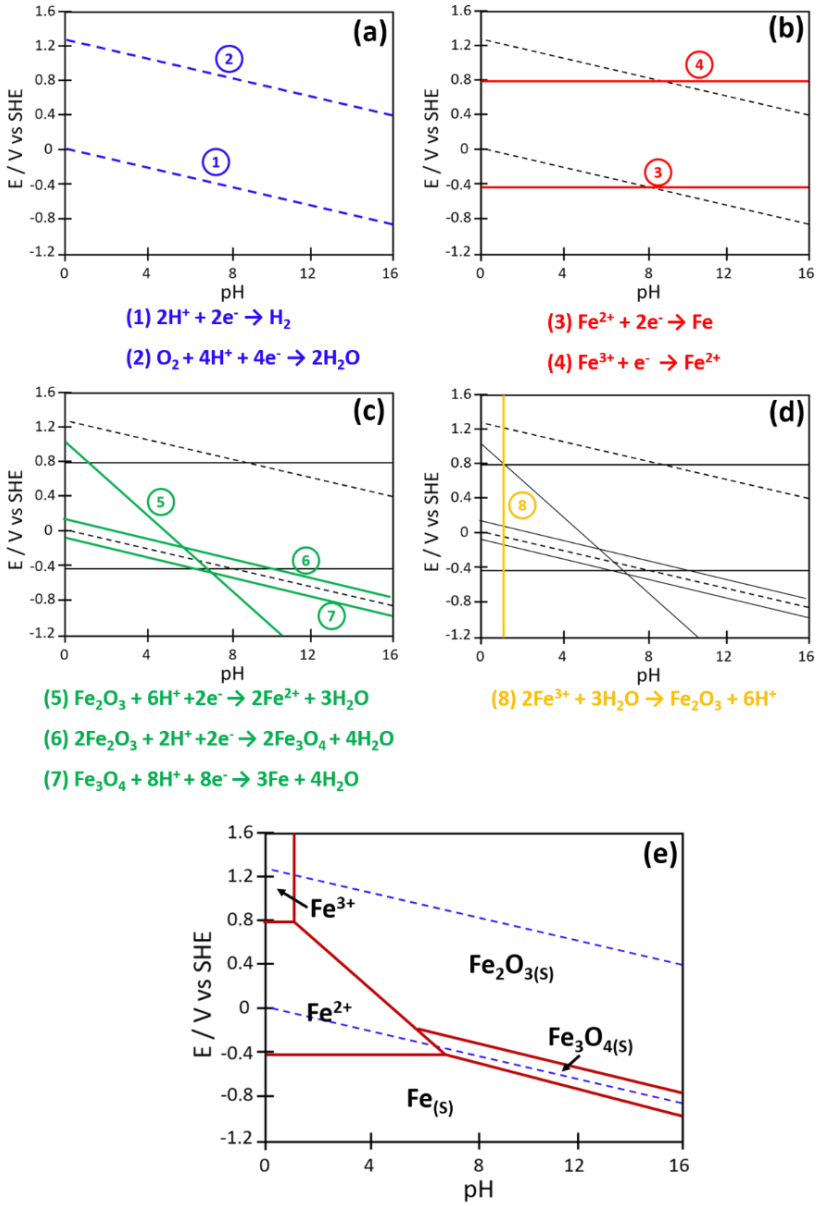

Figure 1. 3. The construction of a simplified Pourbaix diagram (E vs pH) for iron in aqueous solution. **(a)** Catalytic electrochemical processes: (1) hydrogen evolution/oxidation reactions and (2) oxygen evolution/reduction reactions. **(b)** Iron dissolution processes including: (3) iron dissolution and (4) Fe^{2+}/Fe^{3+} reaction. **(c)** Processes associated with the formation of iron oxides: (5) Iron(III) oxide or ferric oxide. (6) and (7) magnetite oxide **(d)** (8) Iron(II) oxide formation (no charge transfer). **(e)** Final Pourbaix diagram for iron with reactions (1) to (8) included. Figure 1.3e was adapted from McCafferty (2010).[8]

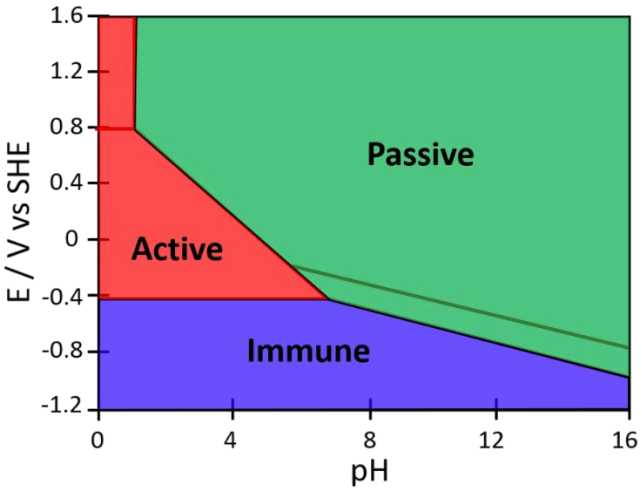

Figure 1. 4. Pourbaix diagram for iron with highlighted reaction domains: red = active, green = passive, blue = immune (cathodic processes).

1.2.3 Kinetics of corrosion reactions: Butler-Volmer equation and mixed potential theory

Whilst the tendency for corrosion processes to occur can be described through the use of thermodynamics, the *rate* at which these reactions take place is concerned with the kinetics associated with the transfer of charge across the electrode surface. The rate of an electrode reaction, *j*, is proportional to the current, *i*, flowing across the surface, which is an experimentally measurable quantity:

$$j = \frac{i}{nFA} \qquad (13)$$

where *A* is the surface area of the electrode. For an electrode reaction (O + ne ⇋ R), the overall rate of reaction (current) is determined by the following steps:[9]

1) The transfer of oxidised (O) or reduced (R) species from the solution to the electrode surface. Frequently referred to as *mass transfer*.
2) The rate of electron transfer at the electrode surface.

3) Chemical reactions that proceed or follow electron transfer on the surface.

4) Additional surface reactions, *e.g.* adsorption and desorption.

As stated previously, an electrode reaction is in equilibrium at the reversible electrode potential, E_{rev}. The associated exchange current density at this potential is denoted, i_o, which describes the rate at which the forward and reverse reactions take place, however the net current, i_{net}, is zero under these conditions. By altering the potential of the electrode away from E_{rev}, a net current is measured arising from the preferred direction of the reaction. The overvoltage, η, defines the extent at which the electrode potential, E, has been altered from E_{rev}.

$$\eta = E - E_{rev} \qquad (14)$$

If $E > E_{rev}$, the electrode is considered to be anodically polarised resulting in positive currents and if $E < E_{rev}$, the electrode is cathodically polarised resulting in negative currents. Considering that potential and current are independent, altering one will affect the other which serves as an important analytical tool in measuring specific electrochemical processes.

The current, i, response measured after polarising an electrode reaction can be described using the Butler-Volmer equation:

$$i = i_0 exp\left[\frac{\alpha n F \eta}{RT}\right] - i_0 exp\left[\frac{-(1-\alpha) n F \eta}{RT}\right] \qquad (15)$$

where α is the charge transfer coefficient. The electrode kinetics as described by the Butler-Volmer equation, can be visualised in Figure 1.5 which shows both *E-i* plot and *E-log(i)* plots. These can be utilised to help explain the multiple electrochemical processes occurring in a corrosion cell.

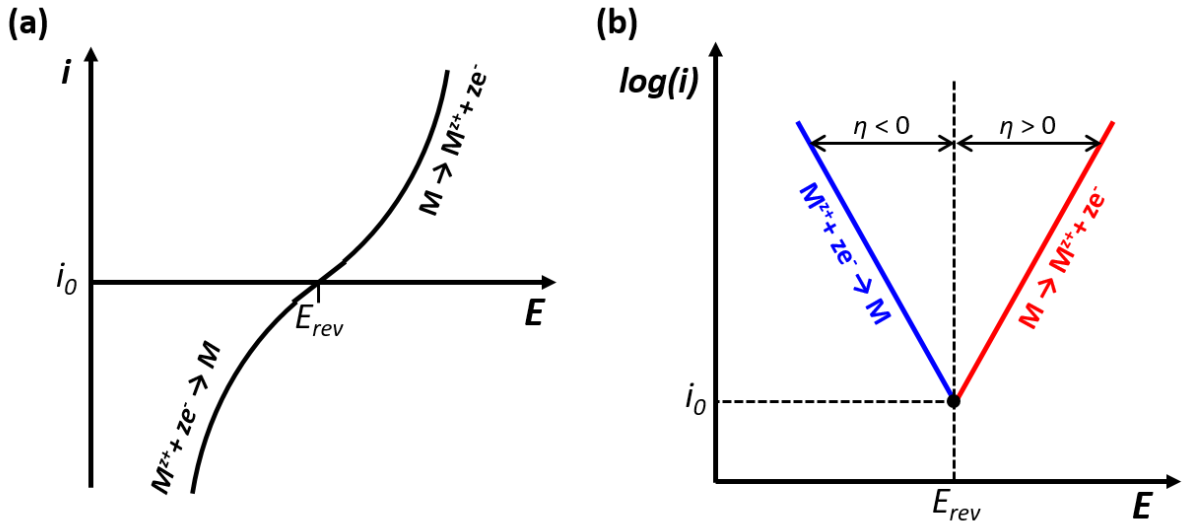

Figure 1. 5. (a) and **(b)** Graphical representations of Butler-Volmer kinetics. Blue and red traces represent cathodic (reduction) and anodic (oxidation) processes respectively. Figure 1.5 was adapted from Stratmann and Frankel (2003).[2]

Corrosion reactions comprise of a combination of oxidation and reduction processes. When an electrode is immersed in electrolyte the conservation of charge principle dictates that to avoid an accumulation of charge, the sum of the oxidation, I_a, and reduction, I_c, currents must be equal:[10]

$$\Sigma I_a + \Sigma I_c = 0 \qquad (16)$$

under such conditions the system sits at an open circuit potential or, as adopted in corrosion science, the corrosion potential, E_{corr}. The corrosion potential is, by definition, a mixed potential as it is influenced by the rate of anodic and cathodic currents, and is best visualised with the use of Evans diagrams (Figure 1.6).[11] It is important to note that the system is not in equilibrium at E_{corr} as the metal is still being oxidised and oxidants in the solution are being reduced.[2] The corrosion current, i_{corr}, is also indicated on the Evans diagram which is equal to the each of the anodic and cathodic currents, or the exchange current. This diagram presents the Butler-Volmer behaviour of both metal dissolution and hydrogen evolution (HER) reactions on the same axis

with the corrosion potential, E_{corr}, being indicated as the intersection between the anodic branch of the iron dissolution reaction and the cathodic branch of the HER. From this diagram we can predict what behaviour is expected in potentiodynamic polarisation experiments which is discussed later in section 1.3.4.

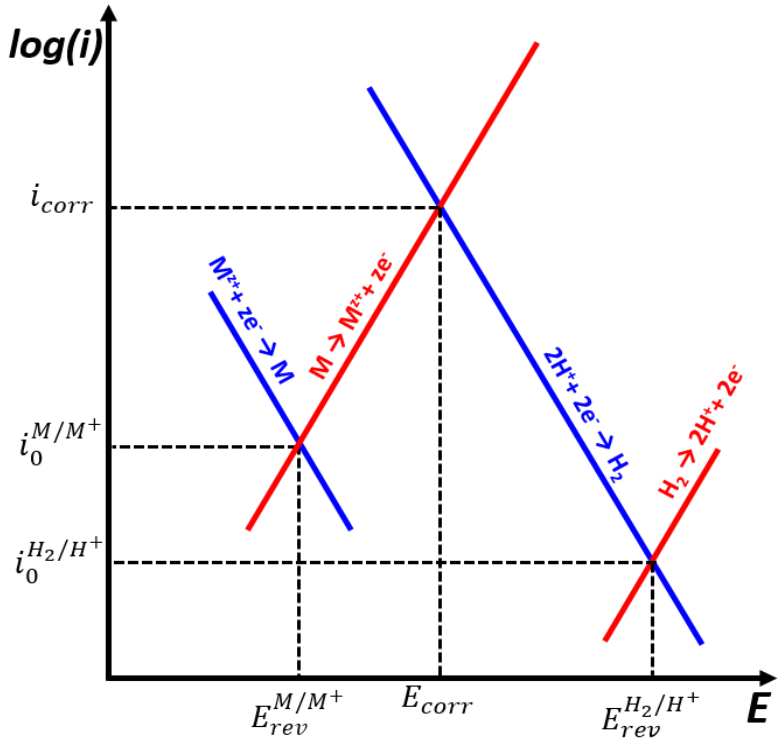

Figure 1. 6. Simplified Evans diagram for a metal in acidic solution where the hydrogen evolution reaction (HER) acts as the cathodic counterpart reaction to metal dissolution. Blue and red traces represent cathodic (reduction) and anodic (oxidation) processes respectively. Figure 1.6 was adapted from Stratmann and Frankel (2003).[2]

1.3 Electrochemical measurement methods and experimental considerations

In section 1.2 it was established that by altering the potential of a metal in electrolyte, different corrosion related processes can be driven. By recording the resulting currents, an indication into how well the metal facilitates these processes can be obtained. In this thesis we employ both *chronoamperometry* and *sweep voltammetry*, which are described below following a description of the basic principle of electrochemical cells and the experimental considerations required.

1.3.1 Electrochemical cells

A two electrode set up (Figure 1.7) comprises of the electrode of interest, referred to as the *working electrode*, and a *reference electrode*, both of which are immersed in a conducting electrolyte. By applying an external potential between the electrodes, E_{app}, a reaction can be activated at the working electrode resulting in a measureable current. As an external potential has been applied to the electrodes the cell is referred to as *electrolytic* as opposed to a *galvanic* where reactions between the two electrodes occur spontaneously without the requirement of a driving force. In this configuration, there are multiple experimental features that need to be considered, the first being the resistance induced by the solution between the electrodes.[9] The effect of solution resistance, R_S, on the applied potential, R_{app}, is shown in Equation 17:

$$E_{app}(vs.Ref) = E_{WE}(vs.Ref) - iR_s \qquad (17)$$

where E_{WE} is the potential applied. The two electrode set up is appropriate if the solution possesses high conductivity.

Another element to consider are the properties of the reference electrode. Most importantly there should be no spontaneous reaction between the reference electrode and the solution. In addition, it should ideally be both reversible and reproducible, which means that both phases of the half-cell reaction taking place at the electrode should always be in equilibrium and should not be disturbed during a measurement.[12]

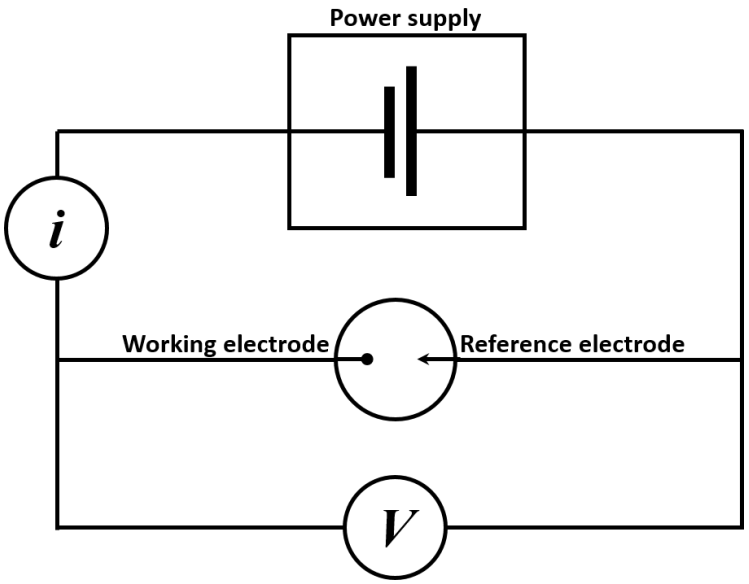

Figure 1. 7. Schematic of a two electrode configuration. Figure 1.7 was adapted from Bard and Falkner (2001).[9]

A three electrode configuration (Figure 1.8) can be adopted if the solution resistance (R_s) is high. In this set up a *counter electrode* is introduced which is made of a material that does not produce any contaminating substances during the measurements (e.g. Pt). The potential is applied between the counter and working electrode, whilst the potential of the working electrode is monitored relative to a separate reference electrode.[9] As there is no current flowing between the reference and the working electrodes, the risk of contamination to either of the electrodes is greatly reduced. As a result they can be positioned in close proximity thus reducing the resistance between the electrodes due to the following resistance-length relationship:

$$R_S \, \alpha \, \rho L \qquad (18)$$

where ρ is the resistivity of the solution and L is the distance between the electrodes. Another advantage of the three electrode set up is that it eliminates the risk of the reference electrode becoming polarised.

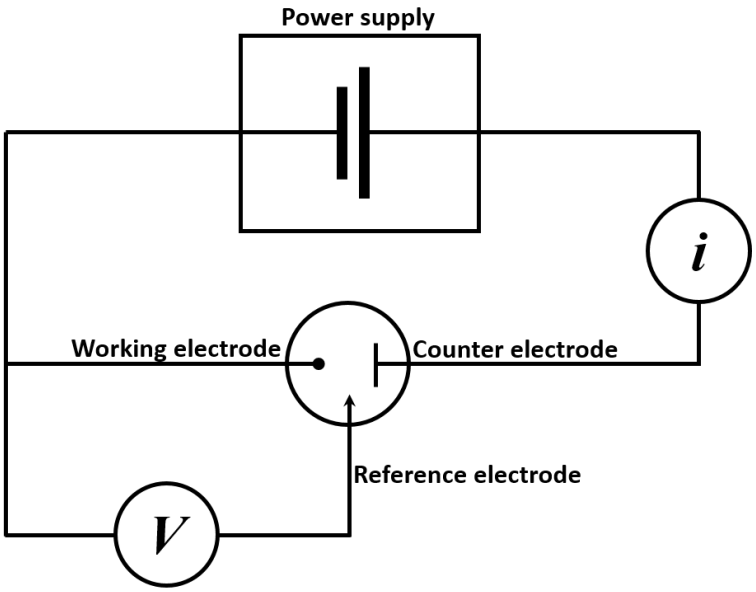

Figure 1. 8. Schematic of a three electrode configuration. Figure 1.8 was adapted from Bard and Falkner (2001).[9]

Another method of reducing the Ohmic drop (iR_s) in an electrochemical cell is to minimise the surface area of the working electrode thus reducing the current flowing in the cell (Equation 13). Small working electrodes are often referred to as *ultramicroelectrodes* (UMEs) which have been extremely popular since their introduction[13] and allow the adoption of two electrode configurations. In addition to minimising currents, UMEs also benefit from advantageous *mass transport* aspects, which are also very important features of SECCM, and as a result will be discussed in more detail below.

1.3.2 Diffusion and mass transport at electrode surfaces

Mass transfer concerns the movement of electroactive species to and from the electrode surface, which can be described by the Nernst-Planck equation:

$$J_j(x,t) = -D_j \frac{\delta C_j(x,t)}{\delta x} + \frac{z_j F}{RT} D_j C_j \frac{\partial \varphi(x,t)}{\delta x} + C_j v(x,t) \qquad (19)$$

where J_j is the number of moles of species j that pass a reference point per second per cm^2 of area normal to the axis of diffusion,[9] D_j is the diffusion coefficient, $\partial C_j/\partial x$ and $\partial \varphi/\delta x$ are the concentration and potential gradients respectively at a distance x from the electrode surface, z_j is the charge and $v(x)$ is the velocity of solution flow. The first term concerns the diffusion of the species whereas the second and third terms represent the influence of migration and convection on the overall flux of species respectively. Notice that Equation 18 only concerns mass transfer in a one-dimensional (x) (planar) case. For the multi-dimensional system, $\partial C_j/\partial x$ and $\partial \varphi/\delta x$ are replaced by ∇C_j and $\nabla \varphi_j$ where ∇ is a Laplacian operator that depends on the geometry of the electrode.

Diffusion is the movement of species under the influence of a concentration gradient. According to *Fick's first law* the flux of a species is proportional to the concentration gradient, which is where the first term in the Nernst-Planck equation originates.

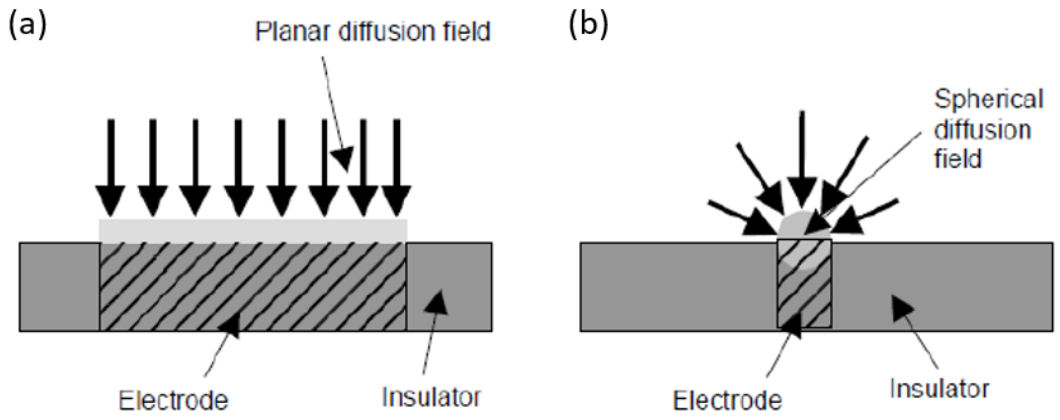

Figure 1. 9. Schematic diagrams of the diffusion patterns originating at inlaid electrodes for the cases of **(a)** a macroscale electrode exhibiting planar diffusion and **(b)** a microelectrode exhibiting spherical diffusion. Figure 1. 9 was adapted from Mallon (2013).[14]

The geometry of the working electrode directly influences the shape of the diffusion field during electrochemical perturbation. In planar diffusion (Figure 1.9a), mass transport takes place in one direction (perpendicular to the working electrode surface) and in spherical diffusion (Figure 1.9b) it takes place in two dimensions (radial to the working electrode). The diffusion limited current for the spherical case is calculated as:

$$i(t) = \frac{nFAD_j^{1/2}C_j}{\pi^{1/2}t^{1/2}} + \frac{nFAD_jC_j}{r_s} \qquad (20)$$

where the first and second terms represent the contributions of planar and radial diffusion respectively. Clearly, Equation 20 shows that if the diffusion field is dominated by radial diffusion, larger mass transport rates are possible. The planar term, also known as the *Cottrell equation*, is also time dependant which is related to the growth of a *diffusion layer*. The thickness, δ, of the diffusion layer (or depletion layer) varies with time:

$$\partial(t)\ \alpha\ \sqrt{D_j t} \qquad (21)$$

Upon the application of a potential, electroactive species closer to the electrode are consumed first. After the species close to the electrode are consumed, the system will then need to pull species from further away which is slower. A resulting concentration gradient dependant on the distance to the electrode is formed, and the thickness of the diffusion layer is defined by the distance between the electrode surface and the region of the solution where the concentration is the value before the application of a driving potential ($t = 0$). Measurements influenced by the diffusion layer are referred as *diffusion limited*.

For a UME at short time scales, the diffusion layer is smaller than the radius of the electrode so planar diffusion dominates, however at longer time scales (at a steady state), when the diffusion layer is comparable to the size of the electrode, the diffusion profile becomes radial.[15] Additionally in a radial diffusion field, the current is time independent as the diffusion layer thickness remains constant. It follows that reducing the size of the working electrode also reduces that time taken for an electrochemical system to reach a steady state. The benefits of small working electrodes are also relevant to SECCM and will be discussed in section 1.7.

Migration refers to the behaviour of any charged species in the presence of an electric field. For example, in an ideal experiment electrical neutrality in an electrochemical cell is maintained via the transfer of ions to and from an electrode surface (e.g. cations are attracted to negative electrodes). However, if other electric fields in the electrolyte influence the path of reactants to and from the electrode, measurement will be limited by migration. To minimise the influence of migration on mass transfer, high concentrations of supporting electrolyte are used. This shields reactants from migratory effects and decreases the probability that they will transfer to the electrode surface uninterrupted to achieve electrical neutrality.[16]

Finally, the convection term is caused by any fluid flow (of velocity v) in the system and can again be made negligible by preventing any vibrations or stirring in the electrolyte.

1.3.3 Chronoamperometry

In chronoamperometry, the potential of the working electrode is stepped from an initial potential, E_i, to a step potential, E_S. The current arising as a result of the application of the step potential is measured with respect to time (Figure 1.10) where the transient response corresponds to the establishment of the diffusion layer in the diffusion limited case. The current response follows Equation 20 assuming no faradaic current flows at E_i and, as stated previously, microelectrodes benefit from the fact that they reach a steady state at larger currents. At short time scales, the first term in Equation 20 dominates the measurement of current which predicts that for t = 0 an infinite current is measured immediately after the potential step. In practise the transient response is also influenced by various experimental factors, such as: the limited rise time of the instrumentation, any ohmic drop in the solution, and the kinetic limitations at the interface of the electrode/electrolyte interface. Therefore, in potentiostatic step experiments, the current value reaches the theoretical value as predicted by the Cottrell equation after a certain time lag.

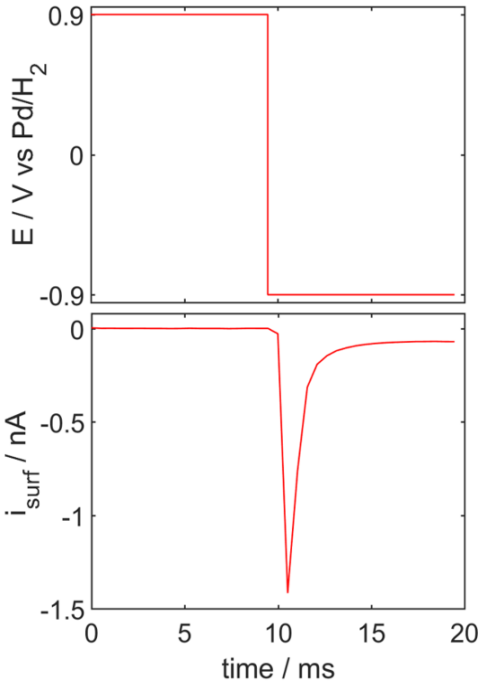

Figure 1. 10. *E-t* and *i-t* plots of chronoamperometry carried out using SECCM on low carbon steel in 5 mM H_2SO_4. Figure 1. 10 was adapted from Yule *et al* (2019)[17] and is also presented in Chapter 4.

1.3.4 Potential sweep voltammetry

In this technique the potential applied to the working electrode is varied linearly with time (fixed *scan rate*) and the current is measured as a function of the applied potential, as depicted by Figure 1.11. The potential sweep is either terminated at a certain potential during a forward sweep (known as *linear sweep voltammetry*) or reversed from a certain potential (known as *cyclic voltammetry*). In corrosion science, this method is commonly referred to as *potentiodynamic polarisation.* By varying the potential at the working electrode, different electrochemical processes can be activated that depend on the nature of the electrode and electrolyte.

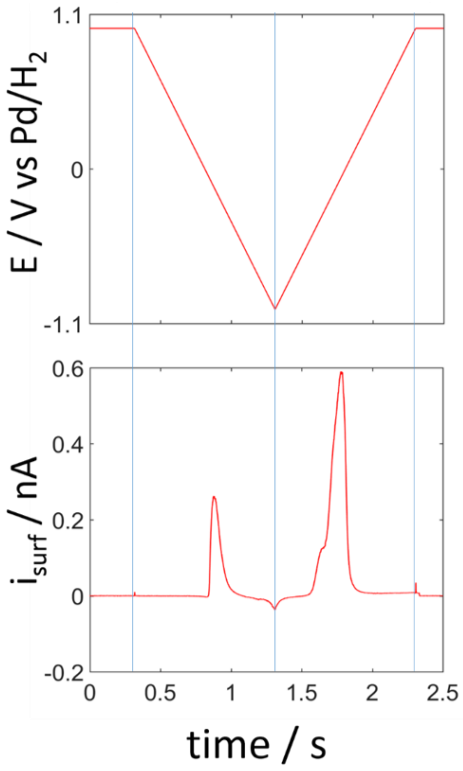

Figure 1. 11. *E-t* and *i-t* plots of cyclic voltammetry carried out using SECCM on low carbon steel in 5 mM H_2SO_4. Figure 1. 11 was adapted from Yule *et al* (2019) and is also presented in Chapter 5.

Using the example of iron, the Pourbaix diagram (Figure 1.3), and Evans diagrams (Figure 1.5) can provide an indication of what to expect from a linear sweep on iron immersed in an electrolyte of a particular pH. Figure 1.12 presents an example *log(i)-E* response (often referred to as a *Tafel plot*) from an example steel in the presence of neutral/basic and acidic electrolyte, with the key difference that in acids iron undergoes dissolution between the cathodic and passive regions. Theoretically the corrosion potential, E_{corr}, and current, $i_{corr,}$ can be extracted from these plots with the use of Tafel extrapolation under suitable experimental conditions. However, in electrochemical measurements that involve corrosion processes, a steady state is near impossible to achieve due to the constantly changing nature of the working electrode. Consequently, in order to improve the precision at which the corrosion potential and current can be extracted from Tafel plots, industry standard corrosion tests recommend

extremely slow scan rates (<1 mV s^{-1}).[18] In the SECCM configuration, slow scan rates are often not suitable for scanning purposes. A discussion of the effect scan rate can have on polarisation measurements in SECCM is discussed in detail in Chapter 3.

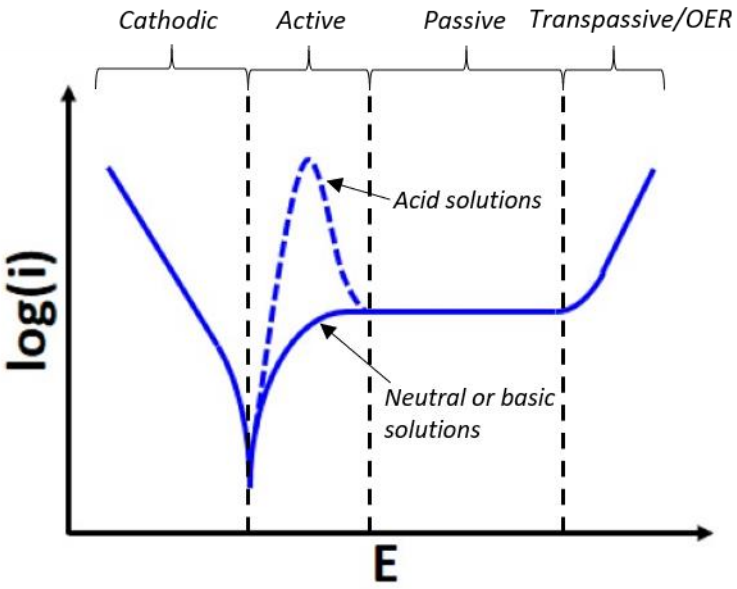

Figure 1. 12. Simplified graphical representation of a Tafel plot for a metal in acidic and neutral/basic media. Figure 1. 12 was adapted from McCafferty (2010).[8]

1.4 Crystal structure and surface characteristics of metals and alloys

Metals are crystalline in solid state and the vast majority are polycrystalline, where each grain is an individual crystal whose orientation differs from that of its neighbouring grains.[19] The grain structure (or its *microstructure*) of a metal can influence its physical properties, such as strength, hardness, ductility, thermal/electrical conductivity and the response to high/low temperatures. For example, microstructure comprising of many finer grains (see Figure 1.13a) usually results in higher strength and toughness compared to a microstructure with larger grains (Figure 1.13b). This is due to the impact of grain boundaries, which act as obstacles to slips and

dislocations in the crystal lattice.[20] Whilst grain boundaries can play a crucial role in strengthening a metal, they can also contribute to its weakening. This can occur if undesirable precipitates migrate towards the boundaries, for example the precipitation of phosphorus at grain boundaries has been shown to, in some circumstances, enhance the effect of intergranular corrosion on stainless steel.[21]

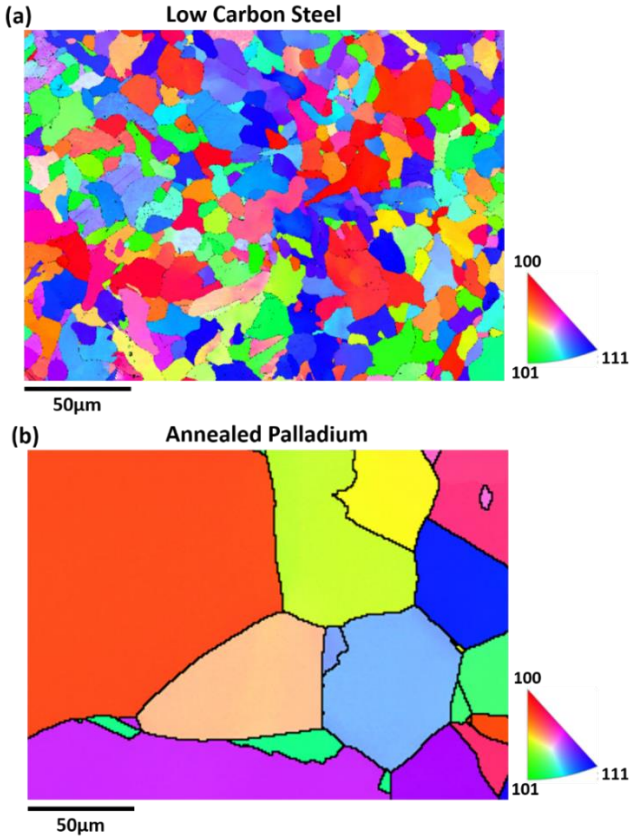

Figure 1. 13. Electron backscatter diffraction (EBSD) maps of **(a)** polycrystalline low carbon steel and **(b)** annealed polycrystalline palladium.

The microstructural characteristics are primarily dictated by the solidification process of the metal or alloy. During the heating of iron and steel, the iron atoms can rearrange themselves into different types of crystal lattices in a process called *allotropic* change. Steels can arrange into a number of crystal structures including: (i) body-centered cubic (BCC), and (ii) face-centered cubic (FCC) which can be visualised in Figure 1.14a. By controlling the

temperature at which steel is heated and the rate at which the steel is cooled, one can control the size of the grains and the type of crystal structure.[22] The planes of the crystal structures exposed at the surface are often represented with *Miller indices*, which are defined by how the plane intersects the main crystallographic structure (*e.g.* cubic). Examples of low index orientations, where the sum of the Miller indices is low, in a cubic lattice are shown in Figure 1.14b. Compared to high index orientations, where the sum of the Miller indices is high, low index planes have a higher atom density (or are more coordinated).[23]

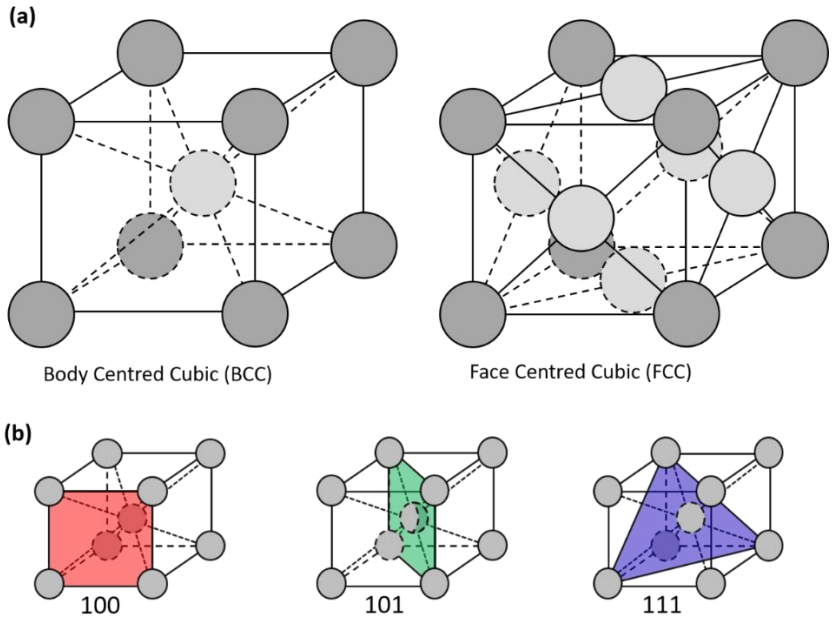

Figure 1. 14. (a) Schematics of the unit cells for body centred cubic (BCC) and face centred cubic (FCC) crystal structures. **(b)** Low index orientations illustrated on a BCC cell.

Another microstructural feature of metal alloys are *inclusions*, which can form as a result of the nucleation of alloying elements or impurities during alloy production.[20] MnS inclusions are very common in steels, for example MnS inclusions visible on a 304 stainless steel surface can be seen in Figure 1.15a, whereas MgSi inclusions and Fe impurities on Al 6061 can be seen in Figure 1.15b.

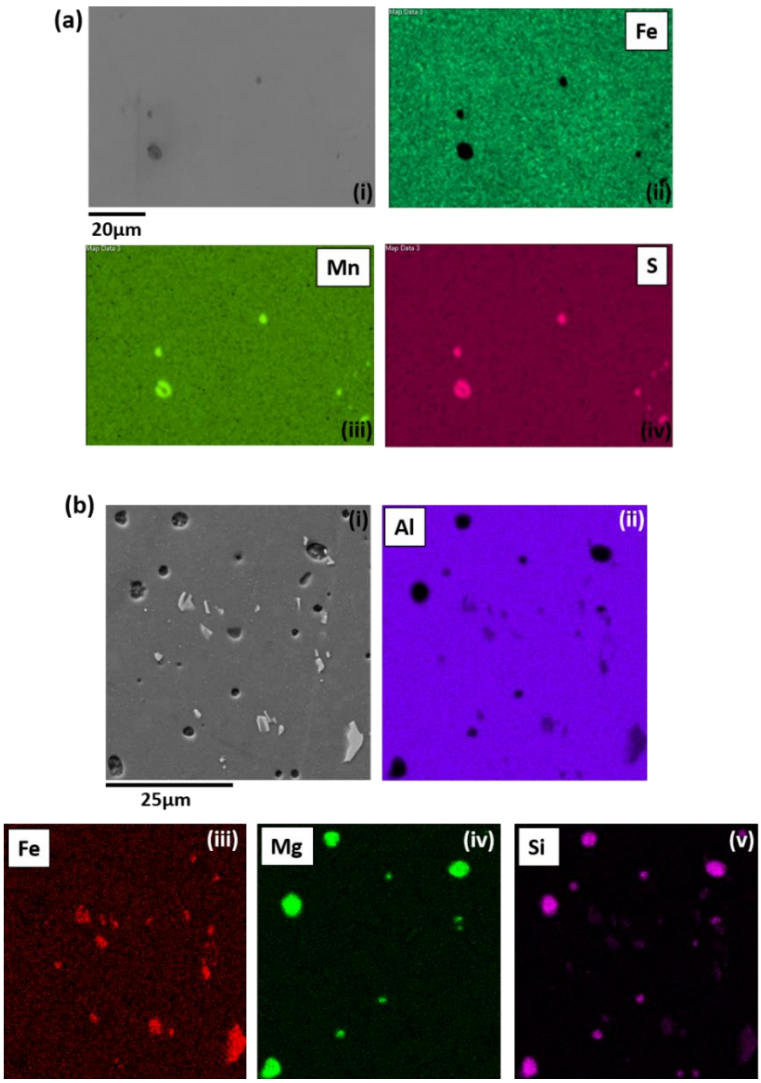

Figure 1. 15. (a) Stainless steel 304L surface, with MnS inclusions, imaged with (i) scanning electron microscopy (SEM) and energy dispersive spectroscopy (EDS) for (ii) Fe, (iii) Mn, and (iv) S. **(b)** Al 6061 surface, with MgSi inclusions and Fe impurities, imaged with (i) SEM and EDS for (ii) Al, (iii) Fe, (iv) Mg, and (v) Si.

1.5 Microstructural influence on corrosion

So far, the microstructural features found on metal/alloy surfaces have been discussed along with a description of how these affect the physical properties of the material. This section will move the focus onto the influence of these microstructural features on the overall corrosion behaviour of metals.

1.5.1 Inclusions

Non-metallic inclusions, in particular sulphide or intermetallic precipitates, are frequently responsible for the onset of pitting corrosion[24] (localised breakdown of the passive film), particularly in industrial metals and alloys.[25] The most studied example of this are MnS inclusions in steel. Wranglén produced the first thorough study in 1974 highlighting the detrimental effects of sulphides in a variety of steels.[26] It was theorised that the mechanism of pit initiation depends on the nobility of the bulk alloy compared to the sulphide inclusion. For example on stainless steels, sulphide inclusions are less noble and as a result are selectively dissolved which creates a vacancy in the steel matrix from which pit growth can occur. This was highlighted by a study in the same year that used thermodynamic calculations on sulphides present in commercial stainless steels to assess the stability of sulphide inclusions, where it was found that sulphides cannot thermodynamically exist at the passive potential of steel.[27] However on carbon steels the surrounding matrix is less noble than the inclusion so the surrounding region is preferentially dissolved instead, which can cause crevice corrosion[28, 29] in the vacancies created around the inclusion[25] or for the inclusion to 'fall off' the surface creating a pit.[26]

Further studies on MnS inclusions[24, 30-33] have attempted to confirm the true mechanism of pitting. For example it has been suggested that in stainless steel, significant reductions in the Cr/Fe ratio is responsible for the reduced passivity around inclusions.[33] More recently in a study using transmission electron microscopy (TEM),[34] it was proposed that heterogeneities within MnS inclusions result in the oxygen reduction reaction (ORR) facilitating MnS dissolution in other regions of the inclusion.

Micro-electrochemical techniques, which will be discussed further in section 1.6, have also been adopted to study MnS inclusions.[35-39] One of the key results from these studies is that the depth of MnS inclusions on steel surfaces effects whether pitting corrosion can occur into the steel matrix. This suggests that the formation of suitably deep crevices either side of the inclusion is required for sustained pit growth, as shown experimentally in Figure 1.16. Another observation was that dissolution was not uniform across the inclusion, instead it occurred primarily at the edges.[38] It was also shown that increasing the amount of chloride in solution resulted in more stable pit growth.[38] In summary, the influence of heterogeneous electrode conditions as a result of the presence of inclusions is fundamental to the initiation of pitting corrosion.

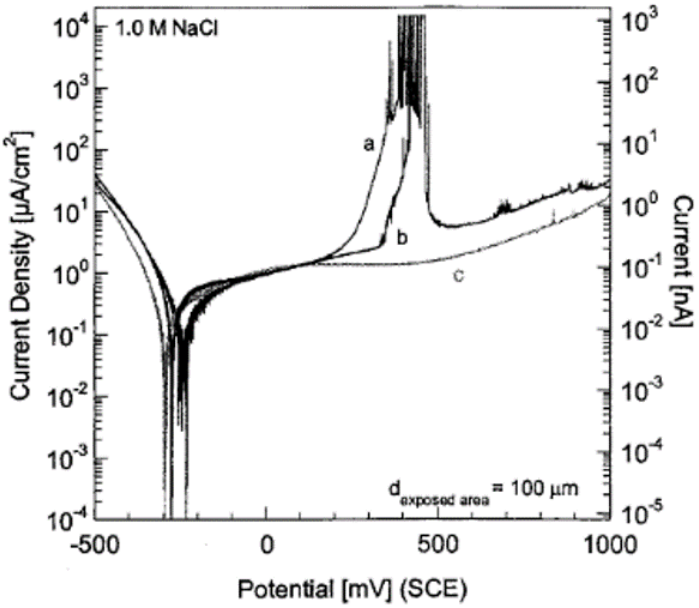

Figure 1. 16. Polarisation experiments, using the electrochemical droplet cell (EDC) method, of a MnS inclusion on 304 stainless steel in 1M NaCl. Polarisation curve 'a' shows the formation of a non-stable pit (curve shows repassivation after pitting event), whereas curve 'b' shows a stable pit as no repassivation is observed. Curve 'c' is taken on stainless steel with no inclusions present and thus no pitting event is observed. Figure 1. 16 was adapted from Webb *et al* (2001).[38]

1.5.2 Grain boundaries

Similarly to inclusions, grain boundaries also contribute to heterogeneity across a metal surface that can lead to *intergranular corrosion*. This involves preferential corrosion at or in the regions close to grain boundaries on polycrystalline materials.[40] The cause of heterogeneities at grain boundaries have been attributed to: i) interface energy as a result of lattice termination between grains,[41, 42] ii) segregation of detrimental impurities/precipitates to grain boundaries,[43] iii) depletion of beneficial solutes away from grain boundaries.[42] Intergranular corrosion can also lead to *intergranular stress corrosion cracking* which is sometimes the cause of catastrophic material failure.[44, 45]

The study of corrosion at grain boundaries has received considerable interest with groups reporting that grain boundaries both increase and decrease the susceptibility to intergranular corrosion. It is believed that grain boundaries are more chemically active than the bulk of the crystal due to their higher surface energy.[46] The reduced atom coordination at grain boundaries is believed to lower the work function allowing easier electron removal and adsorption of species in the electrolyte, which results in higher charge transfer rates at grain boundaries.[47] Therefore, whether a grain boundary is susceptible or protective against corrosion is directly influenced by the nature of the electrolyte. In fact, it has been stated that grain boundaries tend to exasperate the effect of the electrolyte on alloys.[48] For example, in a study on FeAl8, grain boundaries were shown to increase corrosion resistance in pH 6 electrolyte (passive environment), however in pH 1 (active environment) the grain boundaries were shown to decrease corrosion resistance.[49]

There is a large amount of literature that investigates the impact of increasing grain boundary density on the corrosion resistance of nanocrystalline metals and alloys. Many of these studies attribute the changes in corrosion behaviour to the role of grain boundaries promoting certain electrochemical processes. For example, it has been shown that increasing the grain boundary density can increase the stability and the resistance to pitting of passive films in neutral or alkaline electrolytes. This effect has been observed on Al (Na_2SO_4 electrolyte),[50] Co (Na_2SO_4),[51] Ni-Ti alloys (NaCl),[52] and Zn (NaOH and NaCl).[53, 54] A common explanation for this observation is that grain boundaries allow rapid diffusion and possess active electrons promoting oxide formation. It has also been suggested that grain boundaries possess favourable mechanical oxide film adhesion,[55, 56] which further promotes passive film formation. However, in a study on Al-Mg based alloys in Na_2SO_4 it was found that nanocrystalline structure did not significantly influence the stability of the passive film.[57] This suggests that the properties of passive films vary considerably on different substrates.

In more active (non-passivating) environments however (predominately acids), preferential corrosion has been observed at grain boundaries on materials such as Co (H_2SO_4 electrolyte)[58] where enhanced cathodic kinetics were detected on a nanocrystalline substrate. In a study on nanocrystalline Ni (H_2SO_4), increasing the density of grain boundaries was shown to catalyse HER as well as reduce passivation kinetics whilst also compromising passive film stability.[59] Increased grain boundary density has also be shown to increased susceptibility to passive film breakdown on nanocrystalline Cu (Na_2SO_4 and $CuSO_4 + H_2SO_4$).[60, 61] This effect was attributed to an increase in the number of defects in the passive due to irregular film growth over grain boundaries. In stainless steels, the depletion of Cr from grain boundaries reduces the

beneficial influence of Cr on passivation. This effect is caused by the precipitation of carbides ($M_{23}C_6$) at grain boundaries,[62, 63] which has led to attempts to 'engineer' grain boundaries to negate this effect.[64]

The influence of grain boundaries on corrosion is further complicated when the effect of impurity segregation to grain boundaries is considered. This effect has shown to increase corrosion susceptibility on Mg alloys,[65-67] Ti,[68] Co,[69] stainless steel,[70] and Ni.[59] For the study on Ni[59] it is interesting to note that the increase in corrosion susceptibility was due to the enhanced catalysis of the hydrogen evolution reaction (HER). Considering that a common way to increase the grain size (decrease density of grain boundaries) on a metal/alloy is to anneal the sample, the concern has been raised that during annealing, impurities segregate to grain boundaries which can lead to false conclusions of the relationship between grain boundary density and corrosion susceptibility.[61, 68, 71]

1.5.3 Crystal orientation

The variation of crystal orientation also induces a degree of heterogeneity across a metal surface. Despite it being an area of interest, the extent or the way which crystal orientation (also referred to as *surface texture*) influences corrosion behaviour is not well established. The preferential active dissolution of certain crystal orientations has been observed on Fe,[72-75] Mg alloys,[76, 77] Nb,[78] various steels,[79-81] Fe_3Al single crystals[82] and, FePd alloy.[83] A common method of observing this effect is to extract topographical profiles of adjacent grains using atomic force microscopy (AFM) after etching the substrate surface. The results of this method, as adopted by Schreiber *et al*,[72] can be seen in Figure 1.17.

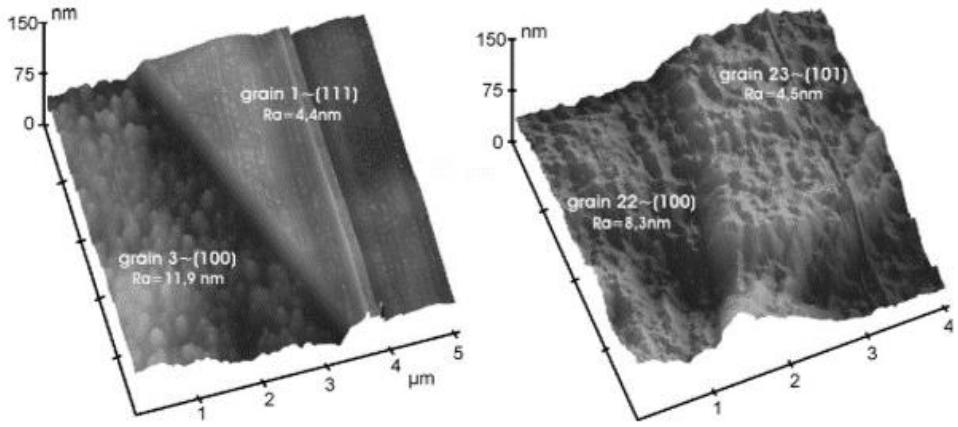

Figure 1. 17. Atomic force microscopy (AFM) maps showing variations in topography between grains after chemical etching on pure iron. Figure 1.17 was adapted from Schreiber *et al*.[72]

Various explanations for this effect have been suggested in these studies, for example Horton *et* al[83] attempted to correlate the extent of dissolution to the surface energy (energy stored in the bonds between atoms in the crystal lattice), where it was expected that dissolution occurs more readily from grains with higher surface energy. The comparison between experimental data and the calculated surface energies revealed similar trends, however an exact correlation was not confirmed likely due to effects from the environment, such as the orientation-dependant adsorption of Cl^- ions. Alternatively, Schreiber *et al*[73] used the packing of the atoms in different crystal orientations to explain their findings. It was theorised that the density of atoms on the surface as well as the spacing distance to the next layer of atoms influences dissolution rates. Similar explanations were adopted by Lill *et al*[81] and Liu *et al*[84] who suggested a more densely packed surface layer reduces 'access' to lower planes resulting in the crystal being more resistant to dissolution.

Different studies have also yielded different trends in dissolution-orientation dependency. Using the example of iron, studies have shown that each of the low index

orientations: (100),[72, 74, 85] (101)[75] and, (111)[73] have demonstrated preferential dissolution compared to the other low index grains. This discrepancy is possibly explained by the different experimental conditions used in each study (*e.g.* acetate buffer pH 6[73] *vs.* sulphuric acid pH 1[72]), which relates to the previous discussion concerning the influence of electrolyte on the corrosion of grain boundaries in section 1.5.4.

These examples of discrepancies in the literature highlight the difficulty in modelling corrosion related systems as the wide contributing factors to the overall process make almost impossible to account for them all. This is a potential reason why a consistent explanation for the influence of crystal orientation on corrosion behaviour is yet to emerge.

The passivating/oxide formation behaviour on different crystal orientations has also been observed on materials such as Al,[86] Fe,[87-89] Ti,[90] Zr,[91] Ta[92] and, Mg.[93] Again, the exposure environment has been observed to have a significant effect on the oxide formation, for example on Mg thick $Mg(OH)_2$ films were formed in alkaline media whereas they were less apparent in neutral solution.[92] Pitting behaviour has also been shown to be orientation dependant on Al,[93] stainless steel[94] and, Cu.[95]

1.6 Local electrochemical scanning methods used in corrosion

The study of corrosion related phenomena on specific microstructural features is very challenging due to the highly localised nature of the features.[96] Through the development of local electrochemical scanning techniques, the possibility to study local electrochemistry on different materials has been introduced.[97-99]

An early example of such a technique is the scanning vibrating electrode technique (SVET), shown schematically in Figure 1.18a, which functions by oscillating an electrode (often Pt) close to an immersed sample surface to detect the current density distribution produced by electrochemical processes occurring at the surface without effecting the surface with the probe.[100] This technique has been widely used in corrosion science[101] and has been effectively utilised to study galvanic corrosion[102, 103] and pitting corrosion.[104, 105]

Scanning kelvin probe (SKP) methods have also been applied to locally scan electrochemically related characteristics. Kelvin probe methods measure variations of work function (or contact potential difference relative to the probe material) across a surface (Figure 1.18c), which is analogous to the corrosion potential,[106] and has also been applied frequently in corrosion science.[107-109] In standard SKP sub-microscopic potential measurements are not possible due to the required probe size.[110] However, SKP can be combined with AFM in a method that is referred to as scanning kelvin probe force microscopy (SKPFM)[111] which can produce resolutions as low as 0.1 μm.[112]

Scanning electrochemical microscopy (SECM) is another local electrochemical scanning technique that utilises a UME to probe reaction product concentration gradients originating from electrochemical processes occurring at electrode surfaces (Figure 1.18b).[113, 114] SECM benefits from high mass transfer rates and negligible potential drop from solution as a result of the dimensions of the UME (described in detail in section 1.3.2). It has also been applied to corrosion research,[115] for example to study pitting corrosion,[116-118] and inclusion dissolution.[32, 119]

SVET, SKP, and SECM have all demonstrated the ability to detect local corrosion phenomena and expose heterogeneous electrochemical responses across macroscale metal surfaces. For example, they have each been shown to be successful in the study of the protective properties and defects on corrosion resistant organic coatings.[98] Despite the benefits these techniques provide, they also suffer from several limitations. Firstly, for the case of SECM and SVET, they require that the entire material of interest is immersed which, especially in corrosive environments, can cause the surface to change during the time it takes to map an area. This can result in misleading electrochemical data, as the experimental conditions change from the first scanning point to the last.[120]

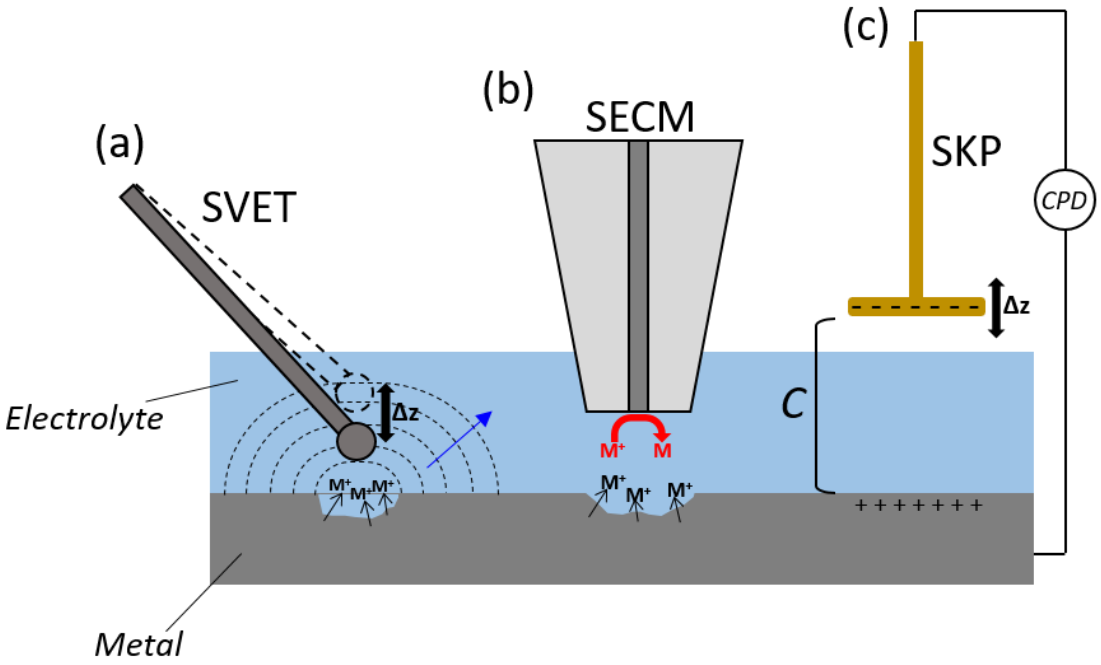

Figure 1. 18. Schematic of local scanning probes used in corrosion science. **(a)** Scanning vibrating electrode technique (SVET) comprising of an oscillating detector, immersed in the electrolyte near the surface, measuring variations in potential gradient (indicated by dashed lines and the blue arrow). **(b)** Scanning electrochemical microscopy (SECM), comprising of an ultramicroelectrode (UME) positioned close to the surface, shown to be electrochemically reducing metal cations (produced by corrosion site) to metal solids. **(c)** Scanning kelvin probe (SKP), usually Au, oscillating above a thin layer of electrolyte covering a metal surface. A capacitance, *C*, is established when the probe and substrate are electronically connected. A contact potential difference, *CPD*, indicates the difference in fermi levels between the probe and substrate. Note that the schematic is not to scale.

Difficulties can also arise if the sample is not completely flat as these techniques can suffer from a convolution of the reactivity and topography of the substrate surface. This arises because SECM and SVET detect the products of the corrosion reactions occurring at the surface, rather than the processes themselves (*i.e.* reactivity is measured indirectly). Therefore, the distance between the probe and substrate needs to be known precisely, otherwise "higher" area of the surface (*i.e.* where probe-to-substrate distance is smaller) will appear to be more active than "lower" areas (*i.e.* where probe-to-substrate distance is larger). This limitation can be overcome by preparing very smooth samples, as well as using sophisticated positioning

instrumentation to ensure a constant probe to surface separation. Nevertheless, if the metal substrate is immersed in a corrosive environment, the topography of the surface will change with time making any efforts to make a completely flat surface irrelevant.[121] For the case of SKP methods, the measurement is dictated by the formation of a capacitor between the surface and the probe, and as a result the probe cannot be immersed in electrolyte. Therefore the conditions in which corrosion information is extracted with SKP are limited to atmospheric conditions.

The electrochemical droplet cell (EDC) method, developed by Suter and Böhni,[35, 36] works on the principle of immersing a small area of an electrode surface with a droplet formed at the end of micro-pipet, as shown in Figure 1.19, allowing *direct* measurement of electrochemical processes at the surface. Electrochemical measurements are only made on the immersed part of the surface, meaning any physical changes will be the result of the electrochemical measurement itself. A silicon gasket is commonly attached to the end of the pipette to both contain the electrolyte and to ensure good contact with the surface.[122] In this configuration, the probe can be manually attached to the surface to carry out static micro-electrochemical measurements. In fact, the EDC was initially developed to study localised corrosion phenomena,[35] and has since been used continuously in this field.[38, 39, 87, 93, 122-129] Chapter 3 in this thesis refers to a review article[130] covering the advantages and limitations of EDC methods in corrosion science, and it also discusses how SECCM overcomes these issues.

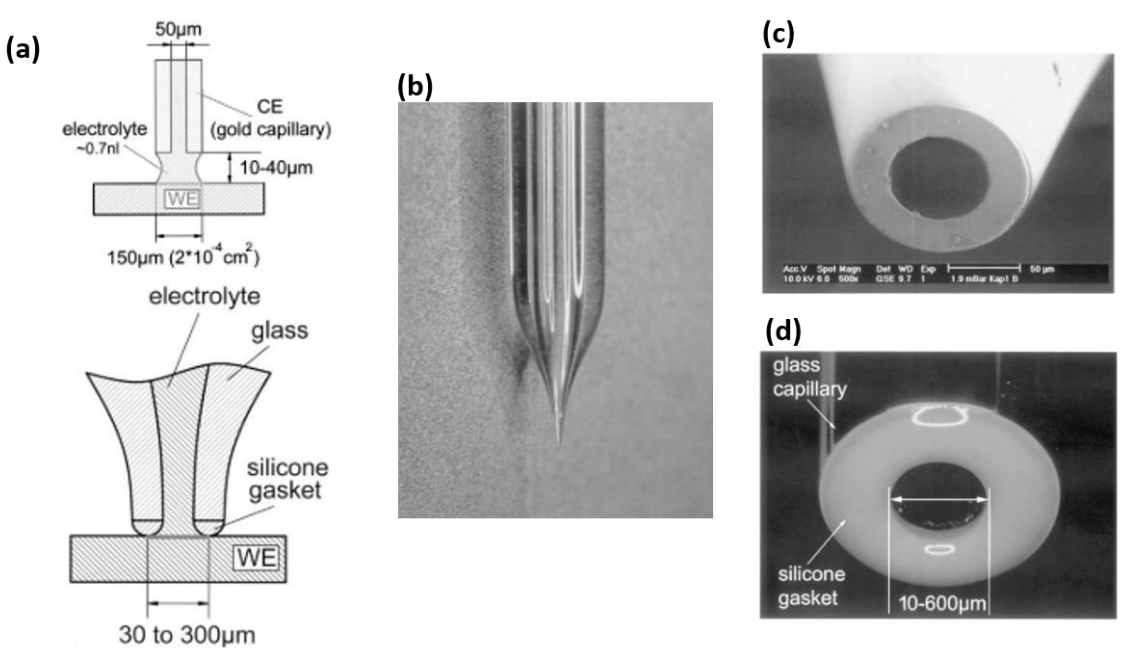

Figure 1. 19. (a) Schematic of the electrochemical droplet cell method with and without the application of a silicon gasket. **(b)** Laser pulled glass capillary. **(c)** SEM image of the end of a capillary of diameter 50 µm. **(d)** SEM image of the end of a capillary equipped with a silicon gasket. Figure 1. 19 was adapted from Lohrengel *et al* (2001).[122]

1.7 Scanning Electrochemical Cell Microscopy (SECCM)

SECCM is based on the same principle as the EDC technique whereby a droplet formed at the end of a pipette filled with electrolyte is utilised to make mirco/nanoscale electrochemical measurements on a variety of materials.[120] In addition to the benefits provided by EDC techniques, SECCM makes vast improvements in terms of usability, speed and reproducibility.[131]

The electrolyte filled glass pipette (with an end diameter ≥ 30 nm, see Figure 1.21), is attached to a piezo electric positioner operating in the direction normal to the surface (*z*-direction), which enables precise movement of the pipette tip towards the substrate. A quasi reference counter electrode (QRCE) is inserted into the barrel(s) along with the solution. The

glass capillary can be used in either single (Figure 1.20) or dual barrel (Figure 1.21) configuration depending on the nature of the substrate.

In dual barrel SECCM, a potential bias (V_2) is applied between to the two QRCEs inducing an ionic current (i_{IC}) across the droplet formed at the end of the pipette. When contact is made with a surface, the morphology of the droplet changes resulting in a change to i_{IC} which is used as a feedback signal to indicate when contact has been established. Equipped with this feedback signal, the approach to and contact with the surface can be automated. By either attaching the pipette or the substrate to a *xy*-direction piezoelectric positioner the droplet can be translated across a surface, meaning an array of individual SECCM experiments can be carried out. During the approach, the probe can also be oscillated with the addition of a lock-in amplifier, resulting in an AC current arising between the QRCEs (i_{AC}). Changes to the phase and amplitude of i_{AC} upon contact with the surface is used as the feedback mechanism in this case.[132] Once contact is established the potential of the QRCEs can be varied relative to the surface resulting in the activation of electrochemical processes. Due to the small size of the working electrode, SECCM benefits from the contribution of radial diffusion, as described in section 1.3.2, so that mass transport to and from the substrate is relatively efficient.[133] The ability to measure fast electrode kinetics combined with sophisticated data recording methods, can result in rapid electrochemical mapping of surfaces. Recently Momotenko *et al* demonstrated the ability to scan 8000 individual sites per second.[134]

An advantage of the dual barrel configuration is that it does not require a conductive surface to establish clean contact between the droplet and the substrate as the feedback signal is not influenced by currents originating from processes at the surface. Additionally, the

magnitude of i_{IC} provides an indication of the size of the droplet, so any changes to the droplet can be detected during an experiment. SECCM can also function in both constant distance and hopping mode. In constant distance mode the magnitude of i_{AC} whilst in contact can provide information on probe-to-substrate separation.[131] During hopping mode the pipette is retracted after each experiment and moved to the next scanning site, which enables SECCM to scan across uneven surfaces and even extract topographical information.[135] The spatio-temporal resolution of SECCM scans is dictated by the hopping distance (distance between measurements), the speed at which the pipette is approached to the surface, and the time of each measurement.

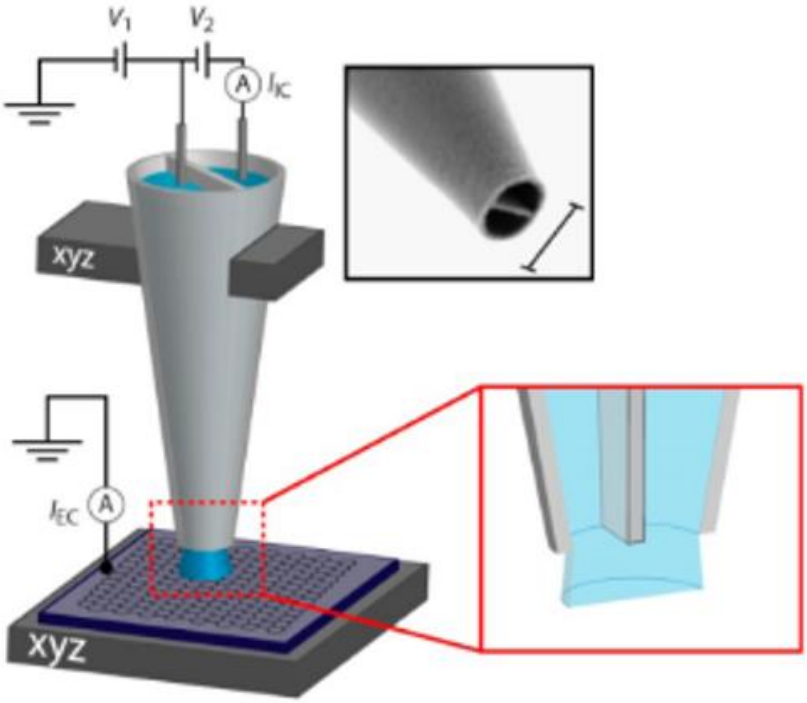

Figure 1. 20. Schematic of SECCM in dual barrel configuration, accompanied with a scanning transmission electron microscopy (STEM) image of the end of a duel barrel pipette of diameter 1 µm. Figure 1. 20 was adapted from Unwin *et al.* (2016).[136]

In the single barrel set up, shown in Figure 1.21, a potential is applied between the QRCE and the substrate (E_{app}). A direct current between the two electrodes is detected once contact is made between the droplet and surface which is used as the feedback mechanism. As a result, this configuration is limited to conductive substrates.[137] An advantage of the single channel approach is that the faster approach rates are achievable, allowing for significantly quicker scan times.

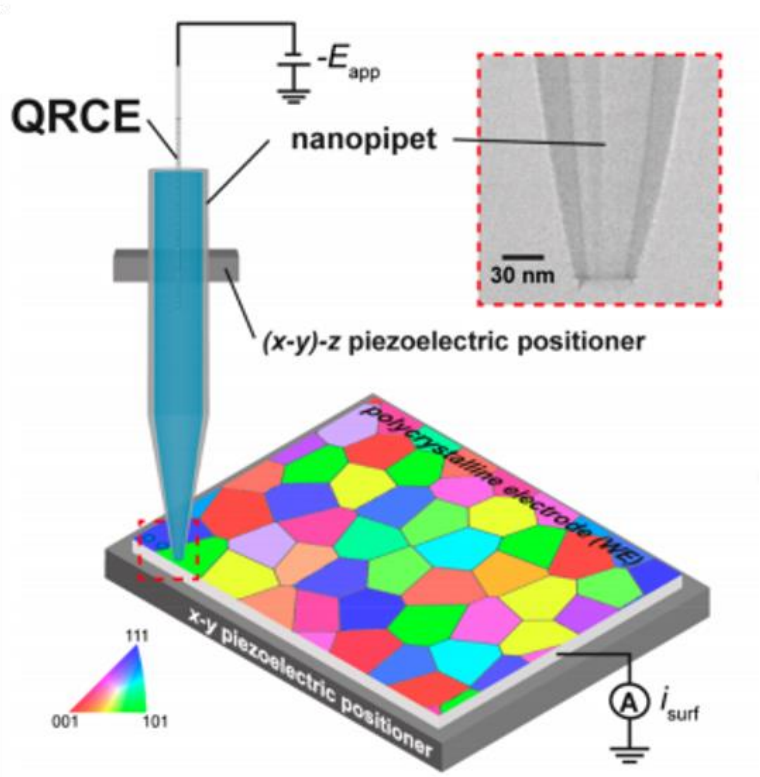

Figure 1. 21. Schematic of SECCM in single barrel configuration, accompanied with a STEM if a single barrel pipette of diameter 30 nm. Figure 1. 21 was adapted from Bentley *et al.* (2019).[138]

SECCM has been successfully utilised to study heterogeneous electrochemical behaviour across a variety of materials with high resolution. For example, polycrystalline Pt substrates have been studied with SECCM to examine orientation-activity dependencies of catalytic and simple redox processes on platinum,[139-142] highlighting the capability to combine

SECCM with other characterisation methods. It has also been very successful in the study of the electrocatalytic characteristics of individual nanoparticles, which effectively showcases the high resolution of the technique, including Au,[135, 143-145] RuO_x,[146] Ag,[147] and $LiMn_2O_4$.[148] The structural influence on the electrochemical behaviour of carbon based materials[136, 149] and other catalytic materials[150, 151] have also been successfully studied using SECCM.

1.8 Outline of thesis

As discussed previously, SECCM has been very effective in resolving relationships between surface structure and electrochemical activity, however it has yet to be adopted in the study of corrosion related processes. The overall aim of this thesis is to assess the suitability of SECCM to study corrosion, and to apply the technique in areas where it can be most effective. Local electrochemical scanning techniques have often been used to study the influence of surface structure, and defects on the susceptibility to corrosion. Due to some of the benefits SECCM provides compared to similar methods, the study of the structure dependence of corrosion related processes was chosen as the focus of this project.

The results presented in Chapter 3 include the initial application of SECCM to corrosion related measurements. Current literature highlighting the limitations of EDC methods in corrosion is reviewed with a description of where SECCM can overcome these limitations. Operating in dual barrel mode with a probe diameter of 2 µm, SECCM is used carry out polarisation measurements on individual grains on polycrystalline low carbon steel in the presence of (neutral pH) 10 mM KNO_3. The passive behaviour is shown to subtly vary between low index orientations by complementing the electrochemical data with crystallographic

information collected with EBSD. Additionally, pitting events are detected when carrying out measurements in areas that contained MnS inclusions (which were analysed using EDS) in results that reflected the literature.

Chapters 4 and 5 include experiments on low carbon steel in the presence of acidic (pH = 2.3) 5 mM H_2SO_4 using single barrel SECCM with a tip diameter of 150 nm. In Chapter 4, chronoamperometry is used to show a dependence of the rate of the hydrogen evolution reaction (HER), the common cathodic process supporting oxidation on metals in acidic media, on crystal orientation. A consistent trend is observed and in an attempt to explain these trends, complementary density functional theory (DFT) calculations of Fe-H bonding energies on each of the low index orientations of iron are carried out. Chapter 4 also includes the detection of enhanced rates of the HER at MnS inclusions and certain grain boundaries. It is noted that the enhancement of the HER due to inclusion and grain boundaries is far more significant compared to variations between grains implying that these surface features are more likely to act as cathodic sites in acidic media.

Chapter 5 uses potential sweep voltammetry to investigate the relationship between iron dissolution and crystal orientation, where a clear and reproducible trend for the low index orientations is observed that is consistent with trends reported in the literature. The SECCM data is again complemented with DFT calculations of the energy required to remove iron atoms from each low index plane. It is shown that grains facilitate higher rates of iron dissolution also require the least energy to remove iron from the lattice, however similarly to the observations made in Chapter 4, it is noted that these calculations should be taken lightly considering the

complexity of real metal surfaces. Additionally, TEM is used to gain a visual image of the effect of SECCM measurements on the surface.

In Chapter 6, SECCM is used to investigate the influence of surface structure on the rate of hydrogen absorption. Initial results collected from low carbon steel in 5 mM H_2SO_4 suggested a relationship, however due to the convolution of different corrosion processes contributing to the measured response, it was impossible to conclude that there was a relationship between surface structure and hydrogen absorption. To remove these issues, SECCM experiments were instead performed on polycrystalline palladium, which is considered the model system to study hydrogen absorption, revealing a clear dependence of the rate of hydrogen absorption on crystal orientation. Additionally, enhanced hydrogen absorption at grain boundaries was also detected. However the enhancement at grain boundaries was expected to be as a result of deformation near the boundary effecting the wetting of the droplet as well as inducing a large number of surface defects.

Overall this thesis has contributed to the expansion of SECCM into the field of corrosion science, whilst also contributing to understanding how the microstructure of metals can influence the behaviour of corrosion related phenomena.

1.9 References

1. Koch, G.; Varney, J.; Thompson, N.; Moghissi, O.; Gould, M.; Payer, J. *International Measures of Prevention, Application, and Economics of Corrosion Technologies IMPACT*; NACE International: 2016.

2. Frankel, G.; Landolt, D., Chapter 1.1 Fundamentals. In *Corrosion and Oxide Films*, Frankel, G.; Stratmann, M., Eds. Wiley-VCH: Germany, 2003; Vol. 4, pp 3-61.

3. Bokstein, B. S.; Mendelev, M. I.; Srolovitz, D. J., *Thermodynamics and Kinetics in Materials Science: A Short Course*. 1st ed.; Oxford University Press: U.S.A, 2005.

4. West, J. M., *Basic Corrosion and Oxidation*. 2nd ed.; Ellis Horwood: U.K., 1986.

5. Pourbaix, M., *Atlas of Electrochemical Equilibria in Aqueous Solutions. IV. Establishment and Interpretation of Potential-pH Equilibrium Diagrams*. 1st ed.; Pergamon Press: London, 1966; p 307-321.

6. Pourbaix, M., *Lectures on Electrochemical Corrosion*. 1st ed.; Springer US: 1973; p 201-295.

7. Talbot, D. E. J.; Talbot, D. R., *Corrosion Science and Technology*. 3rd ed.; Taylor & Francis Group: U.S.A, 2018.

8. McCafferty, E., *Introduction to Corrosion Science*. Springer: London, 2010.

9. Bard, A. J.; Faulkner, L. R., *Electrochemical Methods. Fundamentals and Applications.* 2nd ed.; Wiley: U.S.A, 2001.

10. Ohtsuka, T.; Nishikata, A.; Sakairi, M.; Fushimi, K., *Electrochemical Fundamentals for Corrosion Fundamentals*. Springer: 2018.

11. Evans, U. R., *Metallic corrosion, passivation and protection*. Edward Arnold & Co.: London, 1946.

12. Newman, J.; Thomas-Alyea, K. E., *Electrochemical Systems*. Wiley: U.S.A, 2004.

13. Wighman, R. M., Microvoltammetric electrodes. *Analytical Chemistry* **1981,** *53* (9), 1125A-1134A.

14. Mallon, C.; Keyes, T. E.; Forster, R. J., *Ultrafast Electrochemical Techniques*. John Wiley & Sons, Ltd.: 2013.

15. Bard, A. J.; Stratmann, M.; Unwin, P. R., *Instrumentation and Electroanalytical Chemistry*. Wiley: Germany, 2003.

16. Elgrishi, N; Rountree, K. J; McCarthy B. D; Rountree, E. S; Eisenhart T. T; Dempsey, J. L., A Practical Beginner's Guide to Cyclic Voltammetry. *Journal of Chemical Education* **2018**, 95(2) 197-206

17. Yule, L. C.; Bentley, C. L.; Shkirskiy, V.; Aarons, J.; West, G.; Shollock, B. A.; Unwin, P. R., Nanoscale Active Sites for the Hydrogen Evolution Reaction on Low Carbon Steel. *Journal of Physical Chemistry C* **2019,** *Accepted*, xxxx-xxxx.

18. *ASTM G102-89(2015)e1, Standard Practice for Calculation of Corrosion Rates and Related Information from Electrochemical Measurements*; West Conshohocken, PA, 2015.

19. Suwas, S.; Ray, R. K., *Crystallographic Texture of Materials*. Springer-Verlag: London, 2014.

20. Reardon, A. C., *Metallurgy for the Non-Metallurgist*. Second ed.; ASM International: U.S.A, 2011.

21. Briant, C. L., The Effects of Sulfur and Phosphorus on the Intergranular Corrosion of 304 Stainless Steel. *Corrosion* **1980,** *36* (9), 497-509.

22. Dossett, J. L.; Boyer, H. E., *Practical Heat Treating*. ASM International: U.S.A, 2006.

23. Kelly, A.; Knowles, K. M., Lattice Geometry. In *Crystallography and Crystal Defects*, Wiley: 2012.

24. Frankel, G. S., Pitting Corrosion of Metals. *Journal of The Electrochemical Society* **1998,** *145* (6), 2186-2198.

25. Landolt, D., *Corrosion and Surface Chemistry of Metals*. 1st ed.; CRC Press: U.S.A, 2007.

26. Wranglen, G., Pitting and sulphide inclusions in steel. *Corrosion Science* **1974,** *14* (5), 331-349.

27. Eklund, G. S., Initiation of Pitting at Sulfide Inclusions in Stainless Steel. *Journal of The Electrochemical Society* **1974,** *121* (4), 467-467.

28. Betts, A. J.; Boulton, L. H., Crevice corrosion: review of mechanisms, modelling, and mitigation. *British Corrosion Journal* **2013,** *28* (4), 279-296.

29. Sharland, S. M., A review of the theoretical modelling of crevice and pitting corrosion. *Corrosion Science* **1986,** *27* (3), 289-323.

30. Castle, J. E.; Ke, R., Studies by auger spectroscopy of pit initiation at the site of inclusions in stainless steel. *Corrosion Science* **1990,** *30* (4-5), 409-428.

31. Baker, M. A.; Castle, J. E., The initiation of pitting corrosion at MnS inclusions. *Corrosion Science* **1993,** *34* (4), 667-682.

32. Williams, D. E.; Mohiuddin, T. F.; Zhu, Y. Y., Elucidation of a Trigger Mechanism for Pitting Corrosion of Stainless Steels Using Submicron Resolution Scanning Electrochemical and Photoelectrochemical Microscopy. *Journal of The Electrochemical Society* **1998,** *145* (8), 2664-2672.

33. Ryan, M. P.; Williams, D. E.; Chater, R. J.; Hutton, B. M.; McPhall, S., Why stainless steel corrodes. *Nature* **2002,** *415*, 770-774.

34. Zhang, B.; Ma, X. L., A review—Pitting corrosion initiation investigated by TEM. *Journal of Materials Science & Technology* **2019,** *35* (7), 1455-1465.

35. Böhni, H.; Suter, T.; Schreyer, A., Micro- and nanotechniques to study localized corrosion. *Electrochimica Acta* **1995,** *40* (10), 1361-1368.

36. Suter, T.; Böhni, H., A new microelectrochemical method to study pit initiation on stainless steels. *Electrochimica Acta* **1997,** *42* (20-22), 3275-3280.

37. Suter, T.; Böhni, H., Microelectrodes for studies of localized corrosion processes. *Electrochimica Acta* **1998,** *43* (19), 2843-2849.

38. Webb, E. G.; Suter, T.; Alkire, R. C., Microelectrochemical measurements of the dissolution of single MnS inclusions, and the prediction of the critical conditions for pit initiation on stainless steel. *Journal of the Electrochemical Society* **2001,** *148* (5), B186-B195.

39. Suter, T.; Bohni, H., Microelctrodes for corrosion studies in microsystems. *Electrochimica Acta* **2001,** *47*, 191-199.

40. Scully, J. R., Chaper 4.3 Intergranular Corrosion. In *Corrosion and Oxide Films*, Frankel, G.; Stratmann, M., Eds. Wiley-VCH: Germany, 2003; Vol. 4, pp 344-380.

41. Frankel, G. S.; Vienna, J. D.; Lian, J.; Scully, J. R.; Gin, S.; Ryan, J. V.; Wang, J.; Kim, S. H.; Windl, W.; Du, J., A comparative review of the aqueous corrosion of glasses, crystalline ceramics, and metals. *npj Materials Degradation* **2018,** *2* (1).

42. Reed-Hill, R. E., *Physical Metallurgy Principles*. PWS: U.S.A, 1994.

43. Gupta, D., *Diffusion Processes in Advanced Technological Materials*. Springer: Germany, 2005.

44. Lynch, S., A review of underlying reasons for intergranular cracking for a variety of failure modes and materials and examples of case histories. *Engineering Failure Analysis* **2019,** *100*, 329-350.

45. Briant, C. L.; Banerji, S. K., Intergranularfailure in steel: the role of grain-boundary composition. *International Metals Reviews* **1978,** *23* (1), 164-199.

46. Fontana, M. G., *Corrosion Engineering*. 3rd ed.; McGraw-Hill: 1986.

47. Splinter, S. J.; Rofagha, R.; McIntyre, N. S.; Erb, U., XPS characterization of the corrosion films formed on nanocrystalline Ni-P alloys in sulphuric acid. *Surface and Interface Analysis* **1996,** *24* (3), 181-186.

48. Ralston, K. D.; Birbilis, N., Effect of Grain Size on Corrosion: A Review. *Corrosion* **2010,** *66* (7), 1D-13D.

49. Zeiger, W.; Schneider, M.; Scharnweber, D.; Worch, H., Corrosion behaviour of a nanocrystalline FeAl8 alloy. *Nanostructured Materials* **1995,** *6* (5-8), 1013-1016.

50. Song, D.; Ma, A.-b.; Jiang, J.-h.; Lin, P.-h.; Yang, D.-h., Corrosion behavior of ultra-fine grained industrial pure Al fabricated by ECAP. *Transactions of Nonferrous Metals Society of China* **2009,** *19* (5), 1065-1070.

51. Wang, L.; Lin, Y.; Zeng, Z.; Liu, W.; Xue, Q.; Hu, L.; Zhang, J., Electrochemical corrosion behavior of nanocrystalline Co coatings explained by higher grain boundary density. *Electrochimica Acta* **2007,** *52* (13), 4342-4350.

52. Liu, K. T.; Duh, J. G., Grain size effects on the corrosion behavior of Ni50.5Ti49.5 and Ni45.6Ti49.3Al5.1 films. *Journal of Electroanalytical Chemistry* **2008,** *618* (1-2), 45-52.

53. Youssef, K. M. S.; Koch, C. C.; Fedkiw, P. S., Improved corrosion behavior of nanocrystalline zinc produced by pulse-current electrodeposition. *Corrosion Science* **2004,** *46* (1), 51-64.

54. Li, M. C.; Jiang, L. L.; Zhang, W. Q.; Qian, Y. H.; Luo, S. Z.; Shen, J. N., Electrochemical corrosion behavior of nanocrystalline zinc coatings in 3.5% NaCl solutions. *Journal of Solid State Electrochemistry* **2007,** *11* (9), 1319-1325.

55. Balakrishnan, A.; Lee, B. C.; Kim, T. N.; Panigrahi, B. B., Corrosion Behaviour of Ultra Fine Grained Titanium in Simulated Body Fluid for Implant Application. *Trends in Biomaterials and Artificial Organs* **2008,** *22* (1), 58-64.

56. Tao, S.; Li, D. Y., Tribological, mechanical and electrochemical properties of nanocrystalline copper deposits produced by pulse electrodeposition. *Nanotechnology* **2006,** *17* (1), 65-78.

57. Sikora, E.; Wei, X. J.; Shaw, B. A., Corrosion Behaviour of Nanocrystalline Bulk Al-Mg-Based Alloys. *Corrosion* **2004,** *60* (4), 387-398.

58. Jung, H.; Alfantazi, A., An electrochemical impedance spectroscopy and polarization study of nanocrystalline Co and Co–P alloy in 0.1M H2SO4 solution. *Electrochimica Acta* **2006,** *51* (8-9), 1806-1814.

59. Rofagha., R.; Langer, R.; El-Sherik, A. M.; Erb, U.; Palumbo, G.; Aust, K. T., The corrosion behaviour of nanocrystalline nickel. *Scripta Metallurgica et Materialia* **1991,** *25* (12), 2867-2872.

60. Barbucci, A.; Farne, G.; Matteazzi, P.; Riccieri, R.; Cerisola, G., Corrosion behaviour of nanocrystalline Cu90Ni10 alloy in neutral solution containing chlorides. *Corrosion Science* **1998,** *41* (3), 463-475.

61. Luo, W.; Qian, C.; Wu, X. J.; Yan, M., Electrochemical corrosion behavior of nanocrystalline copper bulk. *Materials Science and Engineering: A* **2007,** *452-453*, 524-528.

62. Joshi, A.; Stein, D. F., Chemistry of Grain Boundaries and Its Relation to Intergranular Corrosion of Austenitic Stainless Steel. *Corrosion* **1972,** *28* (9), 321-330.

63. Matula, M.; Hyspecka, L.; Svoboda, M.; Vodarek, V.; Dagbert, C.; Galland, J.; Stonawska, Z.; Tuma, L., Intergranular corrosion of AISI 316L steel. *Materials Characterization* **2001,** *46* (2-3), 203-210.

64. Shimada, M.; Kokawa, H.; Wang, Z. J.; Sato, Y. S.; Karibe, I., Optimization of grain boundary character distribution for intergranular corrosion resistant 304 stainless steel by twin-induced grain boundary engineering. *Acta Materialia* **2002,** *50*, 2331-2341.

65. Song, G.; Atrens, A.; Dargusch, M., Influence of microstructure on the corrosion of diecast AZ91D. *Corrosion Science* **1998,** *41* (2), 249-273.

66. Ambat, R.; Aung, N. N.; Zhou, W., Evaluation of microstructural effects on corrosion behaviour of AZ91D magnesium alloy. *Corrosion Science* **2000,** *42* (8), 1433-1455.

67. Ben-Hamu, G.; Eliezer, D.; Shin, K. S.; Cohen, S., The relation between microstructure and corrosion behavior of Mg–Y–RE–Zr alloys. *Journal of Alloys and Compounds* **2007,** *431* (1-2), 269-276.

68. Balyanov, A., Corrosion resistance of ultra fine-grained Ti. *Scripta Materialia* **2004,** *51* (3), 225-229.

69. Kim, S., A comparison of the corrosion behaviour of polycrystalline and nanocrystalline cobalt. *Scripta Materialia* **2003,** *48* (9), 1379-1384.

70. Davenport, A. J.; Yuan, Y.; Ambat, R.; Connolly, B. J.; Strangwood, M.; Afseth, A.; Scamans, G. M., Intergranular Corrosion and Stress Corrosion Cracking of Sensitised AA5182. *Materials Science Forum* **2006,** *519-521*, 641-646.

71. Cheng, D.; Tellkamp, V. L.; Lavernia, C. J.; Lavernia, E. J., Corrosion Properties of Nanocrystalline Co–Cr Coatings. *Annals of Biomedical Engineering* **2001,** *29* (9).

72. Schreiber, A.; Rosenkranz, C.; Lohrengel, M. M., Grain-dependent anodic dissolution of iron. *Electrochimica Acta* **2007,** *52* (27), 7738-7745.

73. Schreiber, A.; Schultze, J. W.; Lohrengel, M. M.; Kármán, F.; Kálmán, E., Grain dependent electrochemical investigations on pure iron in acetate buffer pH 6.0. *Electrochimica Acta* **2006,** *51* (13), 2625-2630.

74. Fushimi, K.; Miyamoto, K.; Konno, H., Anisotropic corrosion of iron in pH 1 sulphuric acid. *Electrochimica Acta* **2010,** *55* (24), 7322-7327.

75. Seo, M.; Chiba, M., Nano-mechano-electrochemistry of passive metal surfaces. *Electrochimica Acta* **2001,** *47* (1), 319-325.

76. Xin, R.; Li, B.; Li, L.; Liu, Q., Influence of texture on corrosion rate of AZ31 Mg alloy in 3.5wt.% NaCl. *Materials & Design* **2011,** *32* (8-9), 4548-4552.

77. Song, G.-L.; Mishra, R.; Xu, Z., Crystallographic orientation and electrochemical activity of AZ31 Mg alloy. *Electrochemistry Communications* **2010,** *12* (8), 1009-1012.

78. Wang, W.; Alfantazi, A., Correlation between grain orientation and surface dissolution of niobium. *Applied Surface Science* **2015,** *335*, 223-226.

79. Ulyanov, P. G.; Usachov, D. Y.; Fedorov, A. V.; Bondarenko, A. S.; Senkovskiy, B. V.; Vyvenko, O. F.; Pushko, S. V.; Balizh, K. S.; Maltcev, A. A.; Borygina, K. I.; Dobrotvorskii, A. M.; Adamchuk, V. K., Microscopy of carbon steels: Combined AFM and EBSD study. *Applied Surface Science* **2013,** *267*, 216-218.

80. Lindell, D.; Pettersson, R., Crystallographic effects in corrosion of austenitic stainless steel 316L. *Materials and Corrosion* **2015,** *66* (8), 727-732.

81. Lill, K. A.; Hassel, A. W.; Frommeyer, G.; Stratmann, M., Scanning droplet cell investigations on single grains of a FeAlCr light weight ferritic steel. *Electrochimica Acta* **2005,** *51* (5), 978-983.

82. Brito, P.; Schuller, É.; Silva, J.; Campos, T. R.; Araújo, C. R. d.; Carneiro, J. R., Electrochemical corrosion behaviour of (100), (110) and (111) Fe 3 Al single crystals in sulphuric acid. *Corrosion Science* **2017,** *126*, 366-373.

83. Horton, D. J.; Zhu, A. W.; Scully, J. R.; Neurock, M., Crystallographic controlled dissolution and surface faceting in disordered face-centered cubic FePd. *MRS Communications* **2014,** *4* (3), 113-119.

84. Liu, M.; Qiu, D.; Zhao, M.-C.; Song, G.; Atrens, A., The effect of crystallographic orientation on the active corrosion of pure magnesium. *Scripta Materialia* **2008,** *58* (5), 421-424.

85. Fushimi, K.; Seo, M., An SECM observation of dissolution distribution of ferrous or ferric ion from a polycrystalline iron electrode. *Electrochimica Acta* **2001,** *47* (1), 121-127.

86. Lee, S.; White, H. S., Dissolution of the Native Oxide Film on Polycrystalline and Single-Crystal Aluminum in NaCl Solutions. *Journal of The Electrochemical Society* **2004,** *151* (8), B479-B483.

87. Takabatake, Y.; Fushimi, K.; Nakanishi, T.; Hasegawa, Y., Grain-Dependent Passivation of Iron in Sulfuric Acid Solution. *Journal of the Electrochemical Society* **2014,** *161* (14), C594-C600.

88. Davenport, A. J.; Oblonsky, L. J.; Ryan, M. P.; Toney, M. F., The Structure of the Passive Film That Forms on Iron in Aqueous Environments. *Journal of The Electrochemical Society* **2000,** *147* (6), 2162-2173.

89. Chiba, M.; Seo, M., Mechanoelectrochemical Properties of Passive Iron Surfaces Evaluated by an In Situ Nanoscratching Test. *Journal of The Electrochemical Society* **2003,** *150* (11), B525-B525.

90. Davepon, B.; Schultze, J. W.; König, U.; Rosenkranz, C., Crystallographic orientation of single grains of polycrystalline titanium and their influence on electrochemical processes. *Surface and Coatings Technology* **2003,** *169-170*, 85-90.

91. Schultze, J. W.; Pilaski, M.; Lohrengel, M. M.; König, U., Single crystal experiments on grains of polycrystalline materials: : Oxide formation on Zr and Ta. *Faraday Discuss.* **2002,** *121*, 211-227.

92. Bland, L. G.; Gusieva, K.; Scully, J. R., Effect of Crystallographic Orientation on the Corrosion of Magnesium: Comparison of Film Forming and Bare Crystal Facets using Electrochemical Impedance and Raman Spectroscopy. *Electrochimica Acta* **2017,** *227*, 136-151.

93. Krawiec, H.; Szklarz, Z., Combining the Electrochemical Microcell Technique and the Electron Backscatter Diffraction method to study the electrochemical behaviour of polycrystalline aluminium in sodium chloride solution. *Electrochimica Acta* **2016,** *203* (2015), 426-438.

94. Shahryari, A.; Szpunar, J. A.; Omanovic, S., The influence of crystallographic orientation distribution on 316LVM stainless steel pitting behavior. *Corrosion Science* **2009,** *51* (3), 677-682.

95. Martinez-Lombardia, E.; Lapeire, L.; De Graeve, I.; Verbeken, K.; Kestens, L. A. I.; Terryn, H., Study of the influence of the microstructure on the corrosion properties of pure copper. *Materials and Corrosion* **2016,** *67* (8), 847-856.

96. Frankel, G. S.; Sridhar, N., Understanding localized corrosion. *Materials Today* **2008,** *11* (10), 38-44.

97. Oltra, L., Local electrochemical methods in corrosion research. In *Local Probe Techniques for Corrosion Research*, 2007; pp 1-11.

98. Upadhyay, V.; Battocchi, D., Localized electrochemical characterization of organic coatings: A brief review. *Progress in Organic Coatings* **2016,** *99*, 365-377.

99. Jadhav, N.; Gelling, V. J., Review—The Use of Localized Electrochemical Techniques for Corrosion Studies. *Journal of The Electrochemical Society* **2019,** *166* (11), C3461-C3476.

100. Issacs, H. S., Initiation of Stress Corrosion Cracking of Sensitized Type 304 Stainless Steel in Dilute Thiosulfate Solution. *Journal of The Electrochemical Society* **1988,** *135* (9), 2180-2183.

101. Bastos, A. C.; Quevedo, M. C.; Karavai, O. V.; Ferreira, M. G. S., Review—On the Application of the Scanning Vibrating Electrode Technique (SVET) to Corrosion Research. *Journal of The Electrochemical Society* **2017,** *164* (14), C973-C990.

102. Issacs, H. S., The measurement of the galvanic corrosion of soldered copper using the scanning vibrating electrode technique. *Corrosion Science* **1988,** *28* (6), 547-558.

103. Ogle, K.; Baudu, V.; Garrigues, L.; Philippe, X., Localized Electrochemical Methods Applied to Cut Edge Corrosion. *Journal of The Electrochemical Society* **2000,** *147* (10), 3654-3660.

104. Williams, G.; Coleman, A. J.; McMurray, H. N., Inhibition of Aluminium Alloy AA2024-T3 pitting corrosion by copper complexing compounds. *Electrochimica Acta* **2010,** *55* (20), 5947-5958.

105. Vuillemin, B.; Philippe, X.; Oltra, R.; Vignal, V.; Coudreuse, L.; Dufour, L. C.; Finot, E., SVET, AFM and AES study of pitting corrosion initiated on MnS inclusions by microinjection. *Corrosion Science* **2003,** *45* (6), 1143-1159.

106. Stratmann, M., The investigation of the corrosion properties of metals, covered with adsorbed electrolyte layers—A new experimental technique. *Corrosion Science* **1987,** *27* (8), 869-872.

107. Guillaumin, V.; Schmutz, P.; Frankel, G. S., Characterization of Corrosion Interfaces by the Scanning Kelvin Probe Force Microscopy Technique. *Journal of The Electrochemical Society* **2001,** *148* (5), B163-B173.

108. Williams, G.; McMurray, H. N., Chromate Inhibition of Corrosion-Driven Organic Coating Delamination Studied Using a Scanning Kelvin Probe Technique. *Journal of The Electrochemical Society* **2001,** *148* (10), B377-B385.

109. Schmutz, P.; Frankel, G. S., Corrosion Study of AA2024-T3 by Scanning Kelvin Probe Force Microscopy and In Situ Atomic Force Microscopy Scratching. *Journal of The Electrochemical Society* **1998,** *145* (7), 2295-2306.

110. Rohwerder, M.; Hornung, E.; Stratmann, M., Microscopic aspects of electrochemical delamination: an SKPFM study. *Electrochimica Acta* **2003,** *48* (9), 1235-1243.

111. Melitz, W.; Shen, J.; Kummel, A. C.; Lee, S., Kelvin probe force microscopy and its application. *Surface Science Reports* **2011,** *66* (1), 1-27.

112. Rohwerder, M.; Turcu, F., High-resolution Kelvin probe microscopy in corrosion science: Scanning Kelvin probe force microscopy (SKPFM) versus classical scanning Kelvin probe (SKP). *Electrochimica Acta* **2007,** *53* (2), 290-299.

113. Bard, A. J.; Fan, F. R. F.; Kwak, J.; Lev, O., Scanning electrochemical microscopy. Introduction and principles. *Analytical Chemistry* **1989,** *61* (2), 132-138.

114. Amemiya, S.; Bard, A. J.; Fan, F. R. F.; Mirkin, M. V.; Unwin, P. R., Scanning Electrochemical Microscopy. *Analytical Chemistry* **2008,** *1*, 95-131.

115. Payne, N. A.; Stephens, L.; Mauzeroll, J., The Application of Scanning Electrochemical Microscopy to Corrosion Research. *Corrosion* **2017,** *73* (7), 759-780.

116. Yuan, Y.; Li, L.; Wang, C.; Zhu, Y., Study of the effects of hydrogen on the pitting processes of X70 carbon steel with SECM. *Electrochemistry Communications* **2010,** *12* (12), 1804-1807.

117. Lister, T. E.; Pinhero, P. J., Scanning Electrochemical Microscopy Study of Corrosion Dynamics on Type 304 Stainless Steel. *Electrochemical and Solid-State Letters* **2002,** *5* (1), B33-B36.

118. Gabrielli, C.; Joiret, S.; Keddam, M.; Perrot, H.; Portail, N.; Rousseau, P.; Vivier, V., A SECM assisted EQCM study of iron pitting. *Electrochimica Acta* **2007,** *52* (27), 7706-7714.

119. Davoodi, A.; Pan, J.; Leygraf, C.; Norgren, S., In Situ Investigation of Localized Corrosion of Aluminum Alloys in Chloride Solution Using Integrated EC-AFM/SECM Techniques. *Electrochemical and Solid-State Letters* **2005,** *8* (6), B21-B24.

120. Ebejer, N.; Güell, A. G.; Lai, S. C. S.; McKelvey, K.; Snowden, M. E.; Unwin, P. R., Scanning electrochemical cell microscopy: a versatile technique for nanoscale electrochemistry and functional imaging. *Annual Review of Analytical Chemistry* **2013,** *6*, 329-51.

121. Thomas, S.; Izquierdo, J.; Birbilis, N.; Souto, R. M., Possibilities and limitations of scanning electrochemical microscopy of Mg and Mg alloys. *Corrosion* **2015,** *71* (2), 171-183.

122. Lohrengel, M. M.; Moehring, A.; Pilaski, M., Capillary-based droplet cells: Limits and new aspects. *Electrochimica Acta* **2001,** *47* (1), 137-141.

123. Rault, V.; Vignal, V.; Krawiec, H.; Dufour, F., Quantitative assessment of local misorientations and pitting corrosion behaviour of pearlitic steel using electron backscattered diffraction and microcapillary techniques. *Corrosion Science* **2015,** *100*, 667-671.

124. Perren, R.; Suter, T.; Uggowitzer, P. J.; Weber, L.; Magdowski, R.; Böhni, H.; Speidel, M. O., Corrosion resistance of super duplex stainless steels in chloride ion containing environments: investigations by means of a new microelectrochemical method.II. Influence of precipitates. *Corrosion Science* **2001,** *43*, 727-745.

125. Webb, E. G.; Alkire, R. C., Pit Initiation at Single Sulfide Inclusions in Stainless Steel. *Journal of The Electrochemical Society* **2002,** *149* (6), B286-B286.

126. Suter, T.; Alkire, R. C., Microelectrochemical Studies of Pit Initiation at Single Inclusions in Al 2024-T3. *Journal of The Electrochemical Society* **2001,** *148* (1), B36-B36.

127. Krawiec, H.; Vignal, V.; Oltra, R., Use of the electrochemical microcell technique and the SVET for monitoring pitting corrosion at MnS inclusions. *Electrochemistry Communications* **2004,** *6* (7), 655-660.

128. Krawiec, H.; Vignal, V.; Akid, R., Numerical modelling of the electrochemical behaviour of 316L stainless steel based upon static and dynamic experimental microcapillary-based techniques. *Electrochimica Acta* **2008,** *53* (16), 5252-5259.

129. Andreatta, F.; Lohrengel, M. M.; Terryn, H.; De Wit, J. H. W., Electrochemical characterisation of aluminium AA7075-T6 and solution heat treated AA7075 using a micro-capillary cell. *Electrochimica Acta* **2003,** *48* (20-22), 3239-3247.

130. Andreatta, F.; Fedrizzi, L., The use of the electrochemical micro-cell for the investigation of corrosion phenomena. *Electrochimica Acta* **2016,** *203*, 337-349.

131. Bentley, C. L.; Kang, M.; Unwin, P. R., Scanning electrochemical cell microscopy: New perspectives on electrode processes in action. *Current Opinion in Electrochemistry* **2017,** *6*, 23-30.

132. Ebejer, N.; Schnippering, M.; Colburn, A. W.; Edwards, M. A.; Unwin, P. R., Localized High Resolution Electrochemistry and Multifunctional Imaging : Scanning Electrochemical Cell Microscopy. *Analytical Chemistry* **2010,** *82* (22), 9141-9145.

133. Snowden, M. E.; Gu, A. G.; Lai, S. C. S.; Kelvey, K. M.; Ebejer, N.; Connell, M. A. O.; Colburn, A. W.; Unwin, P. R., Scanning Electrochemical Cell Microscopy: Theory and Experiment for Quantitative High Resolution Spatially-Resolved Voltammetry and Simultaneous Ion-Conductance Measurements. *Analytical Chemistry* **2012,** *84*, 2483-2491.

134. Momotenko, D.; Byers, J. C.; McKelvey, K.; Kang, M.; Unwin, P. R., High-Speed Electrochemical Imaging. *ACS Nano* **2015,** *9* (9), 8942-52.

135. Bentley, C. L.; Unwin, P. R., Nanoscale Electrochemical Movies and Synchronous Topographical Mapping of Electrocatalytic Materials. *Faraday Discussions* **2018,** *210*, 365-379.

136. Unwin, P. R.; Güell, A. G.; Zhang, G., Nanoscale Electrochemistry of sp2 Carbon Materials: From Graphite and Graphene to Carbon Nanotubes. *Accounts of Chemical Research* **2016,** *49* (9), 2041-2048.

137. Williams, C. G.; Edwards, M. A.; Colley, A. L.; Macpherson, J. V.; Unwin, P. R., Scanning micropipet contact method for high-resolution imaging of electrode surface redox activity. *Analytical Chemistry* **2009,** *81* (7), 2486-2495.

138. Bentley, C. L.; Edmondson, J.; Meloni, G. N.; Perry, D.; Shkirskiy, V.; Unwin, P. R., Nanoscale Electrochemical Mapping. *Analytical Chemistry* **2019,** *91* (1), 84-108.

139. Aaronson, B. D. B.; Chen, C. H.; Li, H.; Koper, M. T. M.; Lai, S. C. S.; Unwin, P. R., Pseudo-single-crystal electrochemistry on polycrystalline electrodes: Visualizing activity at grains and grain boundaries on platinum for the Fe^{2+}/Fe^{3+} redox reaction. *Journal of the American Chemical Society* **2013,** *135* (10), 3873-3880.

140. Chen, C.-H.; Meadows, K. E.; Cuharuc, A.; Lai, S. C. S.; Unwin, P. R., High resolution mapping of oxygen reduction reaction kinetics at polycrystalline platinum electrodes. *Physical Chemistry Chemical Physics* **2014,** *16* (34), 18545-18545.

141. Aaronson, B. D.; Lai, S. C.; Unwin, P. R., Spatially resolved electrochemistry in ionic liquids: surface structure effects on triiodide reduction at platinum electrodes. *Langmuir* **2014,** *30* (7), 1915-9.

142. Chen, C. H.; Jacobse, L.; McKelvey, K.; Lai, S. C. S.; Koper, M. T. M.; Unwin, P. R., Voltammetric scanning electrochemical cell microscopy: Dynamic imaging of hydrazine electro-oxidation on platinum electrodes. *Analytical Chemistry* **2015,** *87* (11), 5782-5789.

143. Chen, C. H.; Ravenhill, E. R.; Momotenko, D.; Kim, Y. R.; Lai, S. C. S.; Unwin, P. R., Impact of Surface Chemistry on Nanoparticle-Electrode Interactions in the Electrochemical Detection of Nanoparticle Collisions. *Langmuir* **2015,** *31* (43), 11932-11942.

144. Bentley, C. L.; Kang, M.; Unwin, P. R., Time-Resolved Detection of Surface Oxide Formation at Individual Gold Nanoparticles: Role in Electrocatalysis and New Approach for Sizing by Electrochemical Impacts. *Journal of the American Chemical Society* **2016,** *138* (39), 12755-12758.

145. Bentley, C. L.; Kang, M.; Unwin, P. R., Nanoscale Structure Dynamics within Electrocatalytic Materials. *Journal of the American Chemical Society* **2017,** *139* (46), 16813-16821.

146. Kang, M.; Perry, D.; Kim, Y. R.; Colburn, A. W.; Lazenby, R. A.; Unwin, P. R., Time-Resolved Detection and Analysis of Single Nanoparticle Electrocatalytic Impacts. *Journal of the American Chemical Society* **2015,** *137* (34), 10902-10905.

147. Ustarroz, J.; Kang, M.; Bullions, E.; Unwin, P. R., Impact and Oxidation of Single Silver Nanoparticles at Electrode Surfaces: One Shot versus Multiple Events. *Chem. Sci.* **2016,** *8*, 1841-1853.

148. Tao, B.; Yule, L. C.; Daviddi, E.; Bentley, C. L.; Unwin, P. R., Correlative Electrochemical Microscopy of Li-Ion (De)intercalation at a Series of Individual $LiMn_2O_4$ Particles. *Angew Chem Int Ed Engl* **2019,** *58* (14), 4606-4611.

149. Martin-Yerga, D.; Costa-Garcia, A.; Unwin, P. R., Correlative Voltammetric Microscopy: Structure-Activity Relationships in the Microscopic Electrochemical Behavior of Screen Printed Carbon Electrodes. *ACS Sens* **2019,** *4* (8), 2173-2180.

150. Bentley, C. L.; Kang, M.; Maddar, F.; Li, F.; Walker, M.; Zhang, J.; Unwin, P. R., Electrochemical Maps and Movies of the Hydrogen Evolution Reaction on Natural Crystals of Molybdenite (MoS 2): Basal vs. Edge Plane Activity. *Chemical Science* **2017,** *8*, 6583-6593.

151. Bentley, C. L.; Andronescu, C.; Smialkowski, M.; Kang, M.; Tarnev, T.; Marler, B.; Unwin, P. R.; Apfel, U. P.; Schuhmann, W., Local Surface Structure and Composition Control the Hydrogen Evolution Reaction on Iron Nickel Sulfides. *Angewandte Chemie - International Edition* **2018,** *57* (15), 4093-4097.

CHAPTER 2
Experimental Methods

Experimental sections are also included in each results chapter. They include more detailed information about the methods specific to the chapters. This section will provide a general overview of the methods used throughout the thesis.

2.1 Chemicals and electrode materials

All solutions were prepared with ultra-pure deionised water (Integra HP, U.K.) with a resistivity of 18.2 MΩ cm at 25ºC. Chemicals were used as provided unless otherwise stated and all experiments were performed at room temperature.

In Chapters 3, 4, 5, and 6, low carbon steel samples were mounted in a conductive carbon-based mounting compound (KonductoMet. Buehler, U.S.A) using a mounting press (SimpliMet. Buehler, U.S.A). The samples were subsequently polished with polishing cloths (TriDent and MicroCloth. Buehler, U.S.A) and polishing suspension (9 µm to 1 µm MetaDi Supreme Diamond and 0.05 µm MasterPrep, Buehler, U.S.A) using a polishing machine (AutoMet 300 Pro. Buehler, U.S.A). The surface roughness of the polished samples is expected to follow the quoted value on the polishing suspension used in the final step (50 nm). However, experiments have shown the polishing to be precise enough to reveal varying topography (and thus different polishing rates) between grains (~20nm), as shown in Figure 2.1), which could suggest that finer polishing is achievable than the quoted value on the polishing suspension. It is important to note however, that the topography displayed in Figure 2.1 was extracted using

SECCM which is not its primary function. Atomic force microscopy (AFM) would perhaps be a more appropriate tool to accurately measure how flat of a surface the polishing procedure used herein can achieve.

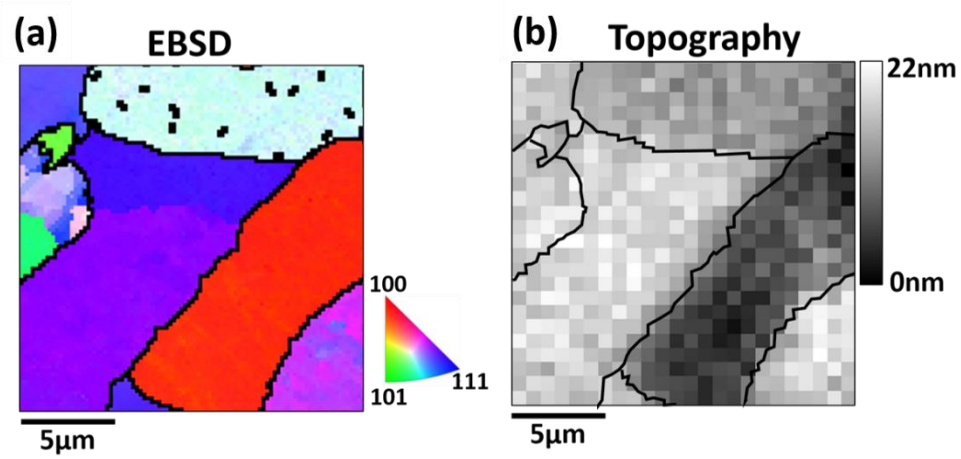

Figure 2. 1. (a) EBSD map of an area of low carbon steel scanned using SECCM. **(b)** Topography, extracted using the approach distance of the SECCM probe during a scan, of the corresponding area of low carbon steel shown in **(a)**

Between each polishing stage the samples were washed with soapy water and acetone before being gently blow dried. Electrical connection was made using conductive copper tape to attach a wire to the sample (Figure 2.1).

The quasi reference counter electrodes (QRCEs) were Ag/AgCl and Pd/H_2. Ag/AgCl electrodes prepared by anodizing silver wire (diameter = 0.125 mm) in saturated KCl solution. Pd/H_2 electrodes were prepared by hydrogenating palladium wire (diameter = 0.125 mm) in 50 mM sulphuric acid solution. The QRCEs were stored in the solution that was used in the SECCM experiment.

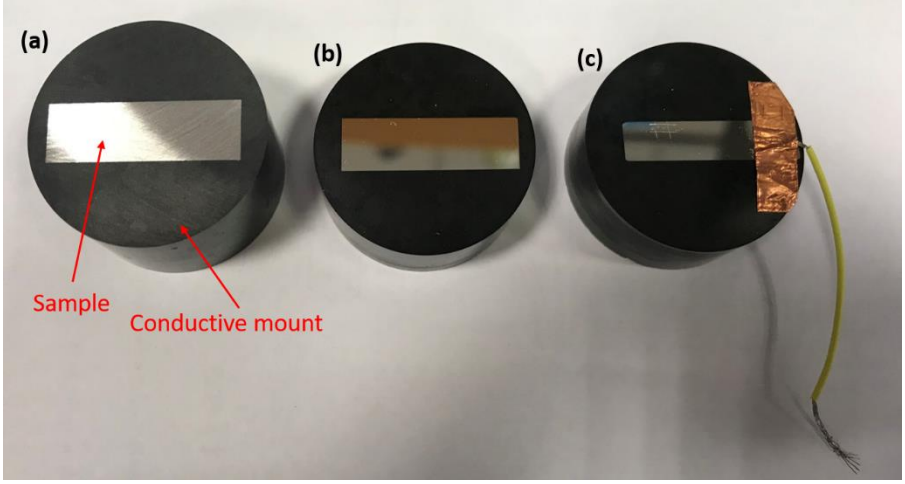

Figure 2. 2. Mounted samples **(a)** before polishing, **(b)** after polishing and **(c)** with wire attached.

2.2 SECCM probe fabrication

All of the pipettes used in this study were produced from glass capillaries (Figure 2.2a) using a laser puller (P-2000, Sutter Instruments). A glass capillary is suspended with a load applied to each end whilst a laser is used to melt the glass in the middle of the capillary, as shown in Figure 2.2c. By adjusting the heating, loads applied and the pulling time, the diameter of the opening of the pulled capillaries can be customised. The capillary material and pulling parameters for each results chapter are also shown in Table 2.1. The pipettes were filled with electrolyte using microfillers (MicroFil, World Precision Instruments). A microscope was used to check for defects and bubbles at the tip of the pipette.

In Chapter 3 the tip of the pipette was silanised with dichlorodimethylsilane to cover the outer wall of the pipette with a hydrophobic coating to help contain the droplet.[1] Silicone oil was used in the pipettes for Chapters 3, 4, 5 and 6, which sits on top of the electrolyte to reduce evaporation of the electrolyte during the experiments.[2]

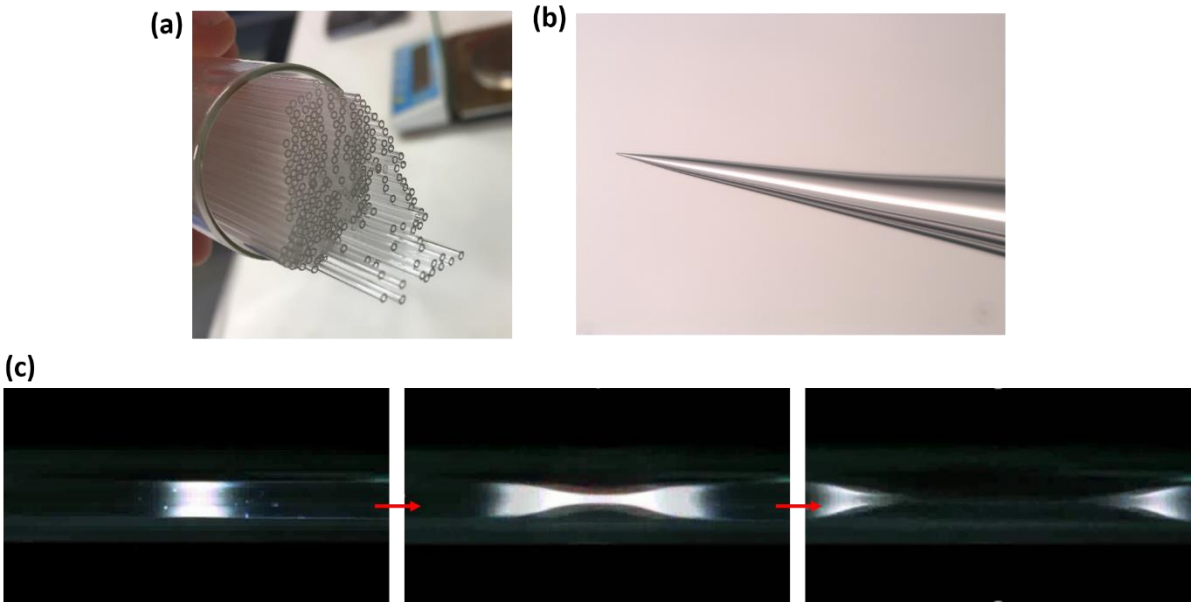

Figure 2. 3. (a) Capillaries photographed before laser pulling. **(b)** Optical image collected using a microscope of the tip of a laser pulled capillary. **(c)** Optical images of a capillary during laser pulling. Figure 2. 1c was adapted from Sutter Instruments.[3]

Table 2. 1. Specification of capillary material, diameter and the pulling parameters used to fabricate pipettes for experiments in Chapters 3, 4, 5 and 6.

Diameter of Pipette	**Capillary material; Dimensions; Supplier**	**Pulling parameters (HEAT, FILAMENT, VELOCITY, DELAY, PULL)**
Chapter 3 ≈ 2 µm	Borosilicate theta glass TGC150-10; outer diameter 1.5 mm, inner diameter 1.24 mm; Harvard Apparatus	Line 1: 800, 4, 40, 130, 30 Line 2: 750, 3, 20, 130, 100
Chapters 4, 5 and 6 ≈ 150-250 nm	Borosilicate glass GC120F-10; outer diameter 1.2 mm, inner diameter 0.9 mm; Harvard Apparatus	Line 1: 350, 3, 30, 220, 0 Line 2: 350, 3, 40, 180, 120

2.3 SECCM operating system

The typical instrumental set up for SECCM is shown in Figure 2.3, details of the instrumentation used can be found in the experimental sections of each results chapter. The sample ([1], Figure 2.3a), is placed in a sample holder ([2], Figure 2.3a) which is then placed on a *xy*-direction piezoelectric positioner ([3], Figure 2.3a) allowing fine movement of the probe across the sample surface. The range of the *xy* positioner varied from 100×100 μm (P-631.2 PIHera XY Piezo stage. PhysikInstrumente) to 500×500 μm (P-625.2 PIHera XY Piezo stage. PhysikInstrumente). The SECCM probe ([4], Figure 2.3a) is attached to a holder that is connected to a *z*-direction piezoelectric positioner (P-753.2 LISA. PhysikInstrumente) enabling fine control of the probe as it is approached to the sample surface ([5], Figure 2.3a). The z-piezo is also attached to a *z*-direction micropositioner which is equipped with a picomotor ([6], Figure 2.3a) and a *xy*-direction micropositioner ([7], Figure 2.3a) enabling coarse control of the probe. The micropositioners are operated manually and work in conjunction with an optical camera ([8, Figure 2.3a) to enable rough positioning of the SECCM probe close to the surface at specific sites on the sample surface.[4]

The SECCM positioning system (Figure 2.3a) is fixed to an optical table (RS2000. Newport, U.S.A) supported by vibration isolating supports ([9], Figure 2.3b) to minimise vibrations during experiments. The SECCM positioning system is enclosed in a Faraday cage ([10], Figure 2.3b) to reduce electrical noise and is also equipped with heat sinks and vacuum panels to reduce variations in temperature. The temperature of the laboratory was controlled by an air-conditioning system and held at a constant 24 ± 1 ºC. The instrumentation ([11], Figure

2.3b) is placed on a separate stand to the optical table and (depending on the SECCM configuration) can include: piezo controllers and monitors, electrometers, signal filters, bipotentiostats, lock-in amplifiers, and a connector box.

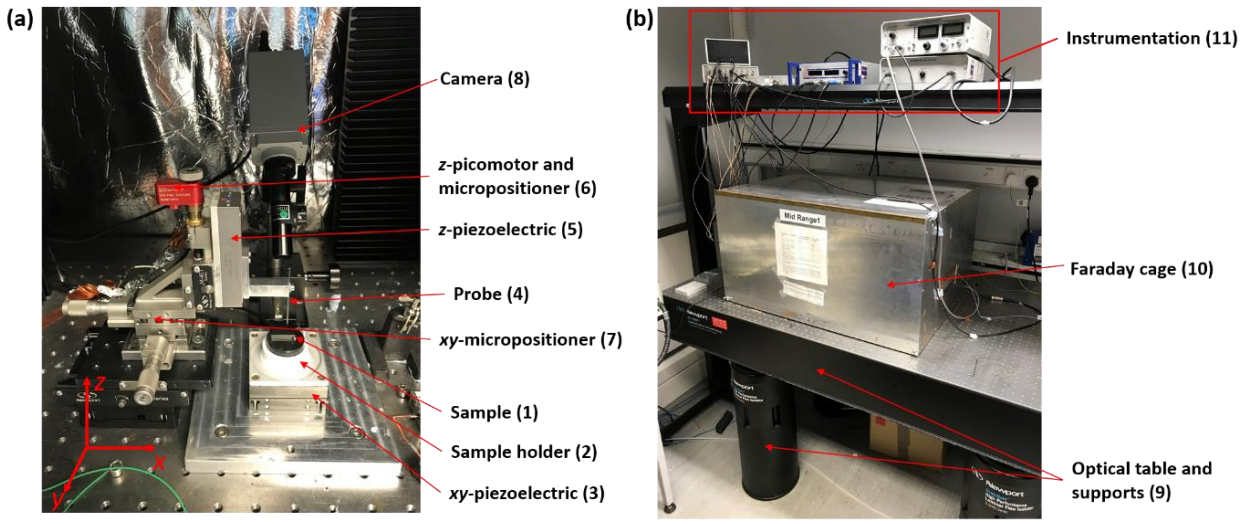

Figure 2. 4. (a) Generic SECCM positioning system with the key components labelled. **(b)** Mounting and encasement of the SECCM system.

All of the instrumentation is passed through a connector box and connected to a PC equipped with a field-programmable gate array (FPGA) card (PCIe-7852R). Using LabVIEW software running the Warwick Electrochemical Scanning Probe Microscopy (WEC-SPM) software, the user interface on the PC can be used to control the instrumentation and record data from multiple sources simultaneously. The data acquisition rate (s^{-1}) was also controlled through the LabVIEW interface. It is important to note that the measured current was passed through a filter with a time constant less than that of the acquisition rate. The recorded data was processed using self-written MATLAB scripts (R2016b, Mathworks, U.S.A).

2.4 Surface characterisation: electron microscopy techniques

2.4.1 Scanning Electron Microscopy (SEM)

The characterisation methods adopted in this thesis are based on scanning electron microscopy (SEM) techniques. By scanning a beam of electrons across a sample surface, information about the topography, texture and composition at the nanoscale can be extracted.[5] By comparing these properties to the electrochemical information gathered using SECCM, one can start to relate surface features to the activity of electrochemical processes. With this information a more detailed understanding of the behaviour of macroscale electrodes can be obtained.

To make locating SECCM scanning areas easier with SEM, reference points or patterns were often marked into the material surface. Once SECCM scans were completed, the area was located on the sample surface using a Zeiss SUPRA FE-SEM (Zeiss, Germany). Using either secondary electron or InLens detectors, the footprints left by individual SECCM experiments from either residue of electrolyte or from physical changes to the surface were visible. An example of this is shown in Figure 2.4. The scanning points could be examined to check for physical changes to the droplet cell during scans and to measure the size of the wetting area of each point so the working electrode area could be obtained. SEM images were collected at 5-10 keV with an aperture diameter of 30-60 µm depending on the resolution requirements to detect SECCM scanning sites.

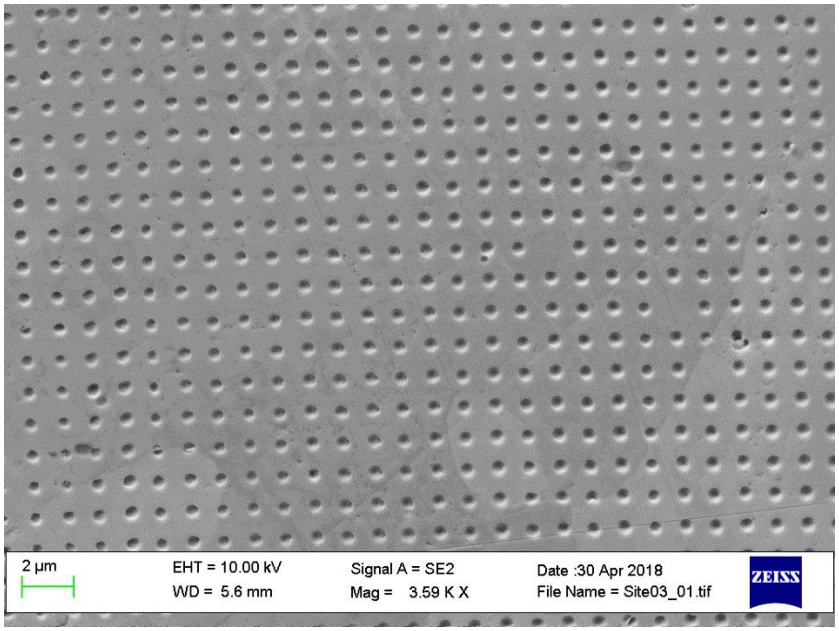

Figure 2. 5. SEM image of the footprints left from SECCM measurements on low carbon steel.

2.4.2 Electron backscatter diffraction (EBSD)

Electron backscatter diffraction (EBSD) enables the identification of individual grain orientations on the surfaces of polycrystalline materials. A phosphor screen is employed to detect diffraction patterns produced by high energy electrons scattering off crystalline materials. These patterns, known as *Kikuchi patterns*, are characteristic of the crystal structure and can be used to identify the orientation at individual scanning points.[6] Maps of orientation can be formed on a point by point basis to build a picture of the crystal structure of a surface (*e.g.* Figure 1.13).

When an electron beam enters a crystal lattice the electrons are scattered in all directions and as a result some of the electrons arrive at lattice planes within the crystal at the correct Bragg angle. Electrons that enter a lattice plane at the Bragg angle are elastically scattered producing a high intensity beam of scattered electrons. This beam of 'Bragg' electrons is scattered in all directions resulting in the formation of a *Kossel cone.*[7] A second symmetrical

Kossel cone is also produced from the opposite side of the lattice plane as shown schematically in Figure 2.5a, resulting in pairs of Kossel cones specific to each lattice plane. The Kikuchi pattern is formed by using a 2D screen to detect the pairs of Kossel cones which is shown in Figure 2.5b. With prior knowledge of the composition of the substrate, the expected Kikuchi patterns originating from the different crystal planes can be super imposed on the measured Kikuchi pattern to find the plane that fits the experimentally measured pattern best (Figure 2.5c).

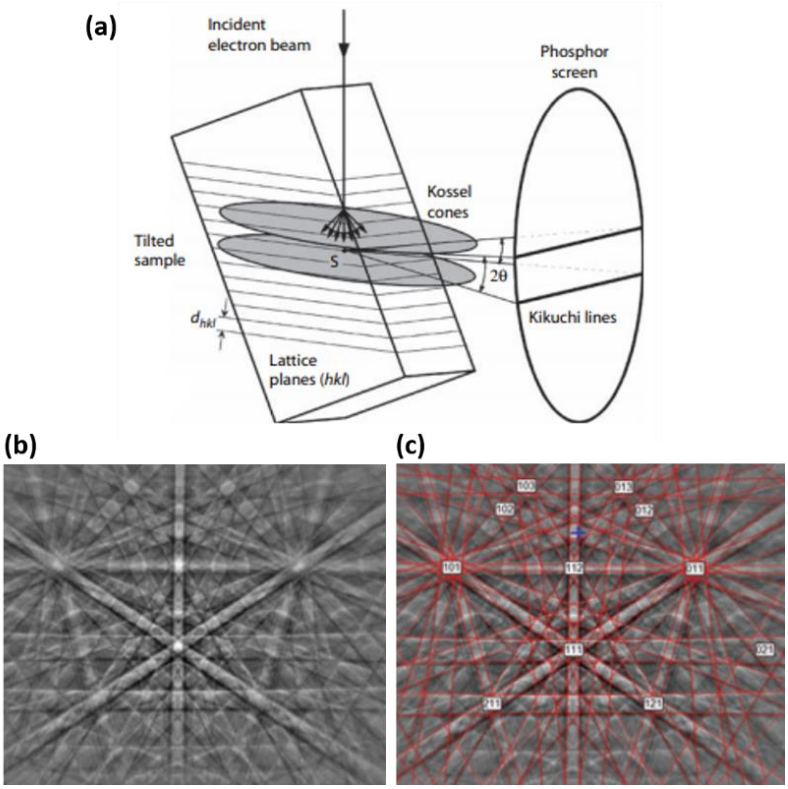

Figure 2. 6. (a) Schematic showing the origin of Kikuchi patterns originating from a crystal structure. **(b)** Kikuchi patterns originating from a copper substrate using EBSD. **(c)** EBSD software fitting predetermined Kikuchi patters to the experimental Kikuchi patterns shown in **(b)**. Figure 2.6a was adapted from O. Engler and V. Randle (2009).[7] Figures 2.6b and 2.6c were adapted from *"EBSD Explained: From data acquisition to advanced analysis"* Oxford instruments (2015).

The quality of the Kikuchi pattern is very sensitive to the quality of the substrate surface. For example, if the surface has been deformed during preparation the intensity of the Kikuchi patterns will be too low for the EBSD software to detect and as a result will not be able to identify the crystal orientation substrate. Figure 2.6a shows an EBSD map collected on low carbon steel where the black regions on the sample indicate where a Kikuchi pattern has not been detected. Interestingly the areas of non-detection are grouped around the edge of the sample which perhaps indicates a deformation induced during the mounting of the sample.

Additionally, Figures 2.6b and 2.6c show EBSD maps collected on freshly polished and one month since polishing low carbon steel. These maps show how contamination of the surface can also lead to indetectable Kikuchi patterns on the surface.

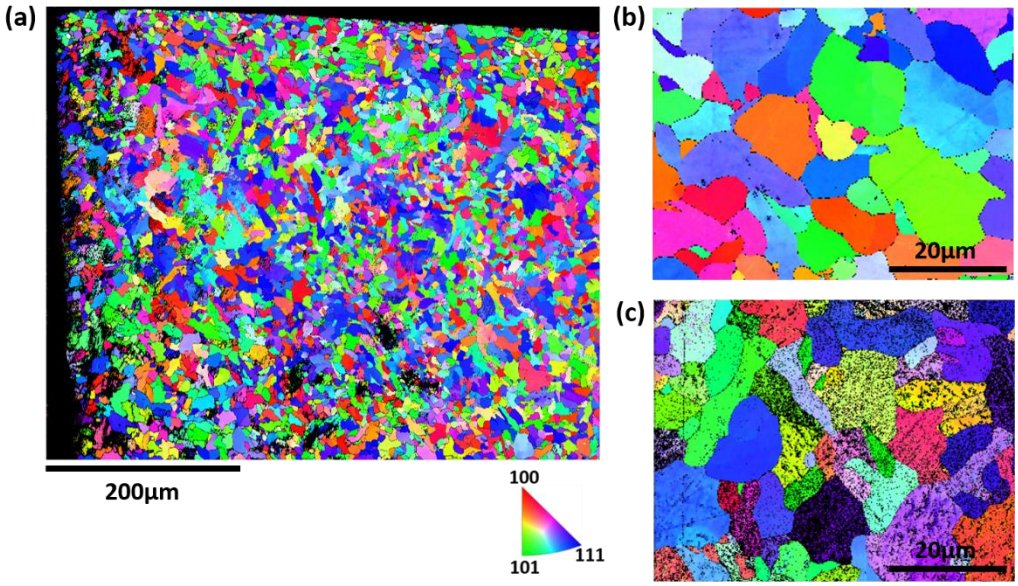

Figure 2. 7. EBSD maps of a low carbon steel surface. **(a)** Large area of low carbon steel with deformation apparent on the edge of the sample. **(b)** EBSD map of a freshly polishing low carbon steel surface. **(c)** EBSD map of a low carbon steel surface one month after polishing.

A Nordlys EBSD detector (Oxford Instruments, U.K.), shown in Figure 2.7, was used to carry out EBSD in this study. EBSD was carried out at 20 keV with the sample tilted 70º to the detector using an aperture diameter of 240 µm. Changes to the surface from SECCM experiments were not significant enough to hinder the detection of different grains with EBSD.

With the information gathered about the grain structure and surface composition of the SECCM scanning area, it was possible to correlate between electrochemical behaviour and microstructure. In Chapters 3, 4, and 5, the main focus was on the electrochemical response of the low index grains (*i.e.* 100, 101 and 111 orientations) so that the trends in the data could be compared to that in the literature, the majority of which focussed was on low index crystal orientations when investigating grain dependant corrosion behaviour. Considering the SECCM probe could not be positioned above specific grains, it was highly unlikely that perfect low index grains could be located and scanned. Therefore, grains that were within 10º of the low index orientations were identified using 5Channel EBSD software (Oxford Instruments, U.K).

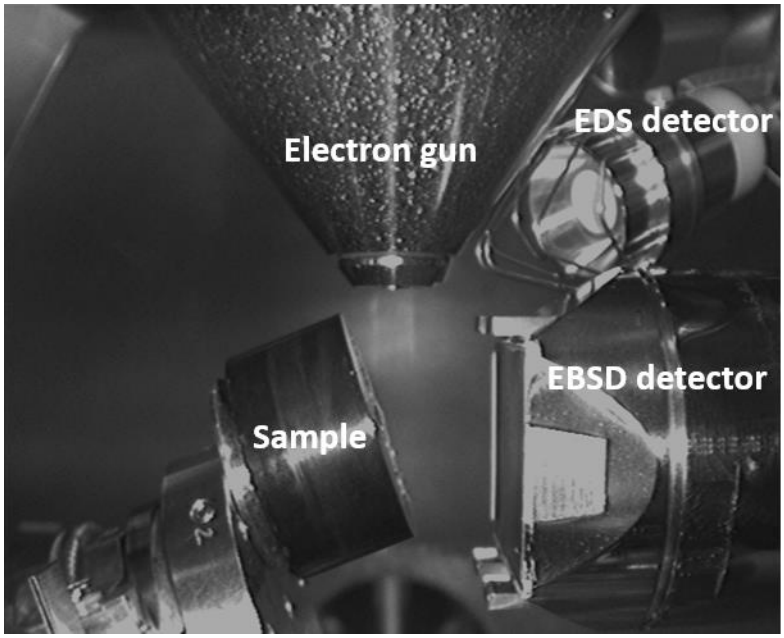

Figure 2. 8. Image of the electron microscopy configuration for SEM, EBSD, and EDS analysis.

2.4.3 Energy dispersive spectroscopy (EDS)

The impact of high energy electrons on to a surface can also produce X-rays with energies characteristic of the surface composition. Incident electrons strike and subsequently eject orbital electrons of the atoms thus creating a vacancy. Electrons from higher energy shells relax and fill the vacancy releasing X-rays in the process. The energy of these X-rays can be used to distinguish different elements which is the principle behind energy dispersive spectroscopy (EDS).[8] In this study, an X-max 50 mm^2 EDS detector (Oxford Instruments, U.K), shown in Figure 2.5, was used to carry out EDS with an acceleration voltage of 10 keV and an aperture of 120 µm.

2.4.4 Focussed ion beam milling – Transmission electron microscopy (FIB-TEM)

The resolution of electron microscopy techniques can be increased by using larger acceleration voltages, which is what is used in transmission electron microscopy (TEM). Beams of high

energy electrons are passed through specimens of thickness less than 0.1 μm, and the resulting scattering of the electrons is detected to build images with resolution as low as 0.1 nm.[8]

To extract and prepare a specimen from a surface ready for TEM, focussed ion beam milling (FIB) is often used.[9] A gallium ion beam, produced using liquid metal ion sources, is focussed with nanoscale precision at areas of a sample surface. The high energy beam can cut through a sample, at a rate dependant of the sample material, so parts of the surface can be extracted.[10] The ion beam can cause significant damage to the surface so platinum is usually to protect areas of the surface required for analysis. The ion beam is also used to thin the extract so that it is suitable for TEM.

2.5 SECCM for corrosion science: experimental challenges

As discussed previously in section 1.7, SECCM has been shown to be very effective at scanning variations in electrochemical behaviour across inhomogeneous electrode surfaces. However, these experiments have been primarily performed on substrates where the surface does not physically change. Therefore, the risk of the droplet at the tip of the SECCM probe becoming unstable is low.

By using SECCM to perform corrosion measurement on more active surfaces, there is a greater risk of the electrochemical measurements becoming influenced by the changing substrate resulting in less reproducible data and higher rates of scan failures. The purpose of this section is to highlight some of experimental challenges one may encounter whilst attempting to perform corrosion measurements with SECCM.

2.5.1 Contamination between scanning points

One of the most common SECCM scan failure mechanisms occurs due measurements being influenced by previous scanning sites. Sometimes the change to the surface, caused by an electrochemical measurement, can extend beyond the droplet diameter which causes the scanning sites to overlap as shown in Figure 2.9. As a result, measurements are never performed on a clean substrate surface. This problem is commonly encountered whilst carrying out initial experiments on an unfamiliar substrate as the extend of reactivity is sometimes unknown. It is therefore important to be conservative when setting a hopping distance (distance between scanning sites) for a new system. Unfortunately, this may limit the maximum resolution achieved with SECCM.

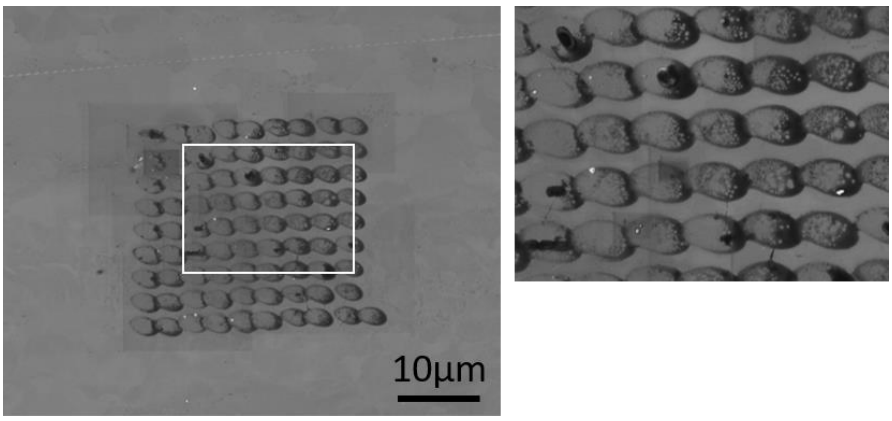

Figure 2. 9. SEM image of an SECCM scan performed on 304L stainless steel in 10 mM NaCl.

In more extreme cases, the corrosion products formed at each scanning sites can begin to merge during a scan forming thick layers of corrosion product as shown in Figure 2.10. This can occur if the system is either too reactive or the time spent in contact at each scanning site is too long resulting in a large build-up of corrosion product. By reducing the measurement time at each scanning site, the risk of this occurring can be reduced.

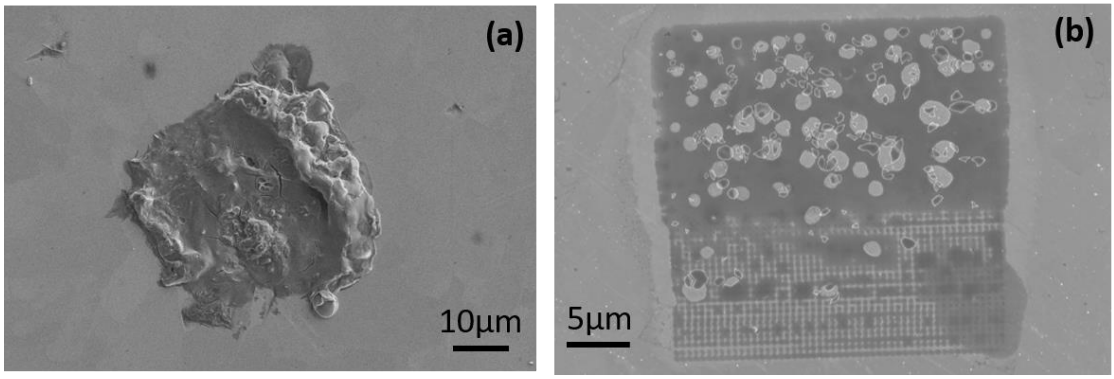

Figure 2. 10. SEM images of SECCM scans performed on low carbon steel in **(a)** 10 mM KNO_3 and **(b)** 10 mM H_2SO_4.

Another source of contamination can come from the tip of the SECCM probe. Corrosion products that form on the tip can build up during the scan and eventually start depositing on the surface as shown in Figure 2.11. The build-up of corrosion products in the tip can also have less obvious effect, where the electrolyte composition can change during a scan. One method of eliminated this risk is to increase the time between measurements which allows any products to diffuse into the upper part of the SECCM pipet.

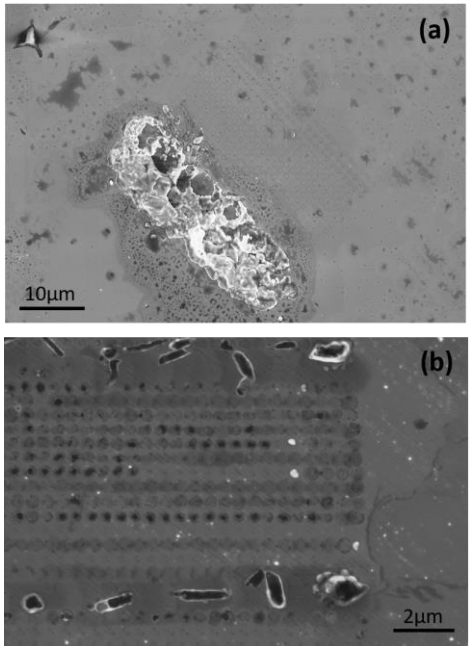

Figure 2. 11. SEM images of SECCM scans performed on low carbon steel in **(a)** 10 mM KNO_3 and **(b)** 10 mM H_2SO_4.

2.5.2 Surface wetting

The extent to which the droplet wets across the electrode surface can also cause problems during SECCM scans. The resolution of an SECCM measurement is limited by the extent of the wetting causing issues when scanning features at the nanoscale. The example shown in Figure 2.12 is of a particularly challenging system (pure Ni in 50 mM KOH) due to extensive wetting.

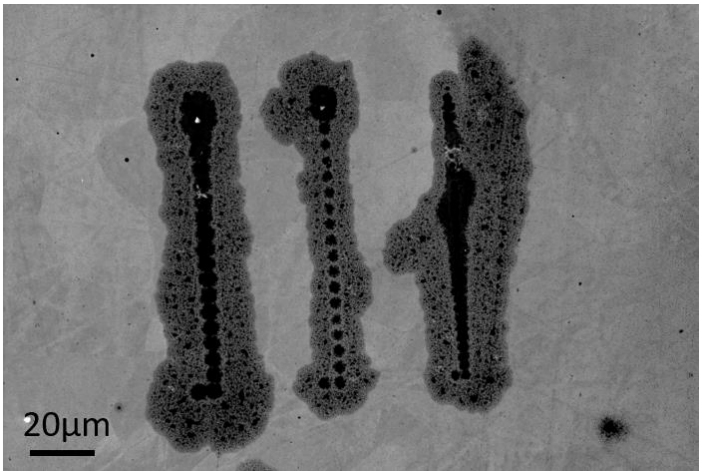

Figure 2. 12. SEM images of SECCM line scans performed on pure Ni in 50 mM KOH.

Aluminium alloys also pose significant challenged due to wetting, as shown in Figure 2.13. Unfortunately, it is very difficult to control the extend of wetting, however it can be minimised by reducing measurement time. This is method is best shown in Chapter 4, where short chronoamperometry measurements were used. Recent SECCM based studies have explored the use of oil layers on top of electrode surfaces as a method of confining the droplet.[11]

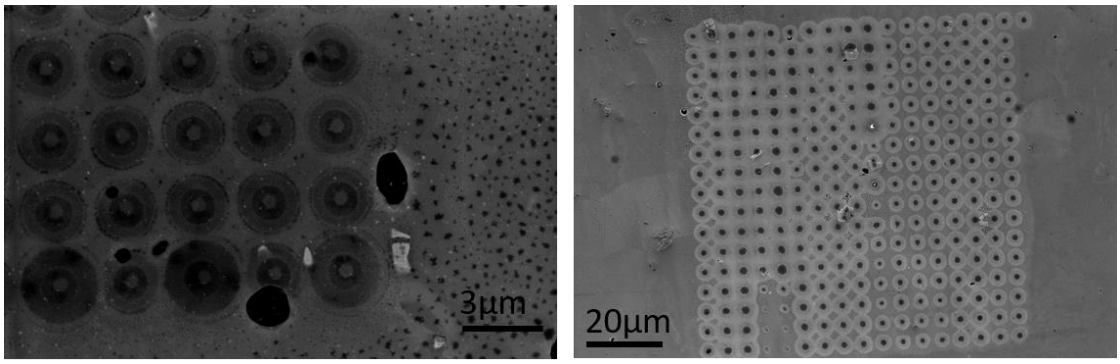

Figure 2. 13. SEM images of SECCM scan areas on 5052 Al in 50 mM H_2SO_4.

Surface features have also been shown to limit the wetting of the SECCM droplet. For example, grain boundaries on pure annealed Ni were observed limiting the extent of the droplet

wetting (Figure 2.14). To eliminate the risk of this occurring, ion milling can be used to ensure the surface is completely flat.

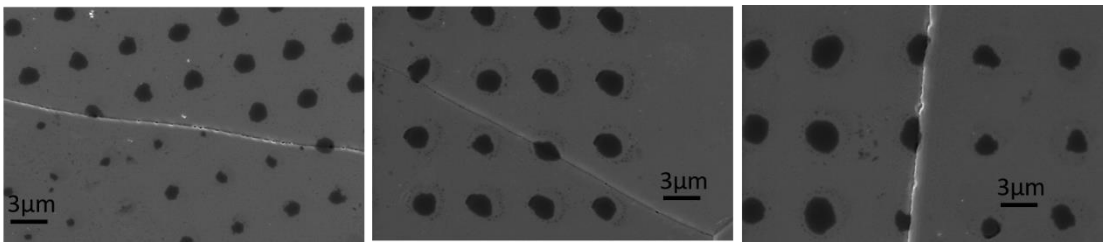

Figure 2. 14. SEM images of SECCM line scans performed on pure Pd in 0.5 M H_2SO_4.

2.5.3 Unstable droplet size

Another common reason why SECCM scans fail is due to the size of the droplet changing during a scan leading to changes in working electrode area causing misleading surface current measurements. Two examples where this effect has been observed is shown in Figure 2. 15.

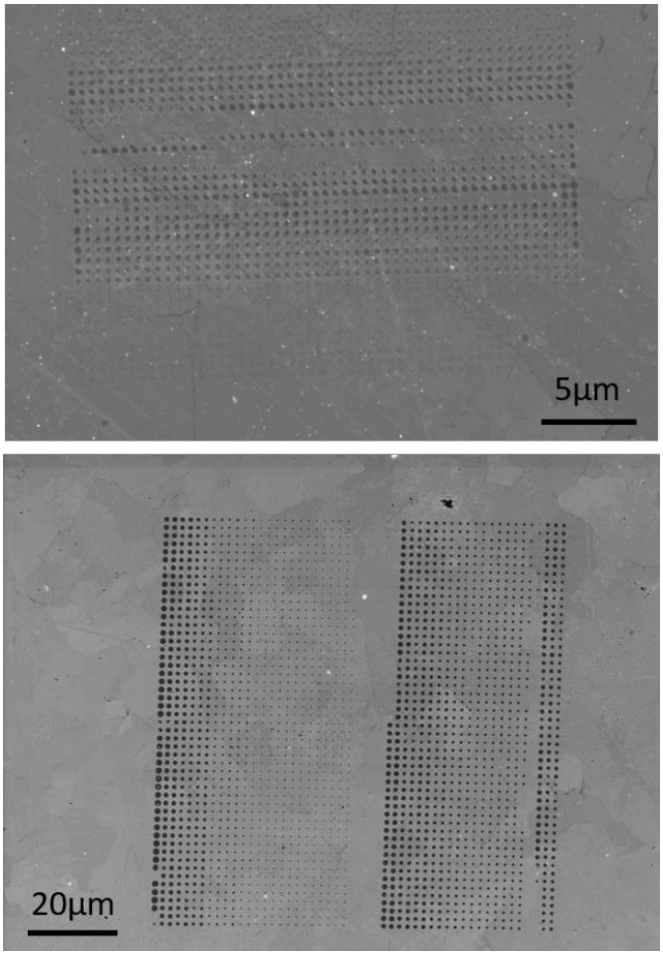

Figure 2. 15. SEM images of SECCM scans performed on low carbon steel in 10 mM H_2SO_4.

In these scans it is unclear why the droplet has changed; however, it is suspected that it is caused by a poorly pulled pipet. If the end of the pipet has an irregular shape, then it may struggle to maintain a constant surface tension across the meniscus of the droplet. This theory is unproven, so if a pipet exhibited this behaviour the usual solution would be to switch to another pipet.

In other cases, surface features can cause the droplet size to change during a SECCM scan. Figure 2.16 shows a collection of scanning points on a low carbon steel surface where the droplet size has changed after making a measurement at a particularly active point (highlighted by the red circle) on the surface.

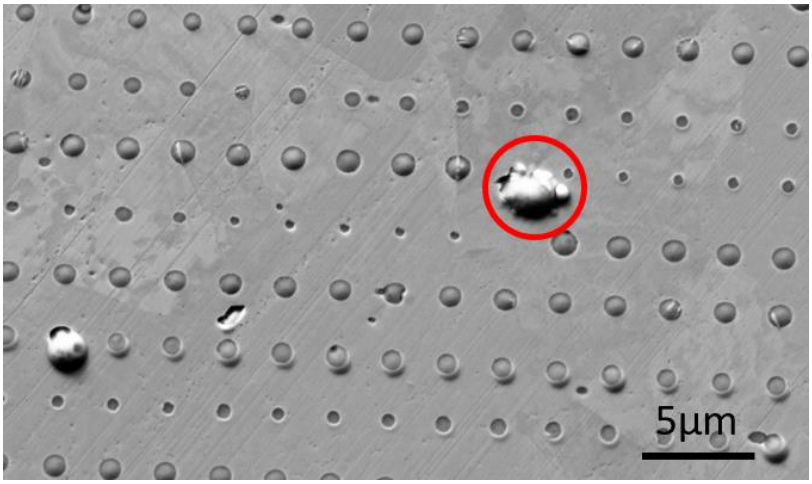

Figure 2. 16. SEM images of a SECCM scan performed on low carbon steel in 10 mM H_2SO_4.

2.5.4 Active/non-passivating electrolytes

Finally, when using active electrolytes that prevent the substrate surface from passivating, extensive corrosion can occur. The example displayed in Figure 2.17 shown the results of scanning a low carbon steel surface using a 50 mM NaCl electrolyte. Once the passive film of the low carbon steel had been reduced extensive corrosion occurred resulting in the contamination of the SECCM droplet and the eventual failure of the scan. This example shows what is perhaps the biggest limitation of SECCM that aggressive environments are generally not viable for technique.

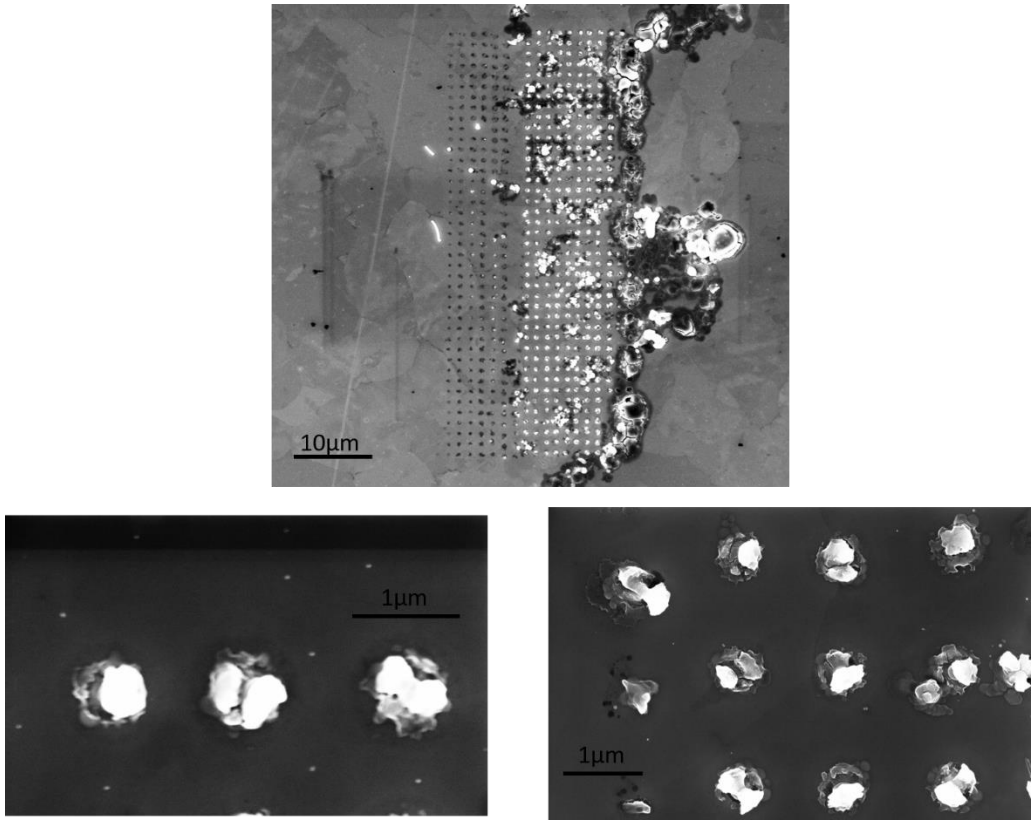

Figure 2. 17. SEM images of a SECCM scan performed on low carbon steel in 50 mM NaCl.

2.6 References

1. Ebejer, N.; Güell, A. G.; Lai, S. C. S.; McKelvey, K.; Snowden, M. E.; Unwin, P. R., Scanning electrochemical cell microscopy: a versatile technique for nanoscale electrochemistry and functional imaging. *Annual Review of Analytical Chemistry* **2013,** *6*, 329-51.

2. Bentley, C. L.; Kang, M.; Maddar, F.; Li, F.; Walker, M.; Zhang, J.; Unwin, P. R., Electrochemical Maps and Movies of the Hydrogen Evolution Reaction on Natural Crystals of Molybdenite (MoS 2): Basal vs. Edge Plane Activity. *Chemical Science* **2017,** *8*, 6583-6593.

3. Sutter Instruments. 2012.

4. Aaronson, B. D. B.; Güell, A. G.; McKelvey, K.; Momotenko, D.; Unwin, P. R., Scanning Electrochemical Cell Microscopy: Mapping, Measuring, and Modifying Surfaces and Interfaces at the Nanoscale. *Nanoelectrochemistry, CRC Press* **2014**, 653-692.

5. Ul-Hamid, *A Beginners' Guide to Scanning Electron Microscopy*. Springer: 2018.

6. Schwartz, A. J.; Kumar, M.; Adams, B. L.; Field, D. P., *Electron Backscatter Diffraction in Materials Science*. Springer: 2009.

7. Engler, O; Randle, V; *Introduction to Texture Analysis: Macrotexture, Microtexture, and Orientation Mapping. 2nd Ed.* CRC Press: 2009.

8. Leng, Y., *Materials Characterization: Introduction to Microscopic and Spectroscopic Methods*. John Wiley & Sons: 2008.

9. Rajput, N. S.; Luo, X., FIB Micro-/Nano-fabrication. In *Micromanufacturing Engineering and Technology*, 2015; pp 61-80.

10. Giannuzzi, L. A.; Stevie, F. A., A review of focused ion beam milling techniques for TEM specimen preparation. *Micron* **1999,** *30* (3), 197-204.

11. Shkirskiy, V; Yule, L. C; Daviddi, E; Bentley, C. L; Aarons, J; West, G; Unwin, P. R. Nanoscale Scanning Electrochemical Cell Microscopy and Correlative Surface Structural Analysis to Map Anodic and Cathodic Reactions on Polycrystalline Zn in Acid Media. *The Journal of the Electrochemical Society* **2020** *167, 41507*

CHAPTER 3

Scanning Electrochemical Cell Microscopy: A Versatile Method for Highly Localized Corrosion Related Measurements on Metal Surfaces

3.1 Abstract

The development of tools that can probe corrosion related phenomena at the (sub)microscale is recognized to be increasingly important in order to understand the surface structural factors (grain orientation, inclusions *etc.*) that control the (electro)chemical stability (corrosion susceptibility, pitting, passivity *etc.*) of metal surfaces. Herein we consider the application of scanning electrochemical cell microscopy (SECCM), a relatively new member of the electrochemical droplet cell (EDC) family, for corrosion research and demonstrate the power of this technique for resolving structure and activity at the (sub)microscale. Hundreds of spatially-resolved (2 μm droplet size) potentiodynamic polarization experiments have been carried out on the several hours timescale and correlated to complementary structural information from electron backscatter diffraction (EBSD) and energy dispersive x-ray spectroscopy (EDS) in order to determine the effect of grain orientation and inclusions on electrochemical processes at low carbon steel in neutral solution (10 mM KNO_3). Through this approach, it has been shown unequivocally that for the low index planes, anodic currents in the passive region (an indicator of corrosion susceptibility) are greatest on (101) planes compared to (100) and (111) planes. Furthermore, individual sub-micron MnS inclusions have been probed and shown to undergo active dissolution followed by rapid respassivation. This study

demonstrates the high versatility of SECCM and the considerable potential of this technique for addressing structure-activity problems in corrosion and electromaterials science.

3.2 Introduction

The corrosion of metals and alloys is often caused by the establishment of local galvanic cells at surface heterogeneities when exposed to a corrosive environment (*e.g.*, an electrolyte solution). The (electro)chemical characteristics of these surface heterogeneities are not completely understood, largely due to the highly localised nature of the processes that occur.[1] As a consequence, the development of techniques that are able to extract spatially-resolved electrochemical information on the nanometer to micrometer length scales that can be correlated with complementary surface information are of great interest in order to resolve the relationship between structure (*e.g.*, metal grain orientation) and function (*e.g.*, corrosion resistance/susceptibility).[2-3]

In this study, we demonstrate how a simple micropipet imaging probe can be deployed in the scanning electrochemical cell microscopy (SECCM)[4] format to perform hundreds of spatially-resolved corrosion-relevant electrochemical measurements on the minutes to hours timescale so as to reveal the local electrochemical properties that are correlated with corresponding surface structure. SECCM operates on a similar principle as the electrochemical droplet cell (EDC) technique,[5] whereby electrochemical measurements are confined to a small area of the surface with the use of a droplet formed at the end of an electrolyte filled micro-capillary, equipped with auxiliary electrode(s). The EDC method allows for the direct, localised

(spatially-resolved) investigation of (semi)conductive electrode substrates, and has previously been used to study microscale corrosion processes on metals such as 304 stainless steel,[6-8] duplex stainless steel,[9-11] and aluminium.[12-13] Herein, we show that SECCM possesses all of the advantages of the EDC technique for corrosion research, while achieving significant improvements in terms of speed, resolution and reproducibility, through the use of a simplified probe design and advanced positioning technology.

SECCM belongs to the scanning electrochemical probe microscopy (SEPM) family of techniques, among which scanning electrochemical microscopy (SECM) is the most used.[3, 14-15] SECM has previously been applied to the study of corrosion processes at materials including, carbon steel,[16] stainless steel,[17-18] pure iron,[19-20] and titanium.[21] Nevertheless, despite its popularity, SECM contrasts with EDC methods in that it probes electrochemical processes (*e.g.*, corrosion) *indirectly* by monitoring the concentrations and fluxes of reactant, product or intermediates (*e.g.*, oxygen, protons or metal ions) by electrochemistry at the probe (tip), and thus only chemical species can be detected amperometrically or, more rarely, potentiometrically. Furthermore, the tip response must remain stable for the entire duration of a scan.

SECCM enables direct voltammetric-amperometric measurements at a series of targeted positions of a sample surface[22-25] and has previously been applied to resolve the relationship between structure and activity in a wide range of electrochemical processes at a diversity of electrode materials (*e.g.*, sp^2 carbon materials,[26] molybdenum disulphide,[27] iron nickel sulphide catalysts,[28] and metallic nanoparticles[23-24]), but has not yet been employed to study corrosion related phenomena. Here, we report the first use of SECCM, operated in

voltammetric mode, for probing spatially-resolved corrosion properties, illustrated through the study of polycrystalline low carbon steel in neutral (10 mM KNO_3) media. Used ubiquitously in construction, the corrosion properties (*i.e.*, susceptibility/resistance) of low carbon steel are known to be significantly influenced by chemical composition (*e.g.*, alloying elements and inclusions) and/or microstructure (*e.g.*, crystallographic orientation and/or phase).[29-30] The structural/compositional dependence is shown unequivocally in this work, where differences in the corrosion susceptibility of the low-index (100), (101) and (111) grains is elucidated from spatially-resolved voltammetric measurements and the direct electrochemical detection and characterisation of sub-micron sized manganese sulphide inclusions is demonstrated.

3.3 Experimental

3.3.1 Chemical reagents and electrode materials

The low carbon steel sample (composition detailed in Table 3.1) was provided by Tata Steel, Research and Development (U.K.). In order to prepare the sample for measurement, the steel sheet was sectioned using an abrasive cutter to give a sample of size (approx.) 5 × 21 × (thickness) 2 mm, which was subsequently mounted in a carbon-based conductive mount using a Buehler SimpliMet 3000 Mounting Press (Buehler, U.S.A.). After mounting, the sample was polished on a polishing cloth (Buehler Trident) using (successively) 9 μm, 3 μm and 1 μm polishing suspensions (Buehler MetaDi Supreme Suspension). The final polishing step was carried out on a polishing cloth (Buehler MicroCloth) using 0.05 μm alumina suspension (MasterPrep Sol-gel, Buehler). After polishing, the sample was washed in acetone, soapy water

and then thoroughly in copious amounts of deionized water, before being gently blown dry. Electrical connection to the sample was made with a copper wire connected to the outside of the conductive mount with carbon tape.

Table 3. 1. Chemical composition of the low carbon steel determined using energy dispersive X-ray spectroscopy.

%	C	Mn	Si	Cr	Al	P	S	Cu
Low Carbon Steel	**0.05**	**0.3**	**<0.03**	**0.06**	**0.03**	**<0.02**	**<0.02**	**0.04**

Potassium nitrate (KNO_3, Sigma-Aldrich), potassium chloride (KCl, Sigma-Aldrich) and dichlorodimethylsilane [$Si(CH_3)_2Cl_2$, Acros Organics, ≥99%] were used as supplied. All solutions were prepared with ultra-pure deionized water (Integra HP, Purite, U.K.), which had a resistivity of 18.2 MΩ.cm at 25°C.

3.3.2 Surface characterisation

All surface characterisation was carried out with a Zeiss SUPRA FE-SEM (Zeiss, Germany), using an X-Max 50 mm^2 energy-dispersive X-ray spectroscopy (EDS) detector (Oxford Instruments, U.K.) and an Nordlys EBSD detector (Oxford Instruments, U.K.). SEM images and EDS data were collected at 5 keV, whereas EBSD images were collected at 20 keV, with the sample tilted at 70° to the detector. Following EBSD characterisation, grains that were chosen for the present study were either on or close to the low index orientations, (100), (101) and (111). The criterion for plane selection set in this study was 10^o deviation from the desired orientation.

3.3.3 Macroscale polarisation measurements

A Teflon cylinder with an inner diameter of 2 mm was attached to the low carbon steel surface with silicone adhesive. A commercial Ag/AgCl reference electrode (3.4 M KCl, eDAQ, Australia) and a platinum counter electrode were inserted into the cylinder which was filled with 10 mM KNO_3 solution. The measurement was carried out at a sweep rate of 80 mV s^{-1} using a CHI400 potentiostat (CH Instruments Inc., U.S.A).

3.3.4 SECCM probe fabrication

The SECCM micropipet probes were pulled from borosilicate theta capillaries (TG 150-10, Harvard Part No. 30-0114, Harvard Apparatus, U.S.A.) using a P-2000 laser puller (Sutter Instruments, USA). The size (overall diameter) of the opening at the end of the pipet was approximately 2 µm, as determined by FE-SEM. To aid meniscus (droplet) confinement, the outer walls of the pulled pipet tip were silanized with dichlorodimethylsilane, as previously described.[4] This was achieved by submerging the tip in $Si(CH_3)_2Cl_2$ with argon flowing from the bottom of the probe at a pressure of 6 bar (this prevented the silane from entering the tip during immersion). During this process, the organosilane becomes covalently attached to the glass surface, to produce a robust and resistant hydrophobic coating on the outer wall of the micropipette that does not contaminate the sample surface or need to be reapplied during the scan. The droplet (meniscus) cell was formed at the end of the pipet by filling each channel of the probe with 10 mM KNO_3 solution. A small amount of silicone oil (Fluka Analytical) was inserted on top of the KNO_3 solution to reduce the evaporation during prolonged SECCM scanning experiments, as previously reported.[27] After filling, Ag/AgCl quasi reference counter

electrodes (QRCEs) were inserted into each channel of the dual barrelled probe. The Ag/AgCl QRCEs were prepared by anodizing 0.125 mm diameter annealed silver wire (Goodfellow, U.K., 99.99%) in a saturated KCl solution, and have previously been shown to possess long-term stability and not to contaminate the surface investigated in a variety of electrolyte solutions.[31] The Ag/AgCl QRCE has a potential of *ca.* 0.25 V vs. saturated calomel electrode (measured potentiometrically) when immersed in 10 mM KNO_3.

3.3.4 SECCM set up

The SECCM set up (shown schematically in Figure 3.1a) has been reported in detail previously.[4, 22] Briefly, the micropipet probe was mounted on a *z*-piezoelectric positioner (P-753.3CD, PhysikInstrumente, Germany) to which a periodic oscillation (perpendicular to the sample) was applied (250 nm peak-to-peak amplitude at a frequency of 286 Hz) by an *ac* signal generated by a lock-in amplifier (SR830, Stanford Research Systems, U.S.A.). A bias potential (V_1) of +0.1 V was applied between the QRCEs in order to generate an ion conductance current (i_{dc}) across the liquid meniscus formed at the end of the probe, which was used as a feedback signal during positioning of the micropipet probe relative to the substrate (steel) surface (*e.g.*, see Figure 3.1b-i below). The micropipet was positioned above the low carbon steel surface using micropositioners for coarse movement and an *xy*-piezoelectric positioner (P-621.2CD, PhysikInstrumente) for fine movement laterally (parallel to the sample).

During operation, the probe was approached to the substrate surface at a constant velocity (*ca.* 0.2 µm/s here) applied to the z-piezoelectric positioners, and once contact between the droplet (meniscus) cell and the surface had been established (the pipet probe itself did not

make contact with the surface), the ion conductance current showed a periodic modulation (*ac* component, i_{ac}) at the same frequency of oscillation (measured with the same lock-in amplifier highlighted above) due to reversible deformation of the droplet.[32] The magnitude of i_{ac} informs on the status of the droplet (*e.g.*, see Figure 3.1b-ii). An i_{ac} set point of 6 pA was used as the feedback signal herein and electrochemistry was performed within the area contacted by the meniscus cell. A substrate voltage of V_2 was applied to one of the QRCEs to control the working electrode (*e.g.*, low carbon steel) potential (E_S), where $E_S = -(V_1/2 + V_2)$,[32] and the working electrode current (i_{surf}) was measured. The size of the confined area (*i.e.*, working electrode area) was determined after each set of measurements by FE-SEM imaging of the droplet "footprint" residue, as discussed in detail below.

Electrochemical measurements at the low carbon steel (working electrode) were made using a cyclic voltammetric "hopping" regime, as described previously.[22, 27, 33] In essence, the micropipet probe made a series of measurements by performing potentiodynamic polarization at predefined locations in a grid. The hopping distance (*i.e.*, spatial resolution) between each pixel was 5 µm to avoid overlap of the probed areas.

The entire SECCM apparatus was supported on an optical table (Thorlabs, U.S.A.) and shielded with a Faraday cage equipped with heat sinks and vacuum panels to minimize noise and variations in temperature (temperature of measurements *ca.* 21ºC). The QRCE potentials were controlled (with respect to ground) with a home-built bipotentiostat and the low carbon steel substrate (working electrode, common ground) current was measured using a home-built electrometer. Each data point in the voltammetric measurements was taken as an average of 1025 samples recorded at 10 µs intervals (*i.e.*, approximately every 10 ms). The scan rates used

in this study were 40, 50 and 80 mVs^{-1} which resulted in data points being acquired every 0.4, 0.5 and 0.8 mV. Data acquisition and fine control of all instrumentation was achieved using an FPGA card (PCIe-7852R) controlled by a LabVIEW 2016 (National Instruments, U.S.A.) interface running the Warwick Electrochemical Scanning Probe Microscopy (WEC-SPM, www.warwick.ac.uk/electrochemistry) software. Data treatment and analysis was carried out using the Matlab R2015b (8.6.0.267246, Mathworks, U.S.A.) and OriginPro 2016 64bit (b9.3.226, OriginLab, U.S.A.) software packages. The standard error of the average potentiodynamic polarization curves was calculated by dividing the standard deviation by the square root of the number of data points.

3.4 Results and Discussion

3.4.1 SECCM: operational principles and practical considerations.

In a recent comprehensive review,[2] droplet cell based-techniques (*i.e.*, the EDC technique) were considered to have several serious limitations in spatially-resolved corrosion research. Our intention here is to show that these limitations are readily overcome with SECCM, positioning it as a powerful technique for spatially-resolved corrosion-related measurements. A first issue raised is that the probe dimensions (*i.e.*, micro-capillary size), which ultimately determines the spatial resolution of the technique, is limited by the current resolution of the potentiostat (*i.e.*, small probes give rise to currents that are too small to measure accurately).[34] This is not an issue for the SECCM set up used herein, as demonstrated by previous studies by our group,[35-39] where

currents as low as a few fA were measured with excellent signal-to-noise and reasonable time resolution, noting the well-known bandwidth-current magnitude trade off.[40]

A second issue concerns the complexity of fabricating the droplet cell micro-probes. In conventional micro-cell experiments, the microcapillary probes are fabricated from pulled glass pipets, which are ground and polished until the required size is achieved, before the application of a silicone rubber gasket on the tip.[5-6] This is a somewhat laborious process. In addition, although the silicone rubber gaskets reportedly improve the versatility and reliability of the conventional micro-cell technique by ensuring electrolyte confinement and contact with the surface,[5-6] the inconsistent quality of the probe-surface contact can lead to a risk of crevice corrosion in the scanning area, thus drastically affecting the electrochemical response.[41] In addition, probe-surface contact is traditionally made manually using a microscope to judge when the gasket has made a seal with the surface,[2] which is both time-consuming and relatively irreproducible, as the contact may vary from point-to-point.

By contrast, the micropipet (or nanopipet)[23-24] probes in SECCM can be fabricated quickly and reproducibly using a laser puller, with no need to apply a silicone rubber gasket.[4, 42] In SECCM, consistent droplet-cell surface contact is achieved by silanizing the outer wall of the probe (detailed in the Experimental Section), to make it hydrophobic, which aids in droplet confinement during meniscus surface contact.[4] As highlighted above, the ion conductance current between the QRCEs in the dual channel probe is sensitive to the size and shape of the meniscus between the end of the pipet and surface, and a set point value of the *ac* conductance current, i_{ac} (*e.g.*, when the droplet initially makes contact with the surface, see Figure 3.1b) ensures consistent meniscus contact, without the need for a gasket. Thus, the approach and

contact of the meniscus with the steel surface is automated and precisely controlled. This is a key advantage of the technique, enabling large numbers of surface measurements to be made in a reasonable time (*vide infra*) and thus making the measurements more statistically sound than with other droplet cell methods (*e.g.*, conventional EDC).

A third issue is the possibility of high ohmic (*iR*) resistance between the working and counter-reference electrodes.[43-44] A significant ohmic drop is expected when large currents are passed between the working and counter electrodes with capillaries on the order of 100 μm.[43] In SECCM, the ion current between the two chambers (i_{dc}, see Figure 3.1b) reveals the pipet resistance, which is *ca.* 50 MΩ herein [$R = E / i_{dc} = +0.1\ V / (2 \times 10^{-9}\ A) = 5 \times 10^{7}\ \Omega$]. Thus, by setting a limit of 5 mV on the ohmic drop, this means that surface currents up to *ca.* 100 pA are essentially immune to ohmic effects, *i.e.*, only in the region where the oxygen evolution reaction (OER) is occurring (*region 3, vide infra*) of the Tafel plots in Figure 3.1d is ohmic drop a consideration. Another risk could be introduced if the potential was biased as far as the transpassive region (not applicable for the system in this study) is the effect of extensive corrosion products on the stability of the probe (QRCEs and electrolyte) between scanning points. To avoid this, previous studies[45] have restricted the applied potential to values outside of the transpassive region.

Finally, the potentiodynamic sweep rate for the polarization experiments is a critically important consideration. Traditionally, the potentiodynamic sweep rates employed in corrosion research are extremely low (<1 mV s^{-1}), which facilitates the straightforward calculation of the corrosion potential (E_{corr},) and corrosion current (i_{corr}), taken indicators of bulk corrosion susceptibility/resistance.[46-47] By contrast, high potentiodynamic sweep rates are preferable in

the micro-droplet format in order to minimise perturbation to the sample surface and solution at the end of the tip and to avoid tip blocking,[12] as well as to reduce the time taken for the electrochemical map to be produced. In addition to changing the timescale of the experiment, current from nonfaradaic processes (i_{nf}) such as double layer charging and stray capacitance becomes more prevalent at high sweep rates, evident in the current-potential (*i-E*) plots in Figure 3.2a, which show voltammetric segments recorded between 0.15 and -1.05 V vs Ag/AgCl QRCE at scan rates between 0.01 Vs^{-1} and 0.5 Vs^{-1}. As shown in Figure 3.2b, the sweep rate has a significant effect on i_{nf} distortion of the logarithmic Tafel plots that gives rise to an apparently sweep rate-dependent E_{corr} and i_{corr}, as noted previously.[46] For this reason these parameters will not be considered as indicators of corrosion resistance/susceptibility herein. Rather, we are able to draw on other parameters from the voltammetric response.

As highlighted above in the Experimental Section, for this work, a voltammetric hopping mode regime[22, 27, 33] was used, whereby a potentiodynamic polarization measurement was made at a series of spatially-resolved 'pixels' on the substrate surface. Returning to Figure 3.1, representative SECCM potentiodynamic polarization curves (plotted in Tafel form), on low carbon steel are very reproducible (Figure 3.1d) which shows Tafel plots obtained from the row (17 sites) of a scan (indicated in Figure 3.1c), alongside the average plot from this row.

The data in Figure 3.1d reflect the expectations from the Pourbaix diagram for an iron electrode in neutral solution.[48] The potential sweep initially starts in the cathodic region (*region 1* in Figure 3.1d), where hydroxide (OH^-) generation dominates, arising from a combination of the oxygen reduction reaction (ORR) and the hydrogen evolution reaction (HER):

$$O_2 + 2H_2O + 4e^- \rightarrow 4OH^- \quad (1)$$

$$2H_2O + 2e^- \rightarrow H_2 + 2OH^- \quad (2)$$

Note that in the SECCM configuration, there is an enhanced flux of O_2 across the air-water-electrode three phase boundary.[49] In addition to the ORR, any existing passive film on the steel surface is expected to be at least partially reduced in the cathodic region of the Tafel plot (*i.e.*, *region 1* in Figure 3.1d).

As the system passes through E_{corr} an active region is not observed, and the steel essentially passivates instantly on the timescale of these measurements. The production of ferrous and ferric hydroxide is expected,[50] for example via the reactions shown in eqs. 3 and 4:

$$Fe + 2H_2O \rightarrow Fe(OH)_2 + 2H^+ + 2e^- \quad (3)$$

$$Fe^{2+} + 3OH^- \rightarrow Fe(OH)_3 + e^- \quad (4)$$

where OH^- arises from the ORR and HER, as noted above (Eq. 1 and 2). *Region 2* is the passive region, where $Fe(OH)_2$ and $Fe(OH)_3$ are further oxidised to form a (semi) protective passive film on the surface,[50] effectively suppressing corrosion throughout this potential range:

$$2Fe(OH)_2 \rightarrow Fe_2O_3 + H_2O + 2H^+ + 2e^- \quad (5)$$

$$3Fe(OH)_3 \rightarrow Fe_3O_4 + H_2O + 2H^+ + 2e^- \quad (6)$$

Region 3 is the region where the oxygen evolution reaction (OER) occurs (Eq. 7).

$$2H_2O \rightarrow O_2 + 4H^+ + 4e^- \quad (7)$$

By comparing the results collected using SECCM (Figure 3.1d) with those collected at the macroscale (Figure 3.1e) it is clear the corrosion potential is shifted more positive when using SECCM. As previously mentioned,[49] the droplet cell configuration enables a high flux of oxygen (across the meniscus/air interface) compared to the "bulk solution" conditions of the macroscopic experiment. Therefore, the ORR is enhanced in SECCM experiments. By assuming the anodic branch for both SECCM and macroscopic experiments behaves similarly, higher rates of cathodic reactions results in the positive shift of the corrosion potential in accordance with mixed potential theory.[51] In addition, in the macroscale Tafel plot a small oxidation peak arises following the corrosion potential which does not appear in the SECCM Tafel plot. This is because the enhanced oxygen reduction in SECCM limits the anodic currents, thus subduing this peak, as the current, i, is a sum of the cathodic, i_c, and anodic processes, i_a, (Eq. 8).

$$i = i_c + i_a \qquad (8)$$

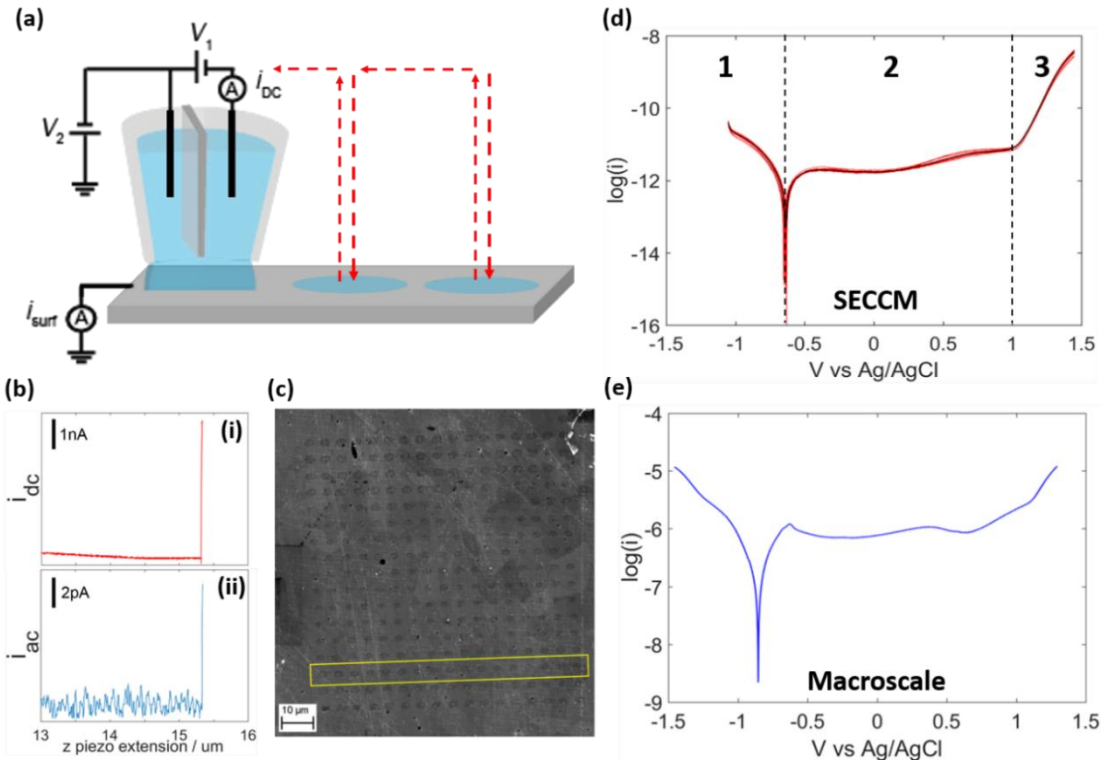

Figure 3. 1. (a) Schematic showing the voltammetric hopping-mode SECCM protocol employed to make spatially-resolved potentiodynamic polarisation measurements at a sample surface. The arrows indicate the path of probe across the surface. **(b)** Plots of the (i) *dc* and (ii) *ac* ionic current versus *z*-position as the micropipet probe is approached towards a low carbon steel surface. The surface was detected at an extension of 15.34 µm. **(c)** FE-SEM image of a 17×17 matrix of droplet 'footprints' on a low carbon steel surface, left after making spatially-resolved potentiodynamic polarization measurements using the SECCM setup outlined in (a). **(d)** Individual (red) and averaged (black) Tafel plots resulting from the row of droplet footprints highlighted by the yellow box in (c), obtained in a 10 mM KNO_3 solution at a sweep rate of 80 mV s^{-1}. The three 'regions' indicated in (d) correspond to: (1) cathodic, (2) passive and (3) the oxygen evolution reaction at the metal electrode surface. **(e)** Tafel plot taken from a macroscopic polarisation measurement of the low carbon steel in 10 mM KNO_3 at a sweep rate of 80 mV s^{-1}.

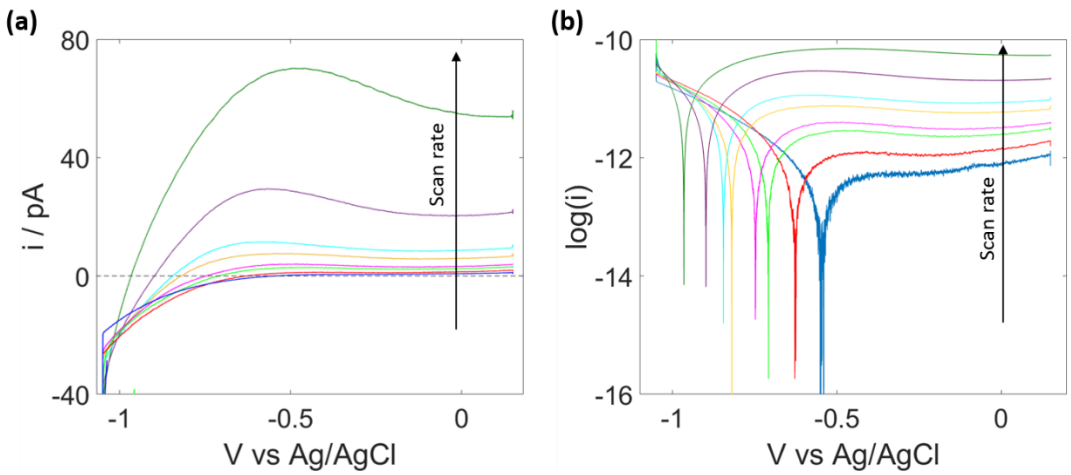

Figure 3. 2. Potentiodynamic polarisation experiments carried out at adjacent sites on a low carbon steel surface in 10 mM KNO_3 with a 2 µm diameter micropipet probe at sweep rates of (top to bottom) 0.5, 0.2, 0.1, 0.08, 0.05, 0.04, 0.02 and 0.01 V s^{-1}. The data are presented as **(a)** *i-E* plots and **(b)** corresponding Tafel plots. The apparent shift in E_{corr} is caused by the increased contribution of nonfaradaic (charging) current to the total measured current with increasing sweep rate (see text).

3.4.2 Crystallographic orientation and corrosion susceptibility in low carbon steel

We now explore the relationship between electrochemical behaviour (*e.g.*, corrosion resistance/susceptibility) and crystallographic (grain) orientation to highlight a major capability of SECCM when spatially-resolved voltammetric data are combined with EBSD data of the same area of the surface (correlated or co-location electrochemical multi-microscopy). Many studies have attempted to explain the link between crystallographic orientation and the electrochemical behaviour of metals, as exemplified by studies of iron,[52-55] pearlitic steel,[56] FeAlCr ferritic steel,[57] 316L stainless steel[58] and aluminium.[59] However, although the crystallographic orientation affects the electrochemical behaviour of metal surfaces to the best of our knowledge, there is no clear trends, nor are there consistent explanations for the differences in electrochemical behaviour observed between the grains.

SECCM was used to electrochemically map an area on a low carbon steel sample, as shown in Figure 3.3a. Each droplet 'footprint' in the image corresponds to an individual potentiodynamic polarization experiment carried out in 10 mM KNO_3 at a sweep rate of 50 mV s^{-1} (*e.g.*, see Figure 3.1c). The 256 individual potentiodynamic polarization experiments were made over a total scan time of 6 hours, and from Figure 3.3a it is clear that the geometry of the droplet cell does not change on this timescale (*i.e.*, the droplet 'footprint' size is reproducible). The same area of the steel surface was subsequently mapped using electron backscatter diffraction (EBSD), as shown in Figure 3.3b. Evidently, a significant number potentiodynamic polarization experiments were made on each of the (100), (110) or (111) orientated grains (and other orientations, Figure 3.3c). This 'pseudo single crystal' approach[60] of the SECCM technique allows multiple crystallographic orientations on a polycrystalline sample to be independently interrogated in a single experiment.

The raw *i-E* data were extracted from each point shown in Figure 3.3a, assigned to a dominant grain (the grains that were chosen and considered suitable for study are shown in Figure 3.3c), and then averaged to give the Tafel plots shown in Figure 3.3d. The results are representative because there are 15, 12 and 26 individual measurements on the (100), (101) and (111) grains, respectively. The cathodic branch of the Tafel plots, corresponding to the ORR, HER and/or reduction of the pre-existing passive film on the low carbon steel surface (discussed above), are very similar for each of the grains, indicating that these reactions do not have a strong surface-orientation-dependence on this surface, under these conditions. In the passive region and moving in the anodic direction the current is comparable on each of the grains up to an applied potential of approximately 0 V vs. Ag/AgCl QRCE, where upon the (101) grain gives

rise to larger anodic currents than the (100) and (111) grains. Considering this potential region corresponds to passive film formation/growth (*e.g.*, see Eqs. 5 and 6), these results suggest that the passive film formed on the (101) grain is less effective at preventing anodic dissolution than that formed on the (100) or (111) grains. Supporting this deduction is an additional electrochemical (SECCM) scan, EBSD and FE-SEM images for the same low carbon steel sample in a different area, with the results summarised in Figure 3.4. Comparing the FE-SEM image in Figure 3.4a, with the EBSD maps in Figure 3.4b to extract the averaged Tafel plots in Figure 3.4d, it is clear that the (101) grain gives rise to higher anodic currents than the (100) or (111) grains in the passive region.

What is also noticeable is that a small peak arises at approximately 0 V vs Ag/AgCl on Figure 3.3d on the (101) and (111) grains, but interestingly not on the (100) grains. Given the potential of this peak, we considered the deposition/stripping of Ag(0) arising from the Ag/AgCl QRCE as a possible origin, however if this were the case, this peak would be seen on all grains, and furthermore such problems are easily avoided with care,[31] as taken in this paper. Therefore we can rule this out as an explanation. Furthermore, detailed analysis of the voltammograms indicated that this peak occurred in all measurements on (101) and (111) grains but not once on the (100) grains. The amount of charge passed under this peak corresponds to ca. 1% of a monolayer over the scanned area which indicates this is a very subtle process. It is therefore very difficult to speculate on the origin of this peak, although this finding does show the capability of SECCM to detect these very subtle grain dependent electrochemical processes.

In previous studies,[52] differences between the relative corrosion susceptibility of the grains have been attributed to the geometry of each grain surface, particularly the surface atom

density. The planar packing factor increases in the order (111) < (100) < (101) (with values 0.340, 0.589 and 0.833, respectively) for the body-centred cubic (BCC) crystal system considered herein. It appears that the higher the density of atoms exposed to the solution (*i.e.*, present at the surface plane), the greater the chance of anodic oxidation, resulting in greater corrosion susceptibility for the densely packed (101) grain compared to the (100) or (111) grains. This is consistent with previous studies[54, 61] that observed the (101) plane on iron to exhibit higher anodic dissolution currents than the (100) plane. This was attributed due to the higher atomic density at the surface of the exposed (101) grains. However, there is also an argument that this difference is due to the nature of the passive film formed on the (101) and (100) grains, as suggested above. It has been reported[62] that a thicker (and therefore perhaps more protective) passive film forms on (100) than (101) grains on iron, which could also be responsible for the increased anodic currents measured on (101) grains.

It is important to note that although the influence of the planar packing factor can be used to explain why there is an increased response from (101) planes in the passive region, it does not explain why little to no difference is observed in the response from the (100) and (111) planes. One reason for this could be that the difference is too subtle to detect, although more likely is that the density of atoms at the surface is not the only influence on the corrosion behaviour of different crystal planes. As noted before, previous studies[52-53, 57, 59] have struggled to maintain consistent explanations for this variation between grains suggesting the problem is more complex and involves other factors than just surface atom density. In a recent review, a number of surface properties affecting the corrosion of carbon steel are discussed in detail.[63]

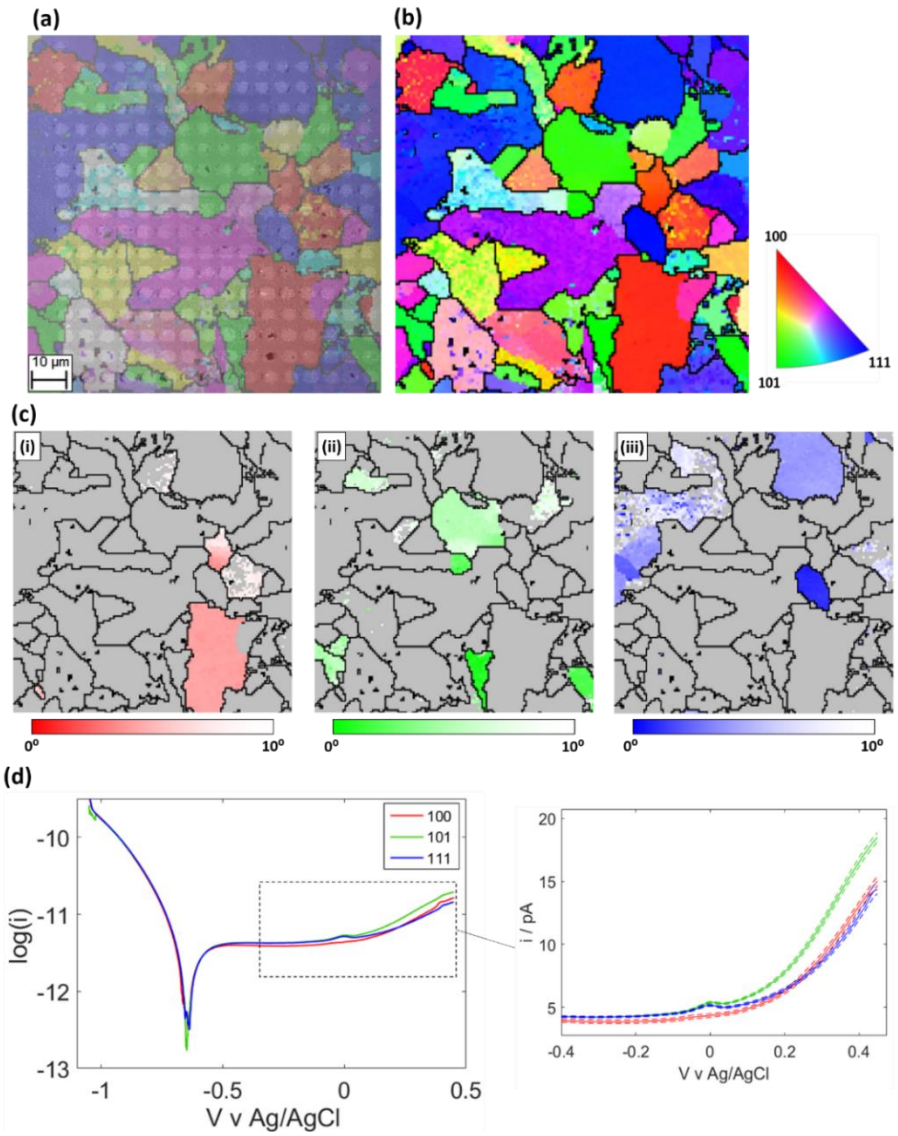

Figure 3. 3. (a) SEM image with the EBSD map superimposed and **(b)** the corresponding EBSD map of the area of the low carbon steel surface that was characterized with SECCM. The droplet 'footprints' remaining after each of the individual 256 potentiodynamic polarisation experiments are clearly visible in (a). **(c)** Grains deemed close enough to the low index planes are shown in **(i)**, **(ii)** and **(iii)** for (100), (101) and (111), respectively. **(d)** Representative Tafel plots obtained on the (100) (red trace), (101) (green trace) and (111) (blue trace) grains on the area of the low carbon steel surface shown in (a) and (b). The plots were obtained by averaging the *i-E* data collected during spatially-resolved potentiodynamic polarization measurements made with SECCM. 15, 12 and 26 individual measurements were averaged on the (100), (101) and (111) grains, respectively. The polarization experiments were carried out in 10 mM KNO_3 at a potentiodynamic sweep rate of 50 mV s^{-1} using a micropipet probe with a diameter of 2 µm. The highlighted section is of the potential region spanning –0.4 to +0.45 V vs. Ag/AgCl, which is shown magnified in the *i-E* plot. The dashed lines included above and below the traces represents the standard error of the data.

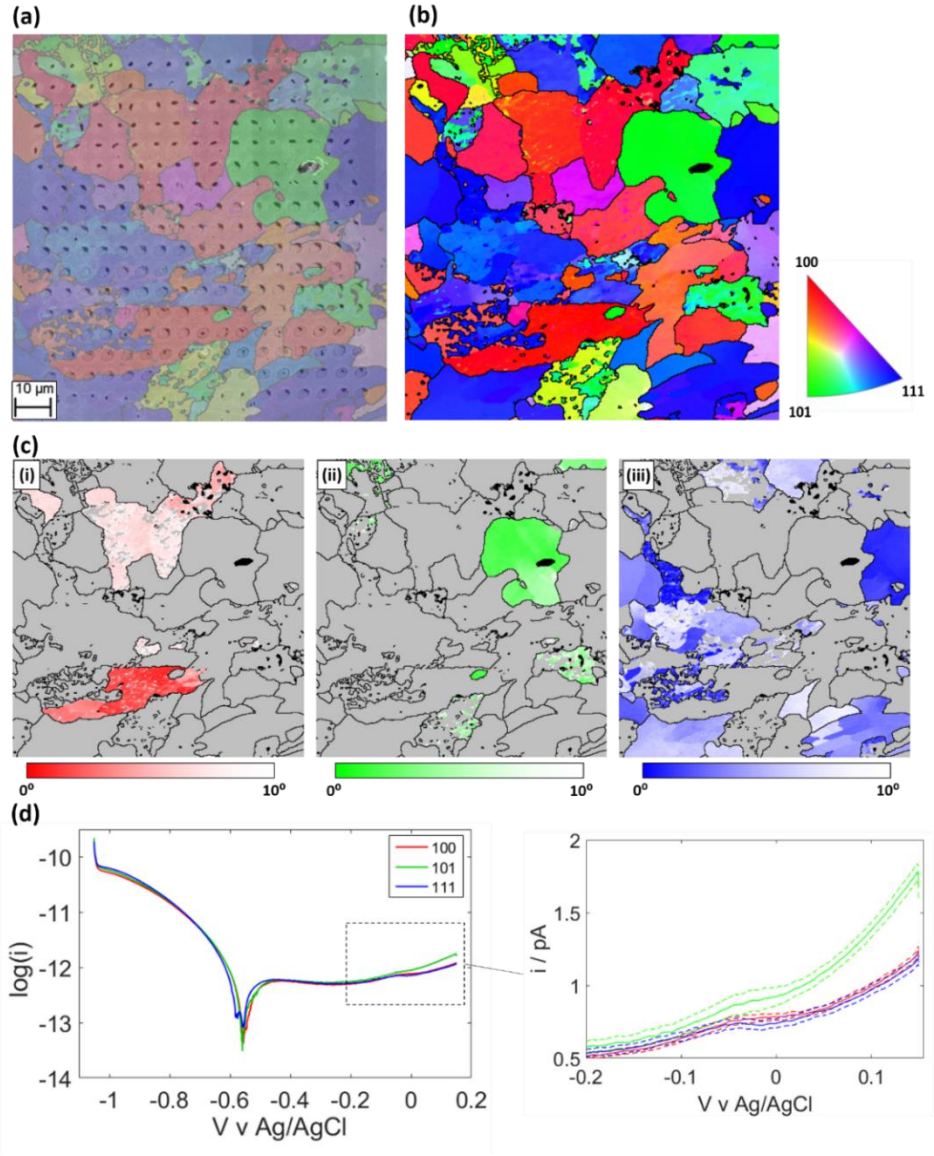

Figure 3. 4. (a) SEM image with the EBSD map superimposed and **(b)** corresponding EBSD map of the area of the low carbon steel surface that was characterized with SECCM. **(c)** Grains deemed close enough to the low index planes are shown in **(i)**, **(ii)** and **(iii)** for (100), (101) and (111), respectively. **(d)** Representative Tafel plots obtained on the (100) (red trace), (101) (green trace) and (111) (blue trace) grains on the area of the low carbon steel surface shown in **(a)** and **(b)**. The data were obtained by averaging the *i-E* data collected during spatially-resolved potentiodynamic polarization measurements made with SECCM. 41, 19 and 38 individual measurements were averaged on the (100), (101) and (111) grains, respectively. The polarization experiments were carried out in 10 mM KNO_3 at a sweep rate of 40 mV s^{-1} using a micropipet probe with a diameter of 2 µm. The highlighted section is of the potential region spanning –0.2 to +0.15 V vs. Ag/AgCl, which is shown magnified in the *i-E* plot. The dashed lines included above and below the traces represents the standard error of the data.

3.4.3 Detecting and probing electrochemistry at MnS inclusions in low carbon steel

MnS inclusions are well-known onset sites for localized (pitting) corrosion in stainless steel and steel alloys.[64-65] As shown in Figure 3.5, the low carbon steel used herein contains MnS inclusions of sizes ranging from 200 nm to 1 μm. It follows that when performing SECCM mapping on an area of this low carbon steel sample, some of the probed areas (droplet footprints) will contain a MnS inclusion.

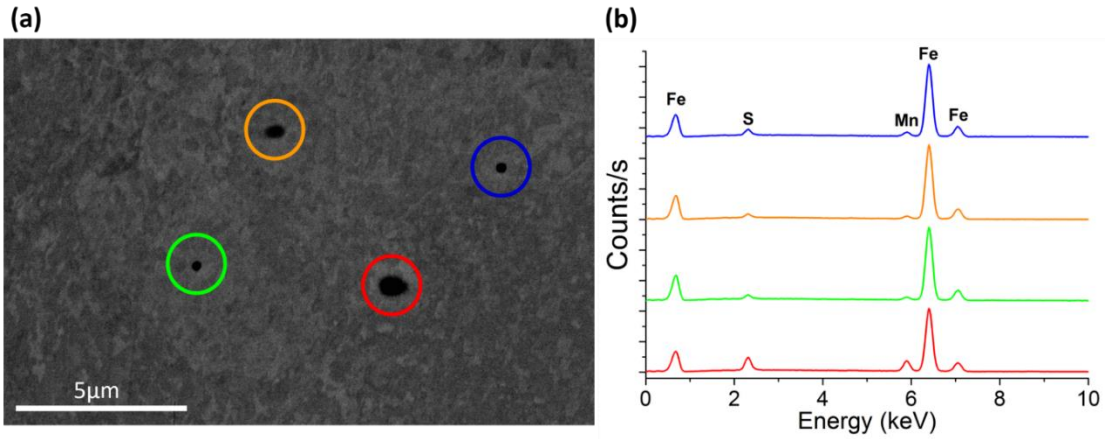

Figure 3. 5. (**a**) SEM image of MnS inclusions (indicated by coloured circles) on a low carbon steel surface. **(b)** Energy dispersive X-ray spectroscopy (EDS) responses of each of the inclusions, with the colours corresponding to the inclusions highlighted in **(a)**.

Potentiodynamic polarization curves obtained in the SECCM format, in areas containing MnS inclusions are shown in Figure 3.6. In each plot, three Tafel curves are shown, corresponding to the site containing the inclusion (labelled 2 in Figure 3.6a) and two adjacent sites containing no inclusions (labelled 1 and 3 in Figure 3.6a). The Tafel plots in Figure 3.6b, obtained at the inclusion sites show an abrupt increase in anodic current in the passive region at a potential of approximately 600 mV vs. Ag/AgCl, which immediately returns to the original passive value, giving rise to an anodic current 'spike'. This 'spike' in the current is consistent with findings of Webb et al.,[66] who used a 100 μm microcapillary to land on rather large MnS

inclusions in 304 stainless steel, and found similar current-potential behaviour on the same inclusions.

Comparing the data in Figure 3.6 to the findings of Webb et al.,[66] it is clear that the current 'spikes' are attributable to the dissolution and immediate re-passivation of the MnS inclusion within the probed droplet cell area. This is also consistent with the fact that the inclusion is still visible within the probed area after the polarization experiment (the inclusions are labelled in Figure 3.6a). These results highlight the excellent spatial resolution achievable with SECCM, in detecting inclusions that are on the sub-micron scale. It is interesting to note that the cathodic branch of the Tafel plots is not significantly affected by the presence of the MnS inclusions (Figure 3.6b). Although this suggests that MnS does not catalyse the ORR/HER under these conditions, it needs to be noted that the inclusions only comprise a very small portion of the probed area (droplet 'footprints', estimated to be <10% from Figure 3.6a). For this reason, in order to be detectable with the micron-sized probe used herein, the sub-micron MnS inclusions would need to possess very high activity relative to the steel surface, as is seen in the anodic case (*i.e.*, the MnS is active, whereas the steel is passive), but not necessarily the cathodic case (*i.e.*, both the MnS and steel are active). Future work will make use of smaller probes, allowing the electrochemical activity of sub-micron surface features, such as inclusions and grain boundaries to be investigated directly.

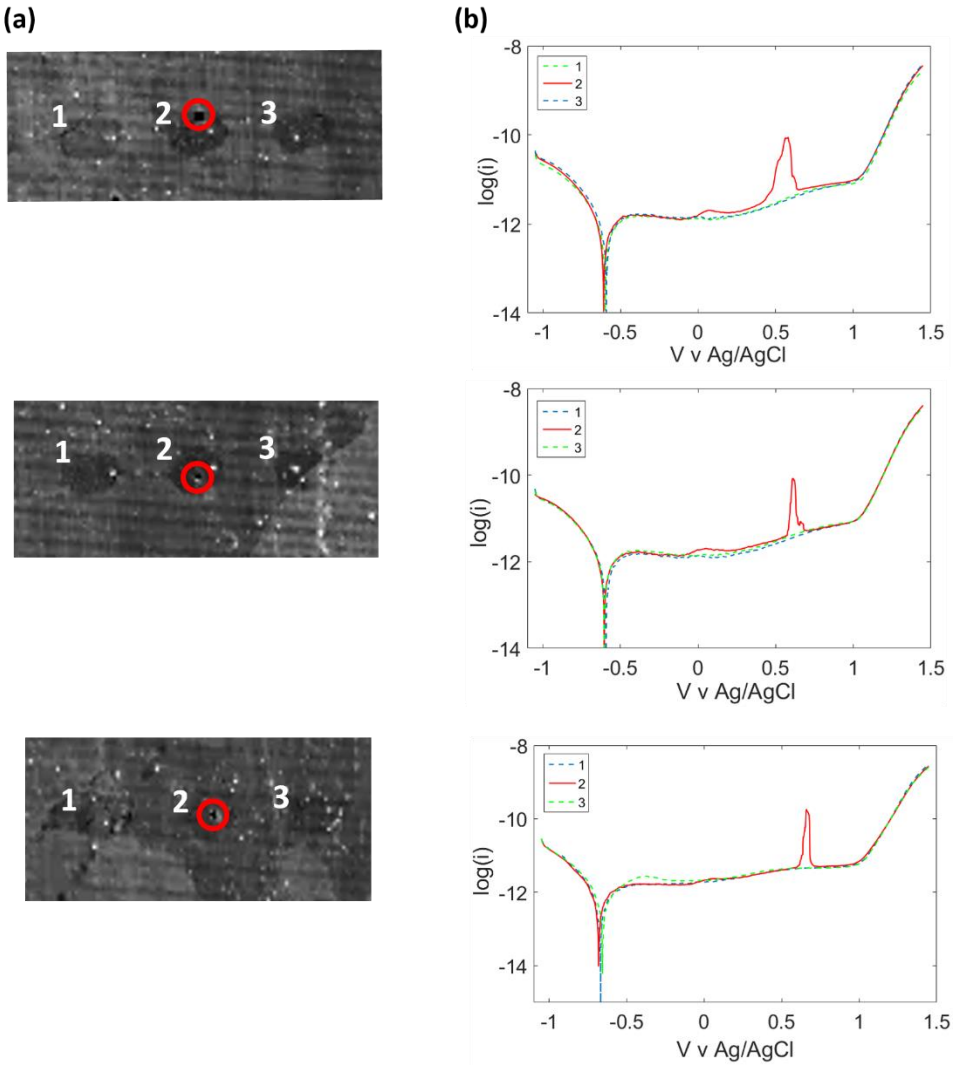

Figure 3. 6. (a) SEM images of adjacent droplet footprints with (2) and without (1 and 3) an MnS inclusion (indicated by a red circle). **(b)** Tafel plots obtained at the corresponding points labelled in (a). The potentiodynamic polarization experiments were performed in the SECCM format (probe diameter = 2 µm) on low carbon steel in 10 mM KNO_3 at a sweep rate of 80 mV s^{-1}.

3.5 Conclusions

Scanning electrochemical cell microscopy (SECCM) has been used to probe local electrochemical phenomena related to corrosion processes at the microscale. The working principles of the technique have been demonstrated and the advantages compared to earlier

electrochemical droplet cells (EDCs) have been outlined. The applicability of SECCM to corrosion-related research has been demonstrated through studies of a body centred cubic (BCC) structured polycrystalline low carbon steel in aqueous electrolyte media (10 mM KNO_3). Through combination of spatially-resolved electrochemical information from SECCM with complementary structural information from EBSD in a *correlative multi-microscopy approach*, it was shown unequivocally that for the low index planes, anodic currents in the passive region (*i.e.*, corrosion susceptibility) were greatest on (101) planes compared to (100) and (111) planes. Thus, the more densely packed (101) was most susceptible to anodic oxidation under these neutral pH conditions. In future studies, electrochemical data will be considered across the entire spectrum of crystallographic orientations, rather than just the low index planes, in order to gain a holistic view of the structural factors controlling corrosion susceptibility/resistance at metal surfaces.

SECCM was additionally applied to study the electrochemical behavior of individual sub-micron MnS inclusions embedded in the low carbon steel surface, which were shown to give rise to large anodic current 'spikes' in the passive region, attributable to the electrochemical dissolution and subsequent repassivation of the inclusion. This aspect of the study highlights the ability of SECCM to probe sub-micron to nanoscale surface features and bodes well for future investigations of inclusions and grain boundaries.

This study has further demonstrated the wide applicability of SECCM in materials research. The technique was successfully applied to perform hundreds of µm-resolved corrosion measurements on the several hours timescale. Recent work[23-24] has demonstrated further improvements of SECCM in terms of speed and resolution, with thousands of nm-resolved

measurements now possible on the tens of minutes timescale. Moving forward, we believe that SECCM will have an important role to play in corrosion science. Understanding structure-activity is highly important in corrosion science, and as demonstrated by this initial study, high-resolution correlation of electrochemical data with the underlying structure and properties of the surface will enhance knowledge of the electrochemical processes that drive corrosion.

3.6 References

1. Frankel, G. S.; Sridhar, N., Understanding Localized Corrosion. *Materials Today* **2008**, *11*, 38-44.

2. Andreatta, F.; Fedrizzi, L., The Use of the Electrochemical Micro-Cell for the Investigation of Corrosion Phenomena. *Electrochimica Acta* **2016**, *203*, 337-349.

3. Payne, N. A.; Stephens, L.; Mauzeroll, J., The Application of Scanning Electrochemical Microscopy to Corrosion Research. *Corrosion* **2017**, *73*, 759-780.

4. Ebejer, N.; Güell, A. G.; Lai, S. C. S.; McKelvey, K.; Snowden, M. E.; Unwin, P. R., Scanning Electrochemical Cell Microscopy: A Versatile Technique for Nanoscale Electrochemistry and Functional Imaging. *Annual Review of Analytical Chemistry* **2013**, *6*, 329-51.

5. Böhni, H.; Suter, T.; Schreyer, A., Micro- and Nanotechniques to Study Localized Corrosion. *Electrochimica Acta* **1995**, *40*, 1361-1368.

6. Suter, T.; Böhni, H., A New Microelectrochemical Method to Study Pit Initiation on Stainless Steels. *Electrochimica Acta* **1997**, *42*, 3275-3280.

7. Suter, T.; Böhni, H., Microelectrodes for Studies of Localized Corrosion Processes. *Electrochimica Acta* **1998**, *43*, 2843-2849.

8. Webb, E. G.; Alkire, R. C., Pit Initiation at Single Sulfide Inclusions in Stainless Steel. *Journal of The Electrochemical Society* **2002**, *149*, B286-B286.

9. Perren, R.; Suter, T.; Uggowitzer, P. J.; Weber, L.; Magdowski, R.; Böhni, H.; Speidel, M. O., Corrosion Resistance of Super Duplex Stainless Steels in Chloride Ion Containing Environments: Investigations by Means of a New Microelectrochemical Method.Ii. Influence of Precipitates. *Corrosion Science* **2001**, *43*, 727-745.

10. Park, C. J.; Kwon, H. S.; Lohrengel, M. M., Micro-Electrochemical Polarization Study on 25% Cr Duplex Stainless Steel. *Materials Science and Engineering A* **2004**, *372*, 180-185.

11. Vignal, V.; Mary, N.; Oltra, R.; Peultier, J. r.; me, A Mechanical–Electrochemical Approach for the Determination of Precursor Sites for Pitting Corrosion at the Microscale. *Journal of The Electrochemical Society* **2006**, *153*, B352-B352.

12. Andreatta, F.; Lohrengel, M. M.; Terryn, H.; De Wit, J. H. W., Electrochemical Characterisation of Aluminium Aa7075-T6 and Solution Heat Treated Aa7075 Using a Micro-Capillary Cell. *Electrochimica Acta* **2003**, *48*, 3239-3247.

13. Birbilis, N.; Buchheit, R. G., Electrochemical Characteristics of Intermetallic Phases in Aluminum Alloys. *Journal of The Electrochemical Society* **2005**, *152*, B140-B140.

14. Bard, A. J.; Fan, F. R. F.; Kwak, J.; Lev, O., Scanning Electrochemical Microscopy. Introduction and Principles. *Analytical Chemistry* **1989**, *61*, 132-138.

15. Amemiya, S.; Bard, A. J.; Fan, F. R. F.; Mirkin, M. V.; Unwin, P. R., Scanning Electrochemical Microscopy. *Analytical Chemistry* **2008**, *1*, 95-131.

16. Yuan, Y.; Li, L.; Wang, C.; Zhu, Y., Study of the Effects of Hydrogen on the Pitting Processes of X70 Carbon Steel with Secm. *Electrochemistry Communications* **2010**, *12*, 1804-1807.

17. Paik, C. H.; White, H. S.; Alkire, R. C., Scanning Electrochemical Microscopy Detection of Dissolved Sulfur Species from Inclusions in Stainless Steel. *Journal of The Electrochemical Society* **2000**, *147*, 4120-4120.

18. Dong, C. F.; Luo, H.; Xiao, K.; Li, X. G.; Cheng, Y. F., In Situ Characterization of Pitting Corrosion of Stainless Steel by a Scanning Electrochemical Microscopy. *Journal of Materials Engineering and Performance* **2012**, *21*, 406-410.

19. Bastos, A. C.; Simões, A. M.; González, S.; González-García, Y.; Souto, R. M., Imaging Concentration Profiles of Redox-Active Species in Open-Circuit Corrosion Processes with the Scanning Electrochemical Microscope. *Electrochemistry Communications* **2004**, *6*, 1212-1215.

20. Izquierdo, J.; Eifert, A.; Souto, R. M.; Kranz, C., Simultaneous Pit Generation and Visualization of Pit Topography Using Combined Atomic Force-Scanning Electrochemical Microscopy. *Electrochemistry Communications* **2015**, *51*, 15-18.

21. Casillas, N.; Charlebois, S. J.; Smyrl, W. H.; White, H. S., Pitting Corrosion of Titanium. *Journal of the Electrochemical Society* **1994**, *141*, 636-642.

22. Bentley, C. L.; Kang, M.; Unwin, P. R., Scanning Electrochemical Cell Microscopy: New Perspectives on Electrode Processes in Action. *Current Opinion in Electrochemistry* **2017**, *6*, 23-30.

23. Bentley, C. L.; Kang, M.; Unwin, P. R., Nanoscale Structure Dynamics within Electrocatalytic Materials. *Journal of the American Chemical Society* **2017**, *139*, 16813-16821.

24. Bentley, C. L.; Unwin, P. R., Nanoscale Electrochemical Movies and Synchronous Topographical Mapping of Electrocatalytic Materials. *Faraday Discussions* **2018**, *210*, 365-379.

25. Ebejer, N.; Schnippering, M.; Colburn, A. W.; Edwards, M. A.; Unwin, P. R., Localized High Resolution Electrochemistry and Multifunctional Imaging : Scanning Electrochemical Cell Microscopy. *Analytical Chemistry* **2010**, *82*, 9141-9145.

26. Unwin, P. R.; Güell, A. G.; Zhang, G., Nanoscale Electrochemistry of Sp2 Carbon Materials: From Graphite and Graphene to Carbon Nanotubes. *Accounts of Chemical Research* **2016**, *49*, 2041-2048.

27. Bentley, C. L.; Kang, M.; Maddar, F.; Li, F.; Walker, M.; Zhang, J.; Unwin, P. R., Electrochemical Maps and Movies of the Hydrogen Evolution Reaction on Natural Crystals of Molybdenite (Mos 2): Basal Vs. Edge Plane Activity. *Chemical Science* **2017**, *8*, 6583-6593.

28. Bentley, C. L.; Andronescu, C.; Smialkowski, M.; Kang, M.; Tarnev, T.; Marler, B.; Unwin, P. R.; Apfel, U. P.; Schuhmann, W., Local Surface Structure and Composition Control the Hydrogen Evolution Reaction on Iron Nickel Sulfides. *Angewandte Chemie - International Edition* **2018**, *57*, 4093-4097.

29. Lopez, D. A.; Perez, T.; Simison, S. N., The Influence of Microstructure and Chemical Composition of Carbon and Low Alloy Steels in Co2 Corrosion . A State-of-the-Art Appraisal. *Materials and Design* **2003**, *24*, 561-575.

30. Guo, J.; Yang, S.; Shang, C.; Wang, Y.; He, X., Influence of Carbon Content and Microstructure on Corrosion Behaviour of Low Alloy Steels in a Cl- Containing Environment. *Corrosion Science* **2008**, *51*, 242-251.

31. Bentley, C. L.; Perry, D.; Unwin, P. R., Stability and Placement of Ag / Agcl Quasi-Reference Counter Electrodes in Confined Electrochemical Cells. *Analytical Chemistry* **2018**, *90*, 7700-7707.

32. Snowden, M. E.; Gu, A. G.; Lai, S. C. S.; Kelvey, K. M.; Ebejer, N.; Connell, M. A. O.; Colburn, A. W.; Unwin, P. R., Scanning Electrochemical Cell Microscopy: Theory and Experiment for Quantitative High Resolution Spatially-Resolved Voltammetry and Simultaneous Ion-Conductance Measurements. *Analytical Chemistry* **2012**, *84*, 2483-2491.

33. Chen, C. H.; Jacobse, L.; McKelvey, K.; Lai, S. C. S.; Koper, M. T. M.; Unwin, P. R., Voltammetric Scanning Electrochemical Cell Microscopy: Dynamic Imaging of Hydrazine Electro-Oxidation on Platinum Electrodes. *Analytical Chemistry* **2015**, *87*, 5782-5789.

34. Lohrengel, M. M.; Moehring, A.; Pilaski, M., Capillary-Based Droplet Cells: Limits and New Aspects. *Electrochimica Acta* **2001**, *47*, 137-141.

35. Ustarroz, J.; Kang, M.; Bullions, E.; Unwin, P. R., Impact and Oxidation of Single Silver Nanoparticles at Electrode Surfaces: One Shot Versus Multiple Events. *Chem. Sci.* **2016**, *8*, 1841-1853.

36. Bentley, C. L.; Kang, M.; Unwin, P. R., Time-Resolved Detection of Surface Oxide Formation at Individual Gold Nanoparticles: Role in Electrocatalysis and New Approach for Sizing by Electrochemical Impacts. *Journal of the American Chemical Society* **2016**, *138*, 12755-12758.

37. Kang, M.; Perry, D.; Kim, Y. R.; Colburn, A. W.; Lazenby, R. A.; Unwin, P. R., Time-Resolved Detection and Analysis of Single Nanoparticle Electrocatalytic Impacts. *Journal of the American Chemical Society* **2015**, *137*, 10902-10905.

38. Chen, C. H.; Ravenhill, E. R.; Momotenko, D.; Kim, Y. R.; Lai, S. C. S.; Unwin, P. R., Impact of Surface Chemistry on Nanoparticle-Electrode Interactions in the Electrochemical Detection of Nanoparticle Collisions. *Langmuir* **2015**, *31*, 11932-11942.

39. Kleijn, S. E. F.; Lai, S. C. S.; Miller, T. S.; Yanson, A. I.; Koper, M. T. M.; Unwin, P. R., Landing and Catalytic Characterization of Individual Nanoparticles on Electrode Surfaces. *Journal of the American Chemical Society* **2012**, *134*, 18558-18561.

40. Kang, M.; Momotenko, D.; Page, A.; Perry, D.; Unwin, P. R., Frontiers in Nanoscale Electrochemical Imaging: Faster, Multifunctional, and Ultrasensitive. *Langmuir* **2016**, *32*, 7993-8008.

41. Krawiec, H.; Vignal, V.; Akid, R., Numerical Modelling of the Electrochemical Behaviour of 316l Stainless Steel Based Upon Static and Dynamic Experimental Microcapillary-Based Techniques. *Electrochimica Acta* **2008**, *53*, 5252-5259.

42. Williams, C. G.; Edwards, M. A.; Colley, A. L.; Macpherson, J. V.; Unwin, P. R., Scanning Micropipet Contact Method for High-Resolution Imaging of Electrode Surface Redox Activity. *Analytical Chemistry* **2009**, *81*, 2486-2495.

43. Birbilis, N.; Padgett, B. N.; Buchheit, R. G., Limitations in Microelectrochemical Capillary Cell Testing and Transformation of Electrochemical Transients for Acquisition of Microcell Impedance Data. *Electrochimica Acta* **2005**, *50*, 3536-3544.

44. Arjmand, F.; Adriaens, A., Microcapillary Electrochemical Droplet Cells: Applications in Solid-State Surface Analysis. *Journal of Solid State Electrochemistry* **2014**, *18*, 1779-1788.

45. Suter, T.; Alkire, R. C., Microelectrochemical Studies of Pit Initiation at Single Inclusions in Al 2024-T3. *Journal of The Electrochemical Society* **2001**, *148*, B36-B36.

46. Zhang, X. L.; Jiang, Z. H.; Yao, Z. P.; Song, Y.; Wu, Z. D., Effects of Scan Rate on the Potentiodynamic Polarization Curve Obtained to Determine the Tafel Slopes and Corrosion Current Density. *Corrosion Science* **2009**, *51*, 581-587.

47. *Astm G102-89(2015)E1, Standard Practice for Calculation of Corrosion Rates and Related Information from Electrochemical Measurements*; West Conshohocken, PA, 2015.

48. Pourbaix, M., *Atlas of Electrochemical Equilibria in Aqueous Solutions. Iv. Establishment and Interpretation of Potential-Ph Equilibrium Diagrams*, 1st ed.; Pergamon Press: London, 1966, p 307-321.

49. Chen, C.-H.; Meadows, K. E.; Cuharuc, A.; Lai, S. C. S.; Unwin, P. R., High Resolution Mapping of Oxygen Reduction Reaction Kinetics at Polycrystalline Platinum Electrodes. *Physical Chemistry Chemical Physics* **2014**, *16*, 18545-18545.

50. Pourbaix, M., *Lectures on Electrochemical Corrosion*, 1st ed.; Springer US, 1973, p 201-295.

51. Fontana, M. G., *Corrosion Engineering*, 3rd ed.; McGraw-Hill, 1986.

52. Schreiber, A.; Schultze, J. W.; Lohrengel, M. M.; Kármán, F.; Kálmán, E., Grain Dependent Electrochemical Investigations on Pure Iron in Acetate Buffer Ph 6.0. *Electrochimica Acta* **2006**, *51*, 2625-2630.

53. Schreiber, A.; Rosenkranz, C.; Lohrengel, M. M., Grain-Dependent Anodic Dissolution of Iron. *Electrochimica Acta* **2007**, *52*, 7738-7745.

54. Seo, M.; Chiba, M., Nano-Mechano-Electrochemistry of Passive Metal Surfaces. *Electrochimica Acta* **2001**, *47*, 319-325.

55. Chiba, M.; Seo, M., Mechanoelectrochemical Properties of Passive Iron Surfaces Evaluated by an in Situ Nanoscratching Test. *Journal of The Electrochemical Society* **2003**, *150*, B525-B525.

56. Rault, V.; Vignal, V.; Krawiec, H.; Dufour, F., Quantitative Assessment of Local Misorientations and Pitting Corrosion Behaviour of Pearlitic Steel Using Electron Backscattered Diffraction and Microcapillary Techniques. *Corrosion Science* **2015**, *100*, 667-671.

57. Lill, K. A.; Hassel, A. W.; Frommeyer, G.; Stratmann, M., Scanning Droplet Cell Investigations on Single Grains of a Fealcr Light Weight Ferritic Steel. *Electrochimica Acta* **2005**, *51*, 978-983.

58. Shahryari, A.; Szpunar, J. A.; Omanovic, S., The Influence of Crystallographic Orientation Distribution on 316lvm Stainless Steel Pitting Behavior. *Corrosion Science* **2009**, *51*, 677-682.

59. Krawiec, H.; Szklarz, Z., Combining the Electrochemical Microcell Technique and the Electron Backscatter Diffraction Method to Study the Electrochemical Behaviour of Polycrystalline Aluminium in Sodium Chloride Solution. *Electrochimica Acta* **2016**, *203*, 426-438.

60. Aaronson, B. D. B.; Chen, C. H.; Li, H.; Koper, M. T. M.; Lai, S. C. S.; Unwin, P. R., Pseudo-Single-Crystal Electrochemistry on Polycrystalline Electrodes: Visualizing Activity at Grains and Grain Boundaries on Platinum for the Fe^{2+}/Fe^{3+} Redox Reaction. *Journal of the American Chemical Society* **2013**, *135*, 3873-3880.

61. Fushimi, K.; Seo, M., An Secm Observation of Dissolution Distribution of Ferrous or Ferric Ion from a Polycrystalline Iron Electrode. *Electrochimica Acta* **2001**, *47*, 121-127.

62. Davenport, A. J.; Oblonsky, L. J.; Ryan, M. P.; Toney, M. F., The Structure of the Passive Film That Forms on Iron in Aqueous Environments. *Journal of The Electrochemical Society* **2000**, *147*, 2162-2173.

63. Dwivedi, D.; Lepková, K.; Becker, T., Carbon Steel Corrosion: A Review of Key Surface Properties and Characterization Methods. *RSC Advances* **2017**, *7*, 4580-4610.

64. Eklund, G. S., Initiation of Pitting at Sulfide Inclusions in Stainless Steel. *Journal of The Electrochemical Society* **1974**, *121*, 467-467.

65. Wranglen, G., Pitting and Sulphide Inclusions in Steel. *Corrosion Science* **1974**, *14*, 331-349.

66. Webb, E. G.; Suter, T.; Alkire, R. C., Microelectrochemical Measurements of the Dissolution of Single Mns Inclusions, and the Prediction of the Critical Conditions for Pit Initiation on Stainless Steel. *Journal of the Electrochemical Society* **2001**, *148*, B186-B195.

CHAPTER 4

Nanoscale Active Sites for the Hydrogen Evolution Reaction on Low Carbon Steel

4.1 Abstract

To fully elucidate the structural controls on corrosion-related processes at metal surfaces, experimental measurements should correlate and compare directly structure and activity at the scale of surface heterogeneities (*e.g.*, individual grains, grain boundaries, inclusions *etc.*). For example, the hydrogen evolution reaction (HER), which usually serves as the cathodic counterpart to anodic metal dissolution in acidic media, may be highly sensitive to surface microstructure, highlighting the need for nanoscale-resolution electrochemical techniques. In this study, we employ scanning electrochemical cell microscopy (SECCM) in conjunction with co-located scanning electron microscopy, electron backscatter diffraction, and energy dispersive X-ray spectroscopy to elucidate the relationship between surface structure/composition and HER activity on low carbon steel in aqueous sulfuric acid (pH ≈ 2.3). Through this *correlative electrochemical multimicroscopy* approach, we show that the HER activity of the low index grains (slightly) decreases in the order (100) > (111) > (101), with grain-dependent free energy of hydrogen adsorption (calculated for the low index planes of iron using density functional theory, DFT) proposed as a tentative explanation for this subtle structural-dependence. More significantly, we show that the HER is greatly facilitated by sub-micron surface defects, specifically grain boundaries and MnS inclusions, directly identifying these heterogeneities as potential "cathodic sites" during (atmospheric) corrosion. This study

demonstrates the considerable attributes of correlative SECCM for identifying nanoscale active sites on surfaces, greatly aiding understanding of corrosion and electrocatalytic processes.

4.2 Introduction

Resolving the relationship between surface microstructure (*e.g.*, crystallographic orientation, inclusions and grain boundaries) and electrochemical processes at metals and alloys is vital to advance understanding of corrosion. Although the structural and compositional heterogeneities of metal surfaces are routinely studied using *ex situ* high-resolution microscopy/spectroscopy,[1] corrosion measurements are often performed with classical macroscopic or "bulk" electrochemical techniques[2] that are unsuitable for assessing heterogeneously active surfaces.[3]

Scanning electrochemical cell microscopy (SECCM) provides a means of making nanoscale electrochemical measurements at distinct target sites by using the droplet (meniscus) formed at the end of an electrolyte-filled nanopipet to wet a small area of an electrode surface and create a local electrochemical cell.[4-6] SECCM is the next-generation of the well-known electrochemical droplet cell (EDC) technique,[7] and differs from the more widely-used scanning electrochemical microscopy (SECM)[8-9] in that with SECCM only small portions of a surface are exposed to solution, through brief meniscus contact from a nanopipet probe at a series of pixels, and electrochemical properties are measured *directly* (*e.g.*, by voltammetry, chronoamperometry, etc.) at each point. This attribute is particularly beneficial for highly reactive surfaces that undergo corrosion. In further contrast to SECM, the SECCM response also reveals the corresponding surface topography synchronously, with ≈2 nm vertical

resolution having been demonstrated,[10] so that the surface location of nanoscale electrochemical measurements are easily identified. Recently, SECCM has been employed to make local electrochemical measurements on single nanoparticles,[10-12] transition metal dichalcogenides,[13-14] polycrystalline metals[15-17] and sp^2 carbon materials[18] using nanopipets with diameters as small as ≈30 nm.[10-11]

SECCM is a potentially powerful tool for corrosion-related research, as demonstrated by proof-of-concept studies that revealed the role of microstructure on the electrochemical (corrosion-related) behavior of low carbon steel in neutral pH solutions.[4] SECCM greatly advances the capabilities of conventional EDC techniques by improving spatiotemporal resolution, throughput (number of measurements on a sample), and the density of data, among other key features.[19] In the present study, we focus on the influence of surface microstructure on the rate of the hydrogen evolution reaction (HER) on low carbon steel in aqueous sulfuric acid (pH ≈ 2.3). Although the HER has traditionally been explored in the context of electrocatalysis,[20] this process serves as the cathodic counterpart to anodic metal dissolution during corrosion in acidic media.[21] In addition to the SECCM "droplet-cell" configuration mimicking the conditions of atmospheric corrosion,[3] low carbon steel is frequently exposed to acid media in many industrial applications, including acid pickling and acid cleaning/descaling.[22] Thus, elucidating the structural-dependency is critical to understanding and further predicting the characteristics of galvanic corrosion cells that are formed on macroscopic metal surfaces during practical use.

In the present study, SECCM has been employed in conjunction with the co-located microscopy techniques scanning electron microscopy (SEM), electron backscatter diffraction

(EBSD) and energy-dispersive X-ray spectroscopy (EDS) to explore the role of crystallographic orientation, grain boundaries and MnS inclusions on the rate of HER at low carbon steel. The study significantly advances our previous work,[4] with considerable improvements in spatial-resolution and imaging time, in addition to the implementation of density functional theory (DFT) calculations to support the grain-dependent electrochemical data. Sub-microscale surface defects (*e.g.*, grain boundaries and MnS inclusions) are revealed as important cathodic sites.

4.3 Experimental

4.3.1 Electrode material and chemical reagents

The low carbon steel sample used in this study (composition detailed in Table 4.1) was of size 5 × 21 × (thickness) 2 mm and was mounted in a carbon-based mounting compound (KonductoMet. Buehler, U.S.A) using a Buehler SimpliMet 4000 Mounting Press (Buehler, U.S.A). Once mounted, the sample was polished on a polishing cloth (TriDent. Buehler, U.S.A) using 9 µm, 3 µm and 1 µm polishing suspensions (MetaDi Supreme Suspension. Buehler, U.S.A). To finish, the sample was polished with 0.05 µm alumina suspension (MasterPrep Alumina. Buehler, U.S.A). The sample was subsequently washed with acetone, soapy water and deionized water, before being blown dry. Sulfuric acid (H_2SO_4, Merck, 96%) was used as supplied and diluted using ultra-pure deionized water (Integra HP, Purite, U.K.), which has a resistivity of 18.2 MΩ cm at 25°C.

Table 4. 1. Chemical composition of the low carbon steel, determined using energy dispersive X-ray spectroscopy.

%	C	Mn	Si	Cr	Al	P	S	Cu
Low Carbon Steel	**0.05**	**0.3**	**<0.03**	**0.06**	**0.03**	**<0.02**	**<0.02**	**0.04**

4.3.2 Surface characterization

SEM, EBSD and EDS characterization was performed with a Zeiss SUPRA FE-SEM (Zeiss, Germany), using a Nordlys EBSD detector (Oxford Instrument, U.K.) and an X-max 50 mm^2 energy-dispersive X-ray spectroscopy (EDS) detector (Oxford Instrument, U.K.). SEM images and EDS data were collected at 10 keV, whereas EBSD images were collected at 20 keV, with the sample tilted at 70° to the detector. Following EBSD characterization, grains selected for further analysis were either on or close to the low index orientations, (100), (101) and (111). The criterion set in this study was <10º deviation from the desired orientation.

4.3.3 SECCM probe fabrication

Borosilicate capillaries (GC120F-10. Harvard Apparatus, U.S.A) were pulled (P-2000 pipet puller, Sutter Instruments, U.S.A) to give 2 nanopipets with an end-diameter of approximately 150 nm (as confirmed by SEM). Pulling parameters: Line 1: HEAT 350, FIL 3, VEL 30, DEL 220, PUL -; Line 2: HEAT 350, FIL 3, VEL 40, DEL 180, PUL 120. For use, each pipet was filled with 5 mM H_2SO_4 which formed a droplet (meniscus) cell at the pipet tip. A small amount of silicone oil (Fluka Analytical) was inserted on top of the sulfuric acid solution (from the back) in order to reduce the evaporation from the pipet, as previously reported.[4, 13] A Pd/H_2 quasi reference counter electrode (QRCE) was then inserted into the electrolyte. The Pd/H_2 QRCEs were prepared by hydrogenating Pd wire, of thickness 0.125mm (Goodfellow, U.K.),

in 50 mM H_2SO_4. The reference potential was calibrated to the Ag/AgCl (3.4 M KCl, eDAQ, Australia) scale, after measurements, by monitoring the "open circuit potential" of the QRCE over a period of 30 minutes.

4.3.4 SECCM configuration

The SECCM set up[4, 11] is shown schematically in Figure 4.1a. In brief, during a typical SECCM experiment, the nanopipet probe was mounted on a z-piezoelectric positioner (P-753.2 LISA. PhysikInstrumente, Germany) and the substrate of interest (low carbon steel, herein) was mounted on a *xy*-piezoelectric positioner (P-621.2 PIHera, PhysikInstrumente). The probe was positioned close to the surface of the low carbon steel substrate using micropositioners (M-461, Newport, U.S.A.), aided by visualization with a PL-B776U camera equipped with a 4× lens (Pixelink, U.S.A.). Micropositioners and piezoelectric positioners were used for coarse and fine control of the probe/substrate in *xyz* space, respectively. During the automated approach (5 µm/s, herein), a voltage (0.463 V vs Ag/AgCl) was applied to the QRCE within the probe such that a surface current (i_{surf}) would flow upon droplet contact with the substrate (*i.e.*, the electrochemical circuit was closed). An i_{surf} threshold of *ca.* 2 pA was used to detect when meniscus contact with the substrate had been made, immediately halting the *z*-approach (*e.g.*, see Figure 4.2a). Note that the pipet itself did not make physical contact with the substrate.

Upon meniscus contact with the substrate, chronoamperometric ($i-t$) measurements were made at a series of predefined locations (*i.e.*, in a grid) to build up an 'electrochemical map' of the surface. The probe was retracted from the surface after each measurement before being moved to the next location in a chronoamperometric 'hopping mode'. A visible droplet

'footprint' was left on the surface after each *i*−*t* experiment, which was visible in FE-SEM and used for subsequent co-located (*ex situ*) surface analysis with EBSD and/or EDS. Measurements of the droplet 'footprint' sizes are displayed in Figure 4.4.

The entire SECCM apparatus was on mounted on an optical table (RS2000. Newport, U.S.A) which was supported by vibration isolating supports (S-2000, Newport, U.S.A) and shielded with a Faraday cage equipped with heat sinks and vacuum panels to minimize noise and variations in temperature. The QRCE potential was controlled with respect to ground and the current flowing at the substrate (at ground) was measured using a home-built electrometer. Current was recorded as an average of 129 samples taken every 4 μs (*i.e.*, approximately every 0.5 ms). A home-built 8th order (low-pass) brick-wall filter unit (time constant = 500 μs) was utilized during data (current) collection. Data acquisition and fine control of all instrumentation was achieved using an FPGA card (PCIe-7852R) controlled by a LabVIEW 2016 (National Instruments, U.S.A) interface running the publically-available Warwick Electrochemical Scanning Probe Microscopy (WEC-SPM, www.warwick.ac.uk/electrochemistry) software. The experimental data were processed using the Matlab R2016b (Mathworks, U.S.A) and OriginPro 2016 64bit (OriginLab, U.S.A) software packages.

4.3.5 Density functional theory calculations

We performed plane wave basis set Kohn-Sham Density Functional Theory (DFT)[23] calculations with a plane-wave kinetic energy cut-off of 600 eV, which was found to give converged binding energies to 2 significant figures. Calculated data were also converged with respect to Brillouin zone sampling, using a Monkhurst-Pack grid of 9 × 9 × 1 k-points with no

origin shift.[24] To account for the core atomic states, ultrasoft pseudopotentials[25] from the pslibrary[26] suite were used in Quantum Espresso[27] for all calculations of hydrogen adsorption. Surfaces were represented as a slab model of iron, with a thickness of 7 layers. In the *z*-direction, perpendicular to the slab, a vacuum gap of 7.5 Angstroms was employed to simulate open boundary conditions. Due of the propensity of hydrogen to introduce a long-range electric dipole moment, we corrected for spurious interactions through the *z*-boundary by using the self-consistent Neugebauer-Scheffler dipole correction scheme.[28]

The methodology for finding the ground state configuration of the cells (bare metal surface energy) was first to perform a variable-cell geometry optimization of the bulk metal cell to find a converged lattice parameter, which we found to be 2.759 Å. We then formed vacuum slabs of the bulk lattice parameter and allowed the surface layers to relax in a fixed-cell geometry optimization, while constraining the position of the two layers furthest from the simulated surface. To perform adsorption studies, hydrogen atoms were added onto the bare metal surface configuration in positions close to the high symmetry adsorption sites (see Figure 4.7), with a perpendicular separation of approximately 2 Å. These configurations were allowed to relax, while keeping the deepest two metal layers constrained, yielding the minimized energies of metal cell and hydrogen in each adsorption configuration. To compute binding energies, E_{ads}, we used the equation:

$$E_{\mathrm{ads}} = E_{\mathrm{H+bare}} - E_{\mathrm{bare}} - E_{\mathrm{H}} \quad (5)$$

where $E_{\mathrm{H+bare}}$, E_{bare}, and E_{H} refer to the energy of the plane with a hydrogen atom adsorbed onto it, the energy of the bare plane and the energy of a hydrogen atom in the center of a vacuum box, respectively. The same parameters were used for the slab calculations.

Throughout these calculations we used an electronic energy convergence tolerance of 2×10^{-6} eV. The Gaussian electronic smearing scheme was used, with a smearing width of 0.1 eV, to account for the metallic nature of this system and the electronic structure was optimized using the Pulay DIIS scheme.[29] We used the BFGS geometry optimization scheme[30] with tolerances of 2×10^{-5} eV/atom in energy, 0.05 eV/Å in maximum force, 0.002 Å in maximum atomic displacement and, in the case of the variable-cell bulk geometry optimization, 0.1 GPa maximum stress.

Considering the calculations were performed on an iron, it was necessary to use spin polarised DFT, being the appropriate method for molecules with unpaired electrons (e.g. free radicals). This is because unpaired electrons are free to occupy both spin states (up and down) and as a result can have different energies depending on the spin state.

4.4 Results and Discussion

4.4.1 SECCM: operational principles

In this study, we employ the single barrel SECCM protocol, detailed in Figure 4.1a, with a pixel acquisition rate of ≈1 s pixel^{-1} using a probe diameter of 150 nm. A potential, $-E_{app}$, was applied to a Pd/H_2 quasi reference counter electrode (QRCE) inserted into the electrolyte in an SECCM nanopipet probe, with respect to the substrate (working electrode) surface. Note that all potentials herein have been calibrated to the Ag/AgCl (3.4 M KCl) scale, after measurements. The SECCM probe was approached to the substrate at a series of predefined locations, and when meniscus contact was made (without physical contact from the nanopipet), a current, i_{surf},

flowed as the electrochemical circuit was closed (*e.g.*, Figure 4.2a). This was used as the feedback signal to halt the approach of the probe (and map the surface topography from the corresponding *x,y,z* coordinates). Upon surface-meniscus contact, electrochemical measurements (Figure 4.1b) were carried out within the confines of the wetted area, the 'footprint' of which was visualized, after experiments, using SEM, with example data shown in Figure 4.1c.

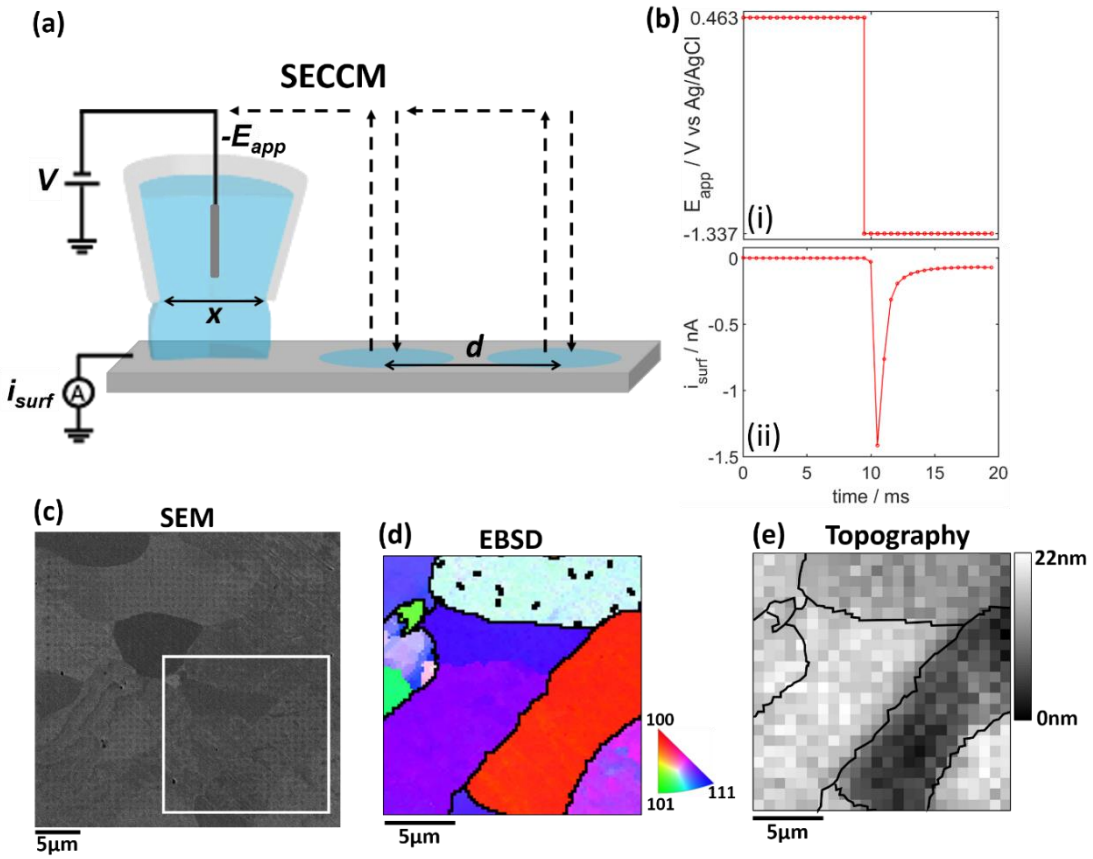

Figure 4. 1. (a) Schematic showing the SECCM hopping-mode protocol used to make spatially resolved electrochemical (i_{surf}–t) measurements on the substrate (working electrode) surface. The arrows indicate the path taken by the probe during the scanning. For this investigation, the diameter of the probe, x, was 150 nm and the 'hopping distance', d, was 800 nm. The nanopipet was filled with 5 mM H_2SO_4 solution (pH ≈ 2.3) and equipped with a Pd/H_2 QRCE. **(b) (i)** Landing potential, E_{app} = 0.463 V vs Ag/AgCl for 10 ms followed by E_{app} = −1.337 V vs Ag/AgCl for 10 ms and **(ii)** representative i_{surf}–t transient, taken from a single hop of a scanning experiment. **(c)** SEM image of a (40 × 40) pixel^2 (32 × 32) µm^2 grid, after SECCM-scanning, with the array of dots 'footprints' denoting the locations of the electrochemical measurements. **(d)** EBSD map obtained from the area delineated by the white box in (c)**. (e)** Corresponding topographical image of the area in highlighted in (c) and (d), constructed from the synchronously obtained z-height data (piezo-position at meniscus contact) in SECCM (no interpolation of data).

Herein, chronoamperometric (current-time, i–t) measurements were made, by stepping E_{app} at each scanning point. The pulse potential was selected after inspection of the linear-sweep voltammogram obtained from low carbon steel in 5 mM H_2SO_4 using the SECCM

configuration, with typical data shown in Figure 4.2b. During the approach, E_{app} was in the passive region (0.463 V vs Ag/AgCl), which provided a reliable feedback signal for positional control (see Figure 4.2a). Upon meniscus contact of the probe with the surface, the potential was maintained at the approach potential for a further 10 ms which 'preconditioned' the surface by forming a thin passive film. E_{app} was then stepped to a driving cathodic potential (-1.337 V vs Ag/AgCl) to quickly reduce the passive film and produce a stable substrate surface current, predominantly from the hydrogen evolution reaction (HER):

$$2H^+ + 2e^- \rightarrow H_2 \qquad (1)$$

Note that the oxygen reduction reaction (ORR) only makes a minor contribution to i_{surf} at E_{app} = −1.337 V vs Ag/AgCl, confirmed by comparing cyclic voltammograms obtained in the presence and absence of air (Figure 4.2b). The current-time transient during the preconditioning is at the background level due to the comparatively low magnitude of the currents relative to the reduction pulse, however, it can be viewed in isolation in Figure 4.2c. This protocol was preferable to running a full voltammetric (current-potential, i−E) curve in the present study for three main reasons. The first reason was to minimize the scanning time (≈1 s pixel^{-1}, compared to ~85 s pixel^{-1} previously).[4] The second reason was that biased steel surfaces promote potential-dependent electrowetting[31] and a potential sweep approach may have introduced uncertainty as to the wetted area, whereas with a fixed potential we were able to measure the wetted area with confidence, after experiments (*vide infra*). The third reason is that sweeping the potential through the active dissolution region (*i.e.*, the large anodic peak seen in Figure 4.2b) causes significant damage to the surface and loads the near-surface electrolyte region (*i.e.*,

the meniscus cell) with soluble Fe-species, which can electro-deposit in the potential-region where the HER occurs, complicating the analysis.

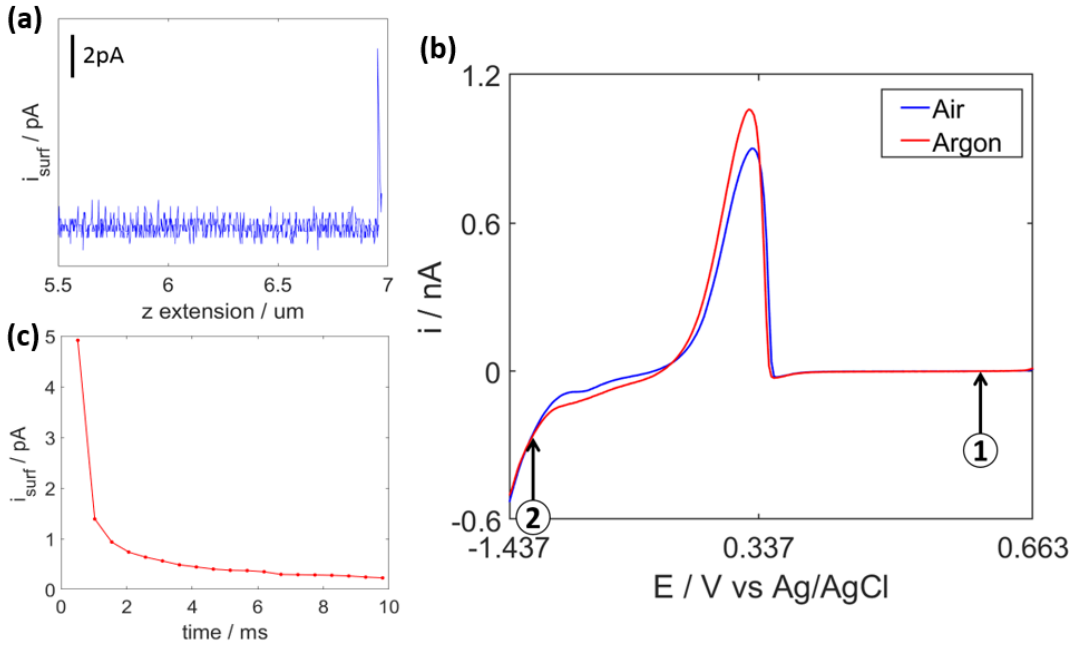

Figure 4. 2. (a) Plot of surface (substrate) current, i_{surf}, versus the extension of the *z*-direction piezo during the approach of the SECCM probe to a low carbon steel surface. In this case, the surface was detected at a *z*-piezo extension of 6.96 µm as indicated by the increase ('spike') in surface current, whereupon the approach was halted. The potential applied during the approach was +0.463 V vs Ag/AgCl. **(b)** Representative SECCM linear sweep voltammograms of low carbon steel in 5 mM H_2SO_4, where the substrate potential ($E_{applied}$) was swept cathodically (*i.e.*, from high to low potential) at 1 Vs^{-1} in air (blue trace) and under argon (red trace) using SECCM. The potentials chosen for chronoamperometry experiments are indicated: (1) Landing and preconditioning: +0.463 V and (2) HER: -1.337 V vs Ag/AgCl. **(c)** i_{surf} response from a single SECCM scanning site on low carbon steel in 5 mM H_2SO_4. Transient arising from an applied potential, E_{app}, of +0.463 V vs Ag/AgCl.

To confirm that any pre-existing passive film was fully reduced upon approaching the steady-state current for the HER (achieved on the 10 ms timescale, *vide infra*), the total charge passed during the reduction pulse was compared to the approximate charge required to remove a film of Fe_2O_3, within the confined area of the droplet cell. Taking 5 nm as a conservative estimate of the thickness of the passive film on low carbon steel (in reality, likely to be <5 nm

thick, as previously reported[32]), the charge required to remove the film is <20% of the charge passed during the decaying portion of the reduction pulse, detailed Figure 4.3. Therefore, it is certain that surface currents arising at the end of the reduction pulse (*i.e.*, beyond 7 ms, *vide infra*) arise predominantly from the HER. The cathodic potential applied is also −0.85 V beyond where the passive potential range ends (Figure 4.2b), therefore there is a considerable driving force for any passive film to be removed.

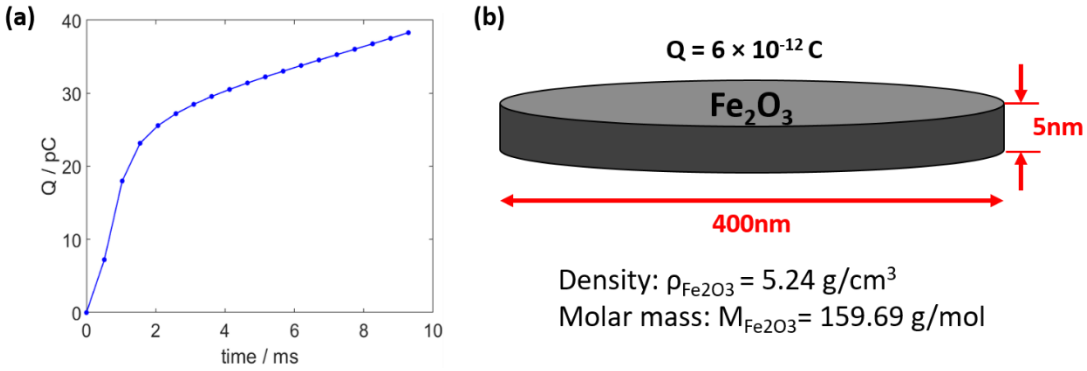

Figure 4. 3. (a) Average *Qt* (charge passed) response for all SECCM scanning sites arising from a -1.337 V vs Ag/AgCl pulse on low carbon steel in 5 mM H_2SO_4. **(b)** Graphic representation of the assumed volume of oxide film (Fe_2O_3) present at each SECCM scanning site on a low carbon steel surface. Charge required to remove 400 nm cylinder of 5 nm thickness of Fe_2O_3: $Q = \frac{V \cdot \rho_{Fe2O3} \cdot F \cdot z}{M_{Fe2O3}}$ where Q = charge transferred, F = Faraday's constant, z = number of electrons transferred, V = volume of Fe_2O_3 cylinder, ρ_{Fe2O3} = density of Fe_2O_3, M_{Fe2O3} = molar mass of Fe_2O_3.

The hopping distance (separation between neighboring pixels) was set conservatively to 800 nm in order to avoid overlap between points of the scan (*i.e.*, to ensure that each measurement was independent of the last; Figure 4.1c). This distance was much larger than the tip diameter (≈150 nm) due to wetting of the metal surface, consistent with previous reports of the enhanced wetting of micro-droplets on steel during cathodic polarization.[31] After identifying the scanned area with SEM, co-located EBSD was performed (*e.g.*, Figure 4.1d), so that

electrochemical activity could be correlated directly with the underlying grain structure (*vide infra*). Furthermore, the wetted area could be measured to calculate local current densities. The wetted area *was ca*. 400 nm diameter on all grains, with no grain dependence, as shown in Figure 4.4. For reference, 100 pA detected with the SECCM configuration, herein, corresponds to a current density of *ca*. 80 mA cm^{-2}. It should be noted that the individual grains were also identifiable from the *z*-height (topographical) data, collected synchronously with the spatially-resolved *i*−*t* data during SECCM imaging (Figure 4.1e). The <20 nm height difference between the individual grains is due to surface-orientation-dependent polishing rates, and that surface height variation can be detected by SECCM highlights the excellent topographical imaging capability of the technique.

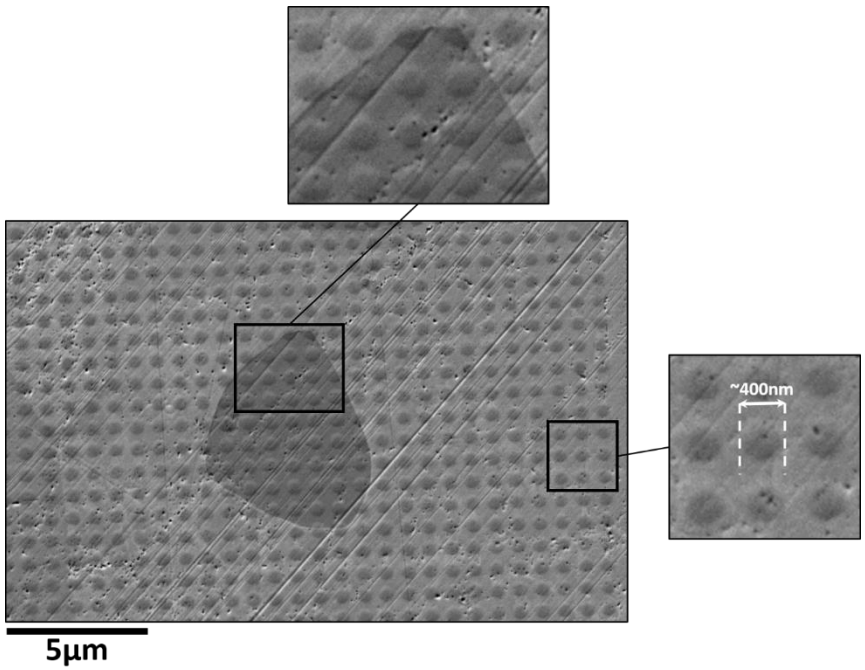

Figure 4. 4. SEM image of a collection of droplet 'footprints' on a low carbon steel surface. The size of the footprints is shown to be consistent. The enlarged regions show that the footprint is not altered by the presence of a grain boundary and a measurement of the diameter of a footprint.

4.4.2 Hydrogen evolution reaction: crystallographic dependence

In this section, we investigate the dependence of the HER rate (measured through the catalytic current) on the crystallographic orientation of low carbon steel, where the high spatial-resolution afforded by SECCM allows us to make a statistically significant number of measurements on individual grains presented by a low carbon steel sample in a 'pseudo single-crystal' approach.[33] The average i_{surf}–t response extracted from all scanning points after stepping the potential from 0.463 V to −1.337 V vs Ag/AgCl for 10 ms is shown in Figure 4.1b. During the first ~6 ms of the pulse, i_{surf}, arising from the HER, is not at steady-state and is also influenced from the finite rise time of the measurement (see Experimental Section for details). After ~6 ms, i_{surf} approaches a steady-state and as a result we focus on this section of the transient for analysis. Note that the relatively short time to steady-state is expected based on the high diffusion coefficient of the hydronium ion (H_3O^+) in aqueous media (9.3×10^{-5} cm^2 s^{-1}, measured previously[34]) combined with the quasi-radial diffusion conditions inherent to the SECCM droplet cell configuration, particularly with the fine probe (*ca.* 150 nm in diameter) employed herein, as discussed in depth previously.[35]

EBSD maps and corresponding spatially-resolved i_{surf} maps taken from two areas of the low carbon steel surface are shown in Figure 4.5a and b, respectively. Note that the i_{surf} maps displayed in Figure 4.5b (and beyond) are calculated by averaging i_{surf} in the 7.2 – 9.8 ms period (*i.e.*, last 6 data points) at the end of the i_{surf}–t transient, justified above. Comparing the EBSD maps to the corresponding spatially-resolved i_{surf} maps reveals a subtle correlation between the crystallographic orientation and the HER activity of the low carbon steel surface.

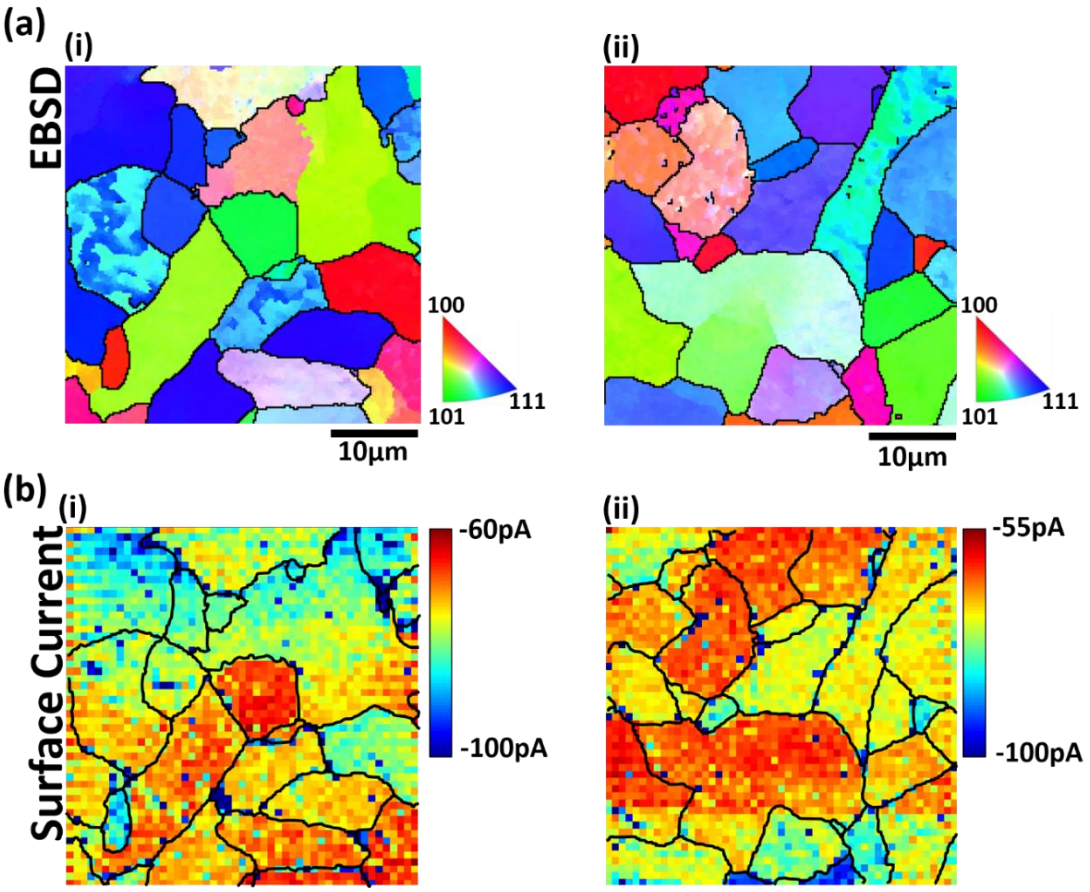

Figure 4. 5. (a) EBSD maps of the areas of the low carbon steel surface that were characterized with SECCM. **(b)** Spatially-resolved i_{surf} maps (2500 pixels) over a (40 × 40) µm^2 area, corresponding to the areas shown above in **(a)**. The i_{surf} values are the average of the last six data points (*i.e.*, 7.2 to 9.8 ms) and the data are presented as the recorded currents (no interpolation). With the SECCM footprint areas defined in the text, the maximum and minimum currents of 100 pA and 55 pA corresponds to current densities of *ca.* 80 and 44 mA cm^{-2}, respectively. The maps were taken at E_{app} = −1.337 V vs Ag/AgCl with a probe of 150 nm diameter containing 5 mM H_2SO_4.

As alluded to above, the HER has been studied predominantly in the context of electrocatalysis, primarily on Pt-based materials,[36] for which the crystallographic orientation (structure) dependence is hotly debated.[37-38] Due to comparatively poor catalytic activity, Fe-based materials (*e.g.*, steel) have received significantly less attention, which is perhaps surprising considering the important role of cathodic processes such as the HER in the corrosion of steel. The majority of literature concerning hydrogen-related processes on steel focuses on hydrogen embrittlement, and the diffusion of hydrogen into bulk steel.[39]

In order to tentatively explain the grain-dependent HER rates on low carbon steel (*i.e.*, Figure 4.5), we performed DFT calculations, focusing on the low index planes, *i.e.*, (100), (101) and 111) of the body centered cubic (BCC) structure of iron. Given that the iron content of the substrate is ~99.5% (see Experimental Section), iron is considered to be representative of the low carbon steel surface and therefore appropriate for DFT. Figure 4.6a identifies the grains that possess an orientation within 10° of the (i) (100), (ii) (101) and (iii) (111) low index planes (shown schematically for a BCC unit cell). Presented in Figure 4.6b is a histogram showing the average surface currents measured between 7.2 to 9.8 ms for all $i-t$ measurements taken on the low index grains (identified in Figure 4.6a), which visually emphasizes why making multiple measurements on each grain improves the validity of any grain dependent trends. Evidently, the HER activity of the low index grains of the low carbon steel surface decreases in the order (100) > (111) > (101), albeit only slightly (*vide infra*), with mean i_{surf} (between 7.2 and 9.8 ms) values of 80 ± 4, 71 ± 2 and 66 ± 3 (mean ± standard deviation), respectively.

Note that although the i_{surf} values between 7.2 and 9.8 ms can be taken as qualitative indicators of relative HER activity, due to the cathodic potential applied (−1.337 V vs Ag/AgCl,

see Figure 4.2b) and low bulk concentration of H^+ ($[H_2SO_4]$ = 5 mM), there is some contribution from mass transport (*i.e.*, the HER is not purely surface-kinetic controlled). To illustrate this, considering that the diffusional flux in SECCM is approximately 10% of that for the same sized disk electrode,[13, 40] and the diffusion coefficient of the hydronium ion (H_3O^+) is 9.3×10^{-5} cm^2 s^{-1} in aqueous media,[34] a steady-state limiting current (i_{ss}) of *ca.* −150 pA is expected from a probe of 150 nm diameter, assuming that mass-transport occurs solely by diffusion. (Note that under steady-state conditions the probe geometry, rather than wetted area determines the local mass-transport rate). As the average i_{surf} values from 7.2 to 9.8 ms (−66 to −80 pA) are *ca.* half of i_{ss}, E_{app} = −1.337 V vs Ag/AgCl lies near the voltammetric half-wave potential, where the reaction (*i.e.*, HER) is under mixed kinetic-diffusion control. Thus, the absolute mean i_{surf} values between 7.2 and 9.8 ms cannot be taken as quantitative measures of the relative HER kinetics (*i.e.*, the relative exchange currents, i_0), but do provide a qualitative indicator of the trends in activity, as discussed in further detail below.

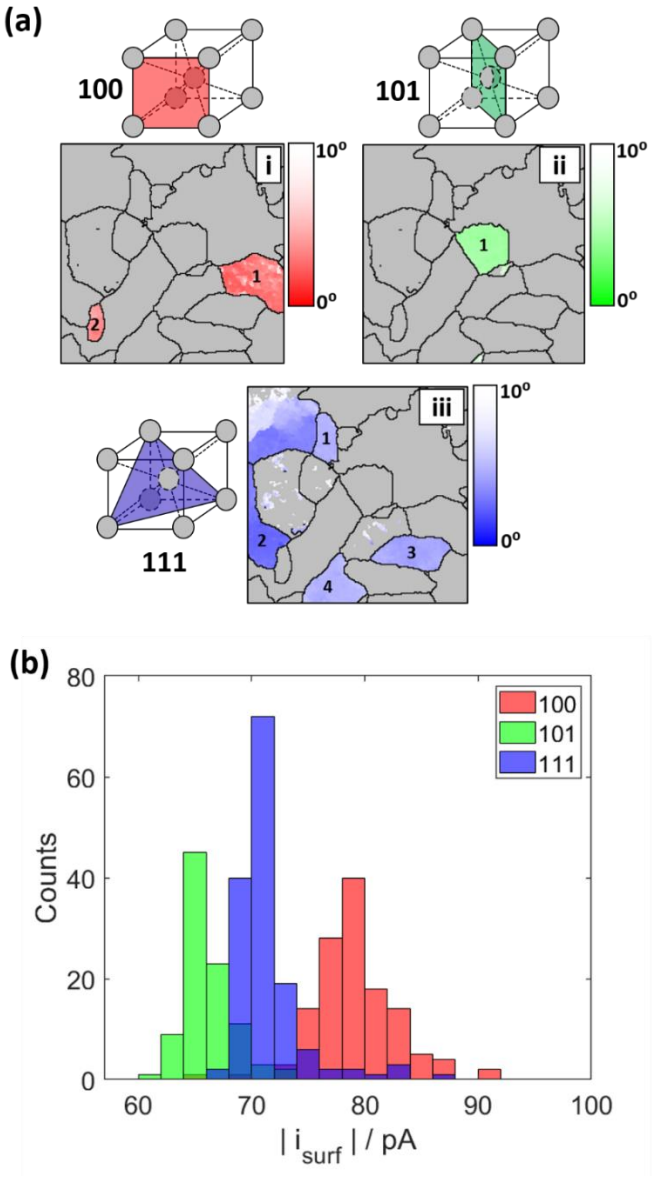

Figure 4. 6. (a) Grains within the area scanned with SECCM that have a crystal orientation within 10º of the (i) (100) (ii) (101) and (iii) (111) low index orientations of low carbon steel. **(b)** Histogram of the average surface currents, i_{surf}, measured from 7.2 to 9.8 ms from each of the measurement landing on the low index grains indicated in (a).

To explore possible explanations for the grain-dependent HER activities, one must first consider the HER mechanism, which is generally accepted to follow one of two electrocatalytic pathways on metal surfaces in acidic media, Volmer-Heyrovsky or Volmer-Tafel:[20]

$$H^+ + e^- + * \rightarrow H^* \quad (2)$$

$$H^* + H^+ + e^- \rightarrow H_2 + * \quad (3)$$

$$2H^* \rightarrow H_2 + 2^* \quad (4)$$

where * donates an adsorption site on the metal surface, and Equations 2, 3 and 4 refer to the Volmer, Heyrovsky and Tafel step, respectively. The hydrogen adsorption free energy, ΔG_H, is generally used as a descriptor of HER activity,[41] where for an optimal electrocatalyst, there is an appropriate balance between the strength of hydrogen adsorption (Volmer, Eq 2) and desorption (Heyrovsky/Tafel, Eqs 3 and 4) from the surface. In other words, if the binding energy is too low (*i.e.*, ΔG_H less negative), the adsorption step (Eq 2) will limit the rate of reaction and likewise the desorption step (Eqs 3 and 4), if the binding energy is too high (*i.e.*, ΔG_H more negative). Thus ΔG_H values for the low index planes of iron were calculated using DFT, as presented in Table 4.2, for the adsorption sites depicted in Figure 4.7. In order to contextualize these values, a classical volcano-type relationship is assumed, taking value calculated for a Pt(111) surface (also presented in Table 4.2) as the approximate value for the 'peak' of the volcano.[42-43] Note that the ΔG_H values calculated for Pt(111) are consistent with previous DFT studies.[44-45]

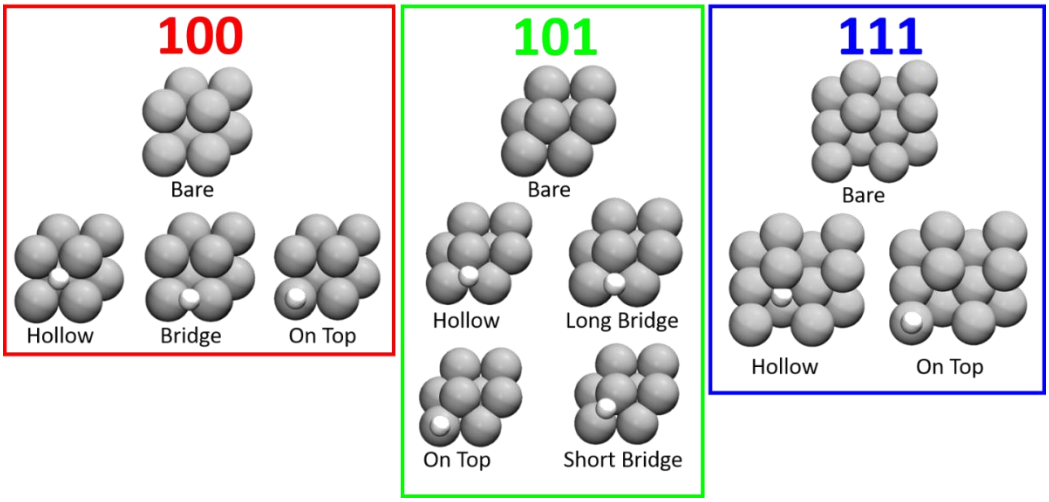

Figure 4. 7. Schematic of each of the low index crystal planes in the body centered cubic (BCC) crystal structure of iron (grey spheres) with the calculated hydrogen adsorption sites (white spheres).

Table 4. 2. ΔG_H values calculated for each adsorption site on the (111) plane of Pt and each of the low index planes (100, 101 and 111) of Fe.

Crystal Plane	Adsorption Location	ΔG_H / eV
Pt(111)	Top	-2.75
	HCP (Hollow)	-2.72
	FCC (Hollow)	-2.77
	Bridge	-2.72
Fe(100)	Bridge	-3.00
	Hollow	-2.97
	On Top	-2.44
Fe(101)	On Top	-2.65
	Hollow	-3.32
	Short Bridge	-3.13
	Long Bridge	-3.28
Fe(111)	On Top	-2.50
	Hollow	-2.30

The calculated ΔG_H values in Table 4.2 are broadly consistent with previous DFT studies on Fe,[46-47] as well as experimentally calculated Fe-H binding energies.[48] Using the

example of the (100) plane, the ΔG_H values for different adsorption sites are more (*e.g.*, Bridge) and less (*e.g.*, On Top) negative than the volcano "peak" [*i.e.*, Pt(111)], meaning the different sites will fall on the ascending and descending branches of the volcano plot,[42-43] respectively, likewise for different grains [*e.g.*, compare Fe(101) and Fe(111)]. This suggests that the rate determining step for HER (equations 2 – 4, above) may vary between adsorption site on a given low index plane, as well as between different low index planes. In any case, taking Pt(111) as the ideal case, we can assume that sites with ΔG_H values closest to Pt(111) will be more facilitative of the HER. Thus, we take the difference between the average ΔG_H value (from all adsorption sites) for Pt(111), $\Delta G_H^{Pt(111)}$, and the average ΔG_H value for each low index plane, $\Delta G_H^{Fe(hkl)}$ on Fe as a qualitative indicator of relative HER kinetics, as summarized in Table 4.3.

Table 4. 3. The calculated average ΔG_H deviations for each of the adsorption sites on the low index orientations of Fe from the average ΔG_H value calculated for Pt(111).

Crystal Plane	$\boldsymbol{\left\lvert \Delta G_H^{Fe(hkl)} - \Delta G_H^{Pt(111)} \right\rvert}$ **/ eV**
Fe(100)	0.26
Fe(101)	0.40
Fe(111)	0.34

The $|\Delta G_H^{Fe(hkl)} - \Delta G_H^{Pt(111)}|$ values increase in the order (100) < (111) < (101), which agrees with the experimentally measured i_{surf} values measured on low carbon steel (Figure 4.6). Despite the agreement, this comparison should be taken *cum grano salis* due to the number of assumptions/simplifications made. First, the DFT model assumes a pristine crystal lattice of Fe (*i.e.*, no imperfections), whereas for a real low carbon steel surface there are likely to be multiple types of crystallographic defects,[49] some of which are considered below (*e.g.*, grain boundaries). Second, the solvent and anions have not been explicitly considered in the DFT simulations, the

latter of which is known to influence HER kinetics on Fe surfaces (*e.g.*, HER inhibition by Cl^- adsorption).[50] Third, although the average $|\Delta G_H^{Fe(hkl)} - \Delta G_H^{Pt(111)}|$ values (Table 4.3) do follow the experimental trend in i_{surf} (Figure 4.6), the calculated ΔG_H values (Table 4.2) are site-specific, meaning each low-index orientation possesses a range of sites with differing HER activities.

Thus, an important outcome from these findings is that while the classical volcano relationship is a convenient and powerful way for predicting the macroscale activity of different materials, as in HER electrocatalysis,[20] it is perhaps oversimplified when predicting the local (nanoscale) response of a heterogeneous electrode surface (*e.g.*, polycrystalline metal). For example, the data in Table 4.2 suggest that the different low-index planes, or indeed the different adsorption sites within a given low-index plane of BCC iron may have large (order-of-magnitude) differences in HER activity, whereas the experimentally determined HER rates were found to show only a subtle grain dependence (Figures 4.5 and 4.6). In reality, as we show below, the rate of HER (and the susceptibility to corrosion-related phenomena) across a (non-ideal) polycrystalline alloy surface is more likely to be influenced by crystallographic defects, *e.g.*, grain boundaries and inclusions.

4.4.3 HER activity at grain boundaries

We next consider the HER activity at grain boundaries between crystallites on polycrystalline surfaces, for which SECCM is becoming a particularly powerful technique.[17, 33] The grain boundaries of polycrystalline metals are critically important in the context of corrosion, serving as sites for well-documented phenomena such as intergranular corrosion.[51] The intergranular

corrosion of steels is commonly attributed to metallurgical features such as the enrichment of detrimental impurities or the depletion of beneficial alloying elements at grain boundaries.[52] This change in surface chemistry often results in preferential dissolution or in some cases, an enhancement in the cathodic half-cell process(es) at grain boundaries.[51]

EBSD and corresponding spatially-resolved i_{surf} maps of a grain boundary (with misorientation angles marked) that exhibits enhanced HER activity are shown in Figure 4.8a and b, respectively. Evidently, elevated cathodic currents are detected at the grain boundary termination (*ca.* 50% increase compared to the surrounding grains), are clear from Figure 4.8b. It should be noted that the difference in HER currents between different low-index grains is on the order of 5−20% (see Figure 4.6), demonstrating that crystallographic defects such as grain boundaries are likely to be far more influential on cathodic corrosion-processes compared to variations in crystal orientation. A further two examples are also presented in Figure 4.8c and d. It is interesting to note that not all of the grain boundaries exhibit enhanced HER activity (*vide infra*), clear from the i_{surf} maps in Figure 4.8, as well as Figure 4.5, above. It should also be noted that in all cases, the elevated currents at the grain boundaries cannot be attributed to distortion of the SECCM meniscus cell (*i.e.*, changes in the probed surface area), as the topographical variation between neighboring grains is on the sub-10 nm scale, confirmed through the synchronously obtained *z*-height data, plotted in Figure 4.9. Additionally Figure 4.4 shows that there is no variation in the wetting between scanning points located at positions on and adjacent to grain boundaries.

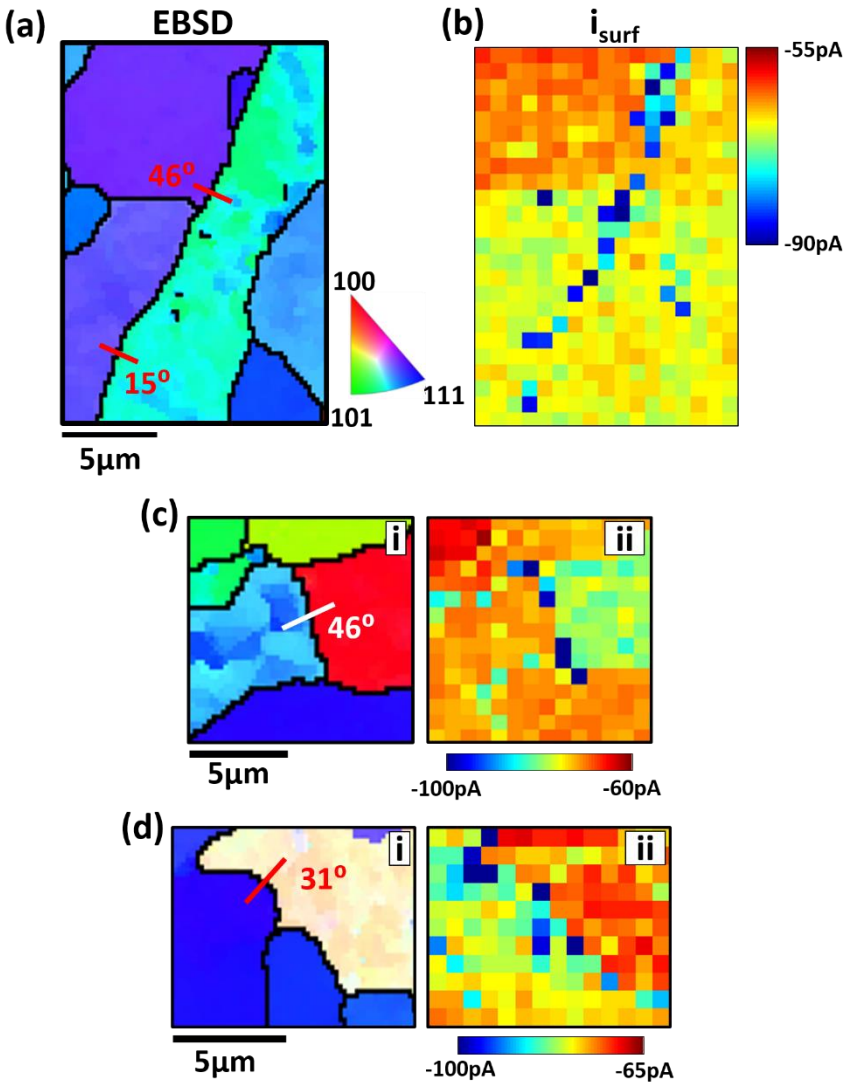

Figure 4. 8. (a) EBSD map of a "cathodically active" grain boundary, with the misorientation between the two neighboring grains labelled inset. **(b)** Spatially-resolved i_{surf} map of the average response from 7.2 to 9.8 ms during a −1.337 V vs Ag/AgCl reduction pulse, in the area of the surface shown in (a). **(c)** and **(d)** EBSD-SECCM i_{surf} map comparisons for two more examples of grain boundaries with enhanced HER activity. There is no interpolation of data in the SECCM images.

Several factors may result in enhanced catalytic activity at grain boundaries. Surface defects, such as grain boundaries, comprise coordinatively unsaturated sites (*i.e.*, atoms with low lattice coordinate numbers) that can serve as the "active sites" for electrocatalytic processes.[3, 53] Indeed, such an effect was proposed in a recent SECCM study,[17] where enhanced electrochemical CO_2 reduction activity was identified at grain boundaries on polycrystalline

Au. Another possibility is that changes in the surface chemistry at grain boundaries (*i.e.*, impurity enrichment or depletion) may give rise to a catalytically active surface that can facilitate the HER. Although we cannot distinguish between these possibilities herein, the results in Figure 4.8 demonstrate unequivocally that certain grain boundaries would be more likely to serve as cathodic sites on a macroscopic surface, during atmospheric corrosion (*i.e.*, in the presence of acid rain).

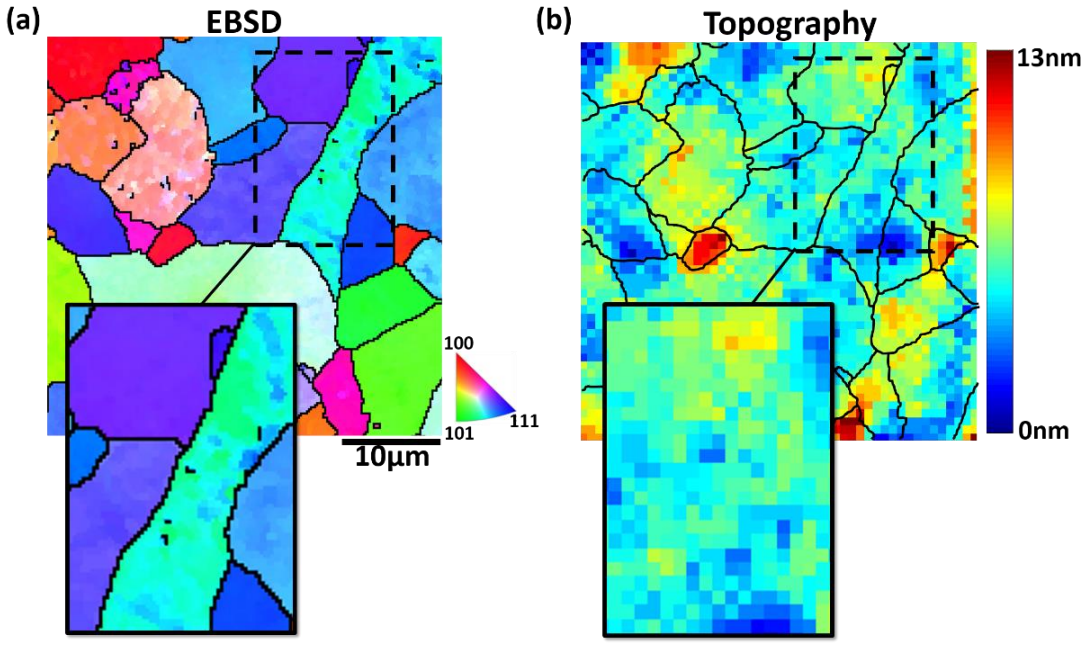

Figure 4. 9. (a) EBSD image of the area scanned with SECCM (main text, Figure 4) with the grain boundary of interest highlighted. **(b)** The corresponding topography map, constructed from the *z*-height data collected synchronously during SECCM.

4.4.4 HER activity at manganese sulfide inclusions

We now consider the response of individual sub-micron MnS inclusions. Figure 4.10a shows an SEM image of an area scanned using SECCM, with the corresponding spatially-resolved i_{surf} map shown in Figure 4.10b. The dark "spots" in Figure 4.10a, two of which are highlighted by the white box, are MnS inclusions, confirmed by performing EDS; sulfur map and spectra shown in Figure 4.10c and d, respectively. Focusing on the electrochemical map in Figure 4.10b, there are two blue pixels indicating off-scale current magnitudes corresponding to the sub-micron MnS inclusions, confirming these sites as local HER "hot spots". Similarly to the case for grain boundaries, the catalytic HER current measured at individual inclusions (up to *ca*. 100% compared to the surrounding grains) is far more significant compared to the difference in activity observed between grains of different crystal orientation (Figure 4.6). Indeed, the exceptionally high activity of these sites is clear to see from the electrochemical activity maps in Figures 4.5 and 4.10, which is further supported by the detection of a range of other inclusions, as shown in Figure 4.11.

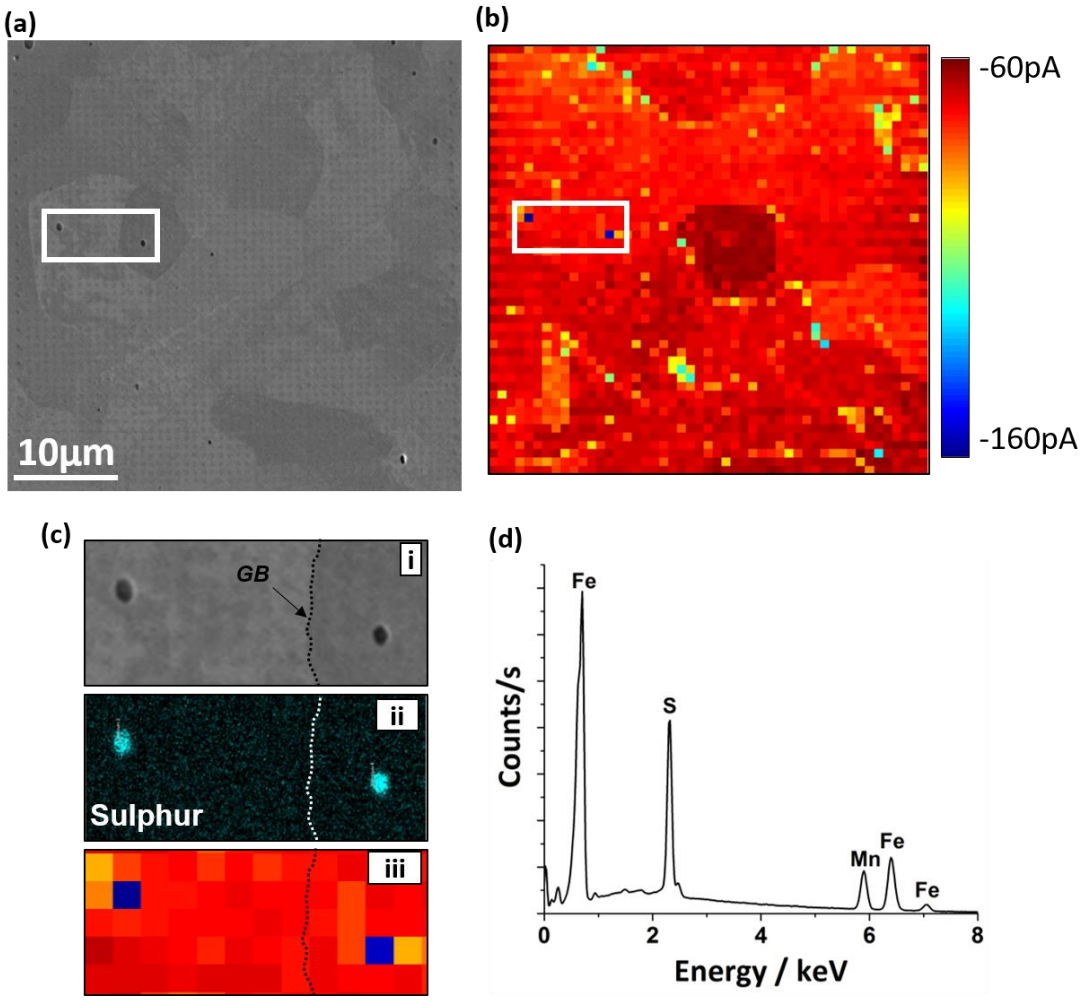

Figure 4. 10. (a) SEM image of the area of low carbon steel scanned with SECCM. The matrix of 50 × 50 scanning points (pixels) can be seen as dark spots on the surface. The darker spots, two of which are highlighted, are MnS inclusions. **(b)** Corresponding spatially resolved i_{surf} map (E_{app} = −1.337 V vs Ag/AgCl), with no interpolation of data. **(c)** Zoomed-in (i) SEM (ii) EDS sulfur map and (iii) i_{surf} images of the boxed area highlighted in (a) and (b). **(d)** EDS spectra of the left inclusion shown in (c). Note that the i_{surf} values are the average of the last six data points (*i.e.*, 7.2 to 9.8 ms).

The EDC technique has previously been used to study the local dissolution of large MnS inclusions in steel[54-55] and we have also used SECCM to observe similar behavior on low carbon steel, in neutral pH media.[4] Here, we have been able to measure the electrochemical (electrocatalytic) activity of inclusions (*ca.* 0.2 – 1 µm in size) more directly (*i.e.*, the inclusions constitute all or most of the probed area). Large MnS inclusions have previously been shown to

be responsible for enhanced hydrogen trapping on steel surfaces, which can lead to hydrogen induced cracking,[56-57] and blistering at these sites.[58] Our results further emphasize the importance of inclusions as highly active cathodic sites on polycrystalline low carbon steel.

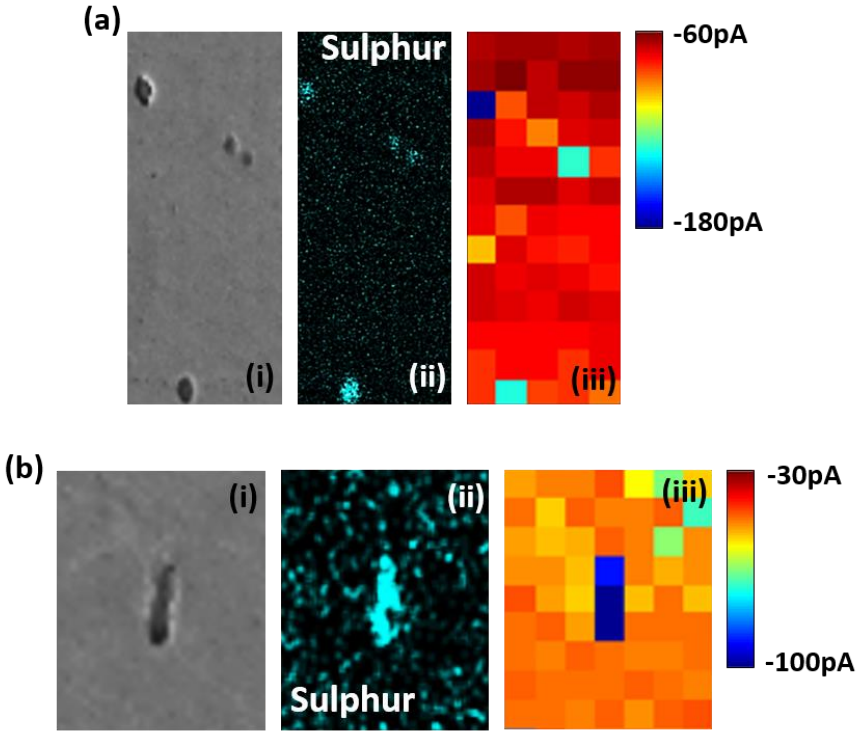

Figure 4. 11. (a) and **(b)** Two further examples of areas of the low carbon steel surface scanned with SECCM containing MnS inclusions. In each case co-located maps are shown that are obtained with (i) SEM, (ii) EDS for sulphur and (iii) i_{surf} at −1.337 V (vs Ag/AgCl).

4.5 Conclusions

In this study, we have leveraged recent technical advances in scanning electrochemical cell microscopy (SECCM) to investigate the structure-dependent cathodic activity of low carbon steel in aqueous sulfuric acid (pH ≈ 2.3), in the context of atmospheric (acid rain) corrosion. Focusing on the HER, and using a fine nanopipet probe (diameter ≈ 150 nm) in a fast

chronoamperometric (*i*–*t*) scan-hopping protocol (*ca.* 1 s pixel^{-1}), we have shown unequivocally that the rate of this reaction varies spatially across the surface of low carbon steel. By combining these spatially-resolved electrochemical data with co-located structural information from SEM, EBSD and EDS in a correlative electrochemical multi-microscopy approach, HER activity on the low-index planes was shown to increase slightly in the order of (100) > (111) > (101), which we attempted to explain through the calculation of grain-dependent ΔG_H values. The high spatial-resolution of SECCM also allowed grain boundary terminations and (sub-micron) MnS inclusions to be directly interrogated; these surface defects exhibit greatly enhanced HER activity compared to the crystallographic planes, indicting them as likely "cathodic sites" during macroscopic (*e.g.*, atmospheric) corrosion. Overall, this study further demonstrates the great potential of SECCM in corrosion science and electrocatalysis. A holistic view of structure-activity of (electro)materials results when local electrochemical maps and movies are combined with co-located microscopy/spectroscopy, and experiments are further supported by theory (*e.g.*, DFT calculations).

4.6 References

1. Suwas, S.; Ray, R. K., *Crystallographic Texture of Materials*; Springer-Verlag: London, 2014.

2. McCafferty, E., *Introduction to Corrosion Science*; Springer: London, 2010.

3. Bentley, C. L.; Kang, M.; Unwin, P. R., Nanoscale Surface Structure-Activity in Electrochemistry and Electrocatalysis. *J. Am. Chem. Soc.* **2019**, *141*, 2179-2193.

4. Yule, L. C.; Bentley, C. L.; West, G.; Shollock, B. A.; Unwin, P. R., Scanning Electrochemical Cell Microscopy: A Versatile Method for Highly Localised Corrosion Related Measurements on Metal Surfaces. *Electrochimica Acta* **2019**, *298*, 80-88.

5. Ebejer, N.; Güell, A. G.; Lai, S. C. S.; McKelvey, K.; Snowden, M. E.; Unwin, P. R., Scanning Electrochemical Cell Microscopy: A Versatile Technique for Nanoscale Electrochemistry and Functional Imaging. *Annual Review of Analytical Chemistry* **2013**, *6*, 329-51.

6. Bentley, C. L.; Kang, M.; Unwin, P. R., Scanning Electrochemical Cell Microscopy: New Perspectives on Electrode Processes in Action. *Current Opinion in Electrochemistry* **2017**, *6*, 23-30.

7. Böhni, H.; Suter, T.; Schreyer, A., Micro- and Nanotechniques to Study Localized Corrosion. *Electrochimica Acta* **1995**, *40*, 1361-1368.

8. Bard, A. J.; Fan, F. R. F.; Kwak, J.; Lev, O., Scanning Electrochemical Microscopy. Introduction and Principles. *Analytical Chemistry* **1989**, *61*, 132-138.

9. Payne, N. A.; Stephens, L.; Mauzeroll, J., The Application of Scanning Electrochemical Microscopy to Corrosion Research. *Corrosion* **2017**, *73*, 759-780.

10. Bentley, C. L.; Kang, M.; Unwin, P. R., Nanoscale Structure Dynamics within Electrocatalytic Materials. *Journal of the American Chemical Society* **2017**, *139*, 16813-16821.

11. Bentley, C. L.; Unwin, P. R., Nanoscale Electrochemical Movies and Synchronous Topographical Mapping of Electrocatalytic Materials. *Faraday Discussions* **2018**, *210*, 365-379.

12. Tao, B.; Yule, L. C.; Daviddi, E.; Bentley, C. L.; Unwin, P. R., Correlative Electrochemistry-Microscopy of Li-Ion (De)Intercalation at Series of Individual Limn2o4 Particles. *Angew. Chem.-Int. Edit.* **2019**, *58*, 4606-4611.

13. Bentley, C. L.; Kang, M.; Maddar, F.; Li, F.; Walker, M.; Zhang, J.; Unwin, P. R., Electrochemical Maps and Movies of the Hydrogen Evolution Reaction on Natural Crystals of Molybdenite (Mos 2): Basal Vs. Edge Plane Activity. *Chemical Science* **2017**, *8*, 6583-6593.

14. Hill, J. W.; Hill, C. M., Directly Mapping Photoelectrochemical Behavior within Individual Transition Metal Dichalcogenide Nanosheets. *Nano Lett* **2019**, *19*, 5710-5716.

15. Chen, C.-H.; Meadows, K. E.; Cuharuc, A.; Lai, S. C. S.; Unwin, P. R., High Resolution Mapping of Oxygen Reduction Reaction Kinetics at Polycrystalline Platinum Electrodes. *Physical Chemistry Chemical Physics* **2014**, *16*, 18545-18545.

16. Wang, Y.; Gordon, E.; Ren, H., Mapping the Nucleation of H2 Bubbles on Polycrystalline Pt Via Scanning Electrochemical Cell Microscopy. *J Phys Chem Lett* **2019**, *10*, 3887-3892.

17. Mariano, R. G.; McKelvey, K.; White, H. S.; Kanan, M. W., Selective Increase in Co_2 Electroreduction Activity at Grain-Boundary Surface Terminations. *Science* **2017**, *358*, 1187-1192.

18. Unwin, P. R.; Güell, A. G.; Zhang, G., Nanoscale Electrochemistry of Sp2 Carbon Materials: From Graphite and Graphene to Carbon Nanotubes. *Accounts of Chemical Research* **2016**, *49*, 2041-2048.

19. Andreatta, F.; Fedrizzi, L., The Use of the Electrochemical Micro-Cell for the Investigation of Corrosion Phenomena. *Electrochimica Acta* **2016**, *203*, 337-349.

20. Seh, Z. W.; Kibsgaard, J.; Dickens, C. F.; Chorkendorff, I.; Norskov, J. K.; Jaramillo, T. F., Combining Theory and Experiment in Electrocatalysis: Insights into Materials Design. *Science* **2017**, *355*.

21. Pound, B., Chapter 2.2 Hydrogen Ingress During Corrosion In *Corrosion and Oxide Films*, Stratmann, M.; Frankel, G., Eds. Wiley-VCH: Germany, 2003; Vol. 4, pp 108-155.

22. Fontana, M. G., *Corrosion Engineering*, 3rd ed.; McGraw-Hill, 1986.

23. Kohn, W.; Sham, L. J., Self-Consistent Equations Including Exchange and Correlation Effects. *Physical Review* **1965**, *140*, A1133-A1138.

24. Monkhorst, H. J.; Pack, J. D., Special Points for Brillouin-Zone Integrations. *Physical Review B* **1976**, *13*, 5188-5192.

25. Vanderbilt, D., Soft Self-Consistent Pseudopotentials in a Generalized Eigenvalue Formalism. *Physical Review B* **1990**, *41*, 7892-7895.

26. Dal Corso, A., Pseudopotentials Periodic Table: From H to Pu. *Computational Materials Science* **2014**, *95*, 337-350.

27. Giannozzi, P., et al., Quantum Espresso: A Modular and Open-Source Software Project for Quantum Simulations of Materials. *Journal of Physics: Condensed Matter* **2009**, *21*, 395502.

28. Neugebauer, J.; Scheffler, M., Adsorbate-Substrate and Adsorbate-Adsorbate Interactions of Na and K Adlayers on Al(111). *Physical Review B* **1992**, *46*, 16067-16080.

29. Pulay, P., Convergence Acceleration of Iterative Sequences. The Case of Scf Iteration. *Chemical Physical Letters* **1980**, *73*, 393-398.

30. Pfrommer, B.; Cote, M.; Louie, S. G.; Cohen, M. L., Relaxation of Crystals with the Quasi-Newton Method. *Journal of Computational Physics* **1997**, *131*, 233-240.

31. Tsuru, T.; Tamiya, K. I.; Nishikata, A., Formation and Growth of Micro-Droplets During the Initial Stage of Atmospheric Corrosion. *Electrochimica Acta* **2004**, *49*, 2709-2715.

32. Davenport, A. J.; Oblonsky, L. J.; Ryan, M. P.; Toney, M. F., The Structure of the Passive Film That Forms on Iron in Aqueous Environments. *Journal of The Electrochemical Society* **2000**, *147*, 2162-2173.

33. Aaronson, B. D. B.; Chen, C. H.; Li, H. J.; Koper, M. T. M.; Lai, S. C. S.; Unwin, P. R., Pseudo-Single-Crystal Electrochemistry on Polycrystalline Electrodes: Visualizing Activity at Grains and Grain Boundaries on Platinum for the Fe^{2+}/Fe^{3+} Redox Reaction. *J. Am. Chem. Soc.* **2013**, *135*, 3873-3880.

34. Longsworth, L. G., Temperature Dependence of Diffusion in Aqueous Solutions. *J Phys Chem-Us* **1954**, *58*, 770-773.

35. Momotenko, D.; Byers, J. C.; McKelvey, K.; Kang, M.; Unwin, P. R., High-Speed Electrochemical Imaging. *ACS Nano* **2015**, *9*, 8942-52.

36. Eftekhari, A., Electrocatalysts for Hydrogen Evolution Reaction. *International Journal of Hydrogen Energy* **2017**, *42*, 11053-11077.

37. Markovic, N. M.; Sarraf, S. T.; Gasteiger, H. A.; Ross Jr, P. N., Hydrogen Electrochemistry on Platinum Low-Index Single-Crystal Surfaces in Alkaline Solution. *Faraday Transactions* **1996**, *92*, 3719-3725.

38. Hoshi, N.; Asaumi, Y.; Nakamura, M.; Mikita, K.; Kajiwara, R., Sructural Effects on the Hydrogen Oxidation Reaction on N(111)-(111) Surface of Platinum. *Journal of Physical Chemistry C* **2009**, *113*, 16843-16846.

39. Dadfarnia, M.; Nagao, A.; Wang, S.; Martin, M. L.; Somerday, B. P.; Sofronis, P., Recent Advances on Hydrogen Embrittlement of Structural Materials. *International Journal of Fracture* **2015**, *196*, 223-243.

40. Snowden, M. E.; Güell, A. G.; Lai, S. C. S.; McKelvey, K.; Ebejer, N.; O'Connell, M. A.; Colburn, A. W.; Unwin, P. R., Scanning Electrochemical Cell Microscopy: Theory and Experiment for Quantitative High Resolution Spatially-Resolved Voltammetry and Simultaneous Ion-Conductance Measurements. *Anal. Chem.* **2012**, *84*, 2483-2491.

41. Norskov, J. K.; Bligaard, T.; Logadottir, A.; Kitchin, J. R.; Chen, J. G.; Pandelov, S.; Stimming, U., Trends in the Exchange Current for Hydrogen Evolution. *Journal of The Electrochemical Society* **2005**, *152*, J23-J26.

42. Santos, E.; Quaino, P.; Schmickler, W., Theory of Electrocatalysis: Hydrogen Evolution and More. *Phys Chem Chem Phys* **2012**, *14*, 11224-33.

43. Strmcnik, D.; Lopes, P. P.; Genorio, B.; Stamenkovic, V. R.; Markovic, N. M., Design Principles for Hydrogen Evolution Reaction Catalyst Materials. *Nano Energy* **2016**, *29*, 29-36.

44. Kozlov, S. M.; Aleksandrov, H. A.; Neyman, K. M., Adsorbed and Subsurface Absorbed Hydrogen Atoms on Bare and Mgo(100)-Supported Pd and Pt Nanoparticles. *Journal of Physical Chemistry C* **2014**, *118*, 15242-15250.

45. Yan, L.; Sun, Y.; Yamamoto, Y.; Kasamatsu, S.; Hamada, I.; Sugino, O., Hydrogen Adsorption on Pt(111) Revisited from Random Phase Approximation. *J Chem Phys* **2018**, *149*, 164702.

46. Ferrin, P.; Kandoi, S.; Nilekar, A. U.; Mavrikakis, M., Hydrogen Adsorption, Absorption and Diffusion on and in Transition Metal Surfaces: A Dft Study. *Surface Science* **2012**, *606*, 679-689.

47. Wang, T.; Wang, S.; Luo, Q.; Li, Y.-W.; Wang, J.; Beller, M.; Jiao, H., Hydrogen Adsorption Structures and Energetics on Iron Surfaces at High Coverage. *Journal of Physical Chemistry C* **2014**, *118*, 4181-4188.

48. Bozso, F.; Ertl, G.; Grunze, M.; Weiss, M., Chemisorption of Hydrogen on Iron Surfaces. *Applications of Surface Science* **1977**, *1*, 103-119.

49. Reed-Hill, R. E., *Physical Metallurgy Principles*; PWS: U.S.A, 1994.

50. Vracar, L. J.; Drazic, D. M., Influence of Chloride Adsorption on Hydrogen Evolution Reaction on Iron. *Journal of Electroanalytical Chemistry* **1992**, *339*, 269-279.

51. Scully, J. R., Chaper 4.3 Intergranular Corrosion. In *Corrosion and Oxide Films*, Frankel, G.; Stratmann, M., Eds. Wiley-VCH: Germany, 2003; Vol. 4, pp 344-380.

52. Briant, C. L.; Andresen, P. L., Grain Boundary Segregation in Austenitic Stainless Steels and Its Effect on Intergranular Corrosion and Stress Corrosion Cracking. *Metallurgical and Materials Transactions A: Physical Metallurgy and Materials Science* **1987**, *19*, 495-504.

53. O'Mullane, A. P., From Single Crystal Surfaces to Single Atoms: Investigating Active Sites in Electrocatalysis. *Nanoscale* **2014**, *6*, 4012-4026.

54. Suter, T.; Bohni, H., Microelctrodes for Corrosion Studies in Microsystems. *Electrochimica Acta* **2001**, *47*, 191-199.

55. Webb, E. G.; Suter, T.; Alkire, R. C., Microelectrochemical Measurements of the Dissolution of Single Mns Inclusions, and the Prediction of the Critical Conditions for Pit Initiation on Stainless Steel. *Journal of the Electrochemical Society* **2001**, *148*, B186-B195.

56. Peng, Z.; Liu, J.; Huang, F.; Hu, Q.; Cheng, Z.; Liu, S.; Cheng, Y., Effect of Submicron-Scale Mns Inclusions on Hydrogen Trapping and Hic Susceptibility of X70 Pipeline Steels. *Steel Research International* **2018**, *89*.

57. Muto, I.; Shinozaki, J.; Omura, T.; Numata, M.; Hara, N., Microelectrochemical Investigation of Hydrogen Absorption and Dissolution Behaviour of Mns Inclusions in Carbon Steel. *ECS Transactions* **2011**, *33*, 9-20.

58. Ren, X.; Chu, W.; Li, J.; Su, Y.; Qiao, L., The Effects of Inclusions and Second Phase Particles on Hydrogen-Induced Blistering in Iron. *Materials Chemistry and Physics* **2008**, *107*, 231-235.

CHAPTER 5

Nanoscale Electrochemical Visualization of Grain-Dependent Anodic Iron Dissolution from Low Carbon Steel

5.1 Abstract

The properties of steels and other alloys are often tailored to suit specific applications through the manipulation of microstructure (*e.g.*, grain structure). Such microscopic heterogeneities are also known to modulate corrosion susceptibility/resistance, but the exact dependency remains unclear, largely due to the challenge of probing and correlating local electrochemistry and structure at complex (alloy) surfaces. Herein, high-resolution scanning electrochemical cell microscopy (SECCM) is employed to perform spatially-resolved potentiodynamic measurements, which, when correlated to co-located structural information from electron backscatter diffraction (EBSD), analytical scanning electron microscopy (SEM) and scanning transmission electron microscopy (STEM), reveal the relationship between anodic metal (iron) dissolution and the crystallographic orientation of low carbon steel in aqueous sulfuric acid (pH 2.3). Considering hundreds of individual measurements made on each of the low-index planes of body-centred cubic (bcc) low carbon steel, the rate of iron dissolution, and thus overall corrosion susceptibility, increases in the order (101) < (111) < (100). These results are rationalized by complementary density functional theory (DFT) calculations, where the experimental rate of iron dissolution correlates with the energy required to remove (and ionize) one iron atom at the surface of a lattice, calculated for each low index orientation. Overall, this

study further demonstrates how nanometre-resolved electrochemical techniques such as SECCM can be effectively utilised to vastly improve the understanding of structure-function in corrosion science, particularly when combined with complementary, co-located structural characterisation (EBSD, STEM *etc*.) and computational analysis (DFT).

5.2 Introduction

The microstructural features of steel and other alloys, such as grains of different crystal orientation, grain boundaries and (sub)microscale inclusions, play an important role in the formation of the local anodic and cathodic cells that drive corrosion processes.[1] Indeed, many studies have attempted to resolve the relationship between surface structure and electrochemical activity with metals such as iron,[2-5] 316L stainless steel[6] and aluminium.[7] Although such studies report that the crystal orientation does influence corrosion behaviour, a consistent trend or explanation for this behaviour has not been forthcoming. This is largely attributed to the difficulty in probing local electrochemistry and structure in the same area at complex surfaces, meaning that in practice measurements are often limited to a few measurements on single grains.[8] For this reason, there is a need for techniques that can probe corrosion-related phenomena with high spatial-resolution, an application where scanning electrochemical probe microscopy (SEPM) techniques are most powerful.[9]

Presently, the most widely-used SEPM method in corrosion science is scanning electrochemical microscopy (SECM).[10-11] Although microscale measurements can be made readily with SECM, it is important to note that SECM interrogates electrochemical processes

indirectly by measuring fluxes and concentrations at an ultramicroelectrode probe. The application of SECM in corrosion-related measurements is non-trivial, particularly at the nanoscale, for several reasons including topographical changes in the surface and complex intermediate/product speciation (*e.g.*, metal ions in anodic dissolution), which need to be easily detected at the tip. In contrast, the electrochemical droplet cell (EDC) technique[12-13] probes electrochemistry *locally* and *directly* by contacting a small (micrometric) area of the surface of interest under a droplet formed at the end of a micropipet probe. Data analysis is more straightforward when using the EDC format, as well-known electrochemical techniques (*e.g.*, potentiodynamic polarisation) are applied directly, which is why the EDC it has found application for the study of many materials, including 304 stainless steel[13-14] and aluminium,[7, 15-16] although two major downsides of this technique are its limited spatial-resolution and low throughput.[17]

Scanning electrochemical cell microscopy (SECCM) is the next generation of the EDC technique, making considerable improvements in terms of spatial resolution, speed and usability.[18-19] In essence, through the use of much finer pipets (typically 30 nm to 1 μm diameter[20]) and piezoelectric positioners, SECCM automates the EDC technique, making possible the rapid translation of a nanoscale droplet cell across an electrode surface to perform high-resolution electrochemical mapping. SECCM has been shown to be extremely powerful for nanoscale structure-function studies, being used to probe the electrochemical activity of, for example, molybdenum disulphide,[21] sp^2 carbon materials,[22] polycrystalline metals,[23-25] iron nickel sulfide catalysts,[26] metallic nanoparticles,[27-28] semiconductors[29] and battery materials.[30] SECCM is also a potentially powerful tool for corrosion-related research, as demonstrated by

our recent proof-of-concept studies investigating the role of microstructure on the passivating behaviour of low carbon steel in pH neutral solutions of KNO_3.[31]

In this study, the local rate of iron dissolution has been correlated to the crystal orientation in order to unveil how different grains may support anodic processes in the formation of galvanic corrosion cells. With SECCM, thousands of spatially-resolved electrochemical (potentiodynamic polarisation) measurements are made using a 150 nm diameter nanopipet probe filled with aqueous sulfuric acid (pH 2.3), over a polycrystalline body centred cubic (bcc) low carbon steel surface. Used widely as a construction material, low carbon steel is both relatively cheap and easily manufactured into particular shapes without splitting or wrinkling.[32] Acidic solutions, such as the sulfuric acid investigated herein, are commonly used to remove scales and corrosion products from carbon steels, however without the extensive use of inhibitors, these cleaning processes can also have a detrimental impact (*i.e.*, corrosion) on the condition of the steel surface.[33] By combining the spatially-resolved electrochemical data from SECCM with structural information from electron backscatter diffraction (EBSD) and scanning transmission electron microscopy (STEM) in the same areas as the electrochemical measurements, microscopic structure (*e.g.*, crystal orientation) is shown to play an important role in modulating the corrosion susceptibility of low carbon steel. We attempt to rationalise these observations by complementary density functional theory (DFT) calculations.

5.3 Experimental

5.3.1 Electrode material and chemical reagents

The substrate used in this study was a low carbon steel, the chemical composition of which is presented in Table 5.1. The samples, of size 5 × 21 mm, were mounted in a conductive mounting compound (KonductoMet. Buehler, U.S.A) using a mounting press (SimpliMet. Buehler, U.S.A). Samples were then polished on a polishing cloth (TriDent. Buehler, U.S.A) with a polishing machine (AutoMet 3000 Pro. Buehler, U.S.A) using 9 µm, 3 µm and 1 µm polishing suspensions followed by a final polish using 0.05 µm alumina suspension (MasterPrep Alumina. Buehler, U.S.A) on a different cloth (MicroCloth. Buehler, U.S.A). To remove contamination from polishing suspensions, samples were cleaned with acetone, soapy water and then deionised water before being blown dry. Sulfuric acid (H_2SO_4, Merck, 96%) was used as supplied. All solutions were prepared with ultra-pure deionised water (Integra HP, Purite, U.K.), which has a resistivity of 18.2 MΩ.cm at 25°C.

Table 5. 1. Chemical composition of the low carbon steel determined using energy dispersive X-ray spectroscopy.

%	C	Mn	Si	Cr	Al	P	S	Cu
Low Carbon Steel	**0.05**	**0.3**	**<0.03**	**0.06**	**0.03**	**<0.02**	**<0.02**	**0.04**

5.3.2 Surface characterisation

SEM and EBSD characterisation was carried out with a Zeiss SUPRA FE-SEM (Zeiss, Germany), using a Nordlys EBSD detector (Oxford Instrument, U.K.). SEM images and EDS data were collected at 10 keV, whereas EBSD images were collected at 20 keV, with the sample

tilted at 70° to the detector. Following EBSD characterisation, grains that were chosen for study were either on or close to the low index orientations, (100), (101) and (111). Criteria set in this study was 10º deviation from the desired orientation.

Before TEM analysis the sample was first extracted from the surface with FIB using a ThermoFisher Scientific Scios DualBeam (ThermoFisher, U.S.A). In brief, an area of the surface chosen for examination was coated in a Pt layer to protect the area from damage. The regions surrounding this area were then subjected to a beam of Ga ions which effectively milled through the surface. Before removal, the examination area was attached to a tungsten rod with the use of deposited Pt, and once attached the area was then cut free from the surface. The extract was then attached to carbon coated copper TEM grid, again with the use of deposited Pt. The extract was then 'thinned' with the Ga ion beam until a cross section of the SECCM scanning site was clearly visible. STEM was subsequently carried out on the thinned sample with a ThermoFisher Talos F200X FEG (ThermoFisher, U.S.A).

5.3.3 SECCM probe fabrication

Borosilicate capillaries (GC120F-10. Harvard Apparatus, U.S.A) were mounted on a laser puller (P-2000. Sutter Instruments, U.S.A) and pulled to give an opening diameter of approximately 150 nm at the end of the pipet (as confirmed by FE-SEM). Pulling parameters: Line 1: HEAT 350, FIL 3, VEL 30, DEL 220, PUL -; Line 2: HEAT 350, FIL 3, VEL 40, DEL 180, PUL 120. The pulled pipet was then filled with 5 mM H_2SO_4, producing a droplet at the tapered end. Silicone oil (Fluka Analytical) was used to reduce evaporation of the solution from the back of the nanopipet by placing a small amount on top of the sulfuric acid solution as

previously utilised.[21, 31] A Pd/H_2 quasi reference counter electrode (QRCE) was then inserted into the electrolyte which were prepared by hydrogenating palladium wire, of thickness 0.125mm, in 50 mM sulfuric acid solution. The Pd/H_2 QRCE was calibrated as the open circuit potential measured against a commercial Ag/AgCl reference electrode (ET072-1, eDAQ, Australia), in 5 mM H_2SO_4 using a CHI400 potentiostat (CH Instruments Inc., U.S.A).

5.3.4 SECCM configuration

The SECCM set up used in this investigation has been discussed in greater detail previously.[28, 31] The nanopipet was mounted on a *z*-piezoelectric positioner (P-753.2 LISA. PhysikInstrumente, Germany) which was then positioned near to the surface manually with a micropositioner and then within the range the *z*-piezoelectric positioner using a *z*-plane picomotor. The sample stage was placed on top of a *xy*-piezoelectric positioner (P-621.2 PIHera, PhysikInstrumente) for fine horizontal movement. As the nanopipet was approached to the surface automatically (at 3 µm/s), a voltage (0.563 V vs Ag/AgCl) was applied to the QRCE so that a surface current (i_{surf}) was detected once the droplet had made contact with the substrate. This surface current response was used as the feedback parameter to halt the approach. The threshold used during approach was set at *ca.* 2 pA for this study. Note that the nanopipet itself did not make contact with the surface.

Upon contacting the substrate surface via the nanopipet meniscus, a potentiodynamic polarisation experiment was performed by sweeping the potential at the QRCE from 0.563 to -1.437 and back to 0.563 V vs Ag/AgCl and the resulting surface current was recorded. Data points were recorded as an average of 129 samples taken every 4 µs (i.e. approximately every

0.5 ms). After the experiment for each scanning point had concluded the nanopipet was then retracted from the surface (at 10 µm/s) and moved automatically to next scanning site defined by the hopping distance. The process was repeated over a grid of scanning sites to map the electrochemical response of the surface.

The entire SECCM apparatus was mounted on an optical table (RS2000. Newport, U.S.A) supported on vibration isolation supports (S-2000. Newport, U.S.A). The set up was also shielded with a Faraday cage equipped with heat sinks and vacuum panels to minimise noise and variations in temperature. The QRCE potential was controlled with respect to ground and the current flow at the substrate was measured using a home-built electrometer. Data acquisition and fine control of all instrumentation was achieved using an FPGA card (PCIe-7852R) controlled by a LabVIEW 2016 (National Instruments, U.S.A) interface running the Warwick Electrochemical Scanning Probe Microscopy (WEC-SPM, www.warwick.ac.uk/electrochemistry) software.

5.3.5 Software and data processing

The experimental data was processed using the Matlab R2016b (Mathworks, U.S.A) and OriginPro 2016 64bit (OriginLab, U.S.A) software packages. The possible identity of the corrosion products formed during SECCM (and observed with STEM imaging) was calculated using the HYDRA and MEDUSA software package (KTH, Sweden),[34] which considers the thermodynamically stable species (*i.e.*, at equilibrium) that may exist under a given experimental condition. The following solid (iron oxysulphate) corrosion products were predicted: $Fe(OH)_2$, $FeSO_4 \cdot 7H_2O$, $Fe_2(SO_4)_3$, Fe_2O_3, FeOOH and $H_3OFe_3(SO_4)_2(OH)_6$.

5.3.6 Density function theory calculations

The Quantum Espresso[35] software toolbox was used to perform plane wave basis set Kohn-Sham Density Functional Theory (DFT)[36] calculations with ultrasoft pseudopotentials.[37] Pseudopotentials were all taken from the PSLibrary, version 1.0.[38] A plane-wave kinetic energy cut-off of 800 eV was found to converge binding energies to at least 2 significant figures (in eV units). A Monkhurst-Pack grid of 4x4x1 *k*-points with no origin shift[39] was found to be adequate to converge energies with respect to Brillouin zone sampling. As previously discussed in Chapter 4, spin polarised DFT was appropriate for the iron system.

Slab models of (100), (101) and (111) Fe planes with a finite thickness of 5 layers were employed to model Fe dissolution energies. A vacuum gap of 7 Å on both sides of the slab in the *z*-direction was used to simulate open boundary conditions. Additionally, any remaining spurious interactions through the *z*-boundary were corrected using the Martyna-Tuckerman dipole correction scheme[40] as implemented in the Environ model.[41-42] The solvation model was used to account for solvent interaction energy terms between the surface and the solvent and between the dissolved iron and the solvent. To parameterise the continuum solvent model for water, the parameters suggested previously[41-42] were used. This was found to converge the surface energies down to 0.001 eV error.

First, a variable-cell geometry optimisation of the bulk metal cell was performed to find a converged lattice parameter. In the case of hcp crystal structure of Fe, these were a = b = c = 2.71177 Å. Slabs formed from the bulk metal were used in a fixed-cell geometry optimisation

constraining the position of the two layers furthest from our simulated surface to calculate the bare surface energy in vacuum (E_{bV}) and in solvent (E_{bS}).

A single layer of Fe atoms was manually removed from the surface. The following equation was used to compute binding energies of the Fe layer (E_{Fe-Fe}):

$$E_{Fe-Fe} = (E_{bS\_n(layers)} - E_{bS\_n-1(layers)} - E_{Fe^{2+}})/n \quad (1)$$

where $E_{Fe^{2+}}$ refers to the energy of a Fe^{2+} cation in the centre of a solvent box, with the same parameters used for the slab calculations. Normalisation by the number of atoms in a layer (n) was used to account for packing densities of individual grains.

An electronic energy convergence tolerance of 2×10^{-6} eV was used throughout these calculations. A Broyden charge density mixing[43] scheme, with local Thomas-Fermi screening[44] and Gaussian electronic smearing, with a smearing width of 0.1 eV were used to account for the metallic nature of our systems. We used the BFGS geometry optimisation scheme[45] with tolerances of 2×10^{-5} eV per atom in energy, 0.05 eV per in maximum force, 0.002 Å in maximum atomic displacement and in the case of the variable-cell, bulk geometry optimisation, 0.1 GPa maximum stress.

5.4 Results and Discussion

5.4.1 SECCM: Operational Principles

The previously reported[27-28] voltammetric hopping-mode SECCM protocol used in this study is shown in Figure 1a. A single-channel nanopipet of diameter ≈ 150 nm, filled with 5 mM H_2SO_4

(pH = 2.3) and equipped with a palladium-hydrogen (Pd-H_2) QRCE, which possessed a potential of 0.437 V vs Ag/AgCl (3.4 M KCl), was employed to perform spatially-resolved potentiodynamic polarisation measurements. The *z*-position of the nanopipet probe, applied potential and surface current (i_{surf}) measured synchronously during a single "hop" of an SECCM scan is shown in Figure 5.1b. During approach of the nanopipet probe to the surface (*i.e.*, extension in the *z*-direction at 3 µm/s, herein, Figure 5.1b-i), a potential (0.563 V vs Ag/AgCl, herein, Figure 5.1b-ii) was applied between the QRCE and the surface (working electrode), such that when the meniscus (droplet) protruding from the end of the probe initially made contact with the surface, a current (i_{surf}) flowed at the substrate surface (in a 2-electrode cell), as the circuit was closed (Figure 5.1b-iii). This was used as a feedback signal (set point) to instantaneously halt the approach of the nanopipet, so that it did not contact the surface. Upon meniscus landing, a local potentiodynamic polarisation experiment (between 0.563 V and -1.437 V vs Ag/AgCl at 2 V/s, herein) was performed, before the probe was retracted and moved to a new site (pixel) with a pre-determined hopping distance, *d* (*vide infra*).

The potential applied between the QRCE and the surface during the approach (0.563 V vs Ag/AgCl) was within the passive region, where a protective passive (oxide) film was formed, for example, via the reaction:

$$2Fe + 3H_2O \rightarrow Fe_2O_3 + 6H^+ + 6e^- \quad (2)$$

Once contact was established between the droplet and the surface, the potential was swept cathodically to enter the active region, where the protective passive film is removed (reduced) and the iron dissolution reaction occurs:

$$Fe \rightarrow Fe^{2+} + 2e^{-} \quad (3)$$

Continuing the potential sweep into the cathodic region, the oxygen reduction reaction (ORR), Eq 4, and (to a more appreciable extent) hydrogen evolution reaction (HER), Eq 5, occur:

$$O_2 + 4H^{+} + 4e^{-} \rightarrow 2H_2O \quad (4)$$

$$2H^{+} + 2e^{-} \rightarrow H_2 \quad (5)$$

Once the cathodic potential sweep was completed, the cycle was then reversed and the potential was swept anodically. Corrosion is a dynamic process and, as a result, the working electrode (low carbon steel) surface changes irreversibly (physically and chemically) during active dissolution. For this reason, only the processes occurring before (*i.e.*, in the passive region) and in the active region during the forward potential sweep have been considered herein (*vide infra*).

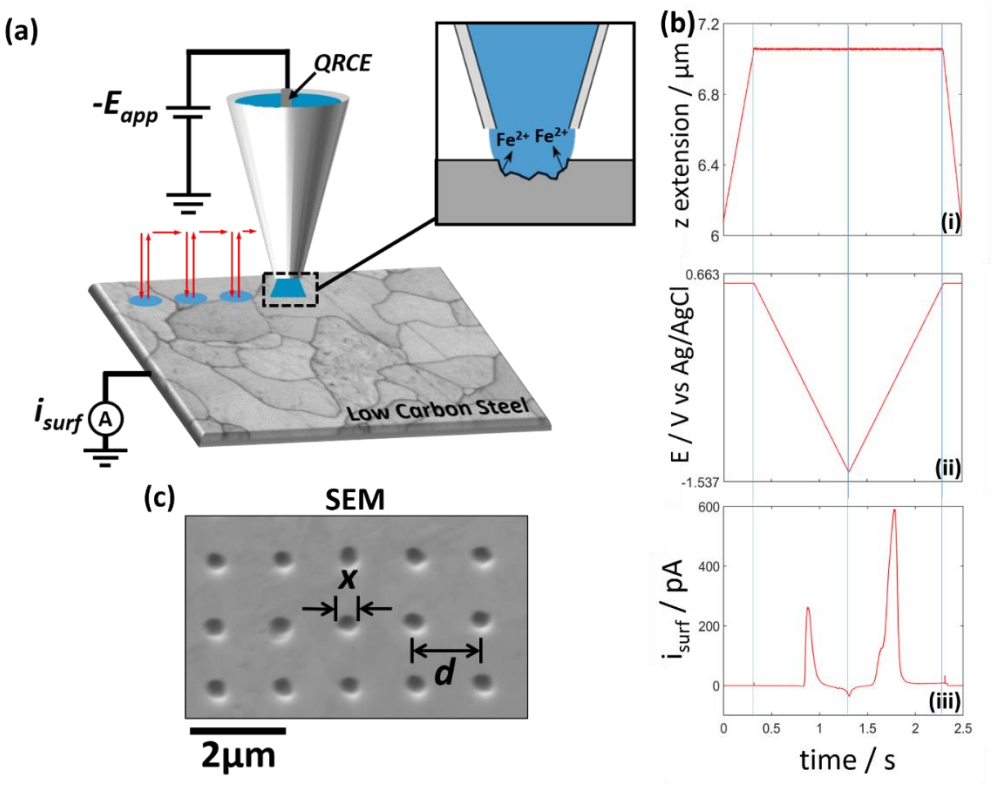

Figure 5. 1. (a) Schematic of the voltammetric hopping-mode protocol of SECCM, used herein. The direction of motion by the probe is indicated by the red arrows. In this study, the nanopipet was filled with 5 mM H_2SO_4 and equipped with a Pd/H_2 QRCE. **(b)** Plots of **(i)** z-extension, **(ii)** applied potential, *E*, **(iii)** surface current, i_{surf}, during a single "hop" of a voltammetric SECCM experiment (voltammetric scan rate, υ = 2 V s^{-1}). **(c)** SEM image taken of the low carbon steel surface, showing 15 individual droplet "footprints", after an SECCM scan. The nanopipet diameter was 150 nm, the hopping distance, *d*, between pixels was 1.2 µm and the droplet "footprint" diameter, *x*, for each measurement was measured as ≈450 nm.

The result of a voltammetric hopping mode experiment on the surface of low carbon steel (using the cyclic potentiodynamic polarisation protocol outlined above) is demonstrated in Figure 5.1c, where each spatially-independent measurement site is seen as an array of droplet "footprints" by using scanning electron microscopy (SEM). A full matrix of the droplet footprints (60 × 60 = 3600 measurements) visible in SEM after SECCM experiments can be found in the Figure 5.2. The diameter of the footprints, *x*, defining the "working electrode area" during each measurement is consistent from point-to-point (≈450 nm). The ultimate spatial-

resolution of the scan is determined by *d*, which was conservatively set to 1.2 µm herein to ensure that each potentiodynamic polarisation measurement was independent of the last.

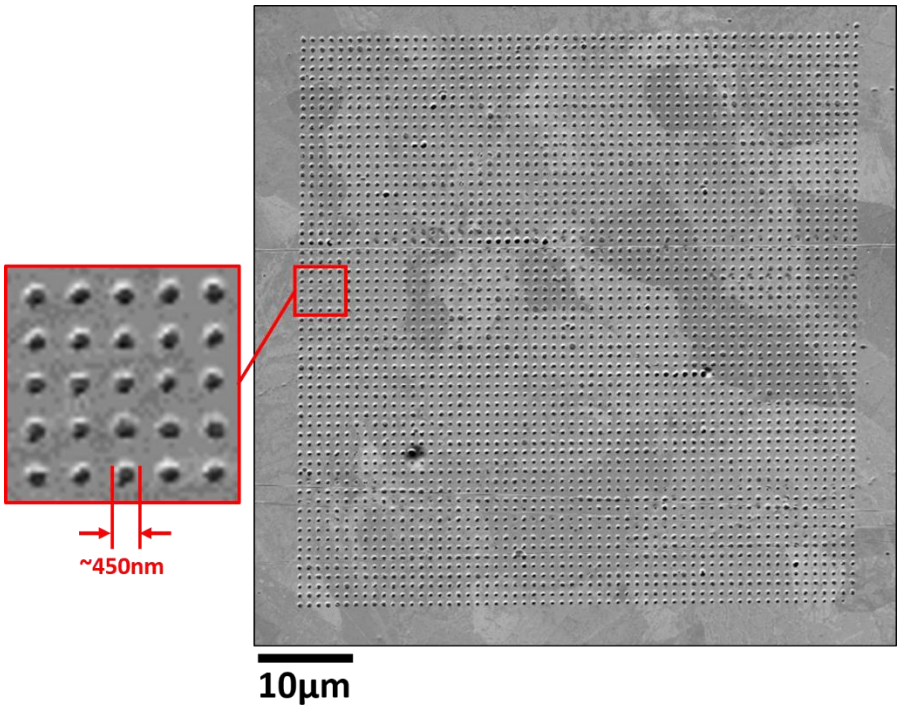

Figure 5. 2. Scanning electron microscopy (SEM) image of an area of a low carbon steel surface that has been scanned using the voltammetric hopping mode SECCM protocol. The array consists of 3600 (60 × 60 pixels^2) individual measurements, each droplet "footprint" ≈450 nm in diameter, covering an area of 72 × 72 µm.

5.4.2 Spatially-resolved potentiodynamic polarisation experiments on low carbon steel

In order to ascertain the structure-dependence of the anodic processes (iron dissolution) on low carbon steel, a 72 × 72 µm^2 (60 × 60 pixel^2) voltammetric SECCM scan was carried out. The potentiodynamic polarisation curve (only forward sweep considered, *vide supra*) obtained by averaging all scanning points (3600 total) is shown in Figure 5.3a. A simplified Pourbaix diagram for pure iron (considered to be representative of the investigated low carbon steel, see

Table 5.1) is also included in Figure 5.3b to indicate the predicted thermodynamically stable species throughout the potential sweep.[46] The low carbon steel surface is initially in a passive state (labelled as ①, Figure 5.3b) from 0.563 V vs Ag/AgCl through to *ca.* -0.24 V, where a small reduction peak (cathodic current) is observed (inset in Figure 5.3a), attributable to passive film reduction (labelled as ②, Figure 5.3b):

$$Fe_2O_3 + 6H^+ + 2e^- \rightarrow 2Fe^{2+} + 3H_2O \qquad (6)$$

The charge passed during this process was calculated to be 20 ± 2 pC, which corresponds to a thickness of ~8 ± 1 nm, assuming an Fe_2O_3 film. Following the reduction peak, in the potential range *ca.* -0.49 V to -0.94 V (active region), iron dissolution (Eq 3) is the dominant process (labelled as ③, Figure 5.3b), giving rise to large oxidation currents (peaking at ≈290 pA, which corresponds to a current density of ≈0.2 A cm^{-2}). The oxidation peak (at -0.587 V) is formed as the increasing corrosion rate resulting from the removal of the protective passive film (Eq 6) is balanced by the decreasing driving force for iron dissolution (Eq 3), as the potential is swept cathodically. Note that due to the fine tip geometry (diameter of ≈150 nm) and relatively dilute supporting electrolyte (5 mM H_2SO_4), ohmic (*iR*, where *R* is the tip resistance, calculated to be 320 MΩ, herein) drop is on the order of ≈90 mV at the oxidation peak. Although this may distort the shape of the potentiodynamic polarisation curve to an extent, it does not affect grain-dependent trends in i_{surf}, considered in detail below. Upon sweeping to potentials negative of -0.937 V, the surface current is dominated by cathodic processes (labelled as ④, Figure 5.3b), where iron re-deposition occurs (reverse of Eq 2), in addition to cathodic (electrocatalytic) processes such as the ORR, Eq 3, and (predominantly) HER, Eq 4. This behaviour is consistent with the macroscopic electrochemical response of similar iron-based materials in acidic media.[1]

Selecting four characteristic potentials (0.063, -0.547, -0.587, -1.437 V vs Ag/AgCl, labelled in Figure 5.3a), spatially-resolved i_{surf} maps are shown in Figure 2c. Comparison of Figure 5.3b with the co-located EBSD map in Figure 5.3d reveals that: (i) tens of potentiodynamic polarisation experiments (*ca.* 20 to 50) are carried out on each grain, statistically validating our inferences below; and (ii) some processes appear to be grain-dependent, while others are grain-independent, explored below. Starting in the passive domain ($E_{app} \approx 0.563$ to -0.237 V vs. Ag/AgCl, Figure 5.3b-i), the low current values in the i_{surf} map do not show discernible features related to the underlying crystal structure. Although this may suggest that the resistivity/protectiveness of the passive film is grain-independent, the i_{surf} values measured in this region are dominated by the background noise (*ca.* 2 pA peak-to-peak, detailed in the Experimental Section), and thus it is likely that any differences between the grains are too minute to detect.

In the active domain ($E_{app} \approx$ -0.487 to -0.937 V vs. Ag/AgCl, Figures 5.3d-ii and 5.3d-iii) there is a clear relationship between crystal orientation (Figure 5.3c) and the rate of iron dissolution, evidenced by grain-dependent i_{surf} values (*vide infra*). In the cathodic region (Figure 5.3b-iv), where the HER is expected to be the dominant process,[47] i_{surf} shows a weaker grain-dependence. As discussed above, the preceding anodic processes are expected to have a significant influence on the processes occurring in the cathodic region due to physical changes to the surface (*e.g.*, surface dissolution and deposition of corrosion products) and compositional changes to the surface and electrolyte (*e.g.*, the formation of soluble Fe^{2+} species within the droplet cell), and Figure 5.3b-iv is thus difficult to interpret. Note that in a companion study,[48] we have employed a potential-pulse waveform (*i.e.*, chronoamperometry) to reveal the

structure-dependence of the HER on low carbon steel in aqueous sulfuric acid (pH 2.3), and this is a better means of elucidating HER kinetics. As such, we do not consider the HER process any further here, but focus on the anodic dissolution of Fe (*vide infra*).

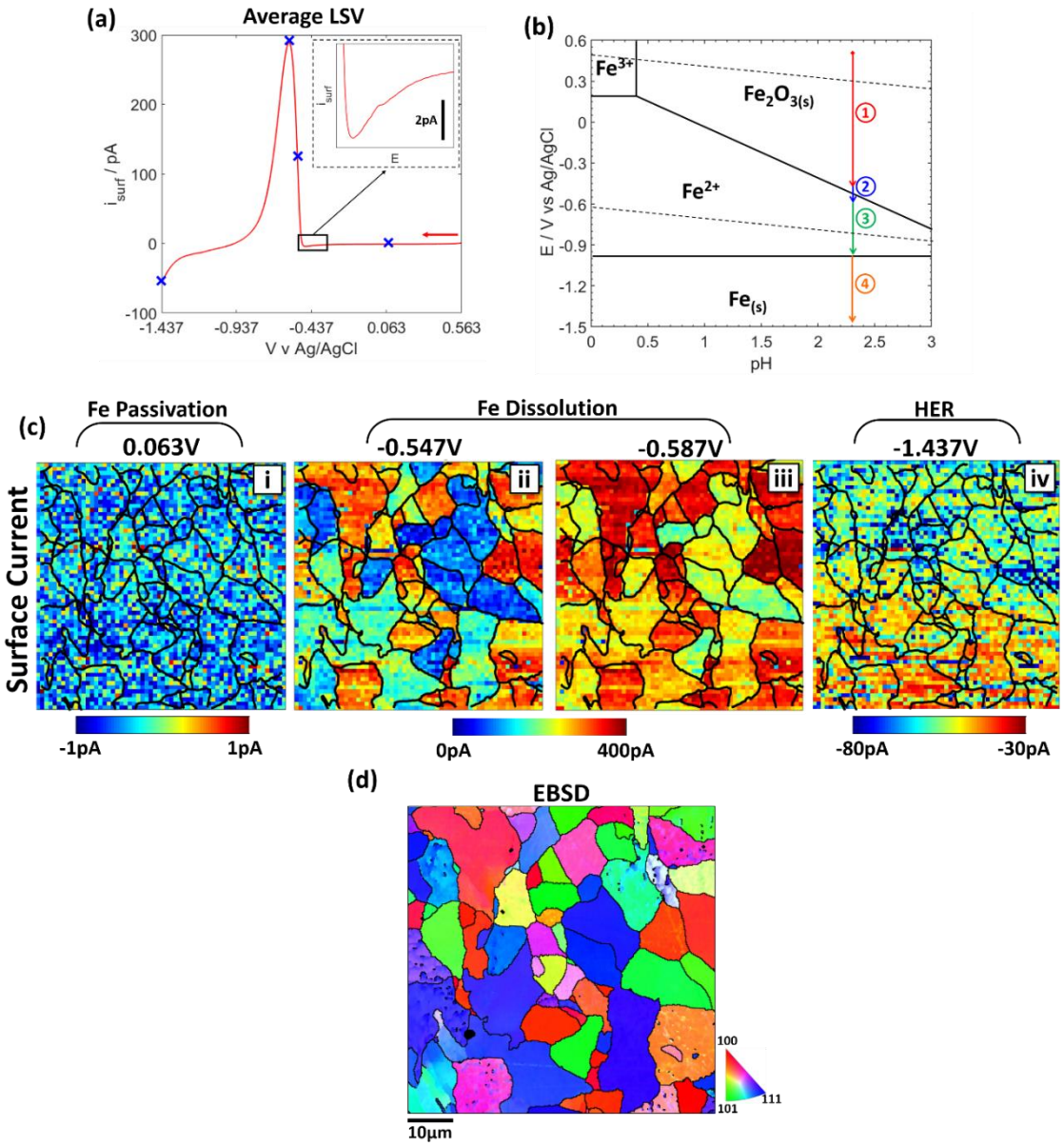

Figure 5. 3. (a) Potentiodynamic polarisation (i–E) curve (υ = 2 V s^{-1}), obtained by averaging the forward sweep of 3600 (60 × 60 $pixel^2$ covering 72 × 72 μm^2) individual measurements on a low carbon steel sample. The nanopipet was ≈150 nm in diameter and filled with 5 mM H_2SO_4. **(b)** Simplified Pourbaix diagram for Fe. Coloured arrows indicate the potential range covered by the potentiodynamic polarisation curve in (a) at pH 2.3, with the numbers on the plot correspond to the following: ① passive film formation, ② passive film reduction, ③ active iron dissolution and ④ cathodic processes (HER and ORR). **(c)** Spatially-resolved i_{surf} maps obtained at **(i)** 0.063 V **(ii)** -0.587V **(iii)** -0.547V and **(iv)** -1.437 V vs Ag/AgCl [indicated on the corresponding average i–E curve in (a)]. Note the different current scales. **(d)** Corresponding EBSD map, showing the crystallographic structure of the area scanned with SECCM in (c).

A small number of individual pixels appear to be far more active than the rest, which are labelled in Figure 5.4a and further examined (*i.e.*, pixel-resolved *i*−*E* curves shown) in detail in the Figure 5.4b. For these "active pixels", the onset potential for active dissolution is *ca.* 100 mV (95-125 mV) more positive, and the anodic peak currents are larger (312 – 836 pA) compared to the surface average *i*−*E* curve (black trace, peak current of 290 pA). Multiple processes appear to contribute to the anodic current, giving rise to a "split peak", with the process occurring at more positive potentials giving rise to unstable current fluctuations (also seen in the passive region, at $E > 0.2$ V vs Ag/AgCl). These additional processes are thought to arise from the oxidation (and dissolution) of manganese sulfide (MnS) inclusions, which has been addressed in our previous study,[31] highlighting MnS inclusions as possible initiation sites for localised corrosion. Under anodic dissolution conditions, the presence of MnS inclusions cannot be confirmed with EDS, after experiments, as the inclusions undergo partial or complete dissolution as the potential sweeps through the active region. However, SEM images after experiments (*e.g.* Figure 5.4c and 5.4d) show a larger deposit of corrosion products and/or greater damage to the surface at these "active pixel" sites.

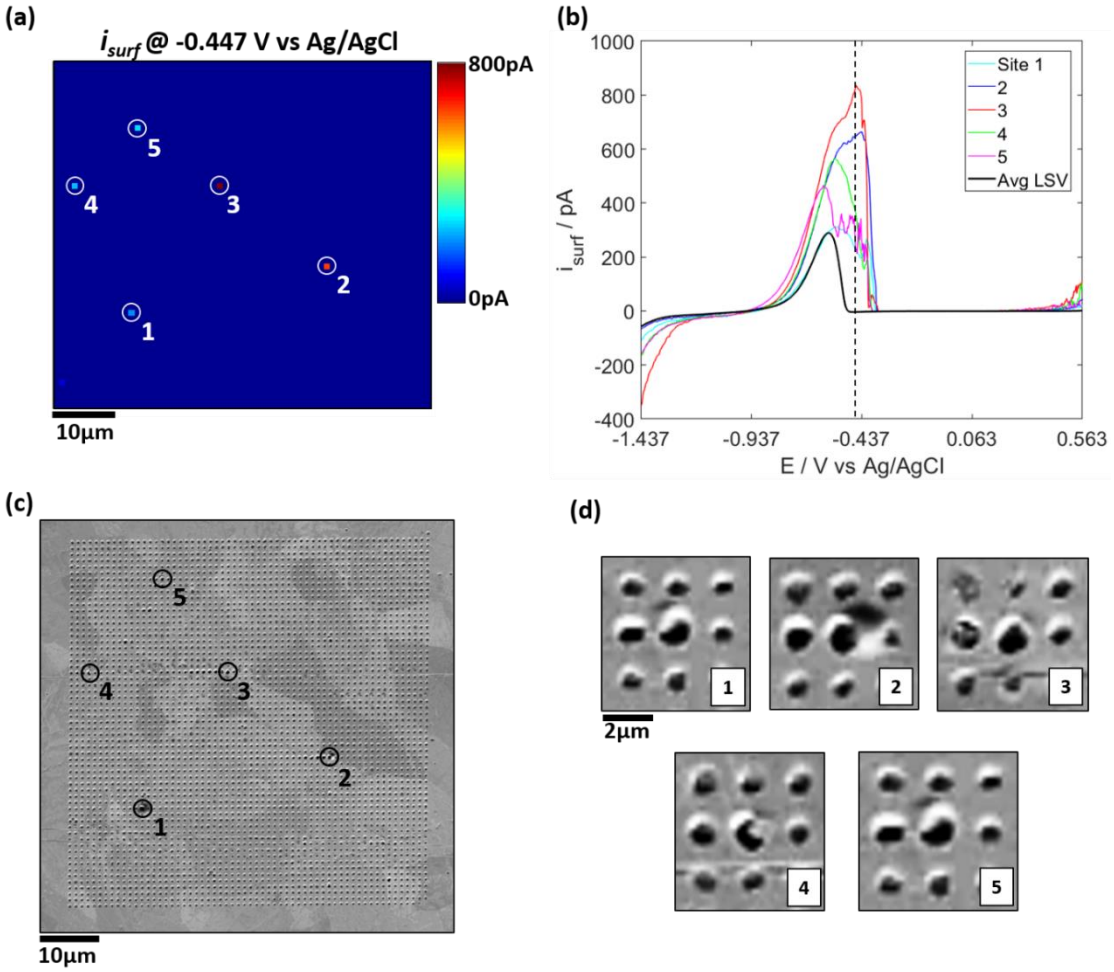

Figure 5. 4. (a) Spatially-resolved i_{surf} map obtained at a potential of -0.447 V vs Ag/AgCl QRCE using the voltammetric SECCM configuration. The i_{surf} maps comprise 3600 pixels (60 × 60 pixels^2) over a 72 × 72 µm area, obtained with a nanopipet probe of diameter ≈ 150 nm containing 5 mM H_2SO_4. **(b)** i–E curves (υ = 2 V s^{-1}) obtained from the 5 highly active pixels (coloured traces) labelled in (a) versus the average response (black trace) obtained from the 3600 pixels across the surface. **(c)** Scanning electron microscopy (SEM) image of corresponding area scanned with SECCM shown in (a). **(d)** Zoomed-in SEM images of the "active pixels" (the centre spot of each 3 × 3 array of spots) indicated in (a) and (c).

Figure 5.3b-ii convincingly shows that electrochemical iron dissolution is influenced by surface structure (*i.e.*, crystallographic orientation), which is further explored in Figure 5.5. Five characteristics of the anodic peak are considered, labelled in Figure 5.5a: the reduction pre-peak potential (V_p^{red}); oxidation peak potential (V_p^{ox}); and the oxidation peak current (i_p)

maps of which are shown in Figures 5.5b, c, and d, respectively. The charge passed during oxidation (Q^{Ox}), which is proportional to the amount of iron dissolved during oxidation and; the full width half maximum of the oxidation peak (*FWHM)*, which indicates the range of potentials over which active dissolution occurs, are also presented in Figure 5.6b, and c, respectively. Other areas of the low carbon steel surface were also mapped using the same SECCM protocol; examples of the spatially-resolved i_p maps are plotted alongside co-located EBSD maps in Figure 5.7, to highlight the reproducibility of the method.

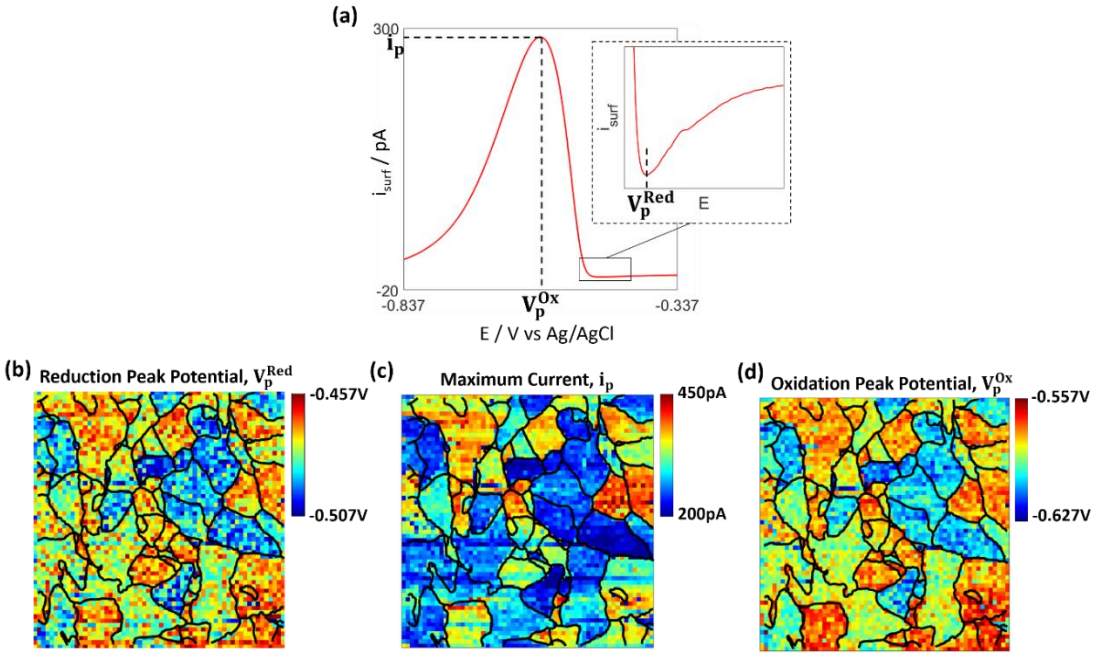

Figure 5. 5. (a) i–E curve (υ = 2 V s^{-1}), obtained by averaging the forward sweep of 3600 (60 × 60 $pixel^2$ covering 72 × 72 μm^2) individual measurements on a low carbon steel, performed in the voltammetric hopping mode SECCM configuration. The nanopipet was ≈150 nm in diameter and filled with 5 mM H_2SO_4. The reduction peak potential, V_p^{Red}, oxidation peak potential, V_p^{Ox}, and oxidation peak current, i_p, are labelled on the plot. Spatially-resolved maps of **(b)** V_p^{Red}, **(c)** i_p and **(d)** V_p^{Ox}.

The cathodic process prior to the active region (signified by V_p^{red}) is attributable to the reduction of the passive film (Eq 5), which leaves the unprotected low carbon steel surface exposed for active dissolution. In other words, V_p^{red} indicates the potential above which the

passive film is stable, or conversely, below which active dissolution will occur. Clearly, the grain-dependence of V_p^{red} indicates that the nature of the passive film, formed during the passive region of the potential sweep, varies between crystallographic facets. This may arise due to variations in the thickness and/or structure of the passive film, both of which could perceivably lead to differing film reduction behaviour. The anodic peak, the position (V_p^{ox}, Figure 5.5c), magnitude (i_p, Figure 5.5d), charge passed (Q^{Ox}, taken as the integral of the peak, Figure 5.6c), width (taken as the full width at half maximum, FWHM, Figure 5.6b) are all grain-dependent. Comparing the maps, the grains that possess passive films that are easiest to reduce (most-positive V_p^{red}, Figure 5.5b) undergo the highest rates of dissolution (highest i_p, Figure 5.5c) over the widest potential range (Figure 5.6b).

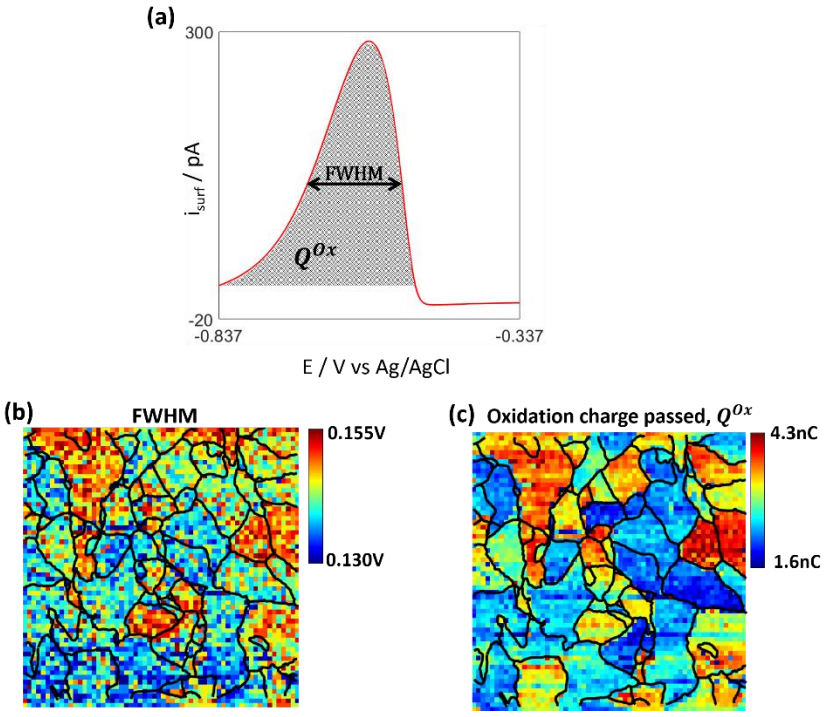

Figure 5. 6. (a) EBSD and **(b)** corresponding spatially-resolved full width at half maximum (FWHM, based on the anodic iron dissolution peak) maps, obtained from a low carbon steel surface. The maps in (b) were obtained in the voltammetric hopping mode SECCM configuration (υ = 2 V s^{-1}), with a nanopipet probe of ≈150 nm diameter containing 5 mM H_2SO_4.

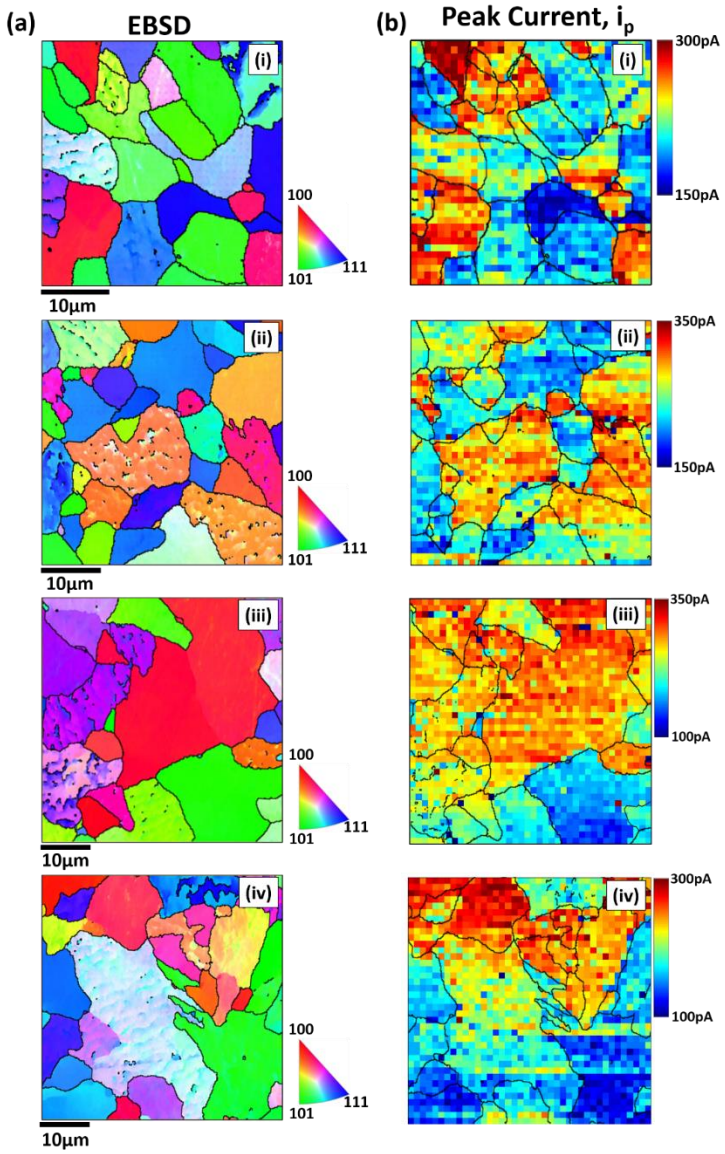

Figure 5. 7. (a) Electron backscatter diffraction (EBSD) and **(b)** corresponding spatially-resolved oxidation peak current (i_p) maps, obtained from various areas of a low carbon steel surface. The maps in (b) were obtained in the voltammetric hopping mode SECCM configuration (υ = 2 V s^{-1}), with a nanopipet probe of ≈150 nm diameter containing 5 mM H_2SO_4.

5.4.3 Grain dependent anodic iron dissolution at low carbon steel

In order to gain an insight into which grains facilitate anodic iron dissolution and further explain these dependencies, we focus on the grains of low-index crystal orientation [*i.e.*, the (100), (101) and (111) crystal facets]. All grains within 10° of the (100), (101) and (111) orientations are

shown in Figure 5.8a-i, ii and iii, respectively, and average potentiodynamic polarisation curves obtained from each of the grains are shown in Figure 5.8b. In total, 130, 264 and 365 individual measurements were taken on the (100), (101) and (111) grains, respectively. Evidently, from Figure 5.8b, the variation in the potentiodynamic polarisation curves within a family of grains [*i.e.*, compare the red curves for (100)] is much less than that between families of grains [*i.e.*, compare the red and green curves for (100) and (101), respectively], demonstrating the strong crystallographic-dependence of anodic iron dissolution. The average LSVs also show that the difference in dissolution current between grains is greater on the right hand side of the oxidation peak compared to the left hand side. In other words, sweeping the potential from positive to negative, the potential at which anodic iron dissolution initiates (*e.g.*, Figure 5.5b and 5.8b, inset) is more strongly grain-dependent than the potential at which iron dissolution ceases.

$V_{\mathrm{p}}^{\mathrm{red}}$ increases in the order (101) < (111) < (100), from which it can be inferred that the passive (oxide) film is the thinnest and/or least protective on the (100) grains. This grain-dependent film composition/structure is consistent with previous studies, where it has been shown that the oxide films electrochemically grown on the (100) and (110) crystal facets of iron have different crystallographic structures.[49] Taking i_{surf} at -0.581 V vs Ag/AgCl as an indicator of the relative rates of iron dissolution in the active region, histograms were constructed from the grain-resolved potentiodynamic polarisation curves, shown in Figure 5.5c. Note that -0.581 V vs Ag/AgCl (indicated in Figure 5.5b) was chosen to minimise the influence from the protective passive film (assumed to be completely removed at *ca.* 100 mV more negative than $V_{\mathrm{p}}^{\mathrm{red}}$) and cathodic processes. Average i_{surf} values increase in the order 218 ± 23, 252 ± 22, and 334 ± 26 pA (mean ± standard deviation) for the (101), (111) and (100) facets, respectively,

which follows the same trend as $V_{\mathrm{p}}^{\mathrm{red}}$, above. Higher values of $V_{\mathrm{p}}^{\mathrm{red}}$ and i_{surf} in the active region indicate greater corrosion susceptibility, which increases in the order: (101) < (111) < (100).

In a previous study on iron, the grain dependence of iron dissolution was studied with atomic force microscopy (AFM), where it was shown that the (100) grains exhibited the largest dissolution rate during electropolishing in acidic media at a constant current density of 0.3 A/cm^2. In a different study on iron single crystals in pH 1 sulfuric acid, it was also found that the dissolution rate for the low index planes increased in the sequence (100) > (111) > (101).[50] Our results, using a different approach, are consistent with this prior work. Furthermore in a study carried out on a light weight ferritic steel, an EDC technique revealed a critical current density (*i.e.*, maximum current during active dissolution) that was *ca.* 50% larger at (100) grains compared to the (111) orientation (compared to *ca.* 31%, herein) in 0.5 M H_2SO_4. Although the material studied herein (low carbon steel) was different to those considered,[3, 8] these studies lend weight to our observation of higher active dissolution currents on the (100) grains compared to the (101) or (111) grains.

There is much speculation in the literature as to why grains exhibit different anodic dissolution rates. For example, it has been theorised[8] that the surface density of the atoms of each grain governs corrosion susceptibility/resistance (also applied to other metals, such as magnesium[51]), where anodic metal dissolution rates decrease with increasing packing density (*i.e.*, densely packed surface atom layers 'shield' the sub-surface layers from interaction with the corrosive electrolyte). For the case of ferrite steel (*i.e.*, the structure of low carbon steel), surface atom density increases in the order 1.2×10^{15}, 1.7×10^{15} cm^{-2} and 1.9×10^{15} atoms cm^{-2} for the (100), (101) and (111) planes, respectively. While this certainly fits our observations

for the (100) grains (Figure 5.8b, red traces), such a naïve analysis cannot explain the higher rates of dissolution observed at the (111) compared to the (101) planes (Figure 5.8b, blue and green traces, respectively). This suggests that there are likely other factors that affect the active dissolution rate of the individual grains, explored further below.

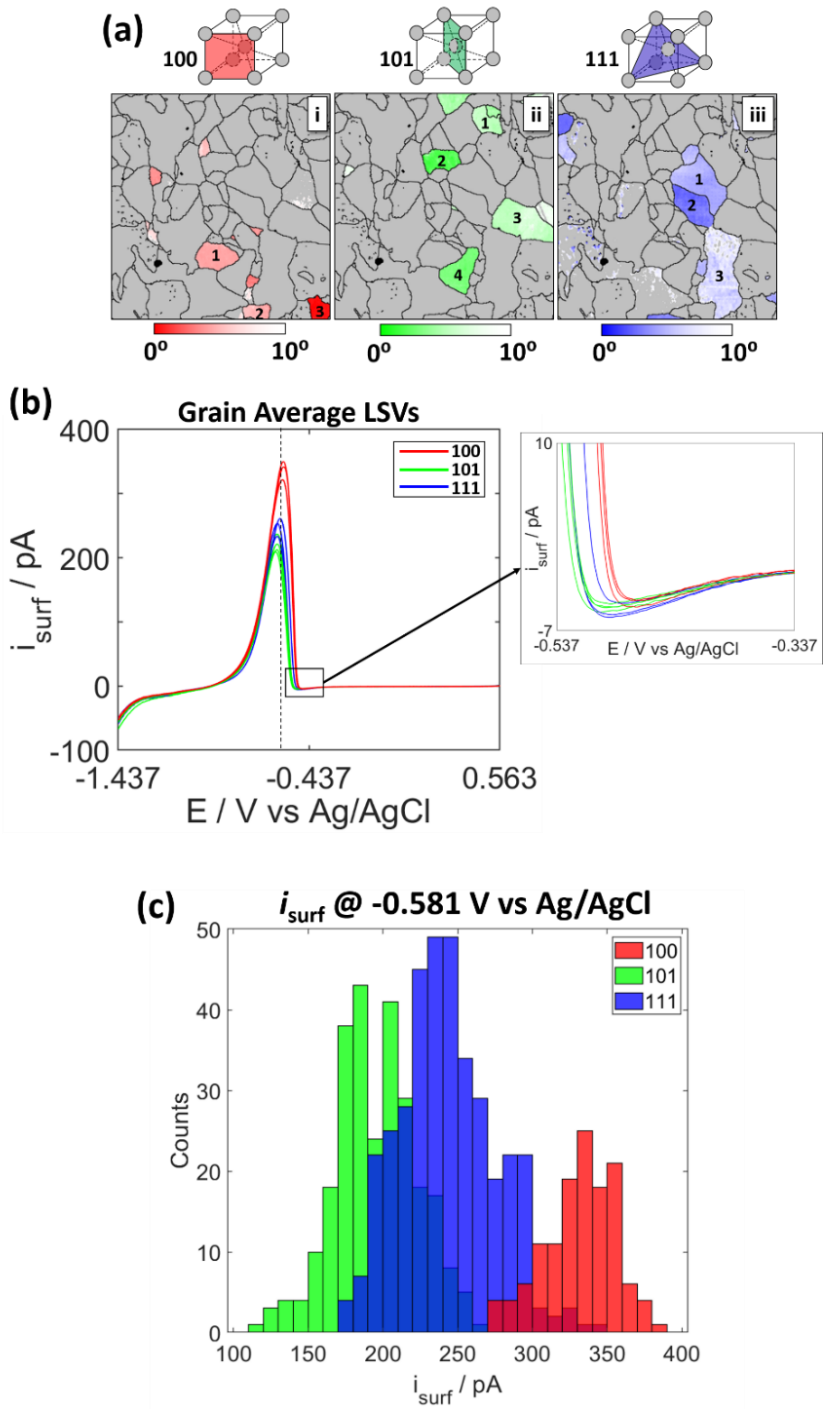

Figure 5. 8. (a) EBSD maps identifying the grains that have crystal orientations within 10° of the low index orientations, **(i)** (100), **(ii)** (101) and **(iii)** (111). **(b)** *i*−*E* curve (υ = 2 V s^{-1}) obtained by averaging the individual measurements performed on each of the low-index orientations [red = (100), blue = (111) and green = (101)], using the voltammetric hopping mode SECCM configuration. The nanopipette was ≈150 nm in diameter and filled with 5 mM H_2SO_4. **(c)** Distribution of i_{surf} measured at -0.581 V vs Ag/AgCl [indicated by dashed line on (b)] on each of the low index orientations.

5.4.4 STEM inspection of individual SECCM scanning sites

To visualise the physical changes to the low carbon steel that occur during SECCM-induced anodic corrosion, focused ion beam (FIB) milling was used to extract a section of the surface containing individual scanning sites (*i.e.*, individual SECCM "pixels"). Note that a pipet probe of diameter ≈ 2 μm was used in this particular experiment to enable the more ready preparation of the cross-section. The step-by-step guide of the FIB milling procedure is shown in Figure 5.9a and is also described in detail in the experimental section. Briefly, prior to FIB milling, a layer of platinum was deposited on top of the area of interest to provide protection from the FIB, shown in Figure 5.9a-(i). The region around the area of interest was milled [Figure 5.9a-(ii) and (iii)] and then removed with a tungsten rod [Figure 5.9a-(iv)] before being attached to a copper TEM grid. The extract was then thinned to electron-beam transparency using the FIB [Figure 5.9a-(v)], exposing a cross-section of the individual SECCM measurement sites, as shown in Figure 5.9b.

An STEM analysis of the cross-sectional structure and composition of a typical area where SECCM measurements were made is shown in Figure 5.9c. There is a deep recess relative to the surrounding areas resulting from the removal of Fe^{2+} during the active dissolution process (Eq 2). Corrosion products are re-deposited over the top of this site (highlighted with a dotted line, thickness of *ca.* 140 nm), producing a layer that contains iron, sulfur and oxygen (electron dispersive spectroscopy, EDS). The EDS map for platinum is included to identify the protective layer from the FIB milling procedure. These corrosion products are likely comprised of iron (II) and iron (III) oxysulfate species, as calculated with the HYDRA and MEDUSA software, which

consider the thermodynamically stable (equilibrium) solid products under a given set of experimental conditions (further details can be found in the Experimental Section).

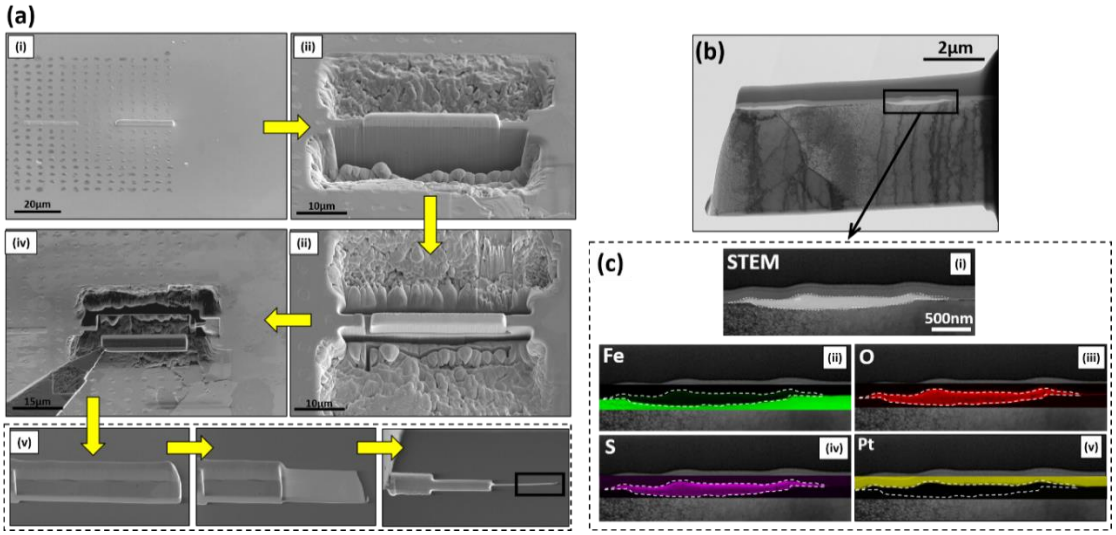

Figure 5. 9. (a) Step-by-step outline of the focussed ion beam (FIB) milling procedure used to extract single SECCM droplet "footprint" sites for cross-sectional analysis. **(i)** Covering the scanning site of interest with a protective platinum layer. **(ii)** and **(iii)** Ga ion beam milling around selected section. **(iv)** Removal of the extract from the low carbon steel matrix. **(v)** Thinning of the extracted section. **(b)** Cross-sectional scanning transmission electron microscopy (STEM) image of the extract. **(c)** (i) STEM image of the cross section of a droplet "footprint" (nanopipet diameter = 2 µm in this experiment), accompanied by corresponding EDS analysis for **(ii)** iron, **(iii)** oxygen **(iv)** sulphur, and **(v)** platinum.

5.4.5 Density functional theory calculations

To explore the possible factors governing the grain-dependent iron dissolution rates, density functional theory (DFT) calculations were performed that consider the binding energies of iron atoms at the surface of a lattice. In brief, we consider the thermodynamic properties for each of the low index crystal planes by calculating the energy required to remove (ionise) one monolayer of iron using the following (simplified) equation:

$$E_{\mathrm{Fe-Fe}} = \frac{1}{N}(E_n - E_{(n-1)} - E_{\mathrm{Fe^{2+}}}) \quad (7)$$

where $E_{\mathrm{Fe\text{-}Fe}}$ represents the binding energy normalised by the number of atoms for a monolayer, E_{n} is the total energy stored in n monolayers of iron atoms, $E_{(\mathrm{n\text{-}1})}$ is the surface energy after removing one monolayer, $E_{\mathrm{Fe^{2+}}}$ is the energy of an Fe^{2+} ion liberated from the surface and *N* is the number of atoms per monolayer. Further details of the calculations can be found in the Experimental Section.

The measured i_{surf} values (at -0.581 V), 218, 252 and 334 pA scale with the calculated $E_{\mathrm{Fe\text{-}Fe}}$ values, -24.253, -24.237 and -24.216 eV for the 101, 111 and 100 planes, respectively (plot shown in Figure 5.10). This means that crystal orientations where Fe atoms are thermodynamically easier to remove (and ionise), evidenced by less negative $E_{\mathrm{Fe\text{-}Fe}}$ values, give rise to higher active iron dissolution rates, evidenced by larger i_{surf} values at active potentials (Figure 5.5). Note that the convergence error for each calculation was ±0.001 eV showing that despite the very subtle differences in energy between orientations, the calculations were sufficiently precise to confirm any trends between the dissolution behaviour of different crystal planes. Although it is consistent with the results herein, it must be noted that the DFT performed is for a simplified system (*i.e.*, a plane of Fe atoms on a lattice, undergoing uniform dissolution/corrosion). The influence of anions (as well as other species present in solution) is not explicitly considered, which are known to influence the corrosion behaviour of steel, the most well-known example being Cl^- ions inducing localised (pitting) corrosion [52]. In reality, the grain-dependent corrosion susceptibility/resistance of low carbon steel is likely to be dependent on solution conditions[2] (*i.e.*, pH, electrolyte composition, *etc.*) which, as demonstrated herein,

is amenable to analysis through SECCM, again highlighting the potential of this technique in corrosion research.

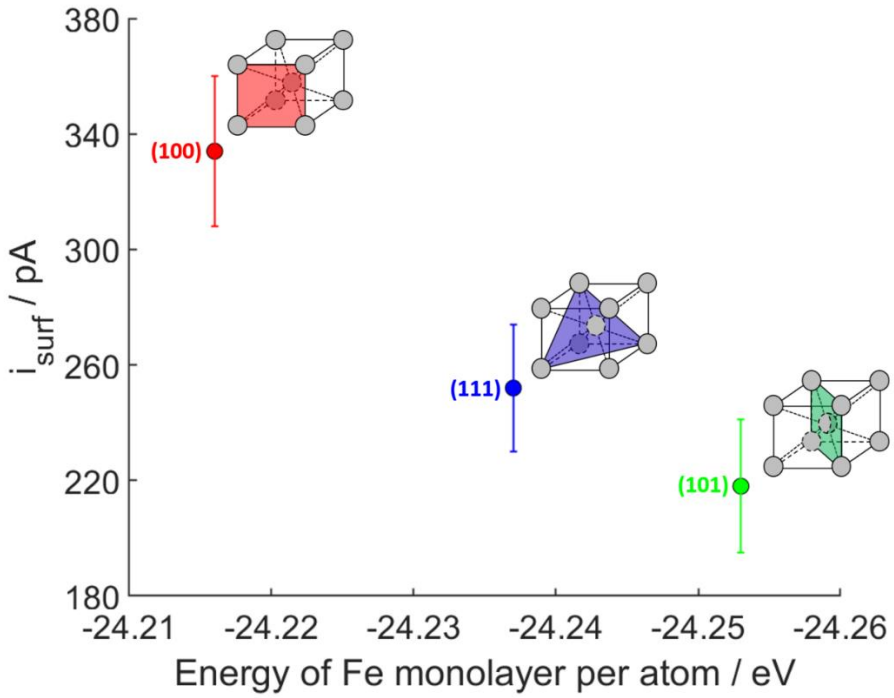

Figure 5. 10. Plot of i_{surf} measured at -0.581 V vs Ag/AgCl for each low index crystal orientations (100, 101 and 111) of low carbon steel in 5 mM H_2SO_4, against the energy required to remove (and ionise) one monolayer of iron from each of the low index surface per atom removed.

5.5 Conclusions

In this study, we have advanced the understanding of the dependence of anodic iron dissolution on the underlying crystallographic structure of low carbon steel in aqueous sulfuric acid (pH 2.3). This was achieved through the combination of local potentiodynamic polarisation experiments from SECCM (>100 measurements analysed on each low-index plane) with co-located structural information from EBSD, which revealed grain-dependent anodic iron dissolution rates that increase in the order (100) > (111) > (101). Local cross-sectional analysis

with STEM imaging revealed a build-up of corrosion products within the dissolved area of an individual droplet "footprint" site, which was suggested to comprise insoluble iron oxysulfate species, formed during the active dissolution of iron. The grain-dependent anodic dissolution rates derived from SECCM were rationalized through complementary DFT calculations, which showed that the rate of iron dissolution, and hence corrosion susceptibility, increases with increasing (*i.e.*, less-negative) $E_{\text{Fe-Fe}}$ values (*i.e.*, the energy required to remove a monolayer of iron from the surface of a lattice). Overall, this study further positions SECCM as an effective tool for analysing the structure-dependent corrosion-related behaviour of metal alloys at the nanoscale, particularly when combined with complementary structural characterisation (*e.g.*, EBSD and STEM) and computational analysis (*e.g.*, DFT calculations).

5.6 References

1. Feser, R., Chapter 2.1 Uniform Corrosion of Metals in Acid, Neutral and Alkaline Electrolytes. In *Corrosion and Oxide Films*, Stratmann, M.; Frankel, G., Eds. Wiley-VCH: Germany, 2003; Vol. 4, pp 67-107.

2. Schreiber, A.; Schultze, J. W.; Lohrengel, M. M.; Kármán, F.; Kálmán, E., Grain Dependent Electrochemical Investigations on Pure Iron in Acetate Buffer Ph 6.0. *Electrochimica Acta* **2006**, *51*, 2625-2630.

3. Schreiber, A.; Rosenkranz, C.; Lohrengel, M. M., Grain-Dependent Anodic Dissolution of Iron. *Electrochimica Acta* **2007**, *52*, 7738-7745.

4. Seo, M.; Chiba, M., Nano-Mechano-Electrochemistry of Passive Metal Surfaces. *Electrochimica Acta* **2001**, *47*, 319-325.

5. Chiba, M.; Seo, M., Mechanoelectrochemical Properties of Passive Iron Surfaces Evaluated by an in Situ Nanoscratching Test. *Journal of The Electrochemical Society* **2003**, *150*, B525-B525.

6. Shahryari, A.; Szpunar, J. A.; Omanovic, S., The Influence of Crystallographic Orientation Distribution on 316lvm Stainless Steel Pitting Behavior. *Corrosion Science* **2009**, *51*, 677-682.

7. Krawiec, H.; Szklarz, Z., Combining the Electrochemical Microcell Technique and the Electron Backscatter Diffraction Method to Study the Electrochemical Behaviour of Polycrystalline Aluminium in Sodium Chloride Solution. *Electrochimica Acta* **2016**, *203*, 426-438.

8. Lill, K. A.; Hassel, A. W.; Frommeyer, G.; Stratmann, M., Scanning Droplet Cell Investigations on Single Grains of a Fealcr Light Weight Ferritic Steel. *Electrochimica Acta* **2005**, *51*, 978-983.

9. Oltra, L., Local Electrochemical Methods in Corrosion Research. In *Local Probe Techniques for Corrosion Research*, 2007; pp 1-11.

10. Payne, N. A.; Stephens, L.; Mauzeroll, J., The Application of Scanning Electrochemical Microscopy to Corrosion Research. *Corrosion* **2017**, *73*, 759-780.

11. Amemiya, S.; Bard, A. J.; Fan, F. R. F.; Mirkin, M. V.; Unwin, P. R., Scanning Electrochemical Microscopy. *Analytical Chemistry* **2008**, *1*, 95-131.

12. Böhni, H.; Suter, T.; Schreyer, A., Micro- and Nanotechniques to Study Localized Corrosion. *Electrochimica Acta* **1995**, *40*, 1361-1368.

13. Suter, T.; Böhni, H., A New Microelectrochemical Method to Study Pit Initiation on Stainless Steels. *Electrochimica Acta* **1997**, *42*, 3275-3280.

14. Webb, E. G.; Alkire, R. C., Pit Initiation at Single Sulfide Inclusions in Stainless Steel. *Journal of The Electrochemical Society* **2002**, *149*, B286-B286.

15. Andreatta, F.; Lohrengel, M. M.; Terryn, H.; De Wit, J. H. W., Electrochemical Characterisation of Aluminium Aa7075-T6 and Solution Heat Treated Aa7075 Using a Micro-Capillary Cell. *Electrochimica Acta* **2003**, *48*, 3239-3247.

16. Birbilis, N.; Buchheit, R. G., Electrochemical Characteristics of Intermetallic Phases in Aluminum Alloys. *Journal of The Electrochemical Society* **2005**, *152*, B140-B140.

17. Andreatta, F.; Fedrizzi, L., The Use of the Electrochemical Micro-Cell for the Investigation of Corrosion Phenomena. *Electrochimica Acta* **2016**, *203*, 337-349.

18. Ebejer, N.; Güell, A. G.; Lai, S. C. S.; McKelvey, K.; Snowden, M. E.; Unwin, P. R., Scanning Electrochemical Cell Microscopy: A Versatile Technique for Nanoscale Electrochemistry and Functional Imaging. *Annual Review of Analytical Chemistry* **2013**, *6*, 329-51.

19. Bentley, C. L.; Kang, M.; Unwin, P. R., Scanning Electrochemical Cell Microscopy: New Perspectives on Electrode Processes in Action. *Current Opinion in Electrochemistry* **2017**, *6*, 23-30.

20. Bentley, C. L.; Edmondson, J.; Meloni, G. N.; Perry, D.; Shkirskiy, V.; Unwin, P. R., Nanoscale Electrochemical Mapping. *Analytical Chemistry* **2019**, *91*, 84-108.

21. Bentley, C. L.; Kang, M.; Maddar, F.; Li, F.; Walker, M.; Zhang, J.; Unwin, P. R., Electrochemical Maps and Movies of the Hydrogen Evolution Reaction on Natural Crystals of Molybdenite (Mos 2): Basal Vs. Edge Plane Activity. *Chemical Science* **2017**, *8*, 6583-6593.

22. Unwin, P. R.; Güell, A. G.; Zhang, G., Nanoscale Electrochemistry of Sp2 Carbon Materials: From Graphite and Graphene to Carbon Nanotubes. *Accounts of Chemical Research* **2016**, *49*, 2041-2048.

23. Aaronson, B. D. B.; Chen, C. H.; Li, H.; Koper, M. T. M.; Lai, S. C. S.; Unwin, P. R., Pseudo-Single-Crystal Electrochemistry on Polycrystalline Electrodes: Visualizing Activity at Grains and Grain Boundaries on Platinum for the Fe^{2+}/Fe^{3+} Redox Reaction. *Journal of the American Chemical Society* **2013**, *135*, 3873-3880.

24. Wang, Y.; Gordon, E.; Ren, H., Mapping the Nucleation of H2 Bubbles on Polycrystalline Pt Via Scanning Electrochemical Cell Microscopy. *J Phys Chem Lett* **2019**, *10*, 3887-3892.

25. Mariano, R. G.; McKelvey, K.; White, H. S.; Kanan, M. W., Selective Increase in Co_2 Electroreduction Activity at Grain-Boundary Surface Terminations. *Science* **2017**, *358*, 1187-1192.

26. Bentley, C. L.; Andronescu, C.; Smialkowski, M.; Kang, M.; Tarnev, T.; Marler, B.; Unwin, P. R.; Apfel, U. P.; Schuhmann, W., Local Surface Structure and Composition Control the Hydrogen Evolution Reaction on Iron Nickel Sulfides. *Angewandte Chemie - International Edition* **2018**, *57*, 4093-4097.

27. Bentley, C. L.; Kang, M.; Unwin, P. R., Nanoscale Structure Dynamics within Electrocatalytic Materials. *Journal of the American Chemical Society* **2017**, *139*, 16813-16821.

28. Bentley, C. L.; Unwin, P. R., Nanoscale Electrochemical Movies and Synchronous Topographical Mapping of Electrocatalytic Materials. *Faraday Discussions* **2018**, *210*, 365-379.

29. Hill, J. W.; Hill, C. M., Directly Mapping Photoelectrochemical Behavior within Individual Transition Metal Dichalcogenide Nanosheets. *Nano Lett* **2019**, *19*, 5710-5716.

30. Tao, B.; Yule, L. C.; Daviddi, E.; Bentley, C. L.; Unwin, P. R., Correlative Electrochemistry-Microscopy of Li-Ion (De)Intercalation at Series of Individual Limn2o4 Particles. *Angewandte Chemie International Edition* **2019**, *58*, 4606-4611.

31. Yule, L. C.; Bentley, C. L.; West, G.; Shollock, B. A.; Unwin, P. R., Scanning Electrochemical Cell Microscopy: A Versatile Method for Highly Localised Corrosion Related Measurements on Metal Surfaces. *Electrochimica Acta* **2019**, *298*, 80-88.

32. Hudd, R. C., Sheet Steel: Low Carbon. In *Encyclopedia of Materials: Science and Technology*, 2nd ed.; 2001; pp 8456-846.

33. Sherif, E.-S. M.; Abbas, A. T.; Halfa, H.; El-Shamy, A. M., Corrosion of High Stength Seel in Concentrated Sulfuric Acid Pickling Solutions and Its Inhibition by 3-Amino-5-Mercapto-1,2,3-Triazole. *International Journal of Electrochemical Science* **2015**, *10*, 1777-1791.

34. Puigdomenech, I. Hydra and Medusa Software. https://www.kth.se/che/medusa.

35. Giannozzi, P., et al., Quantum Espresso: A Modular and Open-Source Software Project for Quantum Simulations of Materials. *Journal of Physics: Condensed Matter* **2009**, *21*, 395502.

36. Kohn, W.; Sham, L. J., Self-Consistent Equations Including Exchange and Correlation Effects. *Physical Review* **1965**, *140*, A1133-A1138.

37. Vanderbilt, D., Soft Self-Consistent Pseudopotentials in a Generalized Eigenvalue Formalism. *Physical Review B* **1990**, *41*, 7892-7895.

38. Dal Corso, A., Pseudopotentials Periodic Table: From H to Pu. *Computational Materials Science* **2014**, *95*, 337-350.

39. Monkhorst, H. J.; Pack, J. D., Special Points for Brillouin-Zone Integrations. *Physical Review B* **1976**, *13*, 5188-5192.

40. Martyna, G. J.; Tuckerman, M. E., A Consistent and Accurate Ab Initio Parametrization of Density Functional Dispersion Correction (Dft-D) for the 94 Elements H-Pu. *The Journal of Chemical Physics* **2010**, *132*, 154104.

41. Andreussi, O.; Dabo, I.; Marzari, N., Revised Self-Consistent Continuum Solvation in Electronic-Structure Calculations. *The Journal of Chemical Physics* **2012**, *136*, 064102.

42. Giannozzi, P., et al., Advanced Capabilities for Materials Modelling with Quantum Espresso. *Journal of Physics: Condensed Matter* **2017**, *29*.

43. Vanderbilt, D.; Louie, S. G., Total Energies of Diamond (111) Surface Reconstructions by a Linear Combination of Atomic Orbitals Method. *Physical Review B* **1984**, *30*, 6118-6130.

44. Trani, F.; Ninno, D.; Cantele, G.; Iadonisi, G.; Hameeuw, K.; Degoli, E.; Ossicini, S., Screening in Semiconductor Nanocrystals:Ab Initioresults and Thomas-Fermi Theory. *Physical Review B* **2006**, *73*.

45. Billeter, S. R.; Turner, A. J.; Thiel, W., Linear Scaling Geometry Optimisation and Transition State Search in Hybrid Delocalised Internal Coordinates. *Physical Chemistry Chemical Physics* **2000**, *2*, 2177-2186.

46. Pourbaix, M., *Atlas of Electrochemical Equilibria in Aqueous Solutions. Iv. Establishment and Interpretation of Potential-Ph Equilibrium Diagrams*, 1st ed.; Pergamon Press: London, 1966, p 307-321.

47. McCafferty, E., *Introduction to Corrosion Science*; Springer: London, 2010.

48. Yule, L. C.; Bentley, C. L.; Shkirskiy, V.; Aarons, J.; West, G.; Shollock, B. A.; Unwin, P. R., Nanoscale Active Sites for the Hydrogen Evolution Reaction on Low Carbon Steel. *Journal of Physical Chemistry C* **2019**, *Accepted*, xxxx-xxxx.

49. Davenport, A. J.; Oblonsky, L. J.; Ryan, M. P.; Toney, M. F., The Structure of the Passive Film That Forms on Iron in Aqueous Environments. *Journal of The Electrochemical Society* **2000**, *147*, 2162-2173.

50. Fushimi, K.; Miyamoto, K.; Konno, H., Anisotropic Corrosion of Iron in Ph 1 Sulphuric Acid. *Electrochimica Acta* **2010**, *55*, 7322-7327.

51. Liu, M.; Qiu, D.; Zhao, M.-C.; Song, G.; Atrens, A., The Effect of Crystallographic Orientation on the Active Corrosion of Pure Magnesium. *Scripta Materialia* **2008**, *58*, 421-424.

52. Angst, U.; Elsener, B.; Larsen, C. K.; Vennesland, Ø., Chloride Induced Reinforcement Corrosion: Rate Limiting Step of Early Pitting Corrosion. *Electrochimica Acta* **2011**, *56*, 5877-5889.

CHAPTER 6

Microstructural Control of the Absorption of Hydrogen into Polycrystalline Palladium

6.1 Abstract

Due to the negative consequences of absorbed hydrogen on the mechanical performance of metals, steels are often designed so that the ingress of hydrogen is minimised. Understanding how microstructural features of metals, such as grain orientations and grain boundaries, influence the rate at which hydrogen is absorbed into a metal would be extremely useful in the design of hydrogen resistant alloys. In this study, scanning electrochemical cell microscopy (SECCM) is employed to perform spatially-resolved cyclic voltammetry to study the influence of microstructure on the hydrogen absorption reaction on polycrystalline palladium foil (considered the model metal for the study of hydrogen absorption) in 0.5 M H_2SO_4. By combining SECCM with electron backscatter diffraction (EBSD), a clear relationship between the crystal orientation and the rate of hydrogen absorption is revealed. Grains that were closest to the low index orientations (*i.e.* (100), (101), and (111)), facilitated the lowest rates of hydrogen absorption, whereas grains of high index orientation (*e.g.* (411)) promoted higher rates. Enhanced hydrogen absorption was also detected at grain boundaries, however it was noted that this was likely due to the deformation induced adjacent to the boundary as a result of the annealing process.

6.2 Introduction

The absorption of hydrogen is known to adversely affect the mechanical properties of steels.[1] As shown in Figure 6.1, Hydrogen atoms can adsorb onto metals (Eq. 1) when in the presence of H_2 or H^+ (gas or in solution). Whilst some of the adsorbed hydrogen desorbs from the surface as H_2 (Eq. 2), some of the hydrogen is absorbed and diffuses into the metal (Eq. 3), occupying interstitial sites in within the crystal lattice.[2] This can reduce the ductility of the metal making it brittle and at risk from cracking when subject to stress.[3] This process is often referred to as hydrogen embrittlement,[4] and due to the industrial implications, the absorption of hydrogen into steels has attracted significant attention.[5-7] One particular area of interest has involved modifying the microstructure of steels to reduce the affinity to hydrogen, including the engineering of grain boundaries and the manipulation of texture. For example, steels with higher grain boundary density have been shown to promote the diffusion of hydrogen,[8] whilst varying levels of hydrogen permeation have been measured between different crystal phases.[9]

$$H^+ + e^- \rightarrow H_{ads} \qquad (1)$$

$$H_{ads} + H_{ads} \rightarrow H_2 \qquad (2)$$

$$H_{ads} \rightarrow H_{abs} \qquad (3)$$

Palladium is considered the model metal to study the hydrogen absorption reaction, due to the high solubility and the rapid entry kinetics of hydrogen into palladium.[10-11] It also possesses the desired properties for hydrogen storage, as palladium can form hydrides (a safe form of stored hydrogen) in ambient conditions.[12] For these reasons, hydrogen absorption on palladium has been frequently studied, particularly in the field of palladium nanomaterials.[13] Considerable effort has been put into understanding and engineering the ideal nanomaterial

morphology for fast hydrogen uptake and release. For example, there have been a number of studies that have focussed on the performance of different crystal facets of palladium nanoparticles.[14-16]

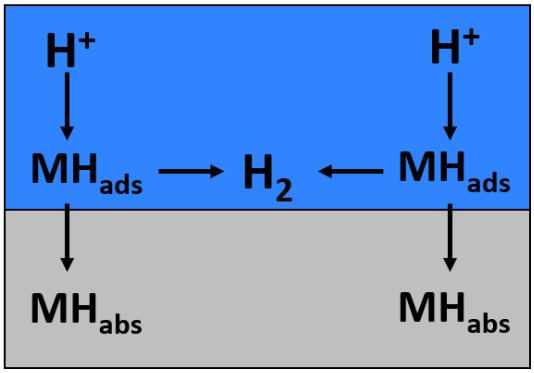

Figure 6. 1. Diagram showing the adsorption and subsequent absorption of hydrogen into a metal.

In this study, we employ scanning electrochemical cell microscopy (SECCM),[17-18] a recent addition to the electrochemical droplet cell (EDC) family, to perform nano/microscale cyclic voltammetry on polycrystalline palladium in the presence of 0.5 M H_2SO_4. SECCM utilises a droplet, formed at the end of a laser pulled nanopipet, to immerse (nanoscale) areas of a working electrode surface. By combining SECCM with electron backscatter diffraction (EBSD), this study investigates the influence of crystal orientation and grain boundaries on the surface controlled kinetics of hydrogen absorption. Due to the high resolution capabilities of SECCM, multiple measurements are possible on individual grains enabling statistical validation of any grain dependent trends, and as previously demonstrated,[19] the small working electrode area enables the probing of individual grain boundaries.

6.3 Experimental

6.3.1 Electrode materials and chemicals

The Palladium foil of 0.6 mm thickness and with dimensions of 10×10 mm (Goodfellow, U.K., 99.95%), was polished on a polishing cloth (TexMat C, Buehler, U.S.A) with a polishing machine (AutoMet 3000 Pro. Buehler, U.S.A.) using 9 μm, 3 μm, and 1μm polishing suspensions (MetaDi Supreme Diamond, Buehler, U.S.A.). The final polish was performed on a different cloth (ChemoMet, Buehler, U.S.A.) with a 0.05 μm polishing suspension (MaterPrep Alumina, Buehler, U.S.A). The polished palladium foil was washed with soapy water and deionised water to remove contamination from polishing suspensions before being blown dry. The Pd foil was then flame annealed with a butane torch flame and quenched in deionised water. Between experiments, the Pd sample was stored in a vacuum.

The chemical composition of the low carbon steel substrate is detailed in Table 6.1. The sample was mounted in a carbon based resin (KonductoMet, Buehler, U.S.A.) with a mounting press (SimpliMet, Buehler, U.S.A.). The sample was polishing with a polishing cloth (TriDent, Bueher, U.S.A.) with the same polishing suspensions used for the palladium sample. A 0.05 μm polishing suspension (MasterPrep, Alumina, Buehler, U.S.A.) was used with a different cloth (MicroCloth, Buehler, U.S.A.) for the final stage of polishing before the sample was cleaned using the same procedure as used for the Pd sample.

Sulfuric acid (H_2SO_4, Merck, 96%) was used as supplied and diluted with ultra-pure deionised water (Integra HP, Purite, U.K.) with a resistivity of 18.2 MΩ·cm at 25ºC. The Ag/AgCl quasi reference counter electrode (QRCE) was prepared by anodising 0.25mm

diameter annealed Ag wire (Goodfellow, U.K., 99.99%) in saturated KCl solution, which has previously shown long-term stability.[20]

Table 6. 1. Chemical composition of the low carbon steel determined using energy dispersive X-ray spectroscopy.

%	C	Mn	Si	Cr	Al	P	S	Cu
Low Carbon Steel	**0.05**	**0.3**	**<0.03**	**0.06**	**0.03**	**<0.02**	**<0.02**	**0.04**

6.3.2 Surface characterisation

Scanning electron microscopy (SEM) and EBSD was performed with a Zeiss SUPRA FE-SEM (Zeiss, Germany), equipped with a Nordlys EBSD detector (Oxford Instrument, U.K.). EBSD mapping was carried out with an acceleration voltage of 20 keV with the sample tilted 70º to the detector. The EBSD data was processed using HKL CHANNEL5 software (Tango, Oxford Instruments, U.K.).

To help visualise the orientation of the grains (measured using EBSD) relative to each of the low index orientations (100, 101, and 111), plots for the average orientation of individual grains were created. The Euler angles (Φ, φ_1, φ_2), that define the orientation of a plane, were used to calculate the Miller indices (*hkl*) for each grain with the use of Equations 4, 5, and 6.

$$h = \sin(\Phi) \cdot \sin(\varphi_2) \qquad (4)$$

$$k = \sin(\Phi) \cdot \cos(\varphi_2) \qquad (5)$$

$$l = \cos(\Phi) \qquad (6)$$

Using the Millar indices, the deviation, θ, of the orientation of each grain (*hkl)* from each low index plane ($h^*k^*l^*$) was calculated using Equation 7.

$$\cos(\theta) = \frac{hh^* + kk^* + ll^*}{\sqrt{h^2 + k^2 + l^2} \cdot \sqrt{h^{*2} + k^{*2} + l^{*2}}} \qquad (7)$$

Using the low index planes as reference points, the orientation of a plane can be plotted in a three dimensional plot where each of the axis correspond to the deviation angle (θ) from each low index plane. All orientations sit on a hyperbolic plane that passes through the coordinates of each of the low index orientations, which can be projected onto a 2D plane, resulting in a convenient method of comparing crystal orientations.

6.3.3 Macroscale electrochemical measurements

Cyclic voltammetry was performed on palladium wire of thickness 0.25mm (Goodfellow, U.K., 99.95%) with a potentiostat (Gamry, U.K.). A commercial Ag/AgCl reference electrode (3.4 M KCl, eDAQ, Australia) and annealed platinum wire were used as a reference and counter electrode respectively.

6.3.4 SECCM configuration

The single channel SECCM configuration (schematic shown in Figure 6.2a) was adopted in this study, as utilised previously.[21] A nanopipette, laser pulled from borosilicate capillaries (Harvard Apparatus, U.S.A.), was filled with 0.5 M H_sSO_4 forming a droplet at the tip of the nanopipette. The Ag/AgCl QRCE was inserted into the electrolyte in the pipette. The nanopipette was mounted on a *z*-piezoelectric positioner (P-753.2 LISA. PhysikInstrumente, Germany) and positioned above the palladium foil sample using micropositioners. The sample was mounted on a *xy*-piezoelectric positioner (P-621.2 PIHera, PhysikInstrumente). As the nanopipette was approached to the surface during a scan a potential, E_{app}, was applied between the QRCE and the sample so when the droplet made contact with the surface a direct current, i_{surf}, would flow

between the two electrodes. This was used as a feedback signal to halt the approach. For measurements under argon, the sample was enclosed within a custom built environmental cell, as shown in Figure 6.2b. An argon flow rate of 60 cm^3/min was used.

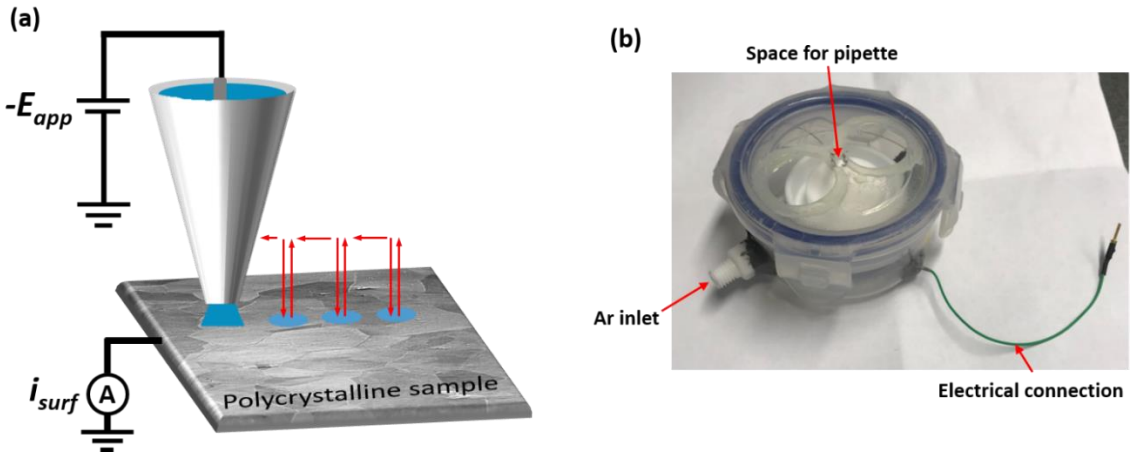

Figure 6. 2. (a) Schematic of the SECCM set up. **(b)** Photograph of the custom built environmental cell used to perform experiments under argon conditions.

6.4 Results and Discussion

6.4.1 Hydrogen effects during chronoamperometry on low carbon steel

Initially, SECCM experiments were performed on low carbon steel in an attempt to measure grain dependant passivation with chronoamperometry in 5 mM H_2SO_4. As shown in Figure 6.3b, the potential was stepped to a potential in the cathodic region (indicated on the cyclic voltammogram in Figure 6.3a, ① and ②) with the purpose of reducing any pre-existing passive film leaving an exposed low carbon steel surface. The potential was then stepped to the passive domain (③ in Figure 6.3a), where the current transient would provide information on the passivating behaviour on each grain. However, as shown in Figure 6.3c, the potential of the cathodic pulse had a large influence on the following anodic (passive) pulse. If the cathodic pulse is applied at a potential where the hydrogen evolution reaction (HER) is possible (Figure 6.3a, ①), the following anodic pulse gives rise to larger oxidation currents compared to the response following a cathodic pulse positive of the HER onset potential where only film reduction takes place (Figure 6.3a, ②).

Figure 6.3c shows a comparison of the anodic pulse (1V vs Pd/H_2) transients following cathodic pulses at -0.4 V for 20 ms (blue trace) and -0.8 V for 20 ms and 30 ms (green and red trace respectively). The plot shows that prolonging the HER pulse results in larger oxidation currents over a longer time period, which potentially suggests that hydrogen absorbed (or adsorbed) during the HER pulse is oxidised during the anodic pulse during the passivation of the surface. In fact a potentiostatic pulse technique has previously been applied to study hydrogen absorption in metals.[22] The principle of the technique is that a metal is charged with

hydrogen at a constant potential for a set period of time, after which the potential is stepped positively resulting in a current transient due to the hydrogen diffusing back to the surface before being reoxidised. However, this technique is only applicable if the oxidation current arising from the anodic pulse is entirely from hydrogen oxidation.

Comparing the transients (Figure 6.3b) arising from the HER pulse and the subsequent oxidation pulse, there is a clear discrepancy between the two transients with respect to the charge passed (0.60 nC and 1.37 nC, for the cathodic and anodic pulses respectively), indicating that an additional anodic process has occurs in addition to hydrogen oxidation. A possible explanation is that iron dissolution is taking place due to the absorbed (and adsorbed) hydrogen preventing the passivation of the low carbon steel surface. A common method to minimise this effect is to coat the metal surface with palladium to prevent the surface from being oxidised.[1, 23-24]

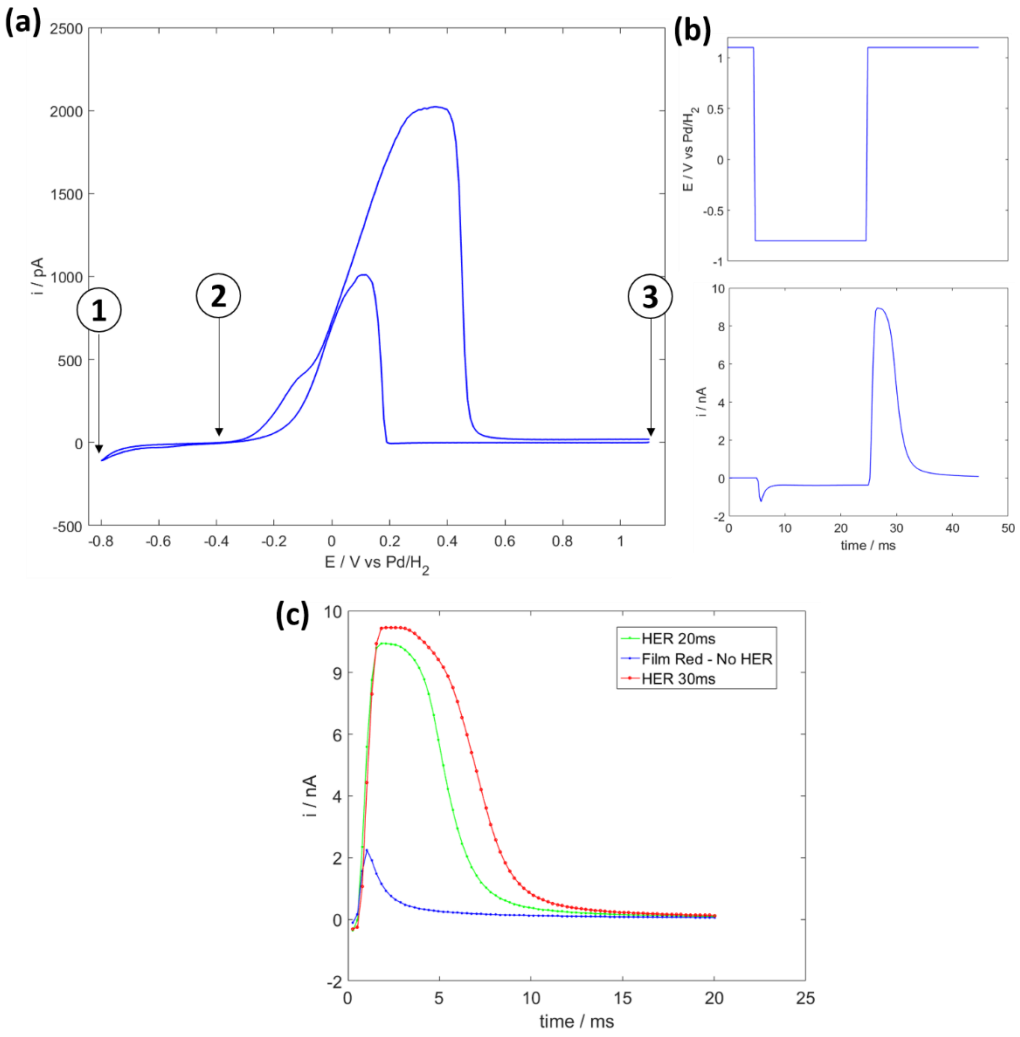

Figure 6. 3. (a) Cyclic voltammogram measured with SECCM on low carbon steel in 5 mM H_2SO_4, at a scan rate v = 2 Vs^{-1}. **(b)** Plots of the potential applied, E, and the measured surface current, i, response during a single SECCM measurement. **(c)** Transient response resulting from an anodic pulse of 1.1 V vs Pd/H_2, following a cathodic pulse at -0.8 V for 20 ms and 30 ms (red and green traces respectively) or -0.4 V for 20 ms (blue trace).

Figure 6.4 shows the results of mapping an area of low carbon steel with SECCM using the pulse protocol shown in Figure 6.3, where the potential was initially stepped to -0.8 V vs Pd/H_2 to drive the HER for 20 ms, before being stepped to +1.1 V vs Pd/H_2. The SEM image of the scanning area (50×50 pixels, spanning 50×50 µm with a hopping distance of 1 µm) is shown in Figure 6.4a. The points of the map where no "footprint" from the SECCM measurement has been left are as a result of the probe falsely detecting the surface, thus never initiating contact

between the droplet and the surface. The average transient (discounting false approaches) from the HER pulse is displayed in Figure 6.4b, accompanied by the surface current map (with grain boundaries superimposed on top) taken at the end of the cathodic pulse (@ 20.02 ms) in Figure 6.4c. The surface current maps clearly show that the rate of HER reflects that of the grain structure.

The transient arising from the subsequent oxidation pulse is displayed in Figure 6.4d, with the surface current maps taken at (i) 3.9, (ii) 4.94, (iii) 10.92, and (iv) 20.02 ms shown in Figure 6.4e. The maps share the same grain dependency, whereby grains that produced higher currents during the cathodic pulse, produce larger oxidation currents on the anodic pulse for a longer time period, which could be suggesting that the amount of hydrogen absorbed is grain dependant. However, as the cathodic pulse showed a grain dependence, it appears the amount of hydrogen that enters the low carbon steel is controlled by the charge transfer kinetics that are influenced by the crystal orientation.

It is clear that interpreting the data shown in Figures 6.3 and 6.4 is extremely complex due to the convolution of processes, such as hydrogen absorption, passive film formation, and anodic dissolution, influencing the transient response during the anodic pulse. However, there is an indication that the ingress of hydrogen into the low carbon steel is influenced by grain orientation. In order to study this effect further, experiments instead are performed on palladium which, as stated previously, is considered the model system to study hydrogen absorption.

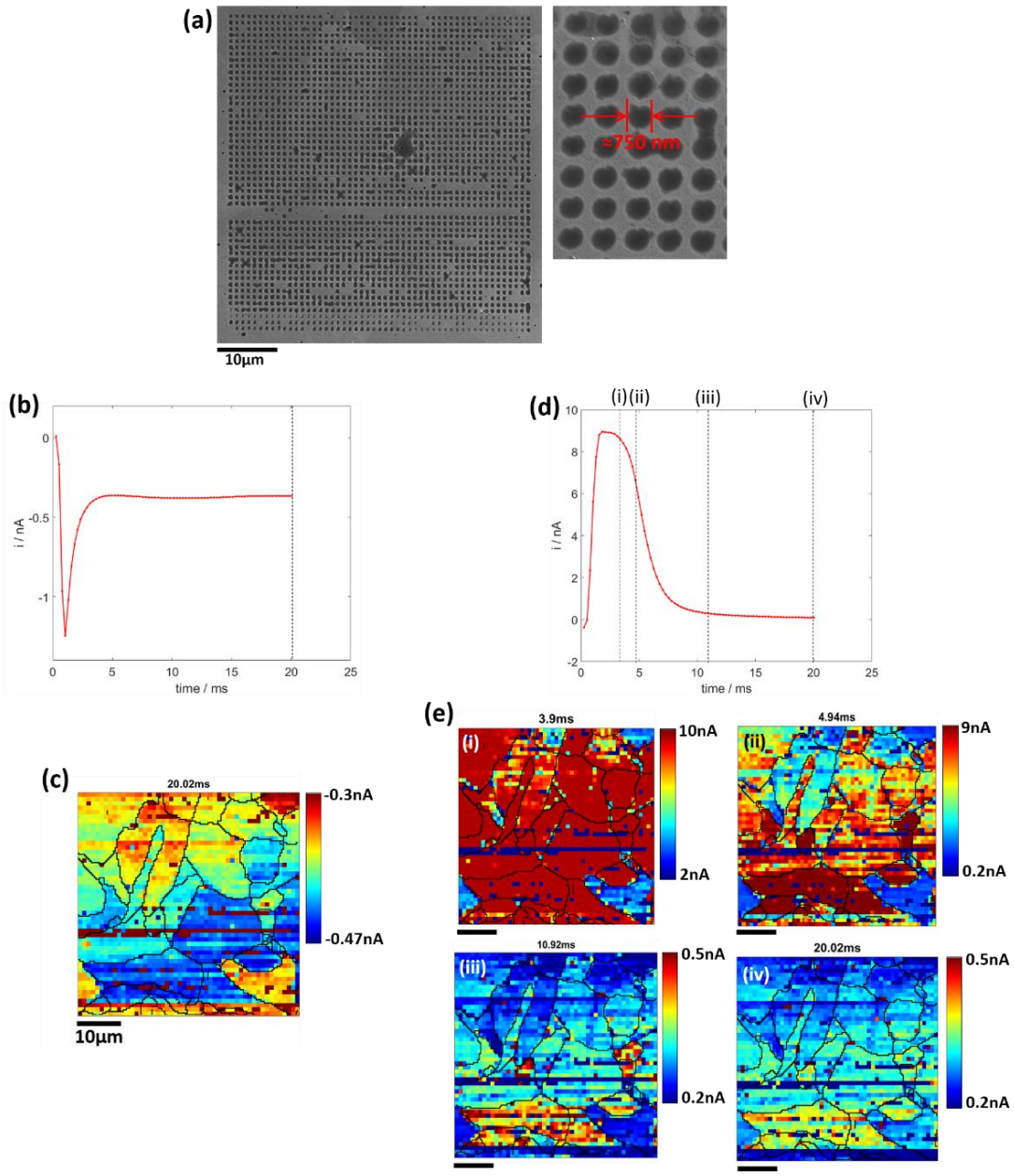

Figure 6. 4. (a) SEM image of an area of low carbon steel scanned with SECCM. **(b)** Average transient response arising from a potential step to -0.8 V vs Pd/H_2. **(c)** Spatially resolved surface current map at 20 ms from the transient shown in **(b)**, collected using SECCM of the area shown in (a). **(d)** Average transient response arising from a potential step to +1.1 V vs Pd/H_2. **(e)** Surface currents maps taken at (i) 3.9, (ii) 4.94, (iii) 10.92, and (iv) 20.02 ms from the transient response shown in **(d)**.

6.4.2 Cyclic voltammetry on palladium: macroscale vs. SECCM

A cyclic voltammogram recorded on annealed palladium wire in de-gassed 0.5 M H_2SO_4 is presented in Figure 6.5a. Starting at 0.6 V and sweeping anodically, the oxidation currents arise from the formation of an oxide film before oxygen evolution occurs at 1.4 V. On the reverse sweep, an oxide film reduction peak is observed at 0.4 V where the charge passed during this peak, is expected to be equal to the charge passed during oxide formation. After the oxide film is removed, the hydrogen absorption is then observed from approximately 0.1 V vs Ag/AgCl. The response of palladium wire is comparable to what has been observed in previous studies.[11, 25] Contrary to cyclic voltammetry performed on nanomaterials,[26] for the case of bulk palladium there is no separation of the peaks for hydrogen adsorption (H_{ads}) and absorption (H_{abs}). The hydrogen evolution reaction (HER) also occurs concurrently with hydrogen absorption until the palladium foil becomes saturated with hydrogen. On inspection of the cyclic voltammogram for platinum wire in Figure 6.5b, which was performed under the same conditions as for the Pd wire (Figure 6.5a), the onset of the HER is located at *c.a.* -180 mV vs Ag/AgCl (3.4 M KCl), which is comparable to that of Pd.[27] Therefore, applying potentials positive of the HER onset potential, one can be confident that currents are arising predominantly from hydrogen absorption.

A comparison of the cyclic voltammograms recorded using SECCM on annealed palladium foil in 0.5 M H_2SO_4 in air (blue trace) and under argon (red trace) is presented in Figure 6.5c. The influence of oxygen is clearly visible at potentials negative of 0 V, where the oxygen reduction reaction (ORR) appears to contribute to the magnitude of the cathodic

currents. For this reason, all SECCM scans on palladium were performed in an argon environment. The effect of performing multiple cycles is also presented in Figure 6.5d.

A nanoscale SECCM measurement can be compared to a bulk measurements as the working electrode area is significantly smaller than the volume of the palladium foil, *i.e.* it acts as an 'infinite' sink for H_{abs}. Considering that, for bulk Pd, the transition from H_{ads} to H_{abs} is very fast,[26] any structural influence on the hydrogen absorption process will be as a result of the charge transfer kinetics characteristic of the Pd surface. Any H_{abs} introduced into the Pd foil during a SECCM measurement will rapidly diffuse away from the measurement site at the surface, therefore upon reversing the potential from the detection of hydrogen desorption is very unlikely.

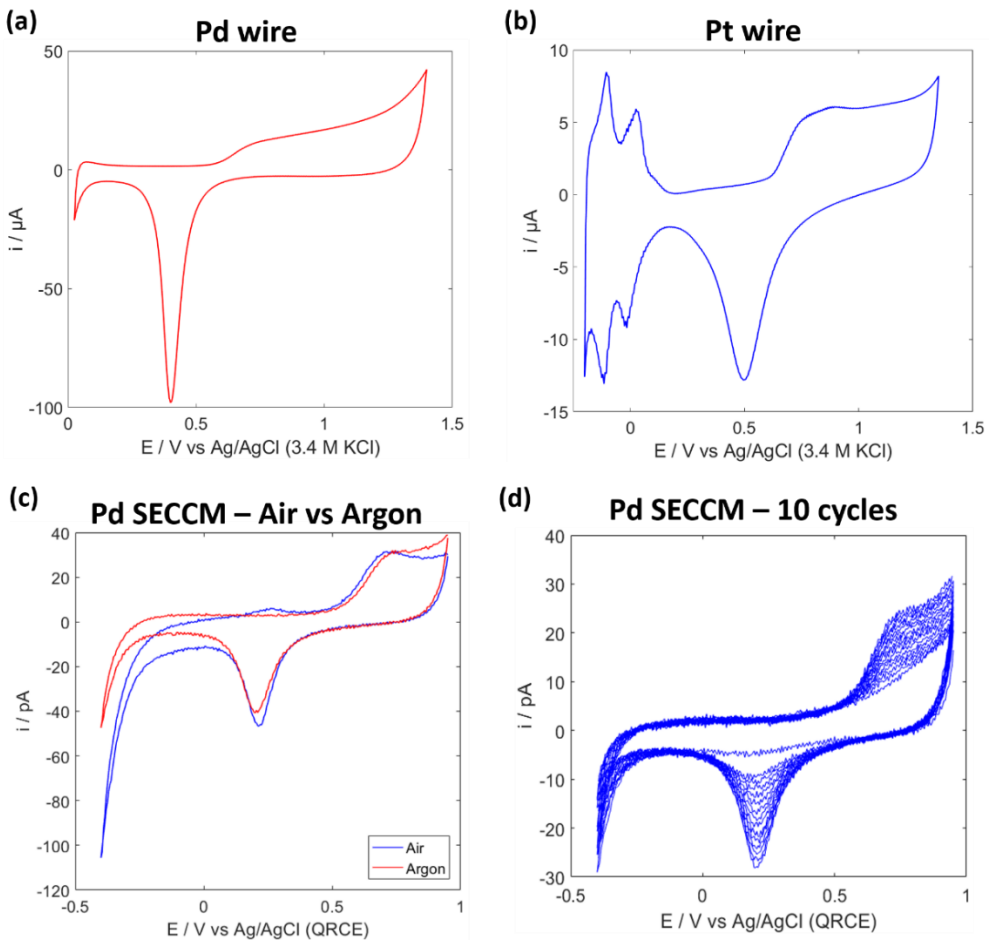

Figure 6. 5. (a) Cyclic voltammogram (CV) recorded from annealed palladium wire in de-gassed 0.5 M H_2SO_4 at a scan rate of v = 0.5 Vs^{-1}. The presented CV is the response following 25 cycles. Note that a commercial Ag/AgCl (3.4 M KCl) reference electrode was used. **(b)** CV recorded from annealed platinum wire with the same conditions used as **(a)**. **(c)** CV recorded with SECCM on palladium foil in 0.5 M H_2SO_4 at scan rate of v = 2 Vs^{-1} after 5 cycles. The droplet diameter was ≈ 900 nm (100 pA of current corresponds to 15.7 $mA \cdot cm^{-2}$ of current density). **(d)** CV recorded with SECCM with the same conditions as **(c)** (under argon), showing the response from 10 cycles.

6.4.3 Electrochemical mapping of palladium with SECCM

Voltammetric SECCM scans, where cyclic voltammetry was performed on a point-by-point basis, were performed on annealed palladium foil to reveal the relationship between crystal orientation and the rate of hydrogen absorption. An example of the results of such as scan is displayed in Figure 6.6, which includes a scan of a 200×175 μm area (41 × 35 pixel^2) with a hopping distance (distance between scanning points) of 5 μm. The average CV from all of the scanning points and the EBSD map of the scanning area are presented in Figures 6.6a and b respectively.

Spatially resolved surface current maps, taken at potentials indicated on Figure 6.6a, are presented in Figures 6.6c, d, and e, for 0.7, -0.2, and -0.45 V vs Ag/AgCl respectively. The map taken at 0.7 V (Figure 6.6c) shows that oxide formation is influenced by crystal orientation, and as expected the surface current recorded during the film reduction (Figure 6.6d) shares the same grain dependence as the film formation. Figure 6.6e shows that hydrogen absorption, the primary interest of this study, is also grain dependant; a relationship which is further discussed in below.

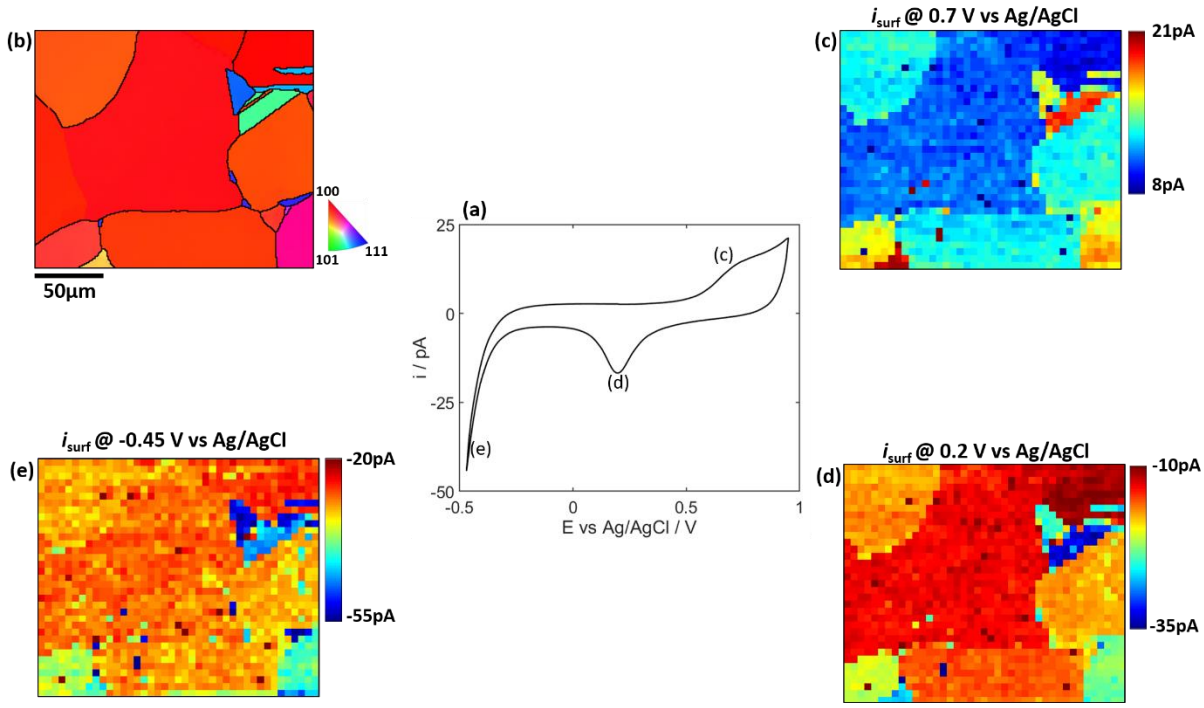

Figure 6. 6. (a) Average cyclic voltammogram from all scanning points of an SECCM map carried out on annealed palladium in 0.5 M H_2SO_4. **(b)** EBSD map of the SECCM scanning area. Spatially resolved surface current maps recorded at **(c)** 0.7 V, **(d)** -0.2 V, and **(e)** -0.45 V vs Ag/AgCl, taken after 4 cycles.

6.4.4 Influence of crystal orientation on hydrogen absorption on palladium

Figures 6.7, 6.8, and 6.9 show examples of three SECCM scans carried out on palladium foil that show how the rate of hydrogen absorption reflects that of the grain structure. Comparing the SEM image of the scanning areas (part (a) in Figures 6.7, 6.8, and 6.9) it is obvious that the droplet diameter is different for each scan resulting in differing magnitudes of surface current. The EBSD maps of each scanning area (shown in (b)) are accompanied with a graphical representation of the deviation of angle between the average orientations of the grains numbered in (b) and each of the low index planes. The construction of the plot in (c) is detailed in the experimental section. The surface current map, taken at -0.45 V vs Ag/AgCl, showing the relative rates of hydrogen absorption across the palladium surface is displayed in (d),

accompanied with the same plot in (c) with the colour of the points representing the average surface current for each grain (e). Figure 6.10 indicates some of the higher index orientations.

Starting with the scan shown in Figure 6.7, grains that are closer to the (100) orientation (appearing red in colour) facilitate lower rates of hydrogen absorption compared to the rest of the map. Grain 3, which is the closest to (100), a deviation of 1.8º, is in fact the least active grain. Interestingly grain 11 appears to have a similar orientation to grains 1 and 7, however they facilitate significantly different rates of hydrogen absorption. This result indicates that small changes in orientation can actually have a major influence the affinity to hydrogen of a surface. Grains 4, 5, and 6, which all possess relatively high index orientations, facilitate the highest reaction rates.

In Figure 6.8, grain 4 is by far the most active grain. Grain 4 appears to have an orientation close to (411) on comparison with Figure 6.10. Incidentally grain 4 is similar in orientation to grain 8 in Figure 6.7 which also facilitated high activity. The least active grain in Figure 6.8 is grain 5, which has an orientation close to the low index (101), a deviation of 3.1º. As previously shown in Figure 6.7, the least active grain also had a relative low index orientation.

For Figure 6.9, grains 1 and 7 possess similar orientations to (411) (likewise with grain 8 in Figure 6.7, and grain 4 in Figure 6.8), and also exhibits the highest activity. Grain 5, which has an orientation close to the low index (111), a deviation of 4.8º, is shown to be the least active grain in Figure 6.9. Similarly to Figures 6.7 and 6.8, the least active grain is also the grain closest to a low index orientation.

In the current literature, the hydrogen absorption properties of different crystal facets on palladium is most commonly studied on nanoparticles. Palladium nanoparticles can take the form of a variety of shapes enclosed by different crystal facets.[28] The orientation of these crystal facets can, although it is not well established, influence the rate at which hydrogen is introduced into the nanoparticle.[15-16] Therefore, the data presented herein, showing how the facet-dependant charge transfer influences the rate of hydrogen absorption could be relevant in the field of nanoparticles. However, comparing the data collected in this study to nanoparticle literature is difficult considering the large differences in experimental conditions.

A more relevant comparison would be to studies of single crystal palladium, however studies of the nature are rare due to the difficulties in producing palladium single crystals. In a study by Hara *et al.* in which a method of preparing Pd single crystals in the form of "bead electrodes" (diameter ≈ 2.5 mm) was proposed,[29] cyclic voltammetry was carried out on Pd(100), (110) and (111). Although different current voltage profiles were measured for each crystal, the volume of data is rather limited so it is difficult to confirm whether the trends are truly representations of each specific crystal plane. This highlights an advantage of SECCM, whereby multiple measurements can be performed on individual grains without the requirement of single crystal materials.

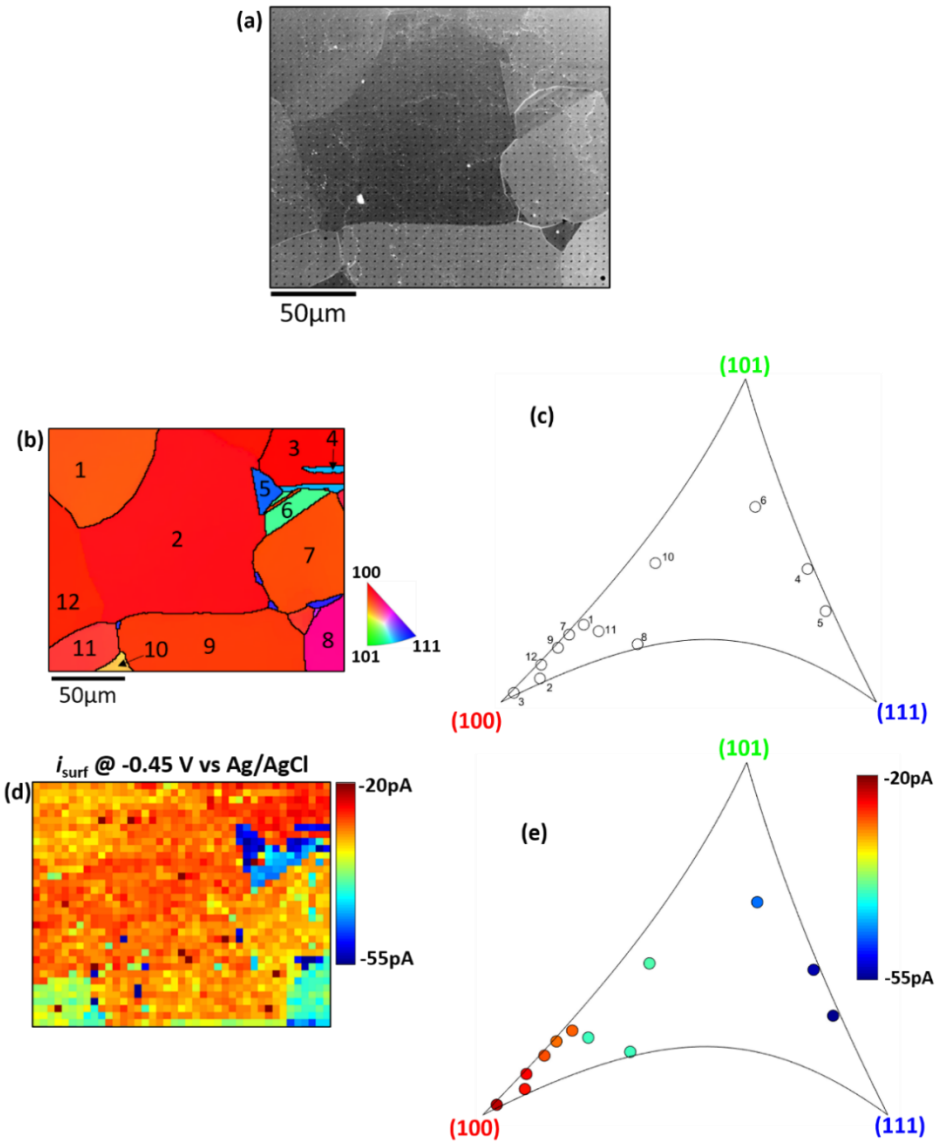

Figure 6. 7. (a) SEM image of the SECCM scanning area on palladium. The scan covers a 200 × 175 µm area comprising of 41 × 35 (1435 total) individual scanning sites (pixels), with a hopping distance of 5 µm. The droplet diameter in this scan was ≈ 900 nm. (100 pA current ≈ 15.7 mA·cm^{-2} of current density). **(b)** EBSD map of the scanned area. **(c)** Plot of the deviations of each grain (labelled in **(b)**) relative to the low index orientations. **(d)** Spatially resolved surface current map taken at -0.45 V vs Ag/AgCl after 4 cycles. **(e)** Plot of the average surface current in conjunction with the deviation relative to the low index orientations of each grain labelled in **(b)**.

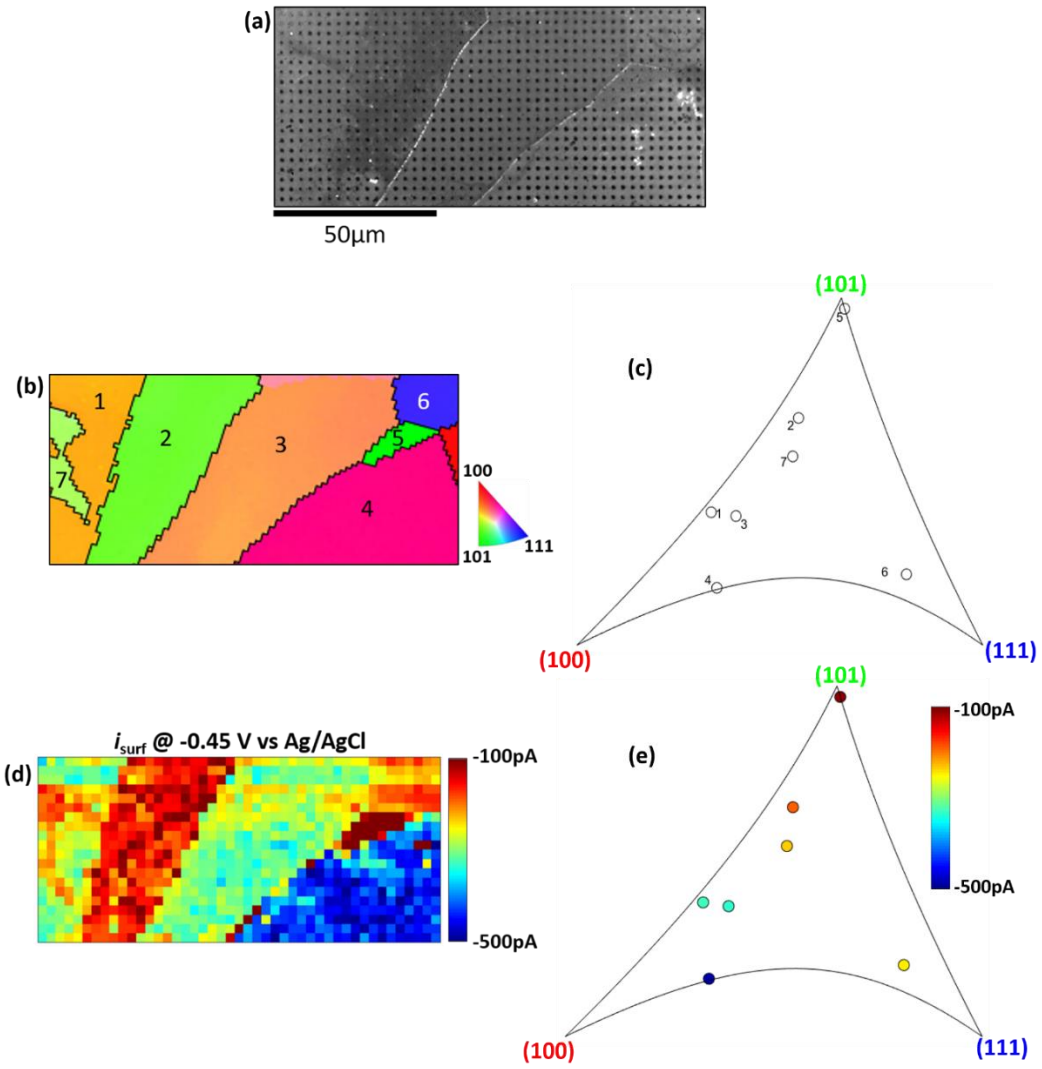

Figure 6. 8. (a) SEM image of the SECCM scanning area on palladium. The scan covers a 138 × 63 µm area comprising of 45 × 20 (900 total) individual scanning sites (pixels), with a hopping distance of 3 µm. The droplet diameter in this scan was ≈ 2 µm. (100 pA current ≈ 3.18 mA·cm^{-2} of current density). **(b)** EBSD map of the scanned area. **(c)** Plot of the deviations of each grain (labelled in **(b)**) relative to the low index orientations. **(d)** Spatially resolved surface current map taken at -0.45 V vs Ag/AgCl after 4 cycles. **(e)** Plot of the average surface current in conjunction with the deviation relative to the low index orientations of each grain labelled in **(b)**.

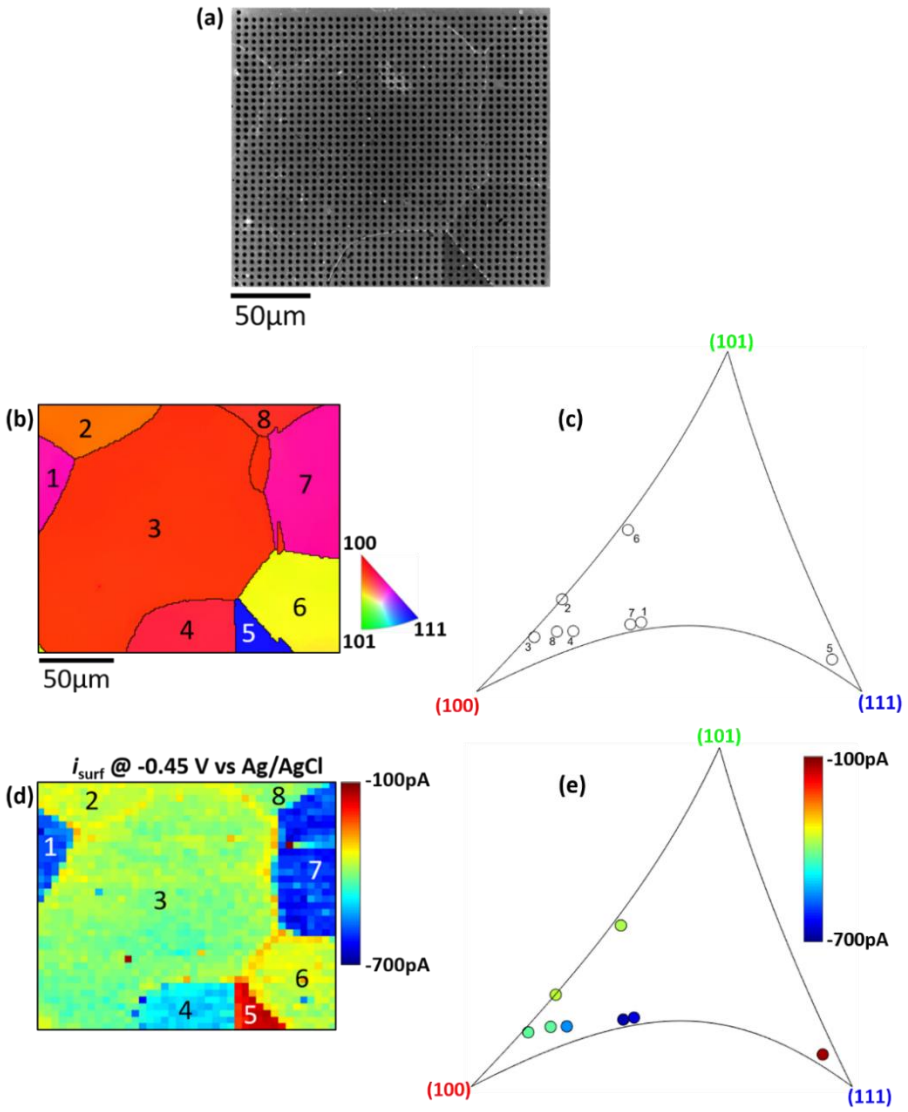

Figure 6. 9. (a) SEM image of the SECCM scanning area on palladium. The scan covers a 200 × 180 µm area comprising of 41 × 37 (1517 total) individual scanning sites (pixels), with a hopping distance of 5 µm. The droplet diameter in this scan was ≈ 2.8 µm. (100 pA current ≈ 1.62 mA·cm^{-2} of current density). **(b)** EBSD map of the scanned area. **(c)** Plot of the deviations of each grain (labelled in **(b)**) relative to the low index orientations. **(d)** Spatially resolved surface current map taken at -0.45 V vs Ag/AgCl after 4 cycles **(e)** Plot of the average surface current in conjunction with the deviation relative to the low index orientations of each grain labelled in **(b)**.

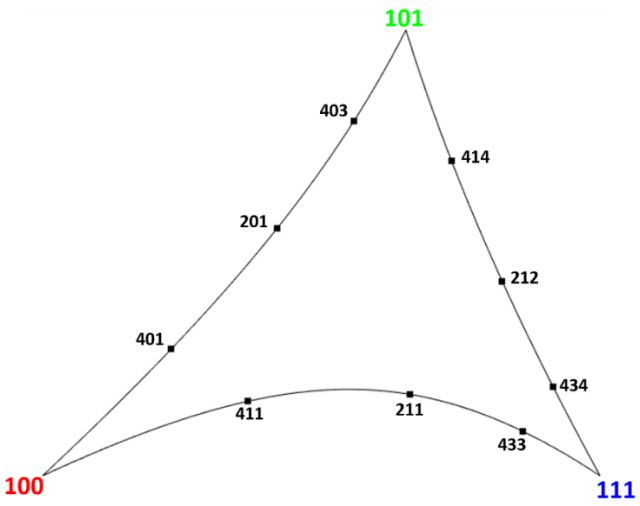

Figure 6. 10. Graphical representation of the misorientation of various high index orientations relative to the low index orientations of (100), (101), and (111).

6.4.5 Probing hydrogen absorption at grain boundaries

Two further scans performed on annealed palladium foil are presented in Figure 6.11a and 6.11b, where SEM images, the EBSD map, and the surface current maps (showing rates of hydrogen absorption) at -0.4 and -0.45 V vs Ag/AgCl, are presented in (i), (ii), (iii), and (iv), respectively. A clear increase in the rate of hydrogen absorption is shown where measurements were made directly on top of individual grains boundaries. Accelerated hydrogen diffusion has previously been detected on materials such as Pd,[30] Ni,[31] and Al,[32] which appears to agree with what is shown in Figure 6.11.

Although the data presented in Figure 6.11 appears to confirm the enhancement of hydrogen absorption at specific grain boundaries, it is also important to consider that the morphology of the region around the grain boundary could also influence the measured surface current values. Figure 6.12 presents a detailed examination, with SEM, of a grain boundary where enhanced hydrogen absorption was detected. A section of the surface current map

(originally presented in Figure 6.11a) is shown in Figure 6.12a, accompanied with SEM images of active sites. Cyclic voltammograms from the active sites (numbered in Figure 6.12a) are also presented in Figure 6.12b.

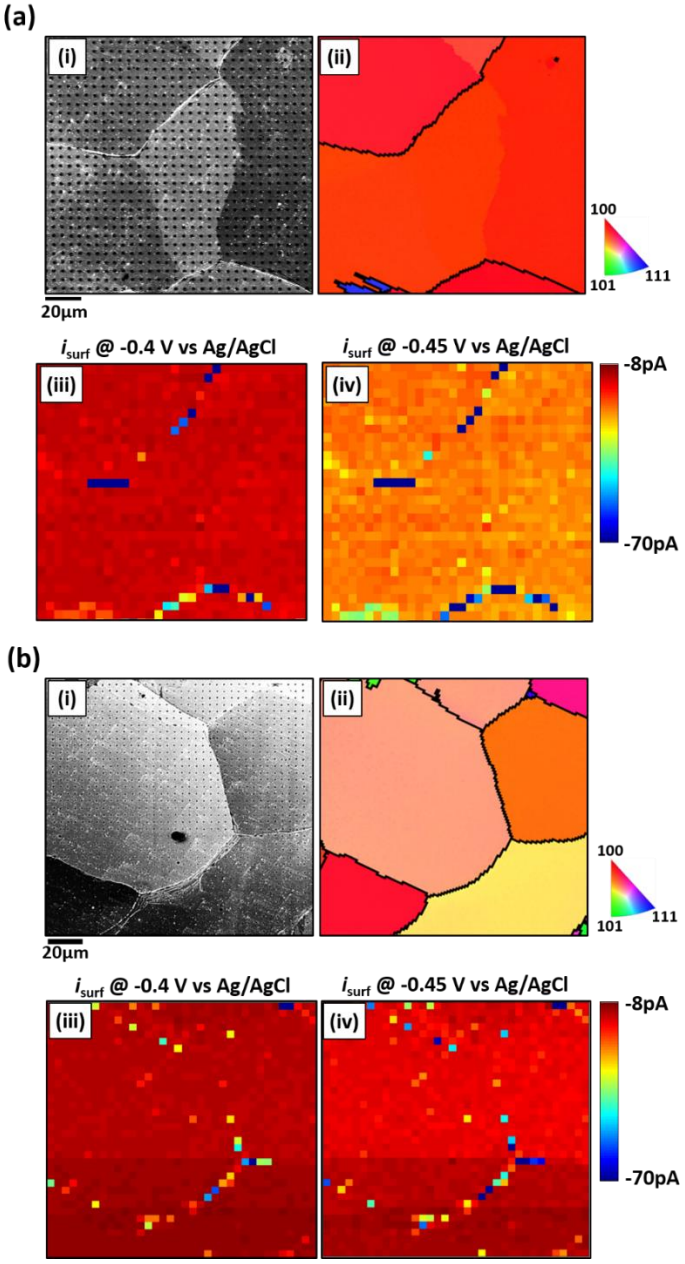

Figure 6. 11. (a) and **(b)**, SECCM scan areas of two regions on annealed palladium. The scans consist of **(a)** 30 × 29 sites (870 total) covering 116 × 112 µm, and **(b)** 36 × 36 sites (1296 total) covering 140 × 140 µm. Both scans employed a hopping distance of 4 µm. SEM images, EBSD maps, and surface current maps (for E = -0.4 V and -0.45 V vs Ag/AgCl) are shown in (i), (ii), (iii), and (iv) respectively.

The SEM images in Figure 6.12a show that the annealing process has induced a degree of deformation at the grain boundary. Firstly, this could influence the wetting of the SECCM droplet cell on the surface thus altering the working electrode surface area. Figure 6.12b shows that the surface current arising from oxide formation/reduction, and from the double layer are also larger at grain boundaries which are likely as a result of increased wetting of the SECCM droplet.

Secondly, in electrocatalysis, it is often postulated that step and defect sites possess preferential conditions for catalytic processes, such as an enhanced ability to bind reactants, and improved bond breaking/forming.[33] Due to the deformation shown in Figure 6.12, it is very possible that an increased density of surface defects are present in the region neighbouring the grain boundary. For example, some of the scanning points that are shown to be active in Figure 6.12a, do not lie on the boundary itself, but are instead situated in deformed areas (*e.g.* points 1 and 2 in Figure 6.12a). These results show that if SECCM is to be used to study activity at grain boundaries, careful analysis of the droplet "footprints" is vital to avoid misleading conclusion about the activity of the grain boundary itself.

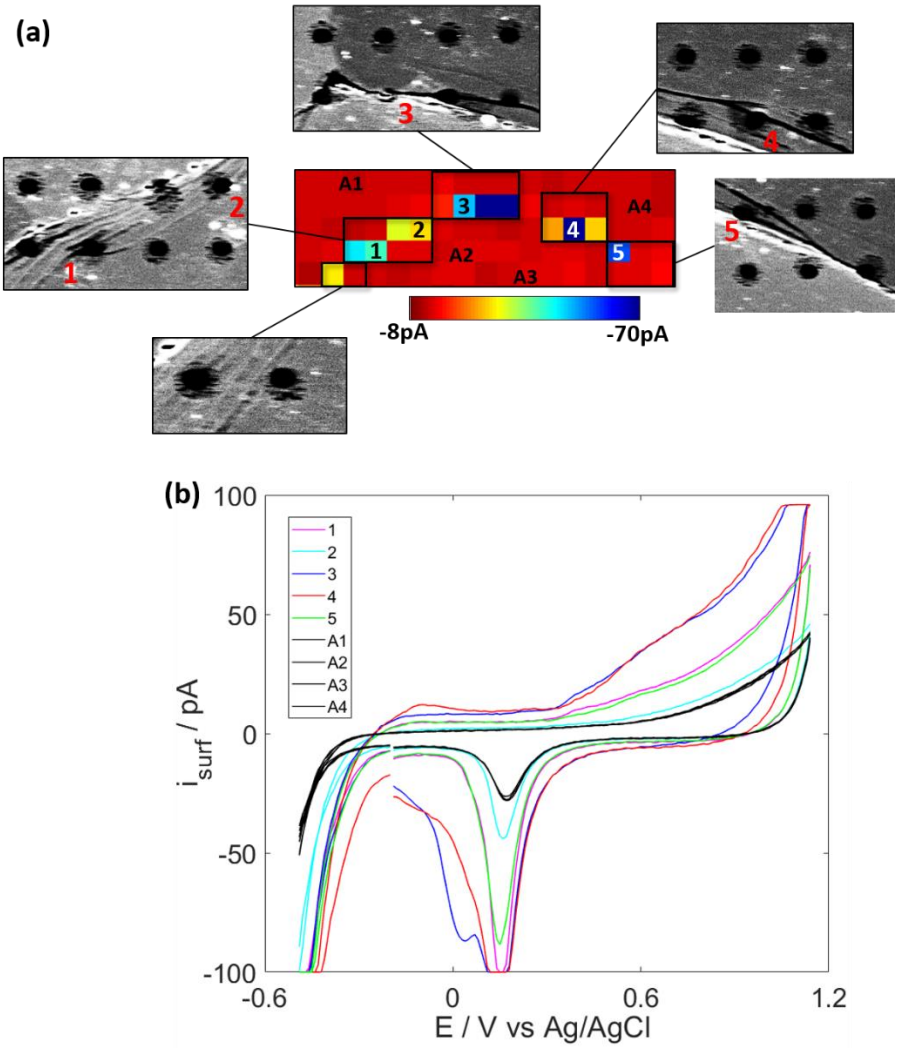

Figure 6. 12. (a) Surface current map, recorded with SECCM at -0.45 V vs Ag/AgCl, of a grain boundary on annealed palladium foil, accompanied with SEM images of the boxed areas. **(b)** Cyclic voltammograms of the scanning points indicated in **(a)**.

6.5 Conclusions

In this study, using palladium as a model system, it was shown that the rate of hydrogen absorption (in 0.5 M H_2SO_4) is influenced by the crystal orientation at the surface. With the use of SECCM, multiple nanoscale cyclic voltammograms were collected at different locations on individual grains, which were subsequently identified with EBSD. The rate of hydrogen

absorption was compared to the orientations of each scanned grain and it was found that grains with orientations close to those of the low index orientations (*i.e.* (100), (101), and (111)) exhibited the lowest rates of absorption. Whilst high index orientations, *e.g.* (411), facilitated higher rates of hydrogen absorption. Initial observations also suggested that enhanced hydrogen absorption took place at grain boundaries. However, it was concluded that deformation adjacent to the grain boundaries influenced the stability of the droplet cell in the SECCM probe, and caused multiple surface defects resulting in a misleading enhancement of electrochemical activity. The preliminary findings in this study may prove useful in improving the understanding of how surface structure can influence the ingress of hydrogen in to metals, which is particularly important to research involving hydrogen embrittlement and hydrogen storage.

6.6 References

1. Pound, B., Chapter 2.2 Hydrogen Ingress During Corrosion In *Corrosion and Oxide Films*, Stratmann, M.; Frankel, G., Eds. Wiley-VCH: Germany, 2003; Vol. 4, pp 108-155.

2. Ohtsuka, T.; Nishikata, A.; Sakairi, M.; Fushimi, K., *Electrochemical Fundamentals for Corrosion Fundamentals*; Springer, 2018.

3. Oriani, R. A., Hydrogen Embrittlement of Steels. *Annual Review of Materials Science* **1978**, *8*, 327-357.

4. Woodtli, J.; Kieselback, R., Damage Due to Hydrogen Embrittlement and Stress Corrosion Cracking. *Engineering Failure Analysis* **2000**, *7*, 427-450.

5. Farrell, K., Cathodic Hydrogen Absorption and Severe Embrittlement in a High Strength Steel. *Corrosion* **1970**, *26*, 105-110.

6. Robertson, I. M.; Sofronis, P.; Nagao, A.; Martin, M. L.; Wang, S.; Gross, D. W.; Nygren, K. E., Hydrogen Embrittlement Understood. *Metallurgical and Materials Transactions A: Physical Metallurgy and Materials Science* **2015**, *46*, 2323-2341.

7. Barrera, O., et al., Understanding and Mitigating Hydrogen Embrittlement of Steels: A Review of Experimental, Modelling and Design Progress from Atomistic to Continuum. *J Mater Sci* **2018**, *53*, 6251-6290.

8. Mine, Y.; Tachibana, K.; Horita, Z., Grain-Boundary Diffusion and Precipitate Trapping of Hydrogen in Ultrafine-Grained Austenitic Stainless Steels Processed by High-Pressure Torsion. *Materials Science and Engineering: A* **2011**, *528*, 8100-8105.

9. Mohtadi-Bonab, M. A.; Szpunar, J. A.; Razavi-Tousi, S. S., Hydrogen Induced Cracking Susceptibility in Different Layers of a Hot Rolled X70 Pipeline Steel. *International Journal of Hydrogen Energy* **2013**, *38*, 13831-13841.

10. Gabrielli, C.; Grand, P. P.; Lasia, A.; Perrot, H., Investigation of Hydrogen Adsorption-Absorption into Thin Palladium Films. I. Theory. *Journal of The Electrochemical Society* **2004**, *151*, A1925-A1936.

11. Gabrielli, C.; Grand, P. P.; Lasia, A.; Perrot, H., Investigation of Hydrogen Adsorption and Absorption in Palladium Thin Films. II. Cyclic Voltammetry. *Journal of The Electrochemical Society* **2004**, *151*, A1937-A1942.

12. Adams, B. D.; Chen, A., The Role of Palladium in a Hydrogen Economy. *Materials Today* **2011**, *14*, 282-289.

13. Konda, S. K.; Chen, A., Palladium Based Nanomaterials for Enhanced Hydrogen Spillover and Storage. *Materials Today* **2016**, *19*, 100-108.

14. Li, G.; Kobayashi, H.; Dekura, S.; Ikeda, R.; Kubota, Y.; Kato, K.; Takata, M.; Yamamoto, T.; Matsumura, S.; Kitagawa, H., Shape-Dependent Hydrogen-Storage Properties in Pd Nanocrystals: Which Does Hydrogen Prefer, Octahedron (111) or Cube (100)? *J Am Chem Soc* **2014**, *136*, 10222-5.

15. Johnson, N. J. J.; Lam, B.; MacLeod, B. P.; Sherbo, R. S.; Moreno-Gonzalez, M.; Fork, D. K.; Berlinguette, C. P., Facets and Vertices Regulate Hydrogen Uptake and Release in Palladium Nanocrystals. *Nat Mater* **2019**, *18*, 454-458.

16. Dekura, S.; Kobayashi, H.; Kusada, K.; Kitagawa, H., Hydrogen in Palladium and Storage Properties of Related Nanomaterials: Size, Shape, Alloying, and Metal-Organic Framework Coating Effects. *Chemphyschem* **2019**, *20*, 1158-1176.

17. Ebejer, N.; Güell, A. G.; Lai, S. C. S.; McKelvey, K.; Snowden, M. E.; Unwin, P. R., Scanning Electrochemical Cell Microscopy: A Versatile Technique for Nanoscale Electrochemistry and Functional Imaging. *Annual Review of Analytical Chemistry* **2013**, *6*, 329-51.

18. Bentley, C. L.; Kang, M.; Unwin, P. R., Scanning Electrochemical Cell Microscopy: New Perspectives on Electrode Processes in Action. *Current Opinion in Electrochemistry* **2017**, *6*, 23-30.

19. Mariano, R. G.; McKelvey, K.; White, H. S.; Kanan, M. W., Selective Increase in Co_2 Electroreduction Activity at Grain-Boundary Surface Terminations. *Science* **2017**, *358*, 1187-1192.

20. Bentley, C. L.; Perry, D.; Unwin, P. R., Stability and Placement of Ag / Agcl Quasi-Reference Counter Electrodes in Confined Electrochemical Cells. *Analytical Chemistry* **2018**, *90*, 7700-7707.

21. Bentley, C. L.; Unwin, P. R., Nanoscale Electrochemical Movies and Synchronous Topographical Mapping of Electrocatalytic Materials. *Faraday Discussions* **2018**, *210*, 365-379.

22. McKibben, R.; Sharp, R. M.; Harrington, D. A.; Pound, B.; Wright, G. A., A Potentiostatic Double-Step Method for Measuring Hydrogen Atom Diffusion and Trapping in Metal Electrodes—I. Theory. *Acta Metallurgica* **1987**, *35*, 253-262.

23. Frappart, S.; Oudriss, A.; Feaugas, X.; Creus, J.; Bouhattate, J.; Thébault, F.; Delattre, L.; Marchebois, H., Hydrogen Trapping in Martensitic Steel Investigated Using Electrochemical Permeation and Thermal Desorption Spectroscopy. *Scripta Materialia* **2011**, *65*, 859-862.

24. Zakroczymski, T., Electrochemical Determination of Hydrogen in Metals. *Journal of Electroanalytical Chemistry* **1999**, *475*, 82-88.

25. Grdeń, M.; Łukaszewski, M.; Jerkiewicz, G.; Czerwiński, A., Electrochemical Behaviour of Palladium Electrode: Oxidation, Electrodissolution and Ionic Adsorption. *Electrochimica Acta* **2008**, *53*, 7583-7598.

26. Zalineeva, A.; Baranton, S.; Coutanceau, C.; Jerkiewicz, G., Electrochemical Behavior of Unsupported Shaped Palladium Nanoparticles. *Langmuir* **2015**, *31*, 1605-9.

27. Trasatti, S., Work Function, Electronegativity, and Electrochemical Behvaiour of Metals. Iii. Electrolytic Hydrogen Evolution in Acid Solutions. *Journal of Electroanalytical Chemistry and Interfacial Electrochemistry* **1972**, *39*, 163-184.

28. Xia, Y.; Xiong, Y.; Lim, B.; Skrabalak, S. E., Shape-Controlled Synthesis of Metal Nanocrystals: Simple Chemistry Meets Complex Physics? *Angew Chem Int Ed Engl* **2009**, *48*, 60-103.

29. Hara, M.; Linke, U.; Wandlowski, T., Preparation and Electrochemical Characterization of Palladium Single Crystal Electrodes in 0.1m H_2SO_4 and $HClO_4$. *Electrochimica Acta* **2007**, *52*, 5733-5748.

30. Iwaoka, H.; Arita, M.; Horita, Z., Hydrogen Diffusion in Ultrafine-Grained Palladium: Roles of Dislocations and Grain Boundaries. *Acta Materialia* **2016**, *107*, 168-177.

31. Brass, A. M.; Chanfreau, A., Accelerated Diffusion of Hydrogen Along Grain Boundaries in Nickel. *Acta Materialia* **1995**, *44*, 3823-3831.

32. Ichimura, M.; Sasajima, Y.; Imabayashi, M., Grain Boundary Effect on Diffusion of Hydrogen in Pure Aluminum. *Materials Transcations* **1991**, *32*, 1109-1114.

33. Koper, M. T., Structure Sensitivity and Nanoscale Effects in Electrocatalysis. *Nanoscale* **2011**, *3*, 2054-73.

CHAPTER 7
Summary

It has been previously established that microstructural features, such as crystal orientation, grain boundaries, and inclusions, can play a significant role in the corrosion behaviour (and failure) of industrial metals and alloys. A popular method of analysing these features is through the use of high resolution analytical electrochemical techniques, which enables detection of the enhancement or inhibition of corrosion related processes at specific nano/microscale sites on metal surfaces. This thesis reports on the introduction of scanning electrochemical cell microscopy (SECCM) into the field of corrosion science. Through its powerful ability to correlate surface structure to electrochemical activity, the behaviour of numerous corrosion related processes was investigated on various microstructural features. Whilst SECCM has shown to be very effective in the results chapters of this thesis, the method also presented significant challenges when it was used to perform corrosion measurements. It should be emphasised that the experiments conditions presented in this thesis were predominantly chosen to avoid the issues highlighted in section 2.5. It is important to note that these challenges should be carefully considered if the use of SECCM is to be expanded further into the field of corrosion science.

Firstly, Chapter 3 presents the initial application of SECCM in the study corrosion related processes. A detailed comparison of SECCM with other local electrochemical measurements methods, in particular with the electrochemical droplet cell (EDC) method is included. It is discussed that SECCM overcomes many of the factors limiting the use of EDC

in corrosion measurements, including: the current resolution of instrumentation, difficulties in probe fabrication, an automated method of initiating droplet contact with the surface, and the Ohmic drop induced by the probe. SECCM scans were performed on low carbon steel in (neutral pH) 10 mM KNO_3, with a tip diameter of ~2 µm, where polarisation measurements were made at each scanning point. EBSD mapping was carried out within the SECCM scan areas so a direct comparison between electrochemical activity and crystal orientation could be achieved. A subtle difference in the passive behaviour of the low index grains was detected whereby (101) grains were shown to facilitate larger currents compared to (100) and (111) orientated grains. A tentative explanation is proposed that the density of atoms specific to each plane is responsible (with the (101) possessing the largest surface atom density) for the differences in passive behaviour. Additionally, pitting events were detected upon landing the SECCM droplet on MnS inclusions, revealing similar behaviour to what has been measured on these inclusions using the EDC configuration in previous studies. This was a key result as it showed that SECCM can successfully reproduce established data from the literature. There were also some improvements to be made from the work in Chapter 3. For example, the time taken for each of the scans to complete was ≈6 hours (for 256 to 289 measurements), which limited productivity and the progression of the project. The long scan times were primarily as a result of the feedback mechanism, where the dual channel-oscillating probe configuration was adopted resulting in slow approach rates, and the slow potential sweep rates, which were necessary to reduce the influence of non-faradaic currents on the already subtle response in the passive domain.

The subsequent work, presented in Chapter 4, showed that the hydrogen evolution reaction (HER) rate, a predominant cathodic process during corrosion in acidic media, is influenced by the microstructure of low carbon steel in 5 mM H_2SO_4 (pH ≈ 2.3). Using the single channel configuration (where the direct current from the surface is used as feedback) with a pipette tip diameter of ~150 nm, single step chronoamperometry measurements revealed a subtle dependence of the HER rate on crystal orientation. For the low index orientations, the following trend was observed: (100) > (111) > (101). Increased wetting of the droplet cell during the application of cathodic potentials had been previously observed, so short transient times were chosen (10 ms) to minimise the droplet thus maintaining a high resolution. This serves as an important topic of consideration for the future use of SECCM for corrosion measurements on metals, as the influence of wetting could limit the resolution of the method. In the single channel configuration, fast approach rates, which were more viable compared to the set up used in Chapter 3, and the short chronoamperometry measurements allowed for significantly faster scans (1600 measurements in < 40 mins). Although DFT calculations, which were used to determine the hydrogen adsorption free energy values for each low index plane, produced a trend that agreed with the trend recorded using SECCM, it was acknowledged that such results should be treated with caution considering the calculations were performed for pristine surfaces as opposed to the real surfaces used in experiments. The HER rates detected at specific grain boundaries and on MnS inclusions were shown to be more significant than the heterogeneous response from different grains. This result indicates that grain boundaries and MnS inclusions are likely to serve as preferential cathodic sites during atmospheric corrosion.

The results presented in Chapter 5 showed how SECCM, combined with EBSD, highlighted the significant influence of crystal orientation on the anodic dissolution of low carbon steel in the presence of 5 mM H_2SO_4 with the use of sweep voltammetry. The dissolution rates recorded on the low index planes were shown to increase in the order (101)< (111) < (100), a trend which has also been observed in the literature. Due to the large amount of data points for each grain, the trends were shown to be statistically robust. DFT analysis was used to calculate to change in surface energy of an iron lattice upon the removal of a single atom, thus modelling the dissolution energies of each low index plane. The trend in dissolution energies was consistent with the results recorded with SECCM, however, as discussed previously, the calculations were performed on a simulated pristine iron surface so should be taken lightly. In order to fully understand the influence surface structure on dissolution rates, more than just the low index orientations should be considered for closer analysis. For future studies, this should include an improved characterisation method for properties of crystal planes (both high and low index) whereby physical properties associated with each crystal plane can be correlated with corrosion behaviour. To gain an insight into the physical changes to the substrate surface caused by an SECCM measurement, FIB milling was employed to extract and expose cross sections of individual scanning sites. The extracts were analysed with STEM to reveal compositional and morphological changes to the surface made during a typical SECCM measurement. The deep recess in the low carbon steel surface as a result of driving iron dissolution was clear to see and acted as a visual confirmation of the electrochemical data. This method of confirming results, recorded with SECCM, with the use of FIB-TEM may prove extremely effective in future

corrosion related studies. A schematic summarising the findings from chapters 3, 4, and 5, for the low carbon steel system is presented in Figure 7.1.

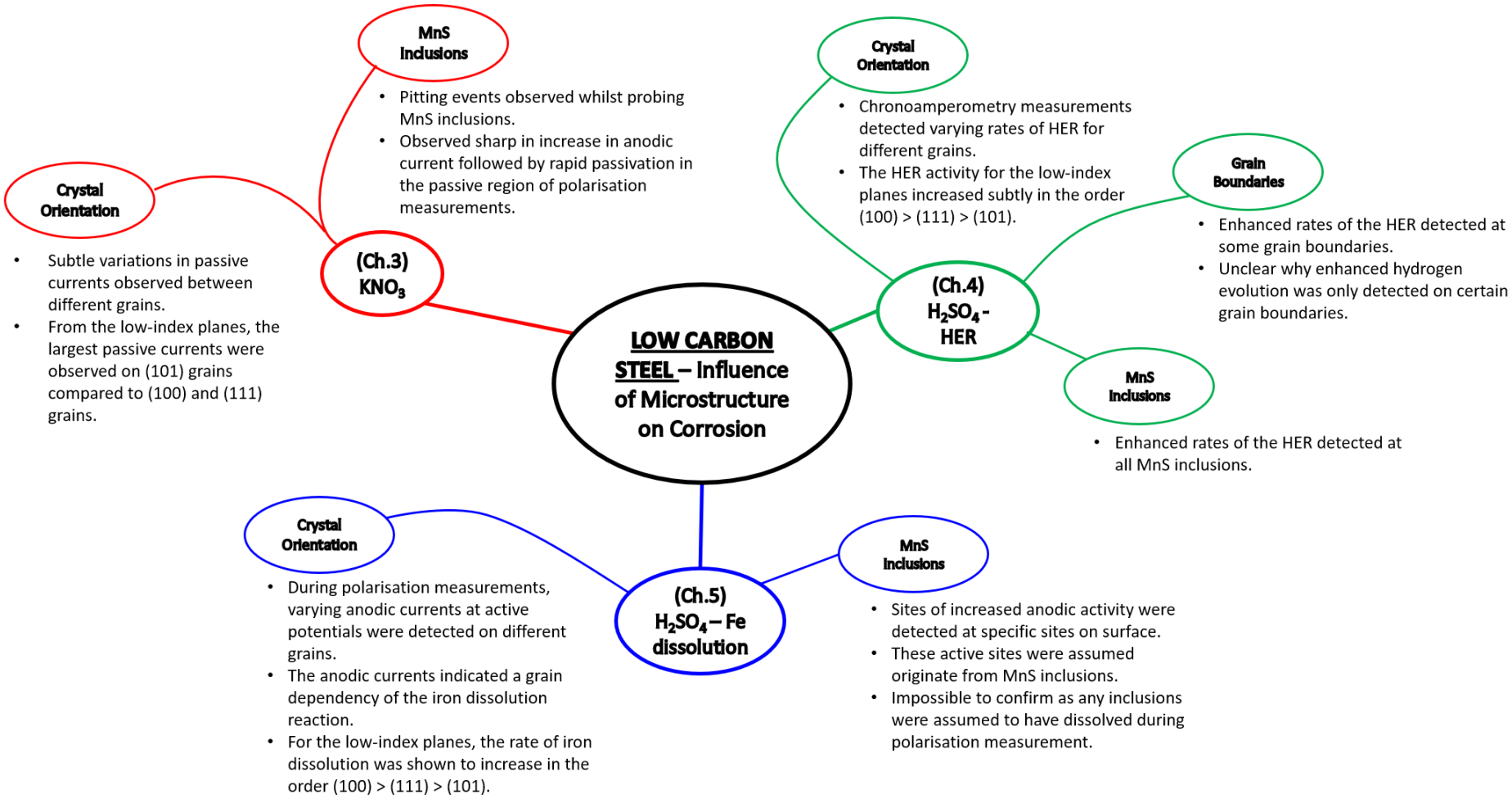

Figure 7. 1. Summary of the findings relating the dependency of corrosion process on the microstructure of low carbon steel. The sections highlighted in red, green, and blue correspond to the results discussed in chapters 3, 4, and 5 respectively.

Finally, in Chapter 6, the rate of hydrogen absorption was also shown to be influenced by crystal orientation. Initial SECCM experiments (using chronoamperometry) that were carried out on low carbon steel in 5 mM H_2SO_4, indicated that the rate of the amount of hydrogen adsorbed/absorbed during cathodic pulses corresponded to the grain structure. As the low carbon steel system was considered overly complicated (multiple competing processes producing a convoluted response) SECCM scans, using cyclic voltammetry, were performed on annealed polycrystalline palladium in 0.5 M H_2SO_4. Palladium was chosen as an appropriate substrate as it is considered the model system to study hydrogen absorption. From the three scans presented in Chapter 6, the grains that were closest to the low index orientations were consistently the least active, whereas grains possessing higher index orientation (*e.g.* (411) grains) were more active. The results indicate that the different charge transfer kinetics specific to different crystal planes influences the rate at which hydrogen is absorbed into metals. Additionally, enhanced rates of hydrogen absorption were also detected at grain boundaries on the palladium surface. On closer inspection however, it was concluded that this enhancement was more likely due to the deformation caused by the annealing process near grain boundaries. This result in particular highlights how important it is to carry out close inspection of the SECCM measurements sites to properly identify all contributing factors to any enhancement of electrochemical processes.

The results in chapters 3, 4, 5, and 6, also give an indication as to which of the two SECCM configurations (single or dual channel) are appropriate for different substrates and media. The single channel approach is the quicker and easier to use of the two methods, as there are less components in the experimental set up (e.g. requires one QRCE and only requires on

channel to be filled with electrolyte). However, it is best suited to more active systems as the approach mechanism requires a reliable surface current for repeatable droplet landings. For example, chapters 4, 5, and 6, all used acidic electrolytes that created unfavourable conditions for passive film formation on the substrates resulting in larger (and easily detectable) surface currents.

For a passive system (e.g. chapter 3) the surface current is less reliable therefore the double barrel configuration is more appropriate as it only requires a change in the shape of the droplet to detect contact with the surface. For example, if an experiment was designed to look for active inclusions on an otherwise passive surface (e.g aluminium) the double barrel approach would be suitable, as it would eliminate the risk of crashing the SECCM probe whilst scanning passive parts of the substrate. Additionally, if the expected behaviour of the substrate is unknown before performing SECCM, the double barrel method would be appropriate to remove the risk of crashing the probe. Finally, by referring to section 2.5 where some of the experimental challenges of applying SECCM to corrosion experiments was discussed, the stability of the droplet whilst physically changing the surface can be a challenge. The double barrel approach provides a feedback current that can give an indication of the droplet size during a scan. This information could be used to explain abnormalities in scan results.

In summary, the results presented in this thesis have shown that SECCM can be an effective tool to study corrosion related phenomena with high spatial resolution, which has been illustrated by the ability to probe the electrochemical behaviour of various microstructural features. Due to the continuous advances of the SECCM configuration in terms of resolution, speed, and environmental control, it follows that it will be possible to study a wider range of

corrosion systems in the near future. However, it is important to realise the experiments detailed in this thesis were designed with no particular industrial application in mind. It follows that in future corrosion studies, the application of SECCM to specific industrial requirements will serve as a true to test of the capabilities of the technique.